Université Pierre et Marie Curie

Sorbonne Universités

École doctorale de Physique en Île-de-France

Institut d'Astrophysique de Paris (IAP)
et
Institut de Physique Théorique (IPhT) du Commissariat à l'Énergie Atomique et aux Énergies Alternatives (CEA) de Saclay

Precision cosmology with the large-scale structure of the universe

par Hélène Dupuy

Thèse de doctorat en cosmologie

dirigée par Francis Bernardeau (chercheur CEA, directeur de l'IAP)

présentée et soutenue publiquement le 11/09/2015

devant un jury composé de (par ordre alphabétique) :

Dr.	Francis Bernardeau	IAP, CEA	Examinateur
Dr.	Diego Blas	CERN (TH-Division)	Examinateur
Pr.	Michael Joyce	LPNHE	Examinateur
Pr.	Eiichiro Komatsu	Max-Planck-Institut für Astrophysik	Rapporteur
Pr.	Julien Lesgourgues	RWTH Aachen University	Rapporteur
Dr.	Jean-Philippe Uzan	IAP, CNRS, IHP	Invité

Contents

Introduction

The title of my PhD thesis, "Precision cosmology with the large-scale structure of the universe", encompasses a wide range of searches, all equally exciting. Cosmology is an ancient questioning: understanding what the universe is made of, how it formed, how it evolved since then and what its future is. Yet it is entering a new era, whence the denomination *precision cosmology*. The investigation method is still the same, i.e. switching back and forth between observations of the sky and formulation of theories, but lately the level of description has amazingly evolved.

The twentieth century has been a golden period for cosmology. On the theoretical side, about a hundred years ago, Albert Einstein's general relativity ([64]) brought the mathematical tools allowing to represent appropriately time and space in a gravitation theory. Soon after appeared the first models based on this theory to describe the structure of the universe and its time evolution. The expansion of the universe has been discovered at the same epoch, jointly thanks to the observations of the astrophysicist Edwin Hubble (carried out and discussed between 1925 and 1929, [94]) and to the relativistic calculations of several theorists, such as Georges Lemaître (in 1927, [103]), Alexandre Friedmann (in 1922, [79]) and Willem de Sitter (in 1917, [53]). A cosmological model naturally emerged from the study of the physics at play in an expanding universe. It is the Big Bang theory, according to which the universe was born 13.8 billion of years ago (from a process called Big Bang and involving unimaginably high energies) and then progressively cooled down and dilated.

In this context, cooling down means dropping from a temperature[1] $T \sim 10^{19}$ GeV to $T \approx 2.73$ K. Such different temperatures lead perforce to extremely di-

[1] In cosmology, it is common to use the electronvolt as unit of temperature, or more precisely the electronvolt divided by the Boltzmann constant since 1 eV / $k_\mathrm{B} \approx 11604.5$ K, k_B being the Boltzmann constant ($k_\mathrm{B} = 1.3806488 \times 10^{-23}$ m^2.kg.s^{-2}.K^{-1}). In practice, one omits the Boltzmann constant so that T(K) $\approx 11604.5\ T$(eV).

versified physical processes. The chain of cosmological eras, each characterized by specific physical processes, is called thermal history of the universe. All stages of the thermal history are not equally understood. In particular, understanding mechanisms involving energies that are not accessible in laboratories is very challenging. Some epochs are thus described very speculatively. Conversely, the Big Bang nucleosynthesis and the recombination era are particularly well depicted. The former is the process during which nuclei heavier than the lightest isotope of hydrogen are created thanks to the trapping of protons and neutrons that previously freely evolved in the cosmic plasma ($T \sim 1$ MeV). The latter refers to the epoch at which electrons and protons first became bound to form electrically neutral hydrogen atoms ($T \sim 3000$ K).

One specificity of the Big Bang model is that it predicts the existence of a radiation which started to propagate freely about 380 000 years after the Big Bang. This "cosmic microwave background", detected incidentally in 1964 by the two physicists Arno Penzias and Robert Wilson ([128]), is nothing but the photons that emerged when the temperature of the cosmic plasma became lower than the temperature of ionization of hydrogen. Its detection was such a strong argument in favor of the Big Bang model that this discovery has been awarded the Nobel Prize in 1978. Nowadays, observing and studying carefully the cosmic microwave background is still one of the driving force of cosmology.

So far, the Big Bang model has not been ruled out by observations. Rather, each new set of cosmological data provided by exploration of space strengthens the so-called "standard model of cosmology". This model relies on the Big Bang theory and assumes the existence of a cosmological constant, which mimics the acceleration of the expansion of the universe, and of cold dark matter, a form of matter proposed in response to some unexpected observations.

More precisely, two observational projects realized in 1998 by the scientific teams headed by the cosmologists Saul Perlmutter, Brian P. Schmidt and Adam Riess showed independently that the expansion of the universe is accelerating ([129, 148]). This breakthrough has been honored with the Nobel Prize in 2011. Gravity being an attractive unstoppable force, astrophysicists originally thought that expansion could only decelerate. It has therefore been necessary to imagine a form of repulsive energy, capable of accelerating the expansion of the universe. This cosmic component of unknown nature has been called dark energy. In the standard model, it is characterized by a parameter denominated cosmological constant and repre-

senting about 70% of the energy content of the universe. Note nevertheless that several alternatives to the cosmological constant (and thus alternatives to the standard model) can be imagined to describe the same effect. At this time, it is still very difficult to determine which representation of dark energy is the most credible. Hopefully, the Euclid space mission ([157]), proposed in 2005 to the European Space Agency and whose launch is planned for 2020, will enrich (or even conclude) the debate.

Besides, many observations suggest the presence of an unfamiliar form of matter, invisible and with a non-zero mass, called dark matter. Dark matter would explain for instance why galaxies and clusters of galaxies seem much more massive when one studies their gravitational properties than when one infers their mass from the light they emit or why the cosmic microwave background displays spatial fluctuations too faint to initiate the formation of structures by gravitational instability (see more details about gravitational instability in section 1.1). In the standard model of cosmology, this dark matter is assumed to be cold, i.e. made of particles whose velocity is already much smaller than the speed of light in vacuum when it decouples from other species. Unveiling the nature and the properties of those dark elements is a major challenge, at the core of modern cosmology. It is the main *raison d'être* of the Euclid mission.

Another very puzzling piece of modern cosmology is cosmic inflation. It is an idea that arose in the late seventies-early eighties to complement the Big Bang model (see the foundational works of the physicists Alexei Starobinsky ([172]), Alan Guth ([84]) and Andrei Linde ([110])). According to this theory, the primordial universe underwent an extremely fast and violent phase of expansion. Adding this step to the thermal history of the universe is useful in many ways to get a coherent whole. However, the paradigm of inflation is not yet perfectly controlled theoretically.

The agreement between the standard model of cosmology and observational surveys is remarkably good. So, at the present time, most cosmologists focus their effort on the refinement of this model. The technical means available today allow to probe a huge quantity of astrophysical objects, of various nature, spread over very large areas of the sky. Specific developments, involving to a large extent numerical simulations and statistical physics, are necessary to deal with such an amount of data. But an exquisite exploration of the universe is useless if there is no comparable progress in theoretical cosmology.

The present thesis is a tiny illustration of the theoretical efforts currently re-

alized in order to anticipate a project such as the Euclid mission. As already mentioned, it has been designed primarily to examine the dark content of the universe. It will moreover supply a catalog of galaxies of unprecedented richness and refinement, showing how galaxies and clusters of galaxies arranged with time to form tremendous filaments, commonly referred to as "the large-scale structure of the universe".

The purpose of this thesis is twofold. A minor part of the time has been dedicated to a study designed to question a leading principle of cosmology, namely the cosmological principle. According to it, on very large scales[2] ($\gtrsim 100$ Mpc), the distribution of matter in the universe is homogeneous and isotropic. Many predictions of modern cosmology ensue from it. In collaboration with Dr. Jean-Philippe Uzan and his PhD student Pierre Fleury, I have participated in a project consisting in simulating observations of supernovae in an inhomogeneous model of the universe in order to infer the impact of inhomogeneities on cosmology. We highlighted in particular the fact that using the same kind of geometrical models to interpret observations corresponding to very different spatial scales could become inappropriate in the precision cosmology era (see chapter 1). The second topic I am specialized in is the enhancement of cosmological perturbation theory methods (see chapter 3 for a quick presentation of the current challenges of cosmological perturbation theory), especially within the nonlinear and/or relativistic regime(s). It is the main task developed in this thesis (see chapters 4, 5 and 6). In particular, I have proposed with my PhD advisor Dr. Francis Bernardeau a new analytic method, which is a multi-fluid approach, to study efficiently the nonlinear time evolution of non-cold species such as massive neutrinos (see chapter 2 for a modest overview of neutrino cosmology). This research project is at the interface between two topical subjects: neutrino cosmology and cosmological perturbation theory beyond the linear regime.

The manuscript is organized as follows. In chapter 1, I take the example of an analytic questioning of the cosmological principle, in which I participated, to illustrate what is at stake in precision cosmology. Chapter 2 introduces basics of neutrino cosmology, with an emphasis on the key role it plays in the study of the formation of the large-scale structure of the universe. In chapter 3, I present standard results of cosmological perturbation theory on which I based most of my PhD work. The three next chapters expose the developments that I realized with my advisor with the aim of incorporating properly massive neutrinos, or any non-

[2] pc stands for parsec, defined so that 1 pc$\approx 3.1 \times 10^{16}$m.

cold species, in analytic models of the nonlinear growth of structure. Chapter 4 presents the method and questions its accuracy. Chapter 5 shows that the results presented in chapter 3, valid for cold dark matter, can then partly be extended to massive neutrinos. Finally, in chapter 6, I explain how our method can be helpful to determine the scales at which nonlinear effects involving neutrinos are substantial and should be accounted for in models of structure formation.

Chapter 1

An illustration of what precision cosmology means

1.1 Is the cosmological principle stringent enough for precision cosmology?

A specificity of cosmology is that the system of interest is studied from inside. Furthermore, it is studied from a given position (the earth and surroundings) at a given time (epoch at which human beings are present on earth). Hence, since light propagates with a finite velocity and the universe has a finite age, only a portion of the universe can be reached observationally. This area is called observable universe and its boundary is called cosmological horizon. Consequently, cosmological models intended to describe the entire universe necessarily involve untestable assumptions (see e.g. [67] for discussions on this subject). In particular, as already mentioned, the standard model of cosmology relies on the cosmological principle, according to which the spatial distribution of matter is homogeneous and isotropic on large scales. This is encoded mathematically in the metric chosen to characterize the geometry of the universe, namely the Friedmann-Lemaître metric (see section 1.3.1).

Of course, the universe is not perfectly smooth. Otherwise, growth of structures from gravitational instability wouldn't have been achievable. It is indeed commonly assumed that density contrasts existed in the primordial universe and initiated the formation of the large-scale structure. More precisely, this scenario is encapsulated in the inflationary paradigm. During this stage, in theory, quantum fluctuations of a cosmic scalar field became macroscopic, generating fluctuations of the metric

([7, 85, 89, 173, 30, 122]). Those metric fluctuations then resulted into density fluctuations, as predicted by general relativity, and thus into gravitational instability. The study of the time evolution of such fluctuations is generally performed thanks to cosmological perturbation theory (see chapter 3). In practice, this means adding perturbations, assumed to be small compared with the background quantities, in the Friedmann-Lemaître metric.

In its minimal version (in particular, in the absence of neutrinos), the standard model of cosmology allows to summarize the properties of the universe in six parameters, called cosmological parameters. Defining them at this stage would be premature since none of the cosmological effects behind them has been introduced yet. Nevertheless, for the record, here is the list:

- the primordial spectrum amplitude A_{s},
- the primordial tilt n_{s},
- the baryon density ω_{B},
- the total non-relativistic matter density ω_{m},
- the cosmological constant density fraction Ω_Λ,
- the optical depth at reionization τ_{reion}.

Their values are not predicted by the model, whence the importance of constraining them observationally. Several kinds of sources provide this opportunity. The leading ones are Type Ia supernovae (SNIa), baryon acoustic oscillations (BAO) and the cosmic microwave background (CMB). A supernova is an astrophysical object resulting from the highly energetic explosion of a star. SNIa are particular supernovae whose spectra contain silicon but no hydrogen. They are useful in particular for the tracking of the expansion history of the universe. More precisely, they give information about the equation of state of dark energy (see e.g. [38, 146]). BAO are periodic fluctuations experimented by the baryonic[1] components of the universe and the knowledge of their properties brings also much to cosmology (see e.g. [5]). CMB observations provide an estimation of cosmological parameters with an exquisite precision, especially when combined with other astrophysical data ([137]).

[1] Baryonic means made of particles called baryons. In particular, all the matter made of atoms is baryonic.

Since its first detection, the CMB has been inspected in great detail by several satellites looking for anisotropies in it. The motivation of such an investigation is the evidence of a dipole anisotropy[2], presented in 1977 in [168] (which brought another Nobel Prize to cosmologists, this time George Fitzgerald Smoot and John C. Mather, in 2006). Higher order anisotropies[3] have then been measured by the satellites COBE (launched in 1989, [167]), WMAP (launched in 2001, [10, 90]) and Planck (launched in 2009, [134]). Those space projects are complementary to ground-based experiments ([145, 175, 165]) and to balloon-borne instruments such as BOOMERanG[4] (launched in late 1998, [52]) and Archeops (launched in 2002, [11]).

The combination "standard model of cosmology + perturbations" seems to be a satisfactory description. As proof, it is in agreement with most existing data. Such an accuracy is a bit surprising given the simplicity of the model and the thoroughness with which the observable universe is explored. For instance, it is assumed that the matter is continuously distributed. This involves in particular a smoothing scale, not explicitly given in the model ([68]). Besides, some observables used in cosmology are "point sources" and thus probe scales at which the cosmological principle does not hold (and furthermore scales that are not accessible by numerical simulations, see section 1.2.2 for more details). This is particularly true for SNIa, which emit very narrow beams probing scales smaller than[5] 1 AU. For this reason, it has been argued in several references that the use of the cosmological principle might lead to misinterpretations (see for instance [33]). This is precisely the kind of questioning raised by the precision cosmology era.

[2]The earth is in motion in the universe. Consequently, when cosmologists measure the temperature of the CMB, one of the celestial hemispheres appears hotter than the other one. This phenomenon is called dipole anisotropy.

[3]Higher order anisotropies are reflective of plasma oscillations that develop when the last scattering surface is reached. They superimpose over dipole anisotropies.

[4]The BOOMERanG experiment has brought a strong support to the inflationary paradigm by showing that the geometry of the universe is Euclidean.

[5]AU stands for astronomical unit, defined so that 1 AU $\approx 1.5 \times 10^{11}$ m.

1.2 Questioning the cosmological principle analytically

1.2.1 Redshift, luminosity distance and Hubble diagram

Redshift

The universe being in expansion, one can observe that galaxies are moving away from the earth. This phenomenon is called recession of galaxies and is not due to a genuine proper motion of galaxies. Galaxies (and other astrophysical objects) are in fact taken away by the dilatation of the universe itself, even if some of them have a proper motion oriented towards us. Because of this relative displacement, the observed wavelengths λ_{obs} are shifted to longer wavelengths (compared to the emitted ones λ_{em}). It is known as cosmological redshift, denoted z and defined so that (see section 1.3.4 for a more general interpretation)

$$z = \frac{\lambda_{\text{obs}} - \lambda_{\text{em}}}{\lambda_{\text{em}}}. \tag{1.1}$$

More precisely, in his contribution to the discovery of the expansion of the universe, Edwin Hubble brought to light a law stating that the recession velocity[6], v_{rec}, of galaxies is proportional to their distance[7] d. Actually, this relation had been previously found by Georges Lemaître but remained almost unnoticed since stated in French. It reads

$$v_{\text{rec}} = H_0 d, \tag{1.2}$$

it is called Hubble's law and H_0 is Hubble's constant. H_0 is usually not considered as part of the six cosmological parameters of the standard model of cosmology but it can be readily computed once those parameters are known[8]. Its value is currently estimated to be $H_0 = (67.8 \pm 0.9)$ km.s^{-1}.Mpc^{-1}([137]). To get information about the expansion of the universe, it is thus useful to make measurements of velocities (or equivalently redshifts) on the one hand and of distances on the other hand.

[6]The recession velocity is the observed velocity to which the peculiar velocity has been subtracted.

[7]The distance at play in Hubble's law is the distance between the source and the observer at the observation time. Because of expansion and since the speed of light is finite, this distance is larger than what it was at the emission time.

[8]Note nevertheless that, H_0 being in one-to-one correspondence with the standard cosmological parameter Ω_Λ, H_0 is sometimes considered as a cosmological parameter instead of Ω_Λ. In practice, the nuance is inconsequential (provided that dark energy is assumed to be a cosmological constant).

Luminosity distance

Distances are not directly measurable. What observers can measure when they probe the sky is e.g. the angular diameter between two points or the amount of energy collected by their telescopes. Cosmologists have introduced several definitions of distances from these observables. For instance, the "luminosity distance" of a source, D_{L}, is easy to define with the help of the intrinsic luminosity of the source L_{source} (energy emitted per unit of time) and of the observed flux F_{obs} (energy received per unit of time and surface). It is given by

$$L_{\mathrm{source}} = 4\pi D_{\mathrm{L}}^2 F_{\mathrm{obs}}. \tag{1.3}$$

SNIa are extremely bright. Furthermore, after their apparition in the sky, the time evolution of their brightness is very well known, which allows one to calibrate their intrinsic luminosity. Those particularities make them precious suppliers of luminosity distances. Such sources are often called standard candles.

Hubble diagram

Building diagrams luminosity distance versus redshift is an efficient way of probing the history of the expansion of the universe since redshifts and distances are related via cosmological parameters. Such diagrams, naturally called Hubble diagrams, are largely used in modern cosmology (see e.g. [2]). An example is given in figure 1.1.

1.2.2 Misinterpretation of Hubble diagrams

The main message of [33] is that, to meet the requirements of precision cosmology, it is crucial to model accurately the propagation of the ultra-narrow beams produced by SNIa. Otherwise, using those observables as widely as it is done in cosmology would be inappropriate.

The fact that there seems to be a paradox between the real universe and its smooth representation was already discussed in the sixties ([199, 50, 19, 83, 98, 144]). More recently, consequences regarding the interpretation of Hubble diagrams have been studied. In particular, according to general relativity, the presence of massive objects (such as clusters of galaxies) affects the geometry of the universe. Since the way light propagates depends on the geometry, this results into a modification of the observed luminosity of sources. This phenomenon is called gravitational

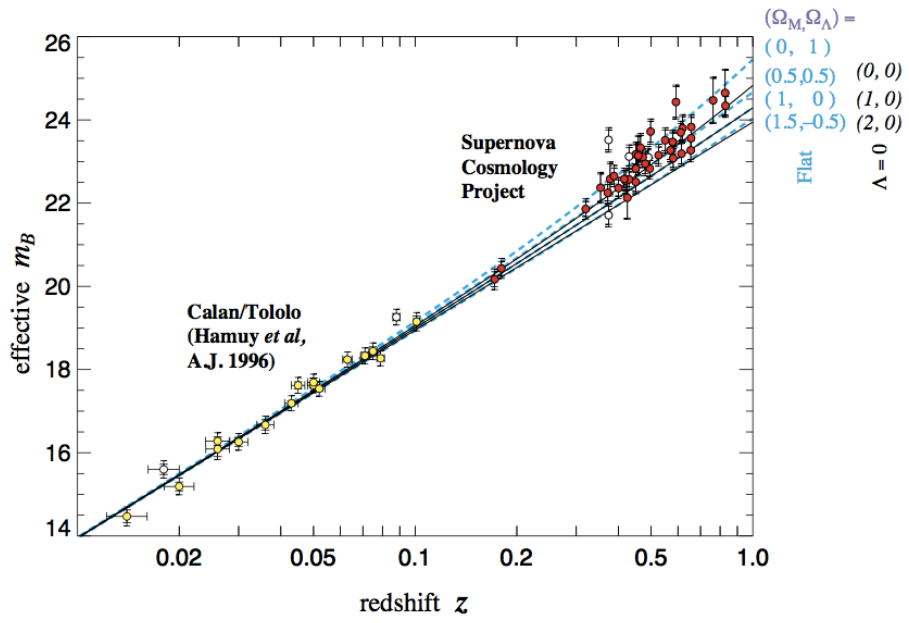

Figure 1.1: One example of a Hubble diagram. It has been obtained from the observation of 42 high-redshift SNIa of the *Supernova Cosmology Project* and 18 low-redshift SNIa of the *Calàn/Tololo Supernova Survey*. m_B is the apparent magnitude in the spectral band B, the magnitude m being related to L_{source} via $m = -2.5 \log L_{\text{source}} + 4.76$. Authors: Perlmutter *et al.*, [129].

lensing and it has been pointed out that it probably induces a scattering in Hubble diagrams ([99, 80, 191, 190, 192]). Because of the thinness of the beams emitted by SNIa, such beams spend most of their propagation time in underdense regions (and rarely, but sometimes, encounter clusters of matter). They are *a priori* too narrow for the effects of such fluctuations of density to be negligible. Yet, Hubble diagrams are interpreted assuming that the geometry of the universe is on average homogeneous and isotropic.

Perturbative approaches, i.e. descriptions in which perturbations are added in the metric, have been proposed ([92, 39, 54]). However, in these works, there is still a smoothing scale at play. It is of the order of 1 arcminute[9] whereas lensing dispersion arises to a large extent from subarcminute scales (see e.g. [48]). Besides, performing an average is problematic since SNIa probe the sky in directions where the density of matter encountered is smaller than the cosmological average (contrary

[9]The arcminute is a unit of angular measurement defined so that $1^\circ = 60$ arcminutes.

to the beams of BAO and CMB, which are large enough for the average density encountered to be representative of the overall cosmological density, [195]). Hubble diagrams are thus prone to an observational selection effect. All these problems are discussed in detail in [33].

Numerical simulations are an alternative to analytic modeling which can take inhomogeneities into account. However, it has been argued in [33] that, because of the limitation in resolution, only the distribution of matter encountered by beams larger than a few tens of kpc can be accurately described by N-body simulations. It is much wider than the characteristic diameter of a SNIa light beam.

1.2.3 An idea to test analytically the impact of inhomogeneities

Since a theoretical study seems necessary to investigate the way in which inhomogeneities affect the aspect of Hubble diagrams, we decided to elaborate analytically a toy model, representing a very inhomogeneous universe, and to study propagation of light in it. More precisely, we chose to consider a geometry of the type "Swiss cheese". Swiss-cheese configurations are obtained from a homogeneous and isotropic basis (i.e. a Friedmann-Lemaître metric) by removing spheres of matter at some places and replacing them by point masses, equal to the mass removed (see figure 1.2 for an illustration and [65, 158] for the cornerstones of Swiss-cheese representations).

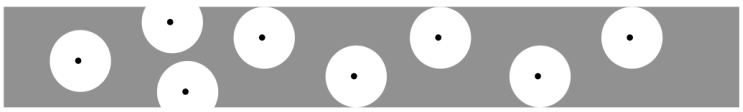

Figure 1.2: A Swiss-cheese configuration. The background is homogeneous. Spheres are empty except at their centers, where a point mass is present. The point mass is equal to the density of the background multiplied by the volume of the blank area surrounding it.

Our model is not intended to be realistic but rather to test the impact of inhomogeneities on light propagation. From a theoretical point of view, it is as justified as the standard homogeneous and isotropic description because it is an exact solution of general relativity which preserves the global dynamics (see section 1.3 for more details).

As a first step, we studied analytically the effect of light crossing a single hole

and implemented it in a Mathematica program. It was then easy to predict the effect of several holes. We proposed to do it with the help of Wronski matrices (see our paper, presented in section 1.5). Eventually, we simulated Hubble diagrams by imagining SNIa beams evolving in our Swiss-cheese universe. To do this, we took inspiration from the SNLS 3 data set ([38]).

The cosmological parameters of this mock universe being under control, we have been able to test the impact of inhomogeneities on cosmology (see section 1.4).

Note that using Swiss-cheese models to study the effect of inhomogeneities is not new at all. The specificity of our study is that it is neither a "modern" Lemaître-Tolman-Bondi (LTB) solution, which is an extension of Swiss-cheese solutions in which point masses are replaced by continuous gradients of density (here is only a sample of the existing LTB studies: [31, 116, 24, 185, 32, 35, 183, 176, 74, 200, 72, 73, 143, 151, 150, 121, 40, 149, 70]) nor a real step backwards into the original works on Swiss-cheese models ([98] and [62]) because our investigation is totally embedded in the framework of modern cosmology. Actually, we were interested in testing a discontinuous distribution of matter, which is not the case for LTB or perturbative approaches, in order to avoid the compensation effects due to a finite smoothing scale. Consequently, we did not expect to obtain results similar to those of the literature.

1.3 Generalities about propagation of light in a Swiss-cheese model

Rather than starting with general considerations about general relativity, I will merely introduce progressively the concepts that help to understand my PhD work. Comprehensive presentations of general relativity suited to the study of cosmology can be found in a broad collection of references (see in particular the indispensable [193] and [120]).

1.3.1 The homogeneous background

The standard model of cosmology assumes that gravitation is well described by general relativity. In general relativity, time and space are not independent quantities, whence the use of the concept of spacetime. In standard cosmology, spacetimes encompass four dimensions and are mathematically characterized by a quantity

called metric. The Friedmann-Lemaître metric emerges naturally when one wants to write a metric in agreement with the cosmological principle and simple enough for analytic calculations to be manageable. Its expression is (see e.g. [194] for a demonstration)

$$\mathrm{d}s^2 = -\mathrm{d}T^2 + a^2(T)\gamma_{ij}\left(x^k\right)\mathrm{d}x^i\mathrm{d}x^j. \tag{1.4}$$

Geometrically, $\mathrm{d}s^2$ is the square of the distance separating two points of the spacetime infinitely close to each other, or equivalently the self scalar product of the infinitesimal vector separating them. In this expression, units are chosen so that the speed of light in vacuum, c, is equal to unity and Latin indices run from 1 to 3. Besides, the Einstein convention is used, which means that a summation over repeated indices is implicitly assumed. In other words, one postulates

$$\gamma_{ij}\left(x^k\right)\mathrm{d}x^i\mathrm{d}x^j \equiv \sum_{i=1}^{3}\sum_{j=1}^{3}\gamma_{ij}\left(x^k\right)\mathrm{d}x^i\mathrm{d}x^j. \tag{1.5}$$

The Einstein convention will be used in all this manuscript. In relativity, time depends on the frame in which it is measured. The proper time of an observer is the time corresponding to his rest frame. The cosmic time T that appears in (1.4) is the proper time of comoving observers, who are by definition observers moving along with the Hubble flow[10] (without peculiar velocity). $a(T)$ is an arbitrary function of the cosmic time. In cosmology, it is called scale factor and it encodes the expansion of the universe, i.e. distances are expected to grow like $a(T)$ in a Friedmann-Lemaître metric[11]. This is the reason why the derivation of the metric (1.4) by A. Friedmann and G. Lemaître in 1922 and 1927 is regarded as part of the discovery of the expansion of the universe. So expansion appears spontaneously when general relativity is applied to cosmology. However, when he published the first cosmological solution of the Einstein equations[12] in 1917, A. Einstein introduced artificially a quantity called cosmological constant to force the universe to be static. It is the observation of the recession of galaxies by E. Hubble that made him eventually

[10]The Hubble flow is the recession motion due to expansion.

[11]It is important to have in mind that it is true for "cosmological" distances only, that is to say for the very high distances separating objects that do not interact via electromagnetic forces or form gravitationally bound systems. For example, it is not true within the solar system or between the atoms of macroscopic objects.

[12]The Einstein equations are fundamental equations of general relativity describing gravitation as a result of a curvature of spacetime by matter and energy.

accept the idea of an expanding universe. Nowadays, the cosmological constant has been reintroduced in the standard model of cosmology to mimic dark energy. The quantities x^k of (1.4) are space coordinates called comoving coordinates. Lastly, γ_{ij} are equal-time hypersurfaces, that is to say the geometrical figures obtained in the four-dimensional spacetime when imposing a given value to T. Assuming that in the universe space has a constant curvature K, one can show that there are only three possible expressions for γ_{ij} (see e.g. [131]):

$$\begin{cases} \gamma_{ij}\mathrm{d}x^i\mathrm{d}x^j = \mathrm{d}\chi^2 + \dfrac{1}{K}\sin^2(\sqrt{K}\chi)\mathrm{d}\Omega^2, \\ \gamma_{ij}\mathrm{d}x^i\mathrm{d}x^j = \mathrm{d}\chi^2 + \chi^2\mathrm{d}\Omega^2, \\ \gamma_{ij}\mathrm{d}x^i\mathrm{d}x^j = \mathrm{d}\chi^2 - \dfrac{1}{K}\sinh^2(\sqrt{-K}\chi)\mathrm{d}\Omega^2, \end{cases} \tag{1.6}$$

where χ is a radial coordinate, $\mathrm{d}\Omega^2 = \mathrm{d}\theta^2 + \sin^2\theta\mathrm{d}\varphi^2$ is the infinitesimal solid angle, φ varies from 0 to 2π, θ from $-\pi$ to π, $\sqrt{|K|}\chi$ from 0 to π when $K > 0$ and from 0 to $+\infty$ otherwise. The first possibility, for which $K > 0$, is characteristic of a space with a spherical geometry. The second one, for which $K = 0$, corresponds to an Euclidean geometry. The last one, for which $K < 0$, describes a hyperbolic geometry.

The Friedmann-Lemaître metric is often written using another definition of time, called conformal time. It is denoted η and it satisfies

$$\mathrm{d}\eta = \frac{\mathrm{d}T}{a(T)}. \tag{1.7}$$

In this framework, the metric reads

$$\mathrm{d}s^2 = a^2(\eta)\left(-\mathrm{d}\eta^2 + \gamma_{ij}\mathrm{d}x^i\mathrm{d}x^j\right). \tag{1.8}$$

The equations describing the time evolution of the scale factor are obtained from the Einstein equations. When they are written in the Friedmann-Lemaître metric, one gets (see [194] or any cosmology course)

$$H^2 = \frac{\kappa}{3}\rho - \frac{K}{a^2} + \frac{\Lambda}{3} \tag{1.9}$$

and

$$\frac{1}{a}\frac{\mathrm{d}^2a}{\mathrm{d}T^2} = -\frac{\kappa}{6}(\rho + 3P) + \frac{\Lambda}{3}. \tag{1.10}$$

H is the Hubble parameter, defined as $H \equiv \frac{1}{a}\frac{\mathrm{d}a}{\mathrm{d}T}$. It gives the velocity at which the universe expands. Λ is a cosmological constant. One can note that Λ could be intentionally fine-tuned to impose a static universe (like A. Einstein initially did) but in general there is no reason for H to be zero. $\kappa \equiv 8\pi G$, G being the gravitational constant, and ρ is the energy density of a cosmic fluid with a pressure P. Those equations are called Friedmann equations. The time evolution of the scale factor being given by second order equations, in addition to H, another observable is necessary to probe the expansion of the universe. It is generally incarnated by the deceleration parameter, denoted q and defined as

$$q = -\frac{\ddot{a}a}{\dot{a}^2}, \tag{1.11}$$

where a dot stands for a time derivative. Equivalently, with the conformal time, the Friedmann equations read

$$\mathcal{H}^2 = \frac{\kappa}{3}\rho a^2 - K + \frac{\Lambda}{3}a^2, \tag{1.12}$$

$$\frac{\mathrm{d}\mathcal{H}}{\mathrm{d}\eta} = -\frac{\kappa}{6}a^2\left(\rho + 3P\right) + \frac{\Lambda}{3}a^2, \tag{1.13}$$

where $\mathcal{H} \equiv \frac{1}{a}\frac{\mathrm{d}a}{\mathrm{d}\eta}$. In our study, we consider pressureless fluids only and we use those results in the homogeneous background of the Swiss-cheese spacetime.

1.3.2 Geometry inside the holes

In astrophysics, it is common to study the gravitational field caused by objects with a spherical symmetry. There exists in general relativity an equivalent of Gauss's law for Newtonian gravity, according to which the gravitational field outside a spherical object depends on the mass of this object only (and thus not on its structure). When a cosmological constant is taken into account, it is encoded in a metric known as the Kottler metric. It has been derived independently by Kottler in 1918 ([102]) and Weyl in 1919 ([197]). It is given by

$$\mathrm{d}s^2 = -A(r)\mathrm{d}t^2 + A^{-1}(r)\mathrm{d}r^2 + r^2\mathrm{d}\Omega^2, \tag{1.14}$$

where

$$A(r) = 1 - \frac{2GM}{r} - \frac{\Lambda r^2}{3}. \tag{1.15}$$

M is the mass of the astrophysical object considered, t is a time coordinate, r a radial coordinate, Λ a cosmological constant and $\mathrm{d}\Omega^2$ the infinitesimal solid angle. For $\Lambda = 0$, this metric is known as the Schwarzschild metric, which is a solution of the Einstein equations derived in 1915 by the astrophysicist Karl Schwarzschild. The Schwarzschild metric is the first solution of general relativity that includes a mass, allowing to study the gravitational effect of e.g. stars, planets or certain types of black holes.

1.3.3 Junction of the two metrics

In order to be a spacetime well-defined in the sense of general relativity, the spacetime resulting from the junction of the Friedmann-Lemaître and Kottler metrics must satisfy the Israel junction conditions ([96]). They impose continuity of two quantities, namely the induced metric and the extrinsic curvature, on junction hypersurfaces. In our study, junction hypersurfaces Σ are given by

$$\Sigma \equiv \{\chi = \chi_\mathrm{h}\}, \tag{1.16}$$

where χ_h is a constant, in the Friedmann-Lemaître metric and by

$$\Sigma \equiv \{r = r_\mathrm{h}(t)\} \tag{1.17}$$

in the Kottler metric.

Continuity of the induced metric

If the coordinates of the Friedmann-Lemaître metric are $X^\alpha = \{T, \chi, \theta, \phi\}$, one can define "intrinsic coordinates" on Σ as[13] $\sigma^a = \{T, \theta, \phi\}$. The parametric equation of the hypersurface (1.16) is therefore $\bar{X}^\alpha(\sigma^a) = \{T, \chi_\mathrm{h}, \theta, \phi\}$. What is called induced metric is the quantity

$$h_{ab} = g_{\alpha\beta}\, j_a^\alpha\, j_b^\beta. \tag{1.18}$$

[13] Latin indices run from 1 to 3 whereas Greek indices run from 0 to 3, the 0 index corresponding to the time coordinate.

$g_{\alpha\beta}$ is the metric tensor of the spacetime in which the hypersurface is immersed. It means that, in this spacetime, the scalar product is given by

$$\vec{u}.\vec{v} = g_{\alpha\beta}u^{\alpha}v^{\beta}. \tag{1.19}$$

It imposes in particular $\mathrm{d}s^2 = g_{\alpha\beta}\mathrm{d}x^{\alpha}\mathrm{d}x^{\beta}$. So the coordinates of the Friedmann-Lemaître metric tensor are given in (1.4) and those of the Kottler metric tensor are given in (1.14). Besides, one defines j_a^{α} as

$$j_a^{\alpha} = \frac{\partial \bar{X}^{\alpha}}{\partial \sigma^a}. \tag{1.20}$$

Similarly, in the Kottler regions, one introduces $X^{\alpha} = \{t, r, \theta, \phi\}$ and one defines intrinsic coordinates as $\sigma^a = \{t, \theta, \phi\}$, whence $\bar{X}^{\alpha}(\sigma^a) = \{t, r_{\mathrm{h}}(t), \theta, \phi\}$.

Using those definitions, the relations imposed by the continuity of the induced metric are eventually

$$\begin{cases} r_{\mathrm{h}}(t) = a(T)\chi_{\mathrm{h}}, \\ \dfrac{\mathrm{d}T}{\mathrm{d}t} = \sqrt{A\left(r_{\mathrm{h}}\right) - \dfrac{1}{A\left(r_{\mathrm{h}}\right)}\left(\dfrac{\mathrm{d}r_{\mathrm{h}}}{\mathrm{d}t}\right)^2}. \end{cases} \tag{1.21}$$

Continuity of the extrinsic curvature

By definition, if the unit vector normal to the hypersurface Σ is denoted n_{μ} and if one calls K_{ab} the extrinsic curvature of this hypersurface, one has

$$K_{ab} = n_{\alpha;\beta}\ j_a^{\alpha}\ j_b^{\beta}. \tag{1.22}$$

I use here the notation " **;** " to indicate a covariant derivative. Its definition can be found in any course in general relativity: for any vector T^{ν},

$$T^{\nu}_{\ ;\mu} = \nabla_{\mu}T^{\nu} = \partial_{\mu}T^{\nu} + \Gamma^{\nu}_{\mu\alpha}T^{\alpha}, \tag{1.23}$$

where the notation ∂_{μ} stands for $\dfrac{\partial}{\partial x^{\mu}}$ and where $\Gamma^{\nu}{}_{\mu\alpha}$ are the Christoffel symbols, related to the metric tensor via

$$\Gamma^{\nu}{}_{\mu\alpha} = \frac{1}{2}g^{\nu\sigma}\left(\partial_{\mu}g_{\sigma\alpha} + \partial_{\alpha}g_{\mu\sigma} - \partial_{\sigma}g_{\mu\alpha}\right), \tag{1.24}$$

with $g^{\alpha\sigma}g_{\sigma\beta} = \delta^{\alpha}{}_{\beta}$, $\delta^{\alpha}{}_{\beta}$ being the Kronecker symbol, i.e. $\delta^{\alpha}{}_{\beta} = 1$ if $\alpha = \beta$ and 0 otherwise. Let us mention here a useful property of the metric tensor allowing to raise and lower indices of vectors conveniently: the metric tensor is defined so that

$$u_\alpha = g_{\alpha\beta}u^\beta \text{ and } u^\alpha = g^{\alpha\beta}u_\beta. \tag{1.25}$$

Generally, the unit vector normal to a hypersurface defined by $\{q = ...\}$ is given by

$$n_\mu = \frac{\partial_\mu q}{\sqrt{g^{\alpha\beta}\ \partial_\alpha q\ \partial_\beta q}}. \tag{1.26}$$

When imposing continuity to K_{ab}, the whole calculation gives finally on Σ

$$\begin{cases} \dfrac{r_\mathrm{h}\ A\left(r_\mathrm{h}\right)}{\sqrt{A\left(r_\mathrm{h}\right) - \dfrac{1}{A\left(r_\mathrm{h}\right)}\left(\dfrac{\mathrm{d}r_\mathrm{h}}{\mathrm{d}t}\right)^2}} = a(T)\chi_\mathrm{h}, \\ 3\left(\dfrac{\mathrm{d}r_\mathrm{h}}{\mathrm{d}t}\right)^2 \partial_r A\left(r = r_\mathrm{h}\right) - 2\dfrac{\mathrm{d}^2 r_\mathrm{h}}{\mathrm{d}t^2} A\left(r_\mathrm{h}\right) - A^2\left(r_\mathrm{h}\right)\ \partial_r A\left(r = r_\mathrm{h}\right) = 0. \end{cases} \tag{1.27}$$

Consequences on the properties of the holes

Equations (1.21) and (1.27) govern the dynamics of the hole boundary by connecting the time and space coordinates of the two metrics. When combined with (1.10), they impose equality between the cosmological constants of the two metrics and the (almost intuitive) relation

$$M = \frac{4\pi}{3}\rho a^3 f_K^3(\chi_h), \tag{1.28}$$

where

$$f_K(\chi) = \frac{\sin\sqrt{K}\chi}{\sqrt{K}},\quad \chi \quad \text{or} \quad \frac{\sinh\sqrt{-K}\chi}{\sqrt{-K}} \tag{1.29}$$

respectively for a positive, zero or negative spatial curvature. Note that, in the Friedmann-Lemaître metric, the hole boundaries χ_h are defined with comoving coordinates, i.e. with coordinates not affected by expansion. Hence, holes are not expected to overlap at any stage.

Such constraints ensure that the holes inserted in the homogeneous background do not modify its global dynamics. The resulting spacetime is indeed an exact

solution of the Einstein equations. In this context, it is possible to insert as many holes as one wants provided that holes do not overlap initially.

1.3.4 Light propagation

Geodesics

The equivalence principle is a pillar of gravitation theory. In classical mechanics, it predicts that the acceleration of massive objects in free fall (i.e. falling under the sole influence of gravity) does not depend on their masses. In other words, gravitation appears as a property of space rather than of objects themselves.

In general relativity, it is reflected by the use of the concept of geodesics. The successive positions occupied by free-falling objects in spacetime are interpreted as a consequence of a bending of this spacetime. Those trajectories, or "world lines", are called geodesics. In metrics with a signature[14] $(-,+,+,+)$, geodesics are curves that extremize the "distances" $\mathrm{d}s^2$ between two points. More precisely, time-like[15] geodesics maximize the distances between time-like world lines connecting two points; space-like[16] geodesics minimize the distances between space-like world lines connecting two points; null[17] geodesics are defined so that the distances between null world lines connecting two points are zero.

To study the propagation of light rays in a spacetime, one thus has to write that photons are particles following null geodesics. The mathematical implementation suited to our study is given in our paper (see section 1.5).

As an illustration, for a null geodesic of a Friedmann-Lemaître universe, (1.4) gives

$$\frac{\mathrm{d}T^2}{a^2(T)} = \gamma_{ij}\left(x^k\right)\mathrm{d}x^i\mathrm{d}x^j. \tag{1.30}$$

[14] With a signature $(-,+,+,+)$ means that there exists a basis in which the scalar product between two 4-dimensional vectors with coordinates (u^0,u^1,u^2,u^3) and (v^0,v^1,v^2,v^3) is $-u^0v^0+u^1v^1+u^2v^2+u^3v^3$. It is the case for the metrics (1.4) and (1.14).

[15] A time-like vector is a vector whose self scalar product is negative and a time-like world line is a curve whose tangent vectors are in any point time-like vectors.

[16] A space-like vector is a vector whose self scalar product is positive and a space-like world line is a curve whose tangent vectors are in any point space-like vectors.

[17] A null vector is a non-zero vector whose self scalar product is zero and a null world line is a curve whose tangent vectors are in any point null vectors.

In the particular case of a radial trajectory[18], for which $\mathrm{d}\Omega^2 = 0$, it leads to

$$\frac{\mathrm{d}T}{a(T)} = \mathrm{d}\chi. \tag{1.31}$$

Let us imagine two photons emitted at times T_1 and $T_1 + \delta T_1$ and observed at times T_0 and $T_0 + \delta T_0$. Since χ is a comoving distance, it is a constant, whence

$$\chi = \int_{T_0}^{T_1} \frac{\mathrm{d}T}{a(T)} = \int_{T_0+\delta T_0}^{T_1+\delta T_1} \frac{\mathrm{d}T}{a(T)}. \tag{1.32}$$

Subtracting integration over the time interval $[T_0 + \delta T_0, T_1]$ on each side, one gets

$$\int_{T_0}^{T_0+\delta T_0} \frac{\mathrm{d}T}{a(T)} = \int_{T_1}^{T_1+\delta T_1} \frac{\mathrm{d}T}{a(T)}. \tag{1.33}$$

If the lags are assumed to be very small compared to T_0 and T_1, the scale factor is expected to be almost constant in (1.33). In this context, one can write

$$\frac{\delta T_0}{a(T_0)} \approx \frac{\delta T_1}{a(T_1)}. \tag{1.34}$$

Furthermore, one can decide that δT_1 is the period of the electromagnetic wave at emission. In that case, δT_0 is the period of the electromagnetic wave measured by the observer. Denoting λ_1 and λ_0 the associated wavelengths, one has (see (1.1))

$$\frac{a(T_0)}{a(T_1)} = \frac{\lambda_0}{\lambda_1} = 1 + z. \tag{1.35}$$

The cosmological redshift can thus be interpreted as a witness of the time evolution of the expansion rate of the universe.

Light beams

Despite their narrowness, beams emitted by SNIa have a finite section. They are collections of light rays. A study of the relative displacements between the rays is therefore required to infer the deformation of the beams, and consequently the change in luminosity distance, induced by the presence of structures in the space-time. It is encoded in the geodesic deviation equation, which governs the time evolution of the "separation vectors" that connect the geodesics of a beam. It is

[18] One can show that such trajectories are indeed geodesics, that is to say that they obey equations of general relativity called geodesic equations. They can be found in any general relativity book.

obtained by considering two geodesics γ_0 and γ_1 described by $x^\mu(\lambda)$, x^μ being the coordinates and λ an affine parameter[19]. Then, between γ_0 and γ_1, one defines a collection of geodesics, each of them being associated with a label $s \in [0,1]$ (γ_0's label is 0 and γ_1's label is 1). To indicate both the geodesic considered and the value of the affine parameter, one uses the notation $x^\mu(\lambda, s)$. Besides, maintaining λ constant and varying s, one gets another collection of curves (which are not geodesics in general). The separation vectors $\xi^\mu = \partial_s x^\mu$ are tangent to this collection of curves and establish a connection between the geodesics. Besides, the vectors $k^\mu = \partial_\lambda x^\mu$ are tangent to the null geodesics (see figure 1.3 and more details in the paper presented in section 1.5).

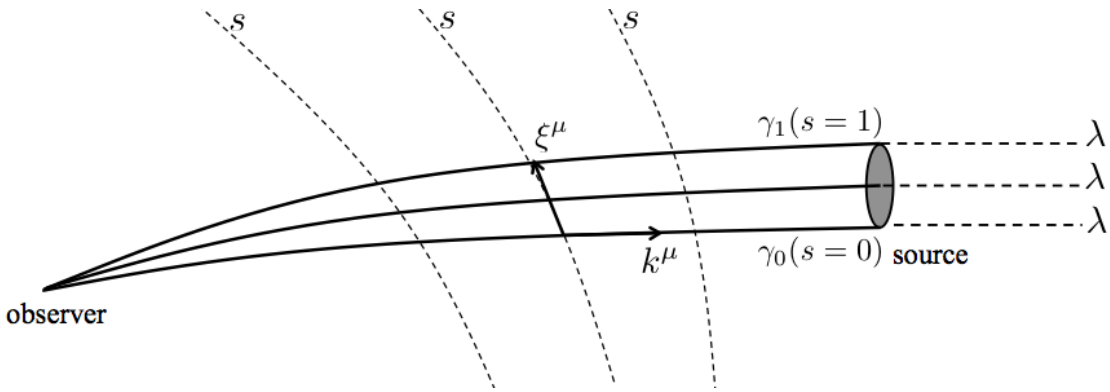

Figure 1.3: A geodesic bundle.

Let us define the acceleration of the separation vector:

$$\frac{\mathrm{D}^2\xi^\mu}{\mathrm{D}\lambda^2} = \nabla_\nu \left(k^\beta \nabla_\beta \xi^\mu\right) k^\nu. \tag{1.36}$$

In a flat spacetime, it is zero because in that case geodesics are straight lines so the variation of ξ^μ with λ is necessarily linear. Hence, a non zero acceleration reveals a curvature. In general relativity, it means that one expects this acceleration to be proportional to the Riemann tensor[20] $R^\mu{}_{\gamma\beta\nu}$. Noticing that $k^\beta \nabla_\beta \xi^\alpha = \xi^\beta \nabla_\beta k^\alpha$ and using the geodesic equation $k^\nu \nabla_\nu k^\mu = 0$, one can see that the quantity $\xi^\mu k_\mu$ is conserved along the geodesic γ_0 $\left(\dfrac{\mathrm{d}\left(\xi^\mu k_\mu\right)}{\mathrm{d}\lambda} = 0\right)$. Consequently, one can parametrize

[19] An affine parameter λ is a parameter defined so that the geodesic equations governing the behavior of geodesics described by $x^\alpha(\lambda)$ take the form $\dfrac{\mathrm{d}^2 x^\alpha}{\mathrm{d}\lambda^2} + \Gamma^\alpha{}_{\mu\nu} \dfrac{\mathrm{d}x^\mu}{\mathrm{d}\lambda} \dfrac{\mathrm{d}x^\nu}{\mathrm{d}\lambda} = 0$.

[20] By definition, $R^\mu{}_{\nu\alpha\beta} = \partial_\alpha \Gamma^\mu{}_{\nu\beta} - \partial_\beta \Gamma^\mu{}_{\nu\alpha} + \Gamma^\mu{}_{\sigma\alpha}\Gamma^\sigma{}_{\nu\beta} - \Gamma^\mu{}_{\sigma\beta}\Gamma^\sigma{}_{\nu\alpha}$.

the curves so that, on γ_0, ξ^μ and k^μ are always orthogonal ($\xi^\mu k_\mu = 0$). The same properties allow to compute the acceleration of γ_1 with respect to γ_0 (see e.g. [131]):

$$\frac{\mathrm{D}^2\xi^\mu}{\mathrm{D}\lambda^2} = -\xi^\beta R^\mu{}_{\gamma\beta\nu} k^\gamma k^\nu \quad . \tag{1.37}$$

It is the geodesic deviation equation.

Once projected on a judicious basis, it leads to the so-called Sachs equation and finally the separation vectors can be related to observables such as the luminosity distance (see our paper, section 1.5).

Strategy adopted to determine the light path

In practice, what we did to determine the light path between a source and an observer is to start from the observer (assumed to stand in the Friedmann-Lemaître region) and to reconstruct, step by step, the trajectory of photons back to the source. The first step is the identification of the coordinates corresponding to a photon leaving the last hole encountered before reaching the observer (resolution of the geodesic equation in the Friedmann-Lemaître metric). Next, the resolution of the Sachs equation gives the behavior of the separation vector. It is then necessary to switch to the Kottler metric to infer the deviation caused by the point mass inside the hole. Identification of the geodesics relies on two conservation laws which reflect that the Kottler metric is static[21] and with a spherical symmetry. It gives the coordinates associated with the event corresponding to photons entering the last hole. Then the Sachs equation is integrated again and one goes back to the Friedmann-Lemaître metric. One can iterate this procedure for an arbitrary number of holes, until one assumes that the source has been reached. Throughout the whole calculation, the evolution of the wavenumber is also studied, which gives the evolution of the cosmological redshift of the source (by comparing the wavenumber at emission and reception times). Thanks to the resolution of the Sachs equation, the luminosity distance is also part of the traceable observables. Consequently, Hubble diagrams can be computed once the observation conditions, the distribution of the holes, the value of the point masses and the redshifts of the sources are specified (full details are given in section 1.5). Besides, they can be easily compared to what they would be in a configuration similar but with no hole.

[21] The fact that it is static is a consequence of Birkhoff's theorem, see e.g. [69].

1.4 Impact of inhomogeneities on cosmology

Cosmological parameters are omnipresent in the equations of our study so the aspect of Hubble diagrams strongly depends on them. We therefore introduced the quantities

$$\Omega_\Lambda = \frac{\Lambda}{3H_0^2}, \quad \Omega_\mathrm{m} = \frac{8\pi G\rho_0}{3H_0^2}, \quad \Omega_\mathrm{K} = -\frac{K}{a_0^2 H_0^2}, \tag{1.38}$$

where an index 0 indicates that the quantity is evaluated at present time. Ω_Λ is one of the six cosmological parameters of the standard model of cosmology. It characterizes the amount of dark energy in the universe. According to [135], results from the Planck satellite lead to the 1σ-constraint[22] $\Omega_\Lambda = 0.686 \pm 0.020$ (the meaning of "1σ-constraint" is given below.). Ω_m characterizes the amount of non-relativistic matter (and is related to the standard cosmological parameter ω_m via $\omega_\mathrm{m} = \Omega_\mathrm{m} h^2$, with h defined so that $H_0 = 100\ h$ km.s^{-1}). It is the sum of the amounts of baryonic matter and cold dark matter. Still from [135] and with the same precision, one estimates $\Omega_\mathrm{m} = 0.315 \pm 0.017$. Ω_K indicates what the spatial curvature of the universe is. It is given by $\Omega_\mathrm{K} = 1 - \Omega_\Lambda - \Omega_\mathrm{m}$. Observational constraints are therefore compatible with $\Omega_\mathrm{K} = 0$, which means that the universe can reasonably be assumed to have a flat geometry.

On the one hand, we used our Hubble diagrams as mock data and tried to interpret them assuming a homogeneous and isotropic geometry. More precisely, we used the Chi-Square Goodness of Fit Test to estimate the values of the parameters (1.38) that best fit the resulting diagrams when the spacetime is entirely characterized by the Friedmann-Lemaître metric. Generally, this test summarizes the discrepancy between observed values O (here the mock data) and the values E expected under the model in question (here the homogeneous model). The generic formula is

$$\chi^2 = \sum_{\text{data}} \frac{(O-E)^2}{\Delta^2}, \tag{1.39}$$

where Δ is an observational error bar[23]. The values of χ^2 give the best fit, i.e. the values of E that best match observations, and confidence contours, i.e. areas in parameter space in which the parameters are expected to lie with a probability

[22] This estimation is yet highly model dependent.
[23] In our study, we estimated Δ by imitating a real catalog of SNIa observations.

exceeding a given value[24] (see e.g. [141] for more details). We found that the estimated cosmological parameters can be very different from the actual parameters characterizing the Swiss-cheese spacetime in which we simulated light propagation. In other words, in some cases, the homogeneity assumption largely affects the estimation of the cosmological parameters (see the detailed study in section 1.5).

Another test we performed is the estimation of the cosmological parameters of the Swiss-cheese model that best reproduce real observations. Using the same χ^2 method, we found that replacing a Friedmann-Lemaître model by a Swiss-cheese one can in some cases induce a significant (regarding the accuracy intended by precision cosmology, i.e. a few percent) difference in the prediction of the parameters (see section 1.5). It required in particular to estimate analytically a luminosity distance-redshift relation of a Swiss-cheese universe. Evaluating such effects is an important issue since the 2013 Planck results ([135]) highlighted a tension between the estimation of H_0 and Ω_m from CMB observations and their estimation from other observables, such as SNIa. In the paper presented in section 1.6, we demonstrate that Swiss-cheese descriptions make possible the reconciliation between the values of Ω_m inferred from Planck and from SNIa. This is illustrated in figure 1.4.

Besides, the 2015 Planck results ([137]) show that the estimation of H_0 from Planck is in fact consistent with its estimation from the recent "Joint Light-curve Analysis" sample of SNIa (constructed from the SNLS and SDSS supernovae data, together with several samples of low redshift supernovae, [20]).

[24] For a Gaussian probability distribution of the parameters, we call "1σ-contours" the contours associated with a 68.3% probability, "2σ-contours" the contours associated with a 95.4% probability and "3σ-contours" the contours associated with a 99.73% probability.

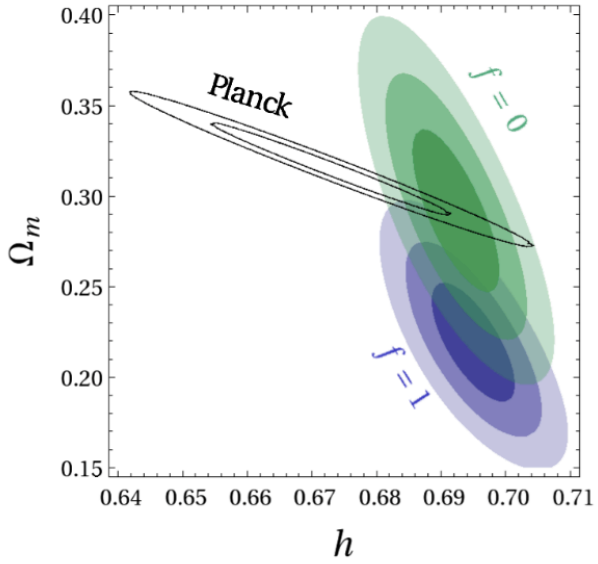

Figure 1.4: Comparison of the constraints obtained by Planck on (Ω_{m}, h), [135], and from the analysis of the Hubble diagram constructed from the SNLS 3 catalog, [86]. f is the "smoothness parameter", which gives the ratio between the volume which is not in form of holes and the total volume. Hence, $f = 1$ corresponds to the Friedmann-Lemaître metric.

1.5 Article "Interpretation of the Hubble diagram in a nonhomogeneous universe"

PHYSICAL REVIEW D **87,** 123526 (2013)

Interpretation of the Hubble diagram in a nonhomogeneous universe

Pierre Fleury,[1,2,*] Hélène Dupuy,[1,2,3,†] and Jean-Philippe Uzan[1,2,‡]

[1]*Institut d'Astrophysique de Paris, UMR-7095 du CNRS, Université Pierre et Marie Curie, 98 bis bd Arago, 75014 Paris, France*
[2]*Sorbonne Universités, Institut Lagrange de Paris, 98 bis bd Arago, 75014 Paris, France*
[3]*Institut de Physique Théorique, CEA, IPhT, URA 2306 CNRS, F-91191 Gif-sur-Yvette, France*

(Received 15 March 2013; published 24 June 2013)

In the standard cosmological framework, the Hubble diagram is interpreted by assuming that the light emitted by standard candles propagates in a spatially homogeneous and isotropic spacetime. However, the light from "point sources"—such as supernovae—probes the Universe on scales where the homogeneity principle is no longer valid. Inhomogeneities are expected to induce a bias and a dispersion of the Hubble diagram. This is investigated by considering a Swiss-cheese cosmological model, which (1) is an exact solution of the Einstein field equations, (2) is strongly inhomogeneous on small scales, but (3) has the same expansion history as a strictly homogeneous and isotropic universe. By simulating Hubble diagrams in such models, we quantify the influence of inhomogeneities on the measurement of the cosmological parameters. Though significant in general, the effects reduce drastically for a universe dominated by the cosmological constant.

DOI: 10.1103/PhysRevD.87.123526 PACS numbers: 98.80.−k, 04.20.−q, 42.15.−i

I. INTRODUCTION

The standard physical model of cosmology relies on a solution of general relativity describing a spatially homogeneous and isotropic spacetime, known as the Friedmann-Lemaître (FL) solution (see e.g. Ref. [1]). It is assumed to describe the geometry of our Universe smoothed on large scales. Besides, the use of the perturbation theory allows one to understand the properties of the large scale structure, as well as its growth from initial conditions set by inflation and constrained by the observation of the cosmic microwave background.

While this simple solution of the Einstein field equations, together with the perturbation theory, provides a description of the Universe in agreement with all existing data, it raises many questions on the reason why it actually gives such a good description. In particular, it involves a smoothing scale which is not included in the model itself [2]. This opened a lively debate on the fitting problem [3] (i.e. what is the best-fit FL model to the lumpy Universe?) and on backreaction (i.e. the fact that local inhomogeneities may affect the cosmological dynamics). The amplitude of backreaction is still actively debated [4–6], see Ref. [7] for a critical review.

Regardless of backreaction, the cosmological model assumes that the distribution of matter is continuous (i.e. it assumes that the fluid approximation holds on the scales of interest) both at the background and perturbation levels. Indeed numerical simulations fill part of this gap by dealing with N-body gravitational systems in an expanding space. The fact that matter is not continuously distributed can however imprint some observations, in particular regarding the propagation of light with narrow beams, as discussed in detail in Ref. [8]. It was argued that such beams, as e.g. for supernova observations, probe the spacetime structure on scales much smaller than those accessible in numerical simulations. The importance of quantifying the effects of inhomogeneities on light propagation was first pointed out by Zel'dovich [9]. Arguing that photons should mostly propagate in vacuum, he designed an "empty beam" approximation, generalized later by Dyer and Roeder as the "partially filled beam" approach [10]. More generally, the early work of Ref. [9] stimulated many studies on this issue. [11–25].

The propagation of light in an inhomogeneous universe gives rise to both distortion and magnification induced by gravitational lensing. While most images are demagnified, because most lines of sight probe underdense regions, some are amplified because of strong lensing. Lensing can thus discriminate between a diffuse, smooth component, and the one of a gas of macroscopic, massive objects (this property has been used to probe the nature of dark matter [26–28]). Therefore, it is expected that lensing shall induce a dispersion of the luminosities of the sources, and thus an extra scatter in the Hubble diagram [29]. Indeed, such an effect does also appear at the perturbation level—i.e. with light propagating in a perturbed FL spacetime—and it was investigated in Refs. [30–35]. The dispersion due to the large-scale structure becomes comparable to the intrinsic dispersion for redshifts $z > 1$ [36] but this dispersion can actually be corrected [37–42]. Nevertheless, a considerable fraction of the lensing dispersion arises from sub-arc minute scales, which are not probed by shear maps smoothed on arc minute scales [43]. The typical angular size of the light beam associated with a supernova (SN) is typically of order 10^{-7} arc sec (e.g. for a source of

*fleury@iap.fr
†helene.dupuy@cea.fr
‡uzan@iap.fr

physical size ~ 1 AU at redshift $z \sim 1$), while the typical observational aperture is of order 1 arc sec. This is smaller than the mean distance between any massive objects.

One can estimate [27] that a gas composed of particles of mass M can be considered diffuse on the scale of the beam of an observed source of size λ_s if $M < 2 \times 10^{-23} M_\odot h^2 (\lambda_s/1\ \mathrm{AU})^3$. In the extreme case for which matter is composed only of macroscopic pointlike objects, then most high-redshift SNeIa would appear fainter than in a universe with the same density distributed smoothly, with some very rare events of magnified SNeIa [27,44,45]. This makes explicit the connection between the Hubble diagram and the fluid approximation which underpins its standard interpretation.

The fluid approximation was first tackled in a very innovative work of Lindquist and Wheeler [46], using a Schwarzschild cell method modeling an expanding universe with spherical spatial sections. For simplicity, they used a regular lattice which restricts the possibilities to the most homogeneous topologies of the 3-sphere [47]. It has recently been revisited in Refs. [48] and in Refs. [49] for Euclidean spatial sections. They both constructed the associated Hubble diagrams, but their spacetimes are only approximate solutions of the Einstein field equations. An attempt to describe filaments and voids was also proposed in Refs. [50].

These approaches are conceptually different from the solution we adopt in the present article. We consider an exact solution of the Einstein field equations with strong density fluctuations, but which keeps a well-defined FL averaged behavior. Such conditions are satisfied by the Swiss-cheese model [51]: one starts with a spatially homogeneous and isotropic FL geometry, and then cuts out spherical vacuoles in which individual masses are embedded. Thus, the masses are contained in vacua within a spatially homogeneous fluid-filled cosmos (see bottom panel of Fig. 2). By construction, this exact solution is free from any backreaction: its cosmic dynamics is identical to the one of the underlying FL spacetime.

From the kinematical point of view, Swiss-cheese models allow us to go further than perturbation theory, because not only the density of matter exhibits finite fluctuations, but also the metric itself. Hence, light propagation is expected to be very different in a Swiss-cheese universe compared to its underlying FL model. Moreover, the inhomogeneities of a Swiss cheese are introduced in a way that addresses the so-called "Ricci-Weyl problem." Indeed, the standard FL geometry is characterized by a vanishing Weyl tensor and a nonzero Ricci tensor, while in reality light mostly travels in vacuum, where conversely the Ricci tensor vanishes—apart from the contribution of Λ, which does not focus light—and the Weyl tensor is nonzero (see Fig. 1). A Swiss-cheese model is closer to the latter situation, because the Ricci tensor is zero inside the holes (see Fig. 2). It is therefore hoped to capture the relevant optical properties of the Universe.

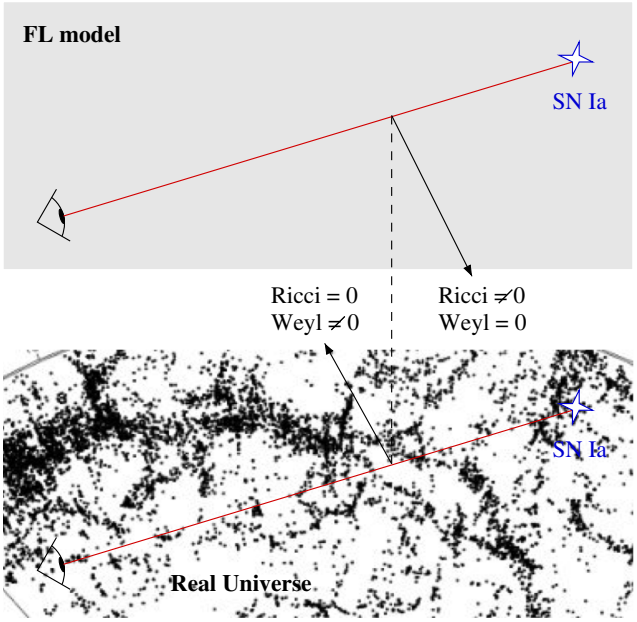

FIG. 1 (color online). The standard interpretation of SNe data assumes that light propagates in purely homogeneous and isotropic space (top). However, thin light beams are expected to probe the inhomogeneous nature of the actual Universe (bottom) down to a scale where the continuous limit is no longer valid.

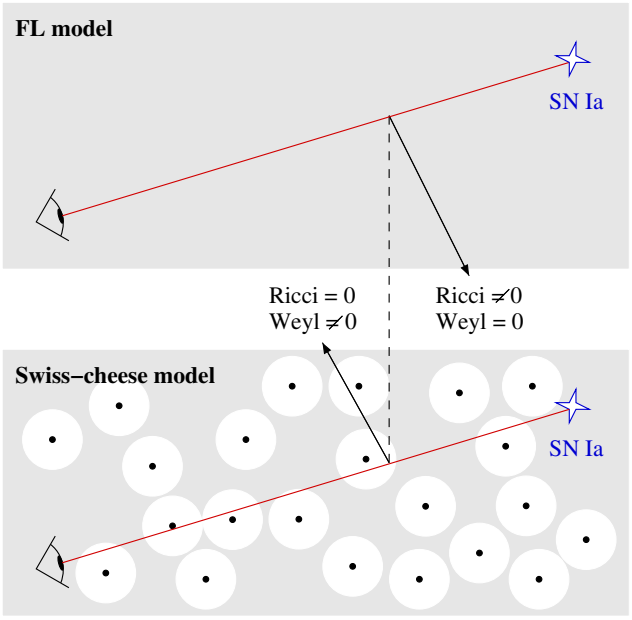

FIG. 2 (color online). Swiss-cheese models (bottom) allow us to model inhomogeneities beyond the continuous limit, while keeping the same dynamics and average properties as the FL model (top).

In fact, neither a Friedmann-Lemaître model nor a Swiss-cheese model can be considered a realistic description of the Universe. They share the property of being exact solutions of the Einstein equations which satisfy the Copernican principle, either strictly or statistically. Swiss-cheese models can be characterized by an extra-cosmological parameter describing the smoothness of their distribution of matter. Thus, a FL spacetime is nothing but a perfectly smooth Swiss cheese. It is legitimate to investigate to which extent observations can constrain the smoothness cosmological parameter, and therefore to quantify how close to a FL model the actual Universe is.

The propagation of light in a Swiss-cheese universe was first investigated by Kantowski [52], and later by Dyer and Roeder [53]. Both concluded that the effect, on the Hubble diagram, of introducing "clumps" of matter was to lower the apparent deceleration parameter. The issue was revived within the backreaction and averaging debates, and the Swiss-cheese models have been extended to allow for more generic distributions of matter inside the holes—instead of just concentrating it at the center—where spacetime geometry is described by the Lemaître-Tolman-Bondi (LTB) solution. The optical properties of such models have been extensively studied (see Refs. [54–62]) to finally conclude that the average luminosity-redshift relation remains unchanged with respect to the purely homogeneous case, contrary to the early results of Refs. [52,53].

In general, the relevance of "LTB holes" in Swiss-cheese models is justified by the fact that they allow one to reproduce the actual large-scale structure of the Universe (with voids and walls). However, though inhomogeneous, the distribution of matter in this class of models remains continuous at all scales. On the contrary, the old-fashioned approach with "clumps" of matter inside the holes *breaks the continuous limit*. Hence, it seems more relevant for describing the small-scale structure probed by thin light beams.

In this article, we revisit and update the studies of Refs. [52,53] within the paradigm of modern cosmology. For that purpose, we first provide a comprehensive study of light propagation in the same class of Swiss-cheese models, including the cosmological constant. By generating mock Hubble diagrams, we then show that the inhomogeneities induce a significant bias in the apparent luminosity-redshift relation, which affects the determination of the cosmological parameters. As we shall see, the effect increases with the fraction of clustered matter but decreases with Λ. For a universe apparently dominated by dark energy, the difference turns out to be small.

The article is organized as follows. Section II describes the construction and mathematical properties of the Swiss-cheese model. In Sec. III, we summarize the laws of light propagation, and introduce a new tool to deal with a patchwork of spacetimes, based on matrix multiplications. In Sec. IV, we apply the laws introduced in Sec. III to Swiss-cheese models and solve the associated equations. The results allow us to investigate the effect of one hole (Sec. V) and of many holes (Sec. VI) on cosmological observables, namely the redshift and the luminosity distance. Finally, the consequences on the determination of the cosmological parameters are presented in Sec. VII.

II. DESCRIPTION OF THE SWISS-CHEESE COSMOLOGICAL MODEL

The construction of Swiss-cheese models is based on the Einstein-Straus method [51] for embedding a point-mass within a homogeneous spacetime (the "cheese"). It consists in cutting off a spherical domain of the cheese and concentrating the matter it contained at the center of the hole. This section presents the spacetime geometries inside and outside a hole (Sec. II A), and how they are glued together (Sec. II B).

A. Spacetime patches

1. The "cheese"—Friedmann-Lemaître geometry

Outside the hole, the geometry is described by the standard FL metric

$$\mathrm{d}s^2 = -\mathrm{d}T^2 + a^2(T)[\mathrm{d}\chi^2 + f_K^2(\chi)\mathrm{d}\Omega^2], \tag{2.1}$$

where a is the scale factor and T is the cosmic time. The function $f_K(\chi)$ depends on the sign of K and thus of the spatial geometry (spherical, Euclidean or hyperbolic),

$$f_K(\chi) = \frac{\sin\sqrt{K}\chi}{\sqrt{K}}, \qquad \chi \quad \text{or} \quad \frac{\sinh\sqrt{-K}\chi}{\sqrt{-K}} \tag{2.2}$$

respectively for $K > 0$, $K = 0$ or $K < 0$. The Einstein field equations imply that the scale factor $a(T)$ satisfies the Friedmann equation

$$H^2 = \frac{8\pi G}{3}\rho - \frac{K}{a^2} + \frac{\Lambda}{3}, \quad \text{with} \quad H \equiv \frac{1}{a}\frac{\mathrm{d}a}{\mathrm{d}T}, \tag{2.3}$$

and where $\rho = \rho_0(a_0/a)^3$ is the energy density of a pressureless fluid. A subscript 0 indicates that the quantity is evaluated today. It is convenient to introduce the cosmological parameters

$$\Omega_\mathrm{m} = \frac{8\pi G\rho_0}{3H_0^2}, \quad \Omega_K = -\frac{K}{a_0^2H_0^2}, \quad \Omega_\Lambda = \frac{\Lambda}{3H_0^2}, \tag{2.4}$$

in terms of which the Friedmann equation takes the form

$$\left(\frac{H}{H_0}\right)^2 = \Omega_\mathrm{m}\left(\frac{a_0}{a}\right)^3 + \Omega_K\left(\frac{a_0}{a}\right)^2 + \Omega_\Lambda. \tag{2.5}$$

2. The "hole"—Kottler geometry

Inside the hole, the geometry is described by the extension of the Schwarzschild metric to the case of a nonzero cosmological constant, known as the Kottler solution [63,64] (see e.g. Ref. [65] for a review). In spherical coordinates (r, θ, φ), it reads

$$\mathrm{d}s^2 = -A(r)\mathrm{d}t^2 + A^{-1}(r)\mathrm{d}r^2 + r^2\mathrm{d}\Omega^2, \tag{2.6}$$

$$\text{with} \quad A(r) \equiv 1 - \frac{r_S}{r} - \frac{\Lambda r^2}{3}, \tag{2.7}$$

and where $r_S \equiv 2GM$ is the Schwarzschild radius associated with the mass M at the center of the hole. It is easy to check that the above metric describes a static spacetime. The corresponding Killing vector $\xi^\mu = \delta^\mu_0$ has norm $g_{\mu\nu}\xi^\mu\xi^\nu = A(r)$ and is therefore timelike as long as $A > 0$. Hence, there are two cases:

(1) If $9(GM)^2\Lambda > 1$, then $A(r) < 0$ for all $r > 0$, so that ξ^μ is spacelike. In this case, the Kottler spacetime contains no static region but it is spatially homogeneous.

(2) If $9(GM)^2\Lambda < 1$, then $A(r) > 0$ for r between r_b and $r_c > r_b$ which are the two positive roots of the polynomial $rA(r)$, and correspond respectively to the black hole and cosmological horizons. We have

$$r_c = \frac{2}{\sqrt{\Lambda}}\cos\left(\frac{\psi}{3} + \frac{\pi}{3}\right), \tag{2.8}$$

$$r_b = \frac{2}{\sqrt{\Lambda}}\cos\left(\frac{\psi}{3} - \frac{\pi}{3}\right), \tag{2.9}$$

with $\cos\psi = 3GM\sqrt{\Lambda}$, so that

$$r_S < r_b < \frac{3}{2}r_S < \frac{1}{\sqrt{\Lambda}} < r_c < \frac{3}{\sqrt{\Lambda}}. \tag{2.10}$$

In the region $r_b < r < r_c$, the Kottler spacetime is static. Note also that $r = r_b$ and $r = r_c$ are Killing horizons, since ξ vanishes on these hypersurfaces.

In practice, we use the Kottler solution to describe the vicinity of a gravitationally bound object, such as a galaxy, or a cluster of galaxies. In this context, we have typically $9(GM)^2\Lambda < 10^{-14}$ (see Sec. VA), so we are in the second case. Moreover, this solution only describes the exterior region of the central object; it is thus valid only for $r > r_{\mathrm{phys}}$, where r_{phys} is the physical size of the object. For the cases we are interested in, $r_{\mathrm{phys}} \gg r_b$, so that there is actually no black-hole horizon.

B. Junction conditions

Any spacetime obtained by gluing together two different geometries, via a hypersurface Σ, is well defined if—and only if—it satisfies the Israel junction conditions [66,67]: both geometries must induce (a) the same 3-metric, and (b) the same extrinsic curvature on Σ.

The junction hypersurface Σ is the world sheet of a comoving 2-sphere, as imposed by the symmetry of the problem. Hence, it is defined by $\chi = \chi_h = \mathrm{cst}$ in FL coordinates, and by $r = r_h(t)$ in Kottler coordinates. Both points of view are depicted in Fig. 3.

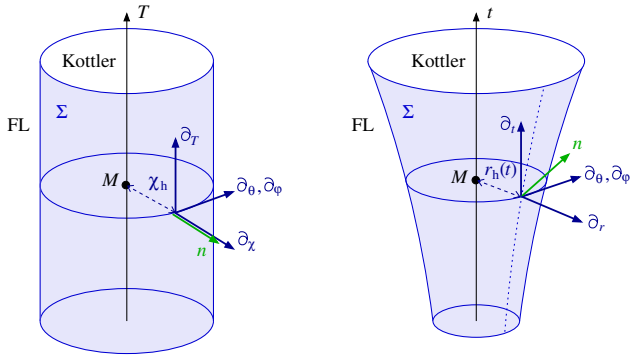

FIG. 3 (color online). The junction hypersurface as seen from the FL point of view with equation $\chi = \chi_h$ (left); and from the Kottler point of view with equation $r = r_h(t)$ (right).

In the FL region, the normal vector to the hypersurface is given by $n^{(\mathrm{FL})}_\mu = \delta^\chi_\mu/a$. The 3-metric and the extrinsic curvature induced by the FL geometry are respectively

$$\mathrm{d}s^2_\Sigma = -\mathrm{d}T^2 + a^2(T)f_K^2(\chi_h)\mathrm{d}\Omega^2, \tag{2.11}$$

$$K^{(\mathrm{FL})}_{ab}\mathrm{d}x^a\mathrm{d}x^b = a(T)f_K(\chi_h)f'_K(\chi_h)\mathrm{d}\Omega^2, \tag{2.12}$$

where $(x^a) = (T, \theta, \varphi)$ are natural intrinsic coordinates for Σ. We stress carefully that, in the following and as long as there is no ambiguity, a dot can denote a time derivative with respect to T or t, so that $\dot{a} = \mathrm{d}a/\mathrm{d}T$ and $\dot{r}_h = \mathrm{d}r_h/\mathrm{d}t$, while a prime can denote a derivative with respect to χ or r, so that $f'_K = \mathrm{d}f_K/\mathrm{d}\chi$ and $A' = \mathrm{d}A/\mathrm{d}r$.

The 3-metric induced on Σ by the Kottler geometry is

$$\mathrm{d}s^2 = -\kappa^2(t)\mathrm{d}t^2 + r_h^2(t)\mathrm{d}\Omega^2, \tag{2.13}$$

where

$$\kappa(t) \equiv \sqrt{\frac{A^2[r_h(t)] - \dot{r}_h^2(t)}{A[r_h(t)]}}. \tag{2.14}$$

Therefore, the first junction condition implies

$$r_h(t) = a(T)f_K(\chi_h), \tag{2.15}$$

$$\frac{\mathrm{d}T}{\mathrm{d}t} = \kappa(t), \tag{2.16}$$

which govern the dynamics of the hole boundary, and relate the time coordinates of the FL and Kottler regions.

The extrinsic curvature of Σ induced by the Kottler geometry, but expressed in (x^a) coordinates, reads

$$K^{(\mathrm{K})}_{ab}\mathrm{d}x^a\mathrm{d}x^b = -\frac{\ddot{r}_h + \kappa^2 A'(r_h)/2}{\kappa^3}\mathrm{d}T^2 + \frac{r_h A(r_h)}{\kappa}\mathrm{d}\Omega^2. \tag{2.17}$$

Hence, the second junction condition is satisfied only if

$$\kappa = \frac{A(r_h)}{f'_K(\chi_h)}, \quad \text{whence} \quad \frac{\mathrm{d}T}{\mathrm{d}t} = \frac{A[a(T)f_K(\chi_h)]}{f'_K(\chi_h)}. \tag{2.18}$$

It is straightforward to show that Eq. (2.18), together with the Friedmann equation (2.3), imply that the Kottler and FL regions have the same cosmological constant, and

$$M = \frac{4\pi}{3}\rho a^3 f_K^3(\chi_h). \tag{2.19}$$

C. Summary

Given a FL spacetime with pressureless matter and a cosmological constant, $a(T)$ is completely determined from the Friedmann equation. A spherical hole of comoving radius χ_h, which contains a constant mass $M = 4\pi\rho a^3 f_K^3(\chi_h)/3$ at its center, and whose geometry is described by the Kottler metric, can then be inserted anywhere. The resulting spacetime geometry is an exact solution of the Einstein field equations.

By construction, the clump inside the hole does not backreact on the surrounding FL region. It follows that many such holes can be inserted, as long as they do not overlap. Note that if two holes do not overlap initially, then they will never do so, despite the expansion of the universe, because their boundaries are comoving.

III. PROPAGATION OF LIGHT

A. Light rays

The past light cone of a given observer is a constant phase hypersurface $w = \text{const}$. Its normal vector $k_\mu \equiv \partial_\mu w$ (the wave four-vector) is a null vector satisfying the geodesic equation, and whose integral curves (light rays) are irrotational:

$$k^\mu k_\mu = 0, \qquad k^\nu \nabla_\nu k_\mu = 0, \qquad \nabla_{[\mu} k_{\nu]} = 0. \tag{3.1}$$

For an emitter and an observer with respective four-velocities u^μ_{em} and u^μ_{obs}, we define the redshift by

$$1 + z = \frac{u^\mu_{\text{em}} k_\mu(\upsilon_{\text{em}})}{u^\mu_{\text{obs}} k_\mu(0)}, \tag{3.2}$$

where υ is an affine parameter along the geodesic, so that $k^\mu = \mathrm{d}x^\mu/\mathrm{d}\upsilon$, and $\upsilon = 0$ at the observation event. The wave four-vector can always be decomposed into temporal and spatial components,

$$k^\mu = (1+z)(u^\mu - d^\mu), \qquad d^\mu u_\mu = 0, \qquad d^\mu d_\mu = 1, \tag{3.3}$$

where d^μ denotes the spatial direction of observation. In Eq. (3.3), we have chosen an affine parameter adapted to the observer, in the sense that $2\pi\nu_0 = u^\mu_{\text{obs}} k_\mu(0) = 1$. This convention is used in all the remainder of the article.

B. Light beams

1. Geodesic deviation equation

A light beam is a collection of light rays, that is, a bundle of null geodesics $\{x^\mu(\upsilon, \gamma)\}$, where γ labels the curves and υ is the affine parameter along them. The relative behavior of two neighboring geodesics $x^\mu(\cdot, \gamma)$ and $x^\mu(\cdot, \gamma + \mathrm{d}\gamma)$ is described by their separation vector $\xi^\mu \equiv \mathrm{d}x^\mu/\mathrm{d}\gamma$. Hence, this vector encodes the whole information on the size and shape of the bundle.

Having chosen $\upsilon = 0$ at the observation event—which is a vertex point of the bundle—ensures that the separation vector field is everywhere orthogonal to the geodesics, $k^\mu \xi_\mu = 0$. In such conditions, the evolution of ξ^μ with υ is governed by the geodesic deviation equation

$$k^\alpha k^\beta \nabla_\alpha \nabla_\beta \xi^\mu = R^\mu{}_{\nu\alpha\beta} k^\nu k^\alpha \xi^\beta, \tag{3.4}$$

where $R^\mu{}_{\nu\alpha\beta}$ is the Riemann tensor.

2. Sachs equation

Consider an observer with four-velocity u^μ. In view of relating ξ^μ to observable quantities, we introduce the Sachs basis $(s^\mu_A)_{A\in\{1,2\}}$, defined as an orthonormal basis of the plane orthogonal to both u^μ and k^μ,

$$s^\mu_A s_{B\mu} = \delta_{AB}, \qquad s^\mu_A u_\mu = s^\mu_A k_\mu = 0, \tag{3.5}$$

and parallel-transported along the geodesic bundle,

$$k^\nu \nabla_\nu s^\mu_A = 0. \tag{3.6}$$

The plane spanned by (s_1, s_2) can be considered a screen on which the observer projects the light beam. The two-vector of components $\xi_A = \xi_\mu s^\mu_A$ then represents the relative position, on the screen, of the light spots corresponding to two neighboring rays separated by ξ^μ.

The evolution of ξ_A, with light propagation, is determined by projecting the geodesic deviation equation (3.4) on the Sachs basis. The result is known as the Sachs equation [1,68,69], and reads

$$\frac{\mathrm{d}^2 \xi_A}{\mathrm{d}\upsilon^2} = \mathcal{R}_{AB}\xi^B, \tag{3.7}$$

where $\mathcal{R}_{AB} = R_{\mu\nu\alpha\beta} k^\nu k^\alpha s^\mu_A s^\beta_B$ is the screen-projected Riemann tensor, called optical tidal matrix. It is conveniently decomposed into a Ricci term and a Weyl term as

$$(\mathcal{R}_{AB}) = \begin{pmatrix} \Phi_{00} & 0 \\ 0 & \Phi_{00} \end{pmatrix} + \begin{pmatrix} -\mathrm{Re}\Psi_0 & \mathrm{Im}\Psi_0 \\ \mathrm{Im}\Psi_0 & \mathrm{Re}\Psi_0 \end{pmatrix} \tag{3.8}$$

with

$$\Phi_{00} \equiv -\frac{1}{2} R_{\mu\nu} k^\mu k^\nu, \qquad \Psi_0 \equiv -\frac{1}{2} C_{\mu\nu\alpha\beta} \sigma^\mu k^\nu k^\alpha \sigma^\beta, \tag{3.9}$$

and where $\sigma^\mu \equiv s^\mu_1 - \mathrm{i} s^\mu_2$.

3. Notions of distance

Since the light beam converges at the observation event, we have $\xi^A(\upsilon = 0) = 0$. The linearity of the Sachs equation then implies the existence of a 2×2 matrix $\mathcal{D}^A{}_B$, called Jacobi matrix, such that

$$\xi^A(v) = \mathcal{D}^A{}_B(v)\left(\frac{\mathrm{d}\xi^B}{\mathrm{d}v}\right)_{v=0}. \tag{3.10}$$

From Eq. (3.7), we immediately deduce that this matrix satisfies the Jacobi matrix equation

$$\frac{\mathrm{d}^2}{\mathrm{d}v^2}\mathcal{D}^A{}_B = \mathcal{R}^A{}_C\mathcal{D}^C{}_B, \tag{3.11}$$

with initial conditions

$$\mathcal{D}^A{}_B(0) = 0, \qquad \frac{\mathrm{d}\mathcal{D}^A{}_B}{\mathrm{d}v}(0) = \delta^A_B. \tag{3.12}$$

We shall also use the short-hand notation $\boldsymbol{\xi} = (\xi^A)$ and $\boldsymbol{\mathcal{D}} = (\mathcal{D}^A{}_B)$ so that Eq. (3.11) reads $\mathrm{d}^2\boldsymbol{\mathcal{D}}/\mathrm{d}v^2 = \boldsymbol{\mathcal{R}}\cdot\boldsymbol{\mathcal{D}}$, with $\boldsymbol{\mathcal{D}}(0) = 0$ and $\dot{\boldsymbol{\mathcal{D}}}(0) = \mathbf{1}$.

Since the Jacobi matrix relates the shape of a light beam to its ''initial'' aperture, it is naturally related to the various notions of distance used in astronomy and cosmology. The *angular distance* D_A is defined by comparing the emission cross-sectional area $\mathrm{d}^2S_\mathrm{source}$ of a source to the solid angle $\mathrm{d}\Omega^2_\mathrm{obs}$ under which it is observed,

$$\mathrm{d}^2S_\mathrm{source} = D_\mathrm{A}^2\mathrm{d}\Omega^2_\mathrm{obs}. \tag{3.13}$$

It is related to the Jacobi matrix by

$$D_\mathrm{A} = \sqrt{|\det\boldsymbol{\mathcal{D}}(v_\mathrm{source})|}, \tag{3.14}$$

where v_source is the affine parameter at emission.

The *luminosity distance* D_L is defined from the ratio between the observed flux F_obs and the intrinsic luminosity L_source of the source, so that

$$L_\mathrm{source} = 4\pi D_\mathrm{L}^2F_\mathrm{obs}. \tag{3.15}$$

It is related to the angular distance by the following distance duality law:

$$D_\mathrm{L} = (1+z)^2D_\mathrm{A}. \tag{3.16}$$

Hence, the theoretical determination of the luminosity distance relies on the computation of the Jacobi matrix.

C. Solving the Sachs equation piecewise

Since we work in a Swiss-cheese universe, we have to compute the Jacobi matrix for a patchwork of spacetimes. It is tempting, in this context, to calculate the Jacobi matrix for each patch independently, and then try to reconnect them. In fact, such an operation is unnatural, because the very definition of $\boldsymbol{\mathcal{D}}$ imposes that the initial condition is a vertex point of the light beam. Thus, juxtaposing two Jacobi matrices is only possible at a vertex point, which is of course too restrictive for us.

We can solve this problem by extending the Jacobi matrix formalism into a richer structure. This requires us to consider the general solution of Eq. (3.7), for arbitrary initial conditions. Thus, we have

$$\boldsymbol{\xi}(v) = \boldsymbol{\mathcal{C}}(v;v_\mathrm{init})\cdot\boldsymbol{\xi}_{v=v_\mathrm{init}} + \boldsymbol{\mathcal{D}}(v;v_\mathrm{init})\cdot\frac{\mathrm{d}\boldsymbol{\xi}}{\mathrm{d}v}\bigg|_{v=v_\mathrm{init}}, \tag{3.17}$$

as for any linear second order differential equation, solved from v_init to v. In the following, $\boldsymbol{\mathcal{C}}(v;v_\mathrm{init})$ is referred to as the *scale matrix*. It is easy to check that both the scale and Jacobi matrices satisfy the Jacobi matrix equation (3.11) but with different initial conditions:

$$\boldsymbol{\mathcal{D}}(v_\mathrm{init};v_\mathrm{init}) = \mathbf{0}, \qquad \frac{\mathrm{d}\boldsymbol{\mathcal{D}}}{\mathrm{d}v}(v_\mathrm{init};v_\mathrm{init}) = \mathbf{1}, \tag{3.18}$$

whereas

$$\boldsymbol{\mathcal{C}}(v_\mathrm{init};v_\mathrm{init}) = \mathbf{1}, \qquad \frac{\mathrm{d}\boldsymbol{\mathcal{C}}}{\mathrm{d}v}(v_\mathrm{init};v_\mathrm{init}) = \mathbf{0}. \tag{3.19}$$

The most useful object for our problem turns out to be the 4×4 *Wronski matrix* constructed from $\boldsymbol{\mathcal{C}}$ and $\boldsymbol{\mathcal{D}}$,

$$\boldsymbol{\mathcal{W}}(v;v_\mathrm{init}) \equiv \begin{pmatrix} \boldsymbol{\mathcal{C}}(v;v_\mathrm{init}) & \boldsymbol{\mathcal{D}}(v;v_\mathrm{init}) \\ \frac{\mathrm{d}\boldsymbol{\mathcal{C}}}{\mathrm{d}v}(v;v_\mathrm{init}) & \frac{\mathrm{d}\boldsymbol{\mathcal{D}}}{\mathrm{d}v}(v;v_\mathrm{init}) \end{pmatrix}, \tag{3.20}$$

in terms of which the general solution (3.17) reads

$$\begin{pmatrix} \boldsymbol{\xi} \\ \frac{\mathrm{d}\boldsymbol{\xi}}{\mathrm{d}v} \end{pmatrix}(v) = \boldsymbol{\mathcal{W}}(v;v_\mathrm{init})\cdot\begin{pmatrix} \boldsymbol{\xi} \\ \frac{\mathrm{d}\boldsymbol{\xi}}{\mathrm{d}v} \end{pmatrix}(v_\mathrm{init}). \tag{3.21}$$

It is clear, from Eq. (3.21), that $\boldsymbol{\mathcal{W}}$ satisfies the relation

$$\boldsymbol{\mathcal{W}}(v_1;v_3) = \boldsymbol{\mathcal{W}}(v_1;v_2)\cdot\boldsymbol{\mathcal{W}}(v_2;v_3). \tag{3.22}$$

Hence, the general solution of the Sachs equation in a Swiss-cheese universe can be obtained by multiplying Wronski matrices, according to

$$\begin{aligned}\boldsymbol{\mathcal{W}}(v_\mathrm{source};0) = {}& \boldsymbol{\mathcal{W}}_\mathrm{FL}(v_\mathrm{source};v^{(1)}_\mathrm{in})\cdot\boldsymbol{\mathcal{W}}_\mathrm{K}(v^{(1)}_\mathrm{in};v^{(1)}_\mathrm{out}) \\ & \cdot\boldsymbol{\mathcal{W}}_\mathrm{FL}(v^{(1)}_\mathrm{out};v^{(2)}_\mathrm{in})\ldots\boldsymbol{\mathcal{W}}_\mathrm{FL}(v^{(N)}_\mathrm{out};0)\end{aligned} \tag{3.23}$$

where $\boldsymbol{\mathcal{W}}_\mathrm{FL}$ and $\boldsymbol{\mathcal{W}}_\mathrm{K}$ are the Wronski matrices computed respectively in the FL region and in the Kottler holes; $v^{(i)}_\mathrm{in}$ and $v^{(i)}_\mathrm{out}$ are the values of the affine parameter respectively at the entrance and the exit of the ith hole.

IV. INTEGRATION OF THE GEODESIC AND SACHS EQUATIONS

Consider an observer lying within a FL region, who receives a photon after the latter has crossed a hole. In this section, we determine the light path from entrance to observation by solving the geodesic equation, and we calculate the Wronski matrix for the Sachs equation.

The main geometrical quantities are summarized in Fig. 4. d^μ is the direction of observation as defined in Eq. (3.3). The spatial sections of the FL region can be described either by comoving spherical coordinates (χ,θ,φ) or, when the spatial sections are Euclidean, by comoving Cartesian coordinates (X,Y,Z).

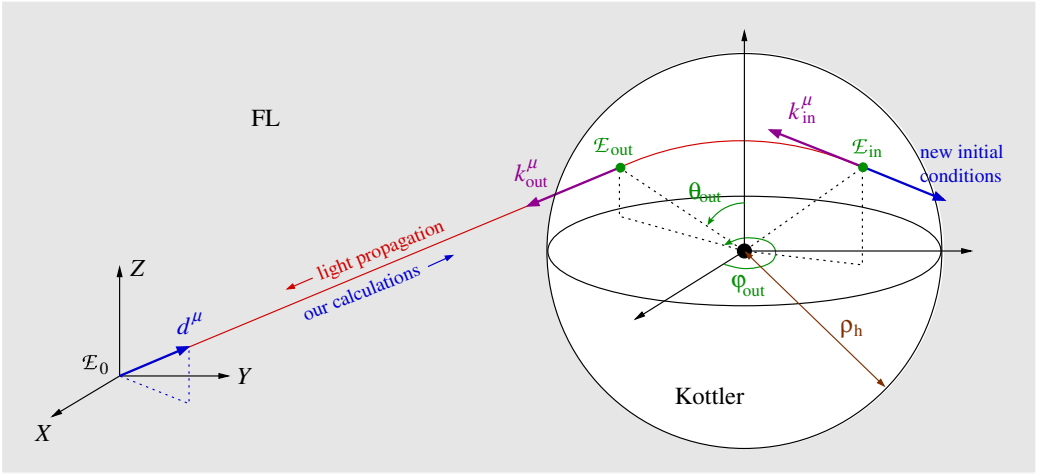

FIG. 4 (color online). A light ray propagates alternatively in FL and Kottler regions. The main geometrical quantities defined and used in Sec. IV are depicted in this simplified view of a single hole.

The hole is characterized by its comoving spatial position $X^i_{\rm h}$, in terms of the FL coordinates, and its mass M, or equivalently its comoving radius $\rho_{\rm h}$. Note that, contrary to Sec. II A, it is no longer denoted $\chi_{\rm h}$, in order to avoid confusion with the radial comoving coordinate of the center of the hole.

A photon enters into the hole with wave vector $k^\mu_{\rm in}$, exits from it with wave vector $k^\mu_{\rm out}$, and reaches the observer with wave vector k^μ_0. We respectively denote $\mathcal{E}_{\rm in}$, $\mathcal{E}_{\rm out}$ and $\mathcal{E}_0$ the associated events. The coordinates of the first two can be expressed either with respect to FL, e.g. as $(T_{\rm in}, X^i_{\rm in})$ in Cartesian coordinates, or with respect to the hole, e.g. as $(t_{\rm in}, r_{\rm in}, \theta_{\rm in}, \varphi_{\rm in})$ in the Kottler spherical coordinate system.

Our calculations go backward in time. Starting from $\mathcal{E}_0$, we first determine $\mathcal{E}_{\rm out}$, $\mathcal{W}_{\rm FL}(v_{\rm out}; v_{\rm obs})$, and second $\mathcal{E}_{\rm in}$, $\mathcal{W}_{\rm K}(v_{\rm in}; v_{\rm out})$. The same operations can then be repeated starting from $\mathcal{E}_{\rm in}$ and so on.

A. Friedmann-Lemaître region (from $\mathcal{E}_0$ to $\mathcal{E}_{\rm out}$)

The geometry of the Friedmann-Lemaître region is given by the metric (2.1) which can be rewritten in terms of the conformal time η, defined by $\mathrm{d}\eta = \mathrm{d}T/a(T)$, as

$$\mathrm{d}s^2 = a^2(\eta)[-\mathrm{d}\eta^2 + \mathrm{d}\chi^2 + f_K^2(\chi)\mathrm{d}\Omega^2]. \tag{4.1}$$

1. Geodesic equation

If one chooses the center $\chi = 0$ of the FL spherical coordinate system on the worldline of the (comoving) observer, then the geodesic equation is easily solved as

$$\chi(\eta) = \eta_0 - \eta, \qquad \theta = \theta_0, \qquad \varphi = \varphi_0, \tag{4.2}$$

which corresponds to a purely radial trajectory. Note however that for a generic origin, this is no longer true. The associated wave vector remains collinear to the observed one, k^μ_0. It is only subject to a redshift induced by the cosmic expansion, so that

$$k^\mu = \left(\frac{a_0}{a}\right)^2 k^\mu_0. \tag{4.3}$$

We stress that, in Eq. (4.3), $\mu = 0$ refers to components on ∂_η, not on $\partial_T = \partial_\eta/a$.

2. Intersection with the hole

Once the geodesic equation has been solved and the position of the hole has been chosen, we can calculate the intersection $\mathcal{E}_{\rm out}$ between the light ray and the hole boundary. *In the particular case of a spatially Euclidean FL solution* ($K = 0$), the Cartesian coordinates $X^i_{\rm out}$ of $\mathcal{E}_{\rm out}$ satisfy the simple system of equations

$$\begin{cases} \delta_{ij}(X^i_{\rm out} - X^i_{\rm h})(X^j_{\rm out} - X^j_{\rm h}) = \rho^2_{\rm h} \\ X^i_{\rm out} = X^i_0 + (\eta_0 - \eta_{\rm out})d^i, \end{cases} \tag{4.4}$$

where $X^i_{\rm h}$ and X^i_0 are the respective Cartesian coordinates of the hole and the observer, while d^i is the spatial direction of observation. Although conceptually similar, the determination of $\mathcal{E}_{\rm out}$ for a FL solution with arbitrary spatial curvature is technically harder.

In general, we deduce from Eq. (4.3) that the wave vector at $\mathcal{E}_{\rm out}$ is $k^\mu_{\rm out} = (a_0/a_{\rm out})^2 k^\mu_0$, where $a_{\rm out} \equiv a(\eta_{\rm out})$.

3. Wronski matrix

In the FL region, the Sachs basis (s_1, s_2) is defined with respect to the fundamental observers, comoving with four-velocity $u = \partial_T$. The explicit form of this basis does not need to be specified here.

The Sachs equation can be solved analytically by means of a conformal transformation to the static metric

$$\mathrm{d}\tilde{s}^2 = a_0^2[-\mathrm{d}\eta^2 + f_K^2(\chi)\mathrm{d}\Omega^2] \equiv \tilde{g}_{\mu\nu}\mathrm{d}x^\mu \mathrm{d}x^\nu. \tag{4.5}$$

Because the geometries associated with $g_{\mu\nu}$ and $\tilde{g}_{\mu\nu}$ are conformal, any null geodesic for $g_{\mu\nu}$ affinely parametrized by v is also a null geodesic for $\tilde{g}_{\mu\nu}$ affinely parametrized by $\tilde{v}$, with $a^2 \mathrm{d}\tilde{v} = a_0^2 \mathrm{d}v$. As $\mathrm{d}v = (a^2/a_0)\mathrm{d}\eta$, it follows that $\tilde{v} = a_0\eta$.

For the static geometry, the optical tidal matrix reads $\tilde{\mathcal{R}} = -(K/a_0^2)\mathbf{1}$, so that the Sachs equation is simply

$$\frac{\mathrm{d}^2\tilde{\boldsymbol{\xi}}}{\mathrm{d}\eta^2} = -K\tilde{\boldsymbol{\xi}}. \tag{4.6}$$

We then easily obtain the Jacobi and scale matrices:

$$\tilde{\mathcal{D}} = a_0 f_K(\eta - \eta_{\mathrm{init}})\mathbf{1}, \qquad \tilde{\mathcal{C}} = f'_K(\eta - \eta_{\mathrm{init}})\mathbf{1}. \tag{4.7}$$

To go back to the original FL spacetime, we use that $\mathrm{d}v = a^2\mathrm{d}\eta$ and the fact that the screen projections of the separation vectors for both geometries are related by $a\tilde{\boldsymbol{\xi}} = a_0\boldsymbol{\xi}$. The final result is

$$\mathcal{D}_{\mathrm{FL}} = a_{\mathrm{init}}\frac{a}{a_0} f_K(\eta - \eta_{\mathrm{init}})\mathbf{1}, \tag{4.8}$$

$$\mathcal{C}_{\mathrm{FL}} = \frac{a}{a_{\mathrm{init}}}[f'_K(\eta - \eta_{\mathrm{init}}) - \mathcal{H}_{\mathrm{init}} f_K(\eta - \eta_{\mathrm{init}})]\mathbf{1}, \tag{4.9}$$

where $\mathcal{H} \equiv a'(\eta)/a(\eta)$ is the conformal Hubble function. This completely determines $\mathcal{W}_{\mathrm{FL}}$.

Note that we can recover the standard expression of the angular distance by taking the initial condition at the observer. The relation (3.14) then implies

$$D_{\mathrm{A}} = \sqrt{\det \mathcal{D}_{\mathrm{FL}}} = \frac{a_0}{(1+z)} f_K(\eta_{\mathrm{source}}), \tag{4.10}$$

where $z = a_0/a - 1$ is the redshift of a photon that only travels through a FL region.

B. Kottler region (from $\mathcal{E}_{\mathrm{out}}$ to $\mathcal{E}_{\mathrm{in}}$)

1. Initial condition at $\mathcal{E}_{\mathrm{out}}$

In the previous section, we have determined $\mathcal{E}_{\mathrm{out}}$ and k^μ_{out} in terms of the FL coordinate system. However, in order to proceed inside the hole, we need to express them in terms of the Kottler coordinate system (t, r, θ, φ).

A preliminary task consists in expressing $\mathcal{E}_{\mathrm{out}}$ and k^μ_{out} in terms of FL spherical coordinates, with origin at the center of the hole. This operation is straightforward. The event $\mathcal{E}_{\mathrm{out}}$ is then easily converted, since (a) we are free to set $t_{\mathrm{out}} = 0$, (b) Eq. (2.15) implies $r_{\mathrm{out}} = a(\eta_{\mathrm{out}})\rho_{\mathrm{h}}$, and (c) the angular coordinates θ_{out}, φ_{out} remain unchanged if the Kottler axes are chosen parallel to the FL ones.

The first junction condition ensures that light is not deflected when it crosses the boundary Σ of the hole. Indeed, the continuity of the metric implies that the connection does not diverge on Σ. Integrating the geodesic equation $\mathrm{d}k^\mu = -\Gamma^\mu_{\alpha\beta}k^\alpha k^\beta \mathrm{d}v$ between v^-_{out} and v^+_{out} then shows that k^μ is continuous at $\mathcal{E}_{\mathrm{out}}$. Therefore, we just need to convert its components from the FL coordinate system to the Kottler one. The result is

$$k^t_{\mathrm{out}} = \frac{a_{\mathrm{out}}}{A(r_{\mathrm{out}})}\left[k^\eta_{\mathrm{out}} + \sqrt{1 - A(r_{\mathrm{out}})}k^\chi_{\mathrm{out}}\right] \tag{4.11}$$

$$k^r_{\mathrm{out}} = a_{\mathrm{out}}\left[\sqrt{1 - A(r_{\mathrm{out}})}k^\eta_{\mathrm{out}} + k^\chi_{\mathrm{out}}\right] \tag{4.12}$$

$$k^\theta_{\mathrm{out}} = k^\theta_{\mathrm{out}} \tag{4.13}$$

$$k^\varphi_{\mathrm{out}} = k^\varphi_{\mathrm{out}}. \tag{4.14}$$

2. Shifting to the equatorial plane

Since the Kottler spacetime is spherically symmetric, it is easier to integrate the geodesic equation in the equatorial plane $\theta = \pi/2$. In general, however, we must perform rotations to bring both $\mathcal{E}_{\mathrm{out}}$ and k_{out} into this plane.

Starting from arbitrary initial conditions $(\mathcal{E}_{\mathrm{out}}, k^\mu_{\mathrm{out}})$, we can shift to the equatorial plane in two steps. In the following, $\boldsymbol{R}_i(\vartheta)$ denotes the rotation of angle ϑ about the x^i-axis. The operations are depicted in Fig. 5.

(i) First, bring $\mathcal{E}_{\mathrm{out}}$ to the point $\mathcal{E}_{\mathrm{out,eq}}$ on the equatorial plane by the action of two successive rotations, $\boldsymbol{R}_z(-\varphi_{\mathrm{out}})$ followed by $\boldsymbol{R}_y(\pi/2 - \theta_{\mathrm{out}})$. The wave vector after the two rotations is denoted k'^μ_{out}.

(ii) Then, bring k'^μ_{out} to the equatorial plane with $\boldsymbol{R}_x(-\psi)$, where ψ is the angle between the projection of k'^μ_{out} on the yz-plane and the y-axis. Note that such a rotation leaves $\mathcal{E}_{\mathrm{out,eq}}$ unchanged.

It follows that, after the three rotations

$$\boldsymbol{R} = \boldsymbol{R}_x(-\psi) \circ \boldsymbol{R}_y\left(\frac{\pi}{2} - \theta_{\mathrm{out}}\right) \circ \boldsymbol{R}_z(-\varphi_{\mathrm{out}}), \tag{4.15}$$

$\mathcal{E}_{\mathrm{out}}$ and k^μ_{out} are changed into $\mathcal{E}_{\mathrm{out,eq}}$ and $k^\mu_{\mathrm{out,eq}}$ which lie in the equatorial plane. In the following, we omit subscripts "eq," keeping in mind that we will have to apply $\boldsymbol{R}^{-1}$ to recover the original system of axes.

3. Null geodesics in Kottler geometry

In the Kottler region, the existence of two Killing vectors associated to statisticity and spherical symmetry implies the existence of two conserved quantities, the energy E and the angular momentum L of the photon. It follows that a null geodesic[1] is a solution of

$$A(r)\frac{\mathrm{d}t}{\mathrm{d}v} = E, \qquad \left(\frac{\mathrm{d}r}{\mathrm{d}v}\right)^2 + \left(\frac{L}{r}\right)^2 A(r) = E^2, \qquad r^2\frac{\mathrm{d}\varphi}{\mathrm{d}v} = L. \tag{4.16}$$

[1] See e.g. Refs. [70,71] for early works on the propagation of light rays in spacetimes with a nonvanishing cosmological constant.

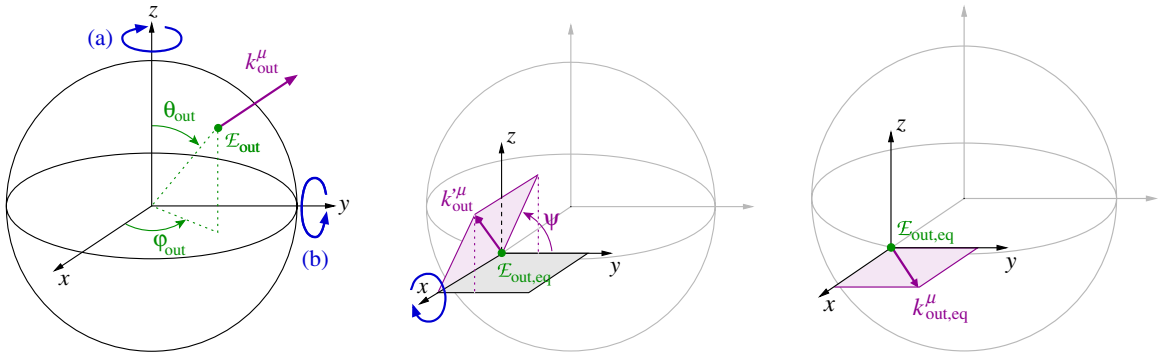

FIG. 5 (color online). An arbitrary initial condition is rotated so that the geodesic lies in the equatorial plane $\theta = \pi/2$. Left: $\mathcal{E}_{\rm out}$ is brought (a) to $\varphi = 0$ by the rotation $\boldsymbol{R}_z(-\varphi_{\rm out})$, and (b) to $\theta = \pi/2$ by the rotation $\boldsymbol{R}_y(\pi/2 - \theta_{\rm out})$. The resulting event and wave vector are denoted $\mathcal{E}_{\rm out,eq}$ and $k'^\mu_{\rm out}$. Middle: $k'^\mu_{\rm out}$ is brought to the equatorial plane by the rotation $\boldsymbol{R}_x(-\psi)$. Right: Final situation.

Introducing the dimensionless variable $u \equiv r_{\rm S}/r$ and the impact parameter $b = L/E$, Eqs. (4.16) imply

$$r_{\rm S}^2\left(\frac{{\rm d}u}{{\rm d}t}\right)^2 = \frac{u^4}{\varepsilon_1^2}P(u)A^2(u), \tag{4.17}$$

$$\left(\frac{{\rm d}u}{{\rm d}\varphi}\right)^2 = P(u), \tag{4.18}$$

$$\frac{r_{\rm S}^2}{E^2}\left(\frac{{\rm d}u}{{\rm d}v}\right)^2 = \frac{u^4}{\varepsilon_1^2}P(u), \tag{4.19}$$

with

$$A(u) = 1 - u - \varepsilon_2 u^{-2}, \qquad P(u) \equiv \varepsilon_1^2 - u^2 A(u), \tag{4.20}$$

and where $\varepsilon_1 \equiv r_{\rm S}/b$ and $\varepsilon_2 \equiv \Lambda r_{\rm S}^2/3$.

Our purpose is now to compute the coordinates $(t_{\rm in}, r_{\rm in}, \varphi_{\rm in})$ and the components $k^\mu_{\rm in}$ of the wave vector at the entrance event $\mathcal{E}_{\rm in}$, given those at $\mathcal{E}_{\rm out}$. The situation is summarized in Fig. 6.

The radius $r_{\rm in}$ (or alternatively $u_{\rm in}$) and time $t_{\rm in}$ at entrance are determined by comparing the radial dynamics of the photon, governed by Eq. (4.17), to the one of the hole boundary. The latter is obtained from Eqs. (2.14) and (2.18). By introducing $u_{\rm h} = r_{\rm S}/r_{\rm h}$, it reads

$$r_{\rm S}\frac{{\rm d}u_{\rm h}}{{\rm d}t} = -u_{\rm h}^2 A(u_{\rm h})\sqrt{1 - A(u_{\rm h})}. \tag{4.21}$$

Equations (4.17) and (4.21) are then integrated[2] as $t_{\rm photon}(u)$ and $t_{\rm hole}(u_{\rm h})$. The entrance radius then results from solving numerically the equation $t_{\rm photon}(u_{\rm in}) = t_{\rm hole}(u_{\rm in})$, which also provides $t_{\rm in}$.

The usual textbook calculation of the deflection angle $\Delta\varphi_\infty$ of a light ray in Kottler geometry yields

$$\Delta\varphi_\infty = 2\varepsilon_1\sqrt{1 + \frac{\varepsilon_2}{\varepsilon_1^2}} = \frac{4GM}{b}\sqrt{1 + \frac{\Lambda b^2}{3}} \tag{4.22}$$

at lowest order in ε_1 and ε_2. However, we cannot use this expression here—although it gives its typical order of magnitude—because $\Delta\varphi_\infty$ represents the angle between the *asymptotic* incoming and outgoing directions of a ray, whereas we must take into account the *finite* extension of the hole (see Fig. 6).

In general, the deflection angle $\Delta\varphi = \varphi_{\rm out} - \varphi_{\rm in}$ is

$$\Delta\varphi = \int_{u_{\rm in}}^{u_{\rm m}} \frac{{\rm d}u}{\sqrt{P(u)}} + \int_{u_{\rm out}}^{u_{\rm m}} \frac{{\rm d}u}{\sqrt{P(u)}} - 2\pi \tag{4.23}$$

where $P(u)$ is the polynomial defined in Eq. (4.20), and $u_{\rm m}$ is the value of u at minimal approach. The integral involved in Eq. (4.23) can be rewritten as

$$\int_u^{u_{\rm m}} \frac{{\rm d}u'}{\sqrt{P(u')}} = \frac{2}{\sqrt{u_3 - u_2}} F\left[\arcsin\sqrt{\frac{u_2 - u}{u_2 - u_1}}, \frac{u_2 - u_1}{u_2 - u_3}\right], \tag{4.24}$$

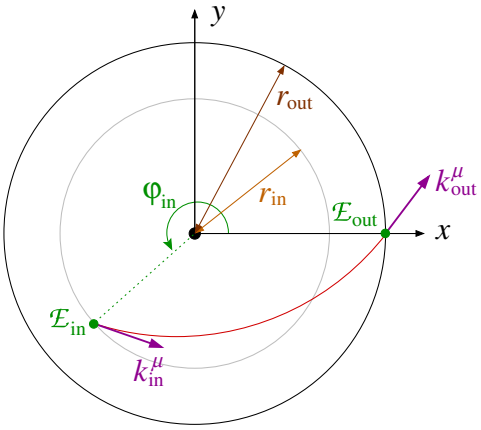

FIG. 6 (color online). Null geodesic in the Kottler region. Depicted with the Kottler coordinate system, the hole grows so that the ray enters with $r_{\rm in}$ and exits with $r_{\rm out} > r_{\rm in}$.

[2]The integration can be performed either numerically, or analytically in the case of Eq. (4.17) and perturbatively for Eq. (4.21).

where $u_1 < u_2 = u_m < u_3$ are the three (real) roots of $P(u)$, and $F(\psi, e)$ denotes the elliptic function of the first kind [72]

$$F(\psi, e) \equiv \int_0^{\psi} \frac{\mathrm{d}\theta}{\sqrt{1 - e\sin^2\theta}}. \tag{4.25}$$

Thus, Eq. (4.24) provides an exact expression of the deflection angle $\Delta\varphi$, and therefore of φ_{in}.

Once $\mathcal{E}_{\mathrm{in}}$ is determined, it is easy to obtain k^{μ}_{in} by using the constants of motion. The result is

$$k^{t}_{\mathrm{in}} = \frac{E}{A(r_{\mathrm{in}})} = \frac{A(r_{\mathrm{out}})}{A(r_{\mathrm{in}})} k^{t}_{\mathrm{out}}, \tag{4.26}$$

$$k^{\varphi}_{\mathrm{in}} = \frac{L}{r^2_{\mathrm{in}}} = \left(\frac{r_{\mathrm{out}}}{r_{\mathrm{in}}}\right)^2 k^{\varphi}_{\mathrm{out}}, \tag{4.27}$$

$$k^{r}_{\mathrm{in}} = -\sqrt{[A(r_{\mathrm{in}})k^{t}_{\mathrm{in}}]^2 - A(r_{\mathrm{in}})(r_{\mathrm{in}}k^{\varphi}_{\mathrm{in}})^2}. \tag{4.28}$$

4. Final conditions at $\mathcal{E}_{\mathrm{in}}$

The last step consists in coming back to the original FL coordinate system. That means (a) using $\boldsymbol{R}^{-1}$ to recover the initial system of axes, and (b) converting the components of $\mathcal{E}_{\mathrm{in}}$ and k^{μ}_{in} in terms of the FL coordinate system. We have already described such operations in Secs. IV B 2 and IV B 1 respectively, except for the time coordinate (since we set $t_{\mathrm{out}} = 0$).

The easiest way to compute the cosmic time T_{in} at entrance is to use the relation $r_{\mathrm{in}} = a(T_{\mathrm{in}})f_K(\rho_{\mathrm{h}})$. In a spatially Euclidean FL spacetime ($K = 0$), we get

$$T_{\mathrm{in}} = \frac{2}{3H_0\sqrt{\Omega_\Lambda}} \operatorname{argsinh}\left[\sqrt{\frac{\Omega_\Lambda}{1-\Omega_\Lambda}}\left(\frac{r_{\mathrm{in}}}{a_0\rho_{\mathrm{h}}}\right)^{3/2}\right]. \tag{4.29}$$

With this last result, we have completely determined the entrance event $\mathcal{E}_{\mathrm{in}}$.

5. Sachs basis and optical tidal matrix

Once the geodesic equation is completely solved, we are ready to integrate the Sachs equation in the Kottler region, that is, to determine the Wronski matrix $\mathcal{W}_{\mathrm{K}}$. Such a task requires us to first define the Sachs basis (s_1, s_2) with respect to which $\mathcal{W}_{\mathrm{K}}$ will be calculated.

The four-velocity u is chosen to be the one of a radially free-falling observer,

$$u \equiv \frac{1}{A(r)}\partial_t + \sqrt{1 - A(r)}\partial_r. \tag{4.30}$$

This choice ensures the continuity of u through the hole frontier, where $u = \partial_T$. The wave four-vector k is imposed by the null geodesic equations, and reads

$$k = \frac{E}{A(r)}\partial_t \pm E\sqrt{1 - \frac{b^2A(r)}{r^2}}\partial_r + \frac{L}{r^2}\partial_\varphi \tag{4.31}$$

where the $\pm$ sign depends on whether the photon approaches ($-$) or recedes ($+$) from the center of the hole.

By definition, the screen vectors s_1, s_2 form an orthonormal basis of the plane orthogonal to both u and k. Here, since the trajectory occurs in the equatorial plane, the first one can be trivially chosen as

$$s_1 \equiv \partial_z = -\frac{1}{r}\partial_\theta. \tag{4.32}$$

The second one is obtained from the orthogonality and normalization constraints, and reads

$$s_2 \equiv \frac{1}{N}\left[\frac{\sqrt{1 - A(r)}}{A(r)}\partial_t + \partial_r + \frac{1}{bA(r)}\left(\sqrt{1 - A(r)} \mp \sqrt{1 - \frac{b^2A(r)}{r^2}}\right)\partial_\varphi\right], \tag{4.33}$$

where the normalization function is

$$N \equiv \frac{r}{bA(r)}\left(1 \mp \sqrt{1 - A(r)}\sqrt{1 - \frac{b^2A(r)}{r^2}}\right). \tag{4.34}$$

Using the Sachs basis defined by Eqs. (4.30), (4.31), (4.32), and (4.33), we can finally compute the optical tidal matrix, and get

$$\mathcal{R} = \begin{pmatrix} -\mathcal{R}(r) & 0 \\ 0 & \mathcal{R}(r) \end{pmatrix}, \tag{4.35}$$

where the function $\mathcal{R}(r)$ is

$$\mathcal{R}(r) \equiv \frac{3}{2}\left(\frac{L}{r_{\mathrm{S}}^2}\right)^2\left(\frac{r_{\mathrm{S}}}{r}\right)^5. \tag{4.36}$$

As expected from the general decomposition (3.8), $\mathcal{R}$ is trace free because only Weyl focusing is at work. Let us finally emphasize that Λ does not appear in the expression (4.36) of $\mathcal{R}(r)$, which is not surprising since a pure cosmological constant does not deflect light.

6. Wronski matrix

The Sachs equations can now be integrated in order to determine the scale matrix $\mathcal{C}_{\mathrm{K}}$ and the Jacobi matrix $\mathcal{D}_{\mathrm{K}}$ that compose the Wronski matrix $\mathcal{W}_{\mathrm{K}}$.

First, since $\mathcal{R}$ is diagonal, the Sachs equations (3.7) only consist of the following two decoupled ordinary differential equations:

$$\frac{\mathrm{d}^2\xi_1}{\mathrm{d}v^2} = -\mathcal{R}[r(v)]\xi_1(v), \tag{4.37}$$

$$\frac{\mathrm{d}^2\xi_2}{\mathrm{d}v^2} = +\mathcal{R}[r(v)]\xi_2(v). \tag{4.38}$$

Clearly, the decoupling implies that the off-diagonal terms of $\mathcal{C}_K$ and $\mathcal{D}_K$ vanish,

$$\mathcal{C}^K_{12} = \mathcal{C}^K_{21} = \mathcal{D}^K_{12} = \mathcal{D}^K_{21} = 0. \tag{4.39}$$

The calculation of the diagonal coefficients requires us to integrate Eqs. (4.37) and (4.38). This cannot be performed analytically because there is no exact expression for r as a function of v along the null geodesic. Indeed, we can write v as a function of r from Eq. (4.19) but this relation is not invertible by hand.

Nevertheless, we are able to perform the integration perturbatively in the regime where $\varepsilon_2/\varepsilon_1 \ll \varepsilon_1 \ll 1$, the relevance of which shall be justified by the orders of magnitude discussed in the next section. Solving Eq. (4.19) at leading order in ε_1, ε_2 leads to

$$u(v) = \frac{\varepsilon_1}{\sqrt{1 + (v - v_m)^2/\Delta v^2}} + \mathcal{O}\left(\varepsilon_1^2, \frac{\varepsilon_2}{\varepsilon_1}\right) \tag{4.40}$$

with $\Delta v \equiv b/E$, and where v_m denotes the value of the affine parameter v at the point of minimal approach. Equation (4.37) then becomes, at leading order in ε_1, ε_2, and using the dimensionless variable $w \equiv (v - v_m)/\Delta v$,

$$\frac{d^2\xi_1}{dw^2} = -\frac{3\varepsilon_1}{2}\left(\frac{1}{1 + w^2}\right)^{5/2}\xi_1. \tag{4.41}$$

The perturbative resolution of Eq. (4.41) from v_{init} to v finally leads to

$$\mathcal{C}^K_{11} = 1 - \frac{3\varepsilon_1}{2}[-B'(w_{init})(w - w_{init}) + B(w) - B(w_{init})] + \mathcal{O}\left(\varepsilon_1^2, \frac{\varepsilon_2}{\varepsilon_1}\right), \tag{4.42}$$

and

$$\mathcal{D}^K_{11} = (v - v_{init}) + \frac{3\varepsilon_1}{2}\Delta v\{w_{init}[B(w) - B(w_{init}) - B'(w_{init})(w - w_{init})] - [C(w) - C(w_{init}) - C'(w_{init})(w - w_{init})]\} + \mathcal{O}\left(\varepsilon_1^2, \frac{\varepsilon_2}{\varepsilon_1}\right), \tag{4.43}$$

where the functions B and C are given by

$$B(w) \equiv \frac{1 + 2w^2}{3\sqrt{1 + w^2}} \quad \text{and} \quad C(w) \equiv \frac{-w}{3\sqrt{1 + w^2}}. \tag{4.44}$$

The expressions of $\mathcal{C}^K_{22}$ and $\mathcal{D}^K_{22}$ are respectively obtained from Eqs. (4.42) and (4.43) by turning ε_1 into $-\varepsilon_1$.

Note that in the limit ε_1, $\varepsilon_2/\varepsilon_1 \to 0$, i.e. $b \to \infty$ and $\Lambda = 0$, we find $\mathcal{C} = \mathbf{1}$ and $\mathcal{D} = (v - v_{init})\mathbf{1}$, which are the expected expressions in Minkowski spacetime.

C. Practical implementation

This section has described the complete resolution of the equations for light propagation in a Swiss-cheese universe. All the results are included in a Mathematica program OneHole which takes, as input, the observation conditions and the properties of the hole; and returns $\mathcal{E}_{in}$, k_{in} and $\mathcal{W}(v_{source}; v_{obs}) = \mathcal{W}_K(v_{in}; v_{out}) \cdot \mathcal{W}_{FL}(v_{out}; v_{obs})$. For simplicity, this program has been written assuming that *the FL region has Euclidean spatial sections* ($K = 0$).

Iterating OneHole allows us to propagate a light signal back to an arbitrary emission event. Eventually, the redshift z is obtained by comparing the wave vector at emission and reception; and the luminosity distance is extracted from the block $\mathcal{D}(v_{source}; v_{obs})$ of the Wronski matrix $\mathcal{W}(v_{source}; v_{obs})$, according to

$$D_L = (1 + z)^2\sqrt{\det \mathcal{D}(v_{source}; v_{obs})}. \tag{4.45}$$

Note finally that, when iterating OneHole, we must also rotate the Sachs basis (s_1, s_2), to take into account that the plane of motion differs for two successive holes.

V. EFFECT OF ONE HOLE

Our method is first applied to a Swiss cheese with a single hole. The purpose is to study the effects on the redshift and luminosity distance—for the light emitted by a standard candle—due to the presence of the hole.

A. Numerical values and "opacity" assumption

The mass M of the clump inside the hole depends on what object it is supposed to model. The choice must be driven by the typical scales probed by the light beams involved in supernova observations. As discussed in the introduction the typical width of such beams is ~AU; for comparison the typical interstellar distance within a galaxy is ~pc. Hence, SN beams are sensitive to the very fine structure of the Universe, including the internal content of galaxies. This suggests that the clump inside the hole should represent a star, so that the natural choice should be $M \sim M_\odot$. Unfortunately, we cannot afford to deal with such a fine description, for numerical reasons.

Instead, the clump is chosen to stand for a gravitationally bound system, such as a galaxy ($M \sim 10^{11}M_\odot$), or a cluster of galaxies ($M \sim 10^{15}M_\odot$). By virtue of Eq. (2.19), the corresponding hole radii are respectively $r_h \sim 1$ Mpc and $r_h \sim 20$ Mpc. It is important to note that this choice keeps entirely relevant as far as the light beam does not enter the clump (so that its internal structure does not matter), that is, as long as

$$b > b_{min} \approx r_{phys}, \tag{5.1}$$

where r_{phys} is the physical size of the clump. For a galaxy $r_{phys} \sim 10$ kpc, and for a cluster $r_{phys} \sim 1$ Mpc. We choose to work under the assumption of Eq. (5.1); in other words *we proceed as if the clumps were opaque spheres*.

In the case of galactic clumps this "opacity" assumption can be justified by the three following arguments (in the case of clusters, however, it is highly questionable).

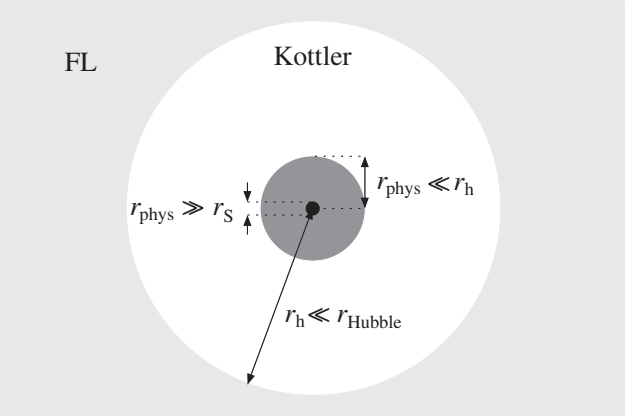

FIG. 7. Geometry and hierarchy of distances for a typical Swiss-cheese hole: $r_{\rm S} \ll r_{\rm phys} \ll r_{\rm h} \ll r_{\rm Hubble}$.

Statistics. Since $r_{\rm phys} \ll r_{\rm h}$ the cross section of the clumps is very small; thus we expect that *most* of the observations satisfy the condition (5.1).

Screening. A galaxy standing on the line of sight can simply be bright enough to flood a SN located behind it. For comparison, the absolute magnitude of a galaxy ranges from -16 to -24 [73], while for a SN it is typically -19.3 [74].

Strong lensing. A light beam crossing a galaxy enters the strong lensing regime, because the associated Einstein radius is $r_{\rm E} \sim \sqrt{r_{\rm S} D_{\rm A,SN}} \lesssim 10$ kpc $\sim r_{\rm phys}$. In this case, we expect a significant magnification of the SN which could be isolated, or even removed during data processing.

The "opacity" assumption is at the same time a key ingredient and a limitation of our approach.

The various distance scales involved in the model are clearly separated. The resulting hierarchy is depicted in Fig. 7, and the typical orders of magnitude are summarized in Table I. The latter includes the small parameters $\varepsilon_1 = r_{\rm S}/b$ and $\varepsilon_2 = \Lambda r_{\rm S}^2/3 \sim (r_{\rm S}/r_{\rm Hubble})^2$. Their values justify *a posteriori* the perturbative expansion performed in Sec. IV B 6, where we assumed that $\varepsilon_2/\varepsilon_1 \ll \varepsilon_1 \ll 1$. In fact, one can show from Eq. (2.19) that $\varepsilon_2 \sim \varepsilon_{1,\rm min}^3$.

In this section and the next one, we *temporarily* set for simplicity the cosmological constant to zero. The FL region is therefore characterized by the Einstein–de Sitter (EdS) cosmological parameters

$$\Omega_{\rm m} = 1, \qquad \Omega_K = 0, \qquad \Omega_\Lambda = 0. \tag{5.2}$$

TABLE I. Typical orders of magnitude for galaxylike ($M \sim 10^{11} M_\odot$) and clusterlike ($M \sim 10^{15} M_\odot$) Swiss-cheese holes.

Type	$r_{\rm S}$ (pc)	$r_{\rm phys}$ (kpc)	$r_{\rm h}$ (Mpc)	ε_1	ε_2
Galaxy	10^{-2}	10	1	10^{-8}–10^{-6}	10^{-23}
Cluster	100	1000	20	10^{-6}–10^{-4}	10^{-15}

The effect of the cosmological constant will be studied in detail in Sec. VII. The value of the Hubble parameter is fixed to $H_0 = h \times 100$ km/s/Mpc, with $h = 0.72$.

B. Setup

In order to study the corrections to the redshift z and luminosity distance $D_{\rm L}$, due to the presence of the hole, we consider the situation depicted in Fig. 8.

Our method is the following. We first choose the mass M inside the hole and the redshift $z_{\rm source}$ of the source. We then fix the comoving distance between the observer and the center of the hole, in terms of the cosmological (FL) redshift $z_{\rm h}^{\rm (FL)}$ of the latter. To finish, we choose a direction of observation, defined by the angle β between the line of sight and the line connecting the observer to the center of the hole.

Given those parameters, the light beam is propagated (in presence of the hole) until the redshift reaches $z_{\rm source}$. We obtain the emission event $\mathcal{E}_{\rm source}$ and the luminosity distance $D_{\rm L}$. We then compute $z_{\rm source}^{\rm (FL)}$ and $D_{\rm L}^{\rm (FL)}$ by considering a light beam that propagates from $\mathcal{E}_{\rm source}$ to the observer without the hole (bottom panel of Fig. 8).

C. Corrections to the redshift

1. Numerical results

The effect of the hole on the redshift is quantified by

$$\delta z \equiv \frac{z - z^{\rm (FL)}}{z^{\rm (FL)}}, \tag{5.3}$$

where we used the short notation z instead of $z_{\rm source}$. Figure 9 shows the evolution of δz with β, for

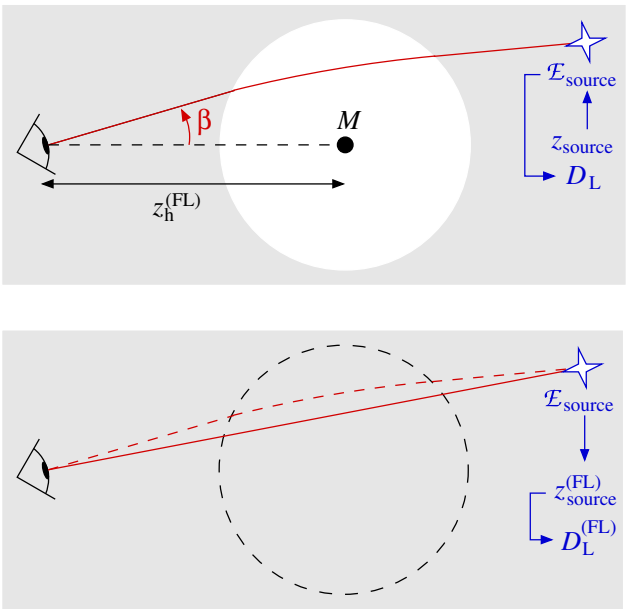

FIG. 8 (color online). Setup for evaluating the effect of one hole on the redshift and luminosity distance.

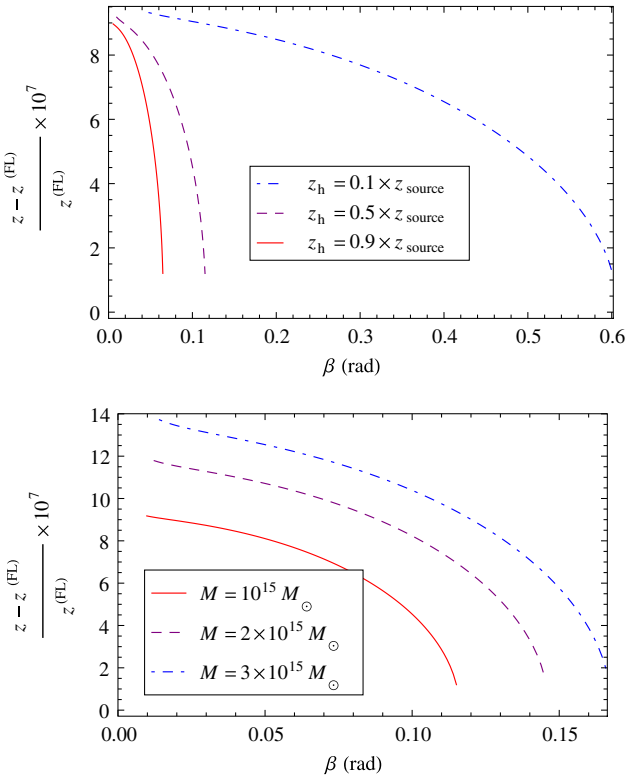

FIG. 9 (color online). Relative correction to the redshift z, due to the hole in the line of sight, as a function of the direction of observation β, for a source at $z_{\mathrm{source}} = 0.05$. Top panel: The mass of the hole is $M = 10^{15} M_\odot$, and three positions between the source and the observer are tested, $z_h^{(\mathrm{FL})}/z_{\mathrm{source}} = 0.1$ (blue, dot-dashed), 0.5 (purple, dashed), and 0.9 (red, solid). Bottom panel: The hole is at $z_h^{(\mathrm{FL})} = 0.5 z_{\mathrm{source}}$ and three values for the mass are tested, $M/10^{15} M_\odot = 3$ (blue, dot-dashed), 2 (purple, dashed), and 1 (red, solid).

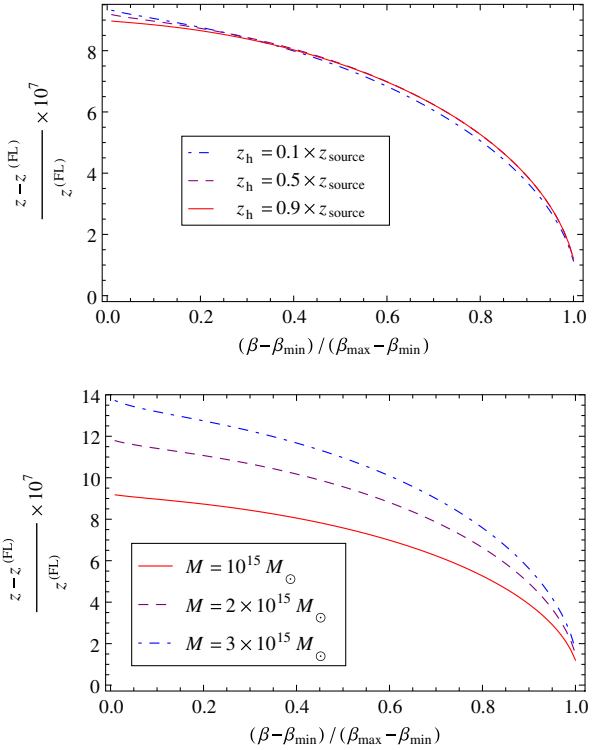

FIG. 10 (color online). Same as Fig. 9, but plotted in terms of the centered and normalized observation direction $(\beta - \beta_{\min})/(\beta_{\max} - \beta_{\min})$.

$z_{\mathrm{source}} = 0.05$ and various hole positions and masses. We have chosen $M \sim 10^{15} M_\odot$ because the effect is more significant and displays fewer numerical artifacts than for $M \sim 10^{11} M_\odot$.

We only consider directions of observation such that the light beam crosses the hole. Thus, $\beta_{\min} < \beta < \beta_{\max}$ where $\beta_{\min}$ and $\beta_{\max}$ depend on the physical cutoff r_{phys}, the radius r_h of the hole, and its distance to the observer $z_h^{(\mathrm{FL})}$. Those dependences can be eliminated by plotting δz as a function of $(\beta - \beta_{\min})/(\beta_{\max} - \beta_{\min})$ instead of β, as displayed in Fig. 10.

As expected, δz tends to zero when β approaches $\beta_{\max}$ (light ray tangent to the hole boundary). We notice that δz does not significantly depend on the distance between the observer and the hole. However, the effect clearly grows with the mass of the hole.

2. Analytical estimation of the effect

The correction in redshift due to hole can be understood as an integrated Sachs-Wolfe effect (see e.g. Chapter 7 of Ref. [1]). As the boundary of the hole grows with time (see Fig. 6), the light signal undergoes a stronger gravitational potential at entrance than at exit. That induces a gravitational redshift δz_{grav} which adds to the cosmological one, and reads

$$1 + \delta z_{\mathrm{grav}} = \frac{k^t_{\mathrm{in}}}{k^t_{\mathrm{out}}} = \frac{A(r_{\mathrm{out}})}{A(r_{\mathrm{in}})}. \tag{5.4}$$

The order of magnitude of δz_{grav} can be evaluated as follows. Let $\delta r = r_{\mathrm{out}} - r_{\mathrm{in}}$ be the increase of the radius of the hole between entrance and exit. The expansion dynamics implies $\delta r \sim \sqrt{\varepsilon_1} \Delta t$, where $\Delta t = t_{\mathrm{out}} - t_{\mathrm{in}} \sim r_{\mathrm{in}}$, r_{out} is the time spent by the photon inside the hole. Using Eq. (5.4), we conclude that

$$\delta z_{\mathrm{grav}} \sim \varepsilon_1^{3/2}. \tag{5.5}$$

For $M = 10^{15} M_\odot$ (clusterlike hole), the numerical values given in Table I yield $\delta z_{\mathrm{grav,max}} \sim 10^{-6}$. This order of magnitude is compatible with the full numerical integration displayed in Figs. 9 and 10.

Such an analytical estimate enables us to understand why δz increases with M, that is, with the size of the hole. Indeed, the bigger the hole, the longer the photon travel time so that the hole has more time to grow, and finally $A(r_{\mathrm{out}}) - A(r_{\mathrm{in}})$ is larger.

D. Corrections to the luminosity distance

The effect of the hole on the luminosity distance can be characterized in a similar way by

$$\delta D_{\mathrm{L}} \equiv \frac{D_{\mathrm{L}} - D_{\mathrm{L}}^{(\mathrm{FL})}}{D_{\mathrm{L}}^{(\mathrm{FL})}}. \tag{5.6}$$

The associated results, in the same conditions as in the previous paragraph, are displayed in Figs. 11 and 12.

We notice that δD_{L} is maximum if the hole lies halfway between the source and the observer, which is indeed expected since the lensing effects scale as

$$\frac{D_{\mathrm{A}}(\text{observer, lens}) \times D_{\mathrm{A}}(\text{lens, source})}{D_{\mathrm{A}}(\text{observer, source})}, \tag{5.7}$$

which typically peaks for $z_{\mathrm{lens}} \approx z_{\mathrm{source}}/2$. The maximal amplitude of the correction is of order 10^{-4}, for masses ranging from $10^{15} M_\odot$ to $3 \times 10^{15} M_\odot$. Just as for the redshift, the effect increases with the size of the hole.

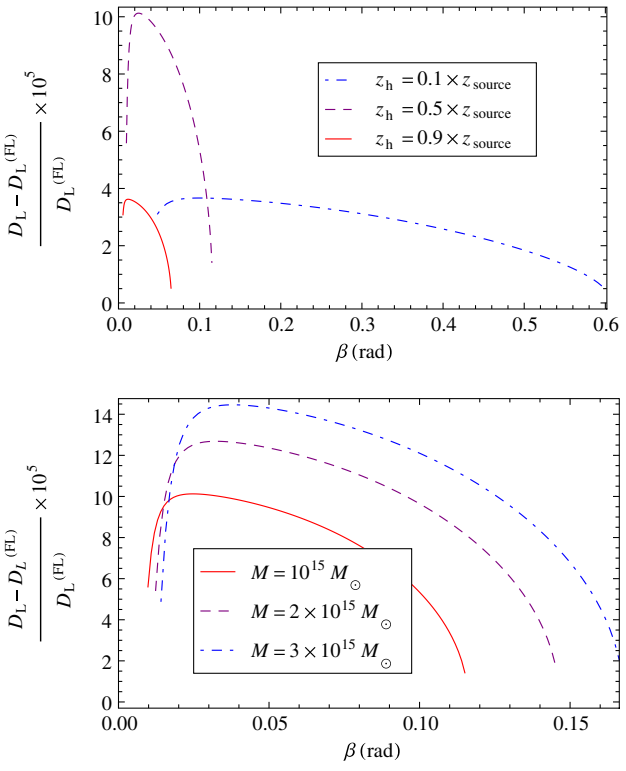

FIG. 11 (color online). Relative correction to the luminosity distance D_{L}, due to the hole in the line of sight, as a function of the direction of observation β, for a source at $z_{\mathrm{source}} = 0.05$. Top panel: The mass of the hole is $M = 10^{15} M_\odot$, and three positions between the source and the observer are tested, $z_{\mathrm{h}}^{(\mathrm{FL})}/z_{\mathrm{source}} = 0.1$ (blue, dot-dashed), 0.5 (purple, dashed), and 0.9 (red, solid). Bottom panel: The hole is at $z_{\mathrm{h}}^{(\mathrm{FL})} = 0.5 z_{\mathrm{source}}$ and three values for the mass are tested, $M/10^{15} M_\odot = 3$ (blue, dot-dashed), 2 (purple, dashed), and 1 (red, solid).

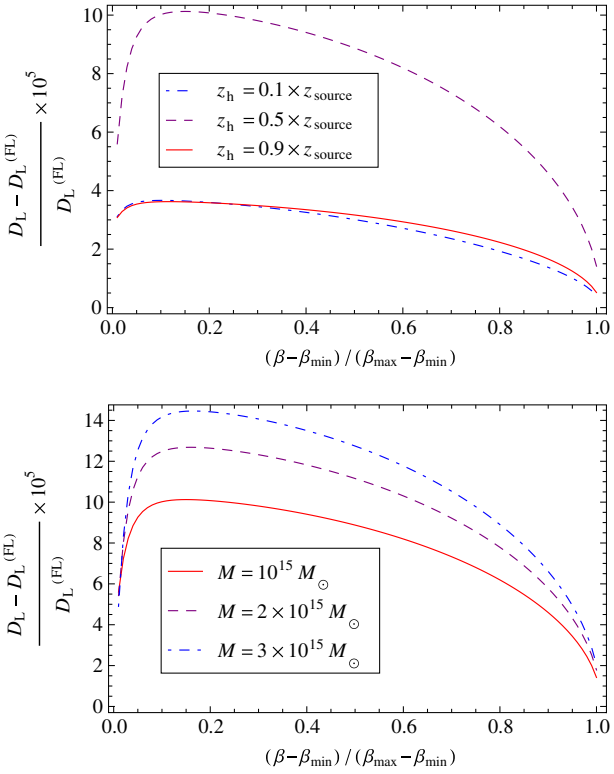

FIG. 12 (color online). Same as Fig. 11, but plotted in terms of the centered and normalized observation direction $(\beta - \beta_{\min})/(\beta_{\max} - \beta_{\min})$.

Note that δD_{L} can be related to the relative magnification μ, frequently used in the weak-lensing formalism, and defined by

$$\mu \equiv \left(\frac{D_{\mathrm{A}}^{(\mathrm{FL})}}{D_{\mathrm{A}}}\right)^2 = \left(\frac{1+z}{1+z^{(\mathrm{FL})}}\right)^4 \left(\frac{D_{\mathrm{L}}^{(\mathrm{FL})}}{D_{\mathrm{L}}}\right)^2. \tag{5.8}$$

Hence, if the correction on z is negligible compared to the one of D_{A}, then the relation between δD_{L} and μ is

$$\delta D_{\mathrm{L}} \approx \frac{1}{\sqrt{\mu}} - 1. \tag{5.9}$$

E. Summary

The presence of a single hole between the source and the observer induces both a correction in redshift and luminosity distance. For a hole with mass $M \sim 10^{15} M_\odot$, the relative amplitudes of those corrections are $\delta z \sim 10^{-7}$–10^{-6} and $\delta D_{\mathrm{L}} \sim 100 \delta z$. The same study for $M \sim 10^{11} M_\odot$ leads to similar results with $\delta z \sim 10^{-10}$–10^{-9}. Therefore, the effects of a single hole seem negligible.

VI. EFFECT OF SEVERAL HOLES

We now investigate a Swiss-cheese model containing many holes arranged on a regular lattice. Again, in this entire section, the cosmological parameters characterizing the FL region are the EdS ones.

A. Description of the arrangement of holes

1. Smoothness parameter

The smoothness of the distribution of matter within a Swiss cheese can be quantified by a parameter f constructed as follows. Choose a region of space with—comoving or physical—volume V, where $V^{1/3}$ is large compared to the typical distance between two holes. Thus, this volume contains many holes, the total volume of which is $V_{\rm holes}$, while the region left with homogeneous matter occupies a volume $V_{\rm FL} = V - V_{\rm holes}$. We define the smoothness parameter by

$$f \equiv \lim_{V\to\infty} \frac{V_{\rm FL}}{V}. \tag{6.1}$$

In particular, $f = 1$ corresponds to a Swiss cheese with no hole—that is, perfectly smooth—while $f = 0$ corresponds to the case where matter is under the form of clumps. Of course, f also characterizes the ratio between the energy density of the continuous matter and the mean energy density.

2. Lattice

We want to construct a Swiss cheese for which the smoothness parameter is as small as possible. If all holes are identical, this close-packing problem can be solved by using, for instance, a hexagonal lattice. The corresponding arrangement is pictured in Fig. 13. The minimal value of the smoothness parameter is in this case

$$f_{\rm min} = 1 - \frac{\pi}{3\sqrt{2}} \approx 0.26. \tag{6.2}$$

In order to reach a smoothness parameter smaller than $f_{\rm min}$, one would have to insert a second family of smaller holes. By iterating the process, one can in principle make f as close as one wants to zero.

B. Observations in a unique line of sight

We now focus on the corrections to the redshift and luminosity distance of a source whose light travels through the Swiss-cheese universe described previously. We study the influence of (a) the distance between the source and the observer, (b) the smoothness parameter f, and (c) the mass M of the holes.

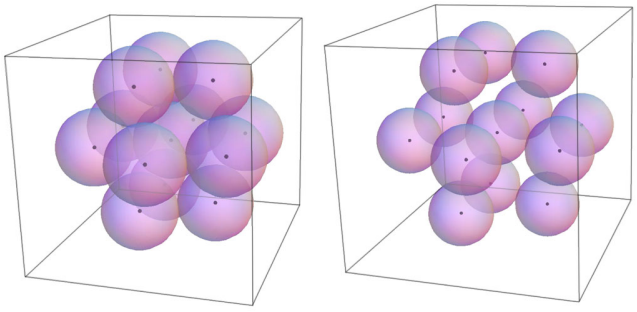

FIG. 13 (color online). Hexagonal lattice of identical holes. On the left, the arrangement is close-packed, so that the smoothness parameter is $f = f_{\rm min} \approx 0.26$. On the right, $f = 0.7$.

1. Setup

After having chosen the parameters (f, M) of the model, we arbitrarily choose the spatial position of the observer in the FL region, and fix its direction of observation. The method is then identical to the one of Sec. V. The light beam is propagated from the observer until the redshift reaches the one of the source, z. The ending point defines the emission event $\mathcal{E}_{\rm source}$. We emphasize that only emission events occurring in the FL region are considered in this article.

2. Influence of the smoothness parameter

In this paragraph, the mass of every hole is fixed to $M = 10^{11} M_\odot$ (galactic holes). The relative corrections to the redshift δz and luminosity distance $\delta D_{\rm L}$, as functions of the redshift z of the source, have been computed and are displayed in Fig. 14 for different values of the smoothness parameter f.

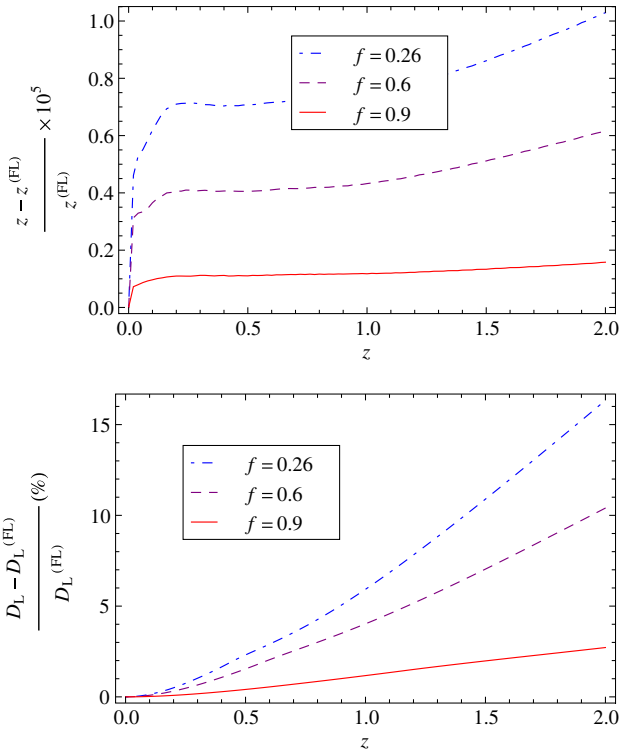

FIG. 14 (color online). Relative corrections to the redshift z (top panel) and luminosity distance $D_{\rm L}$ (bottom panel) as functions of z, for an arbitrary light beam traveling through a Swiss-cheese universe. All holes are identical; their mass is $M = 10^{11} M_\odot$. Three different smoothness parameters are tested: $f = 0.26$ (blue, dot-dashed), 0.6 (purple, dashed), and 0.9 (red, solid).

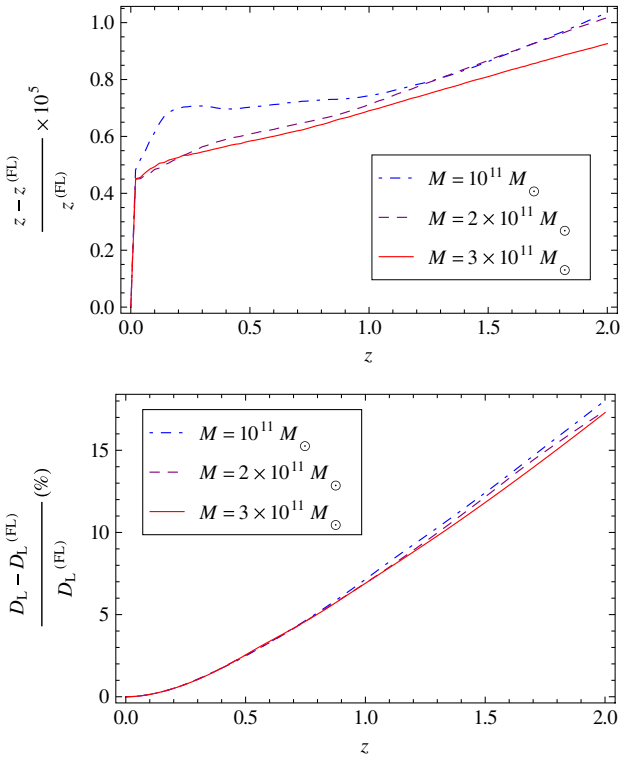

FIG. 15 (color online). Same as Fig. 14 but with $f = 0.26$ and three different values for the masses: $M/10^{11}M_\odot = 1$ (blue, dot-dashed), 2 (purple, dashed), and 3 (red, solid).

While the corrections to the redshift remain small—typically $\delta z < 10^{-5}$—the cumulative effect of lensing on the luminosity distance is significant. For instance, a source at $z \sim 1.5$ would appear 10% farther in a Swiss cheese with $f = 0.26$, than in a strictly homogeneous universe. Both δz and δD_L increase with z and decrease with f, as intuitively expected. Thus, the more holes, the stronger the effect. As examples, the light beam crosses ~300 holes for ($f = 0.26$, $z = 0.1$) or ($f = 0.9$, $z = 1$), but it crosses ~2000 holes for ($f = f_{\rm min}$, $z = 1$).

3. Influence of the mass of the holes

We now set the smoothness parameter to its minimal value $f_{\rm min} \approx 0.26$, and repeat the previous analysis for various hole masses. The results are displayed in Fig. 15.

We conclude that neither δz nor δD_L depends significantly on M, that is, on the size of the holes. Thus, what actually matters is not the number of holes intersected by the beam, but rather the total time spent inside holes.

C. Statistical study for random directions of observation

The previous study was restricted to a single line of sight, but since a Swiss-cheese universe is not strictly homogeneous, the corrections to z and D_L are expected to vary from one line of sight to another. As pointed out by e.g. Refs. [57,61], such a restrictive analysis can lead to overestimate the mean corrections induced by inhomogeneities. Besides, as stressed by Ref. [8], the dispersion of the data is crucial for interpreting SN observations. Hence, the conclusions of the previous subsection need to be completed by a statistical study, with randomized directions of observation.

Since the effect on the redshift is observationally negligible, we focus on the luminosity distance. After having set the parameters (f, M) of the model, we fix the position of the observer in the FL region. Then, for a given redshift z, we consider a statistical sample of $N_{\rm obs}$ randomly distributed directions of observation $\vec{d} \in \mathcal{S}^2$, and compute $\delta D_L(z, \vec{d})$ for each one.

Figure 16 shows the probability distribution of δD_L for sources at redshifts $z = 0.1$ (top panel) and $z = 1$ (bottom panel). We compare two Swiss-cheese models with the same smoothness parameter $f = f_{\rm min}$ but with different values for the masses of their holes ($M = 10^{11}M_\odot$ and $10^{15}M_\odot$). The histograms of Fig. 16 are generated from statistical samples which contain $N_{\rm obs} = 200$ directions of observation each.

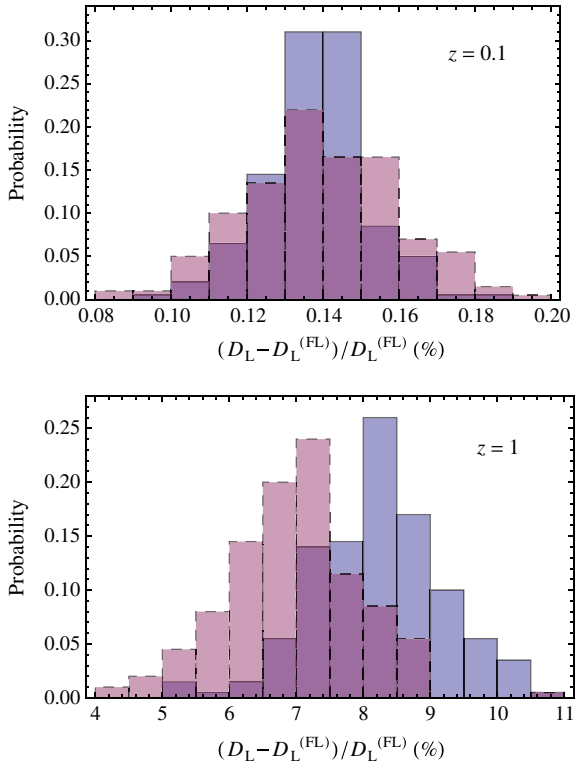

FIG. 16 (color online). Probability distribution of the relative correction to the luminosity distance for random directions of observation, at $z = 0.1$ (top panel) and $z = 1$ (bottom panel). The smoothness parameter is $f = f_{\rm min}$ and two different values for the masses of the holes are tested: $M = 10^{11}M_\odot$ (blue, solid) and $M = 10^{15}M_\odot$ (purple, dashed).

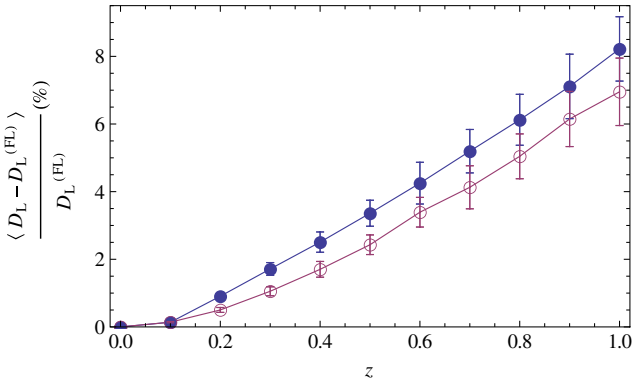

FIG. 17 (color online). Evolution, with redshift z, of the relative correction to the luminosity distance averaged over $N_{\rm obs} = 200$ random directions of observation. Error bars indicate the dispersion $\sigma_{\delta D_L}$ around the mean correction $\langle \delta D_L \rangle$. As in Fig. 16, we compare Swiss-cheese models with $M = 10^{11} M_\odot$ (blue, filled markers) and $M = 10^{15} M_\odot$ (purple, empty markers).

From the statistical samples, we can compute the mean correction $\langle \delta D_L \rangle(z)$ and its standard deviation $\sigma_{\delta D_L}(z)$, whose evolutions are plotted in Fig. 17.

The results displayed in Fig. 17 confirm the conclusions of Sec. VI B. The distance-redshift relation in a Swiss cheese is biased with respect to the one of a purely homogenous universe. This effect is statistically significant, we indeed estimate (empirically) that

$$\langle \delta D_L \rangle(z) \approx 8 \times \sigma_{\delta D_L}(z). \tag{6.3}$$

The bias slightly decreases with the mass parameter M. However, it can be considered quite robust because a variation of 4 orders of magnitude for M only induces a variation of $\sim 10\%$ for the bias.

The intrinsic dispersion of D_L, associated with $\sigma_{\delta D_L}$, can be compared with the typical dispersion of the observation. For instance, at $z = 1$ the former is $\sim 1\%$, while the latter is estimated to be typically $\sim 10\%$ [75]. It follows that the dispersion induced by the inhomogeneity of the distribution of matter remains small compared to the observational dispersion.

D. Summary and discussion

This section has provided a complete study of the effect of inhomogeneities on the Hubble diagram, investigating both the corrections to the redshift and luminosity distance of standard candles. The Swiss-cheese models are made of identical holes, defined by their mass M, and arranged on a regular hexagonal lattice. The fraction of matter remaining in FL regions defines the smoothness parameter f. For the hexagonal lattice, $f_{\rm min} \approx 0.26$.

The effect on the redshift is negligible ($\delta z < 10^{-5}$), while the correction to the luminosity distance is significant ($\delta D_L > 10\%$ at high redshift). Compared to the homogeneous case, sources are systematically demagnified in a Swiss-cheese universe. The effect increases with z and decreases with f.

Our results differ from those obtained in Swiss-cheese models with LTB solutions inside the holes. In the latter case, a source can be either demagnified if light mostly propagates through underdense regions [54,55,59] (and if the observer is far away from a void, see Ref. [76]), or magnified otherwise. It has been proven in Refs. [58,61,62] that the global effect averages to zero when many sources are considered. Hence, LTB holes introduce an additional dispersion to the Hubble diagram, but no statistically significant bias. On the contrary, in the present study, light only propagates through underdense regions, because we only consider light beams which remain far from the hole centers. This assumption has been justified in Sec. V A by an "opacity" argument. The bias displayed by our results is mostly due to the selection of the light beams which can be considered observationally relevant.

Our results also differ qualitatively from those obtained in the framework of the perturbation theory. In Ref. [31], the probability density function $P(\mu)$ of the weak lensing magnification μ, due to the large scale structure, has been analytically calculated by assuming an initial power spectrum with slope $n = -2$. Just as for LTB Swiss-cheese models, the magnification shows no intrinsic bias (i.e. $\langle \mu \rangle = 1$), but it is shown that $P(\mu)$ peaks at a value $\mu_{\rm peak}$ slightly smaller than 1. Hence, a bias of order $\mu_{\rm peak} - \langle \mu \rangle$, which is typically 1% at $z = 1$, can emerge from observations because of insufficient statistics. However, this bias is far smaller than the one obtained in our Swiss-cheese model, of order $2\delta D_L \sim 15\%$ at $z = 1$.

Besides, the dispersion around the mean magnification is stronger for perturbation theory ($\sim 10\%$) than for both LTB and Kottler Swiss-cheese models ($\sim 2\%$).

VII. COSMOLOGICAL CONSEQUENCES

Since the Hubble diagram is modified by the presence of inhomogeneities, the resulting determination of the cosmological parameters must be affected as well.

More precisely, consider a Swiss-cheese universe whose FL regions are characterized by a set of cosmological parameters $(\Omega_{\rm m}, \Omega_K, \Omega_\Lambda)$, called *background* parameters in the following. If an astronomer observes SNe in this inhomogeneous universe and constructs the resulting Hubble diagram, but fits it with the usual FL luminosity-redshift relation—that is, assuming that he lives in a strictly homogeneous universe—then he will infer *apparent* cosmological parameters $(\bar{\Omega}_{\rm m}, \bar{\Omega}_K, \bar{\Omega}_\Lambda)$ which shall differ from the background ones. Evaluating this difference is the purpose of Secs. VII A, VII B, and VII C.

The natural question which comes after is, assuming that our own Universe is well described by a Swiss-cheese model, what are the *background* cosmological parameters

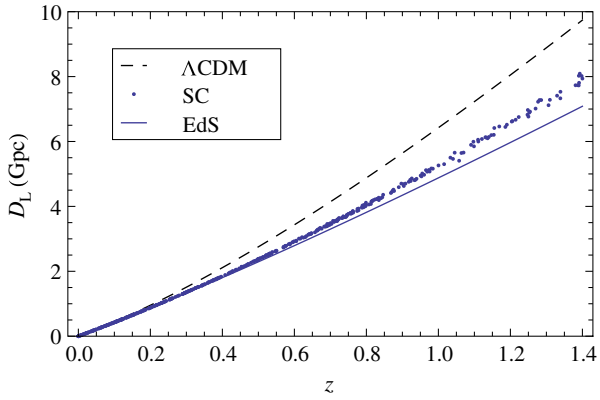

FIG. 18 (color online). Hubble diagram of a Swiss-cheese universe (dots) with $f = f_{\rm min}$, $M = 10^{11} M_\odot$ and EdS background cosmology. For comparison, we also display the distance-redshift relations of purely FL universes, with EdS parameters (blue, solid) and $(\Omega_{\rm m}, \Omega_K, \Omega_\Lambda) = (0.3, 0, 0.7)$ (black, dashed).

which best reproduce the actual SN observations? This issue is addressed in Sec. VII D.

A. Generating mock Hubble diagrams

The Hubble diagram observed in a given Swiss-cheese universe is constructed in the following way. We first choose the parameters of the model: f, M, and the background cosmology $(\Omega_{\rm m}, \Omega_\Lambda = 1 - \Omega_{\rm m})$.[3] We then fix arbitrarily the position of the observer in the FL region, and we simulate observations by picking randomly the line of sight $\vec{d}$, the redshift $z \in [0, z_{\rm max}]$, and we compute the associated luminosity distance $D_{\rm L}(z, \vec{d})$ as in Sec. VI. In order to make our mock SNe catalog resemble the SNLS 3 data set [77], we choose $z_{\rm max} = 1.4$ and $N_{\rm obs} = 472$.

An example of mock Hubble diagram, corresponding to a Swiss-cheese model with $f = f_{\rm min}$, $M = 10^{11} M_\odot$ and $(\Omega_{\rm m}, \Omega_K, \Omega_\Lambda) = (1, 0, 0)$ is plotted in Fig. 18. As a comparison, we also displayed $D_{\rm L}(z)$ for a homogeneous universe with (1) the same cosmological parameters, and (2) with $(\Omega_{\rm m}, \Omega_K, \Omega_\Lambda) = (0.3, 0, 0.7)$.

B. Determining apparent cosmological parameters

The apparent cosmological parameters $\bar{\Omega}_{\rm m}$, $\bar{\Omega}_\Lambda$ and $\bar{\Omega}_K = 1 - \bar{\Omega}_{\rm m} - \bar{\Omega}_\Lambda$ are determined from the mock Hubble diagrams by performing a χ^2 fit. The χ^2 is defined by

$$\chi^2(\bar{\Omega}_{\rm m}, \bar{\Omega}_\Lambda) \equiv \sum_{i=1}^{472} \left[\frac{\mu_i - \mu_{\rm FL}(z_i | \bar{\Omega}_{\rm m}, \bar{\Omega}_\Lambda)}{\Delta \mu_i} \right]^2, \qquad (7.1)$$

where μ no longer denotes the magnification, but rather the distance modulus associated with $D_{\rm L}$, so that

$$\mu \equiv 5 \log_{10} \left(\frac{D_{\rm L}}{10 \text{ pc}} \right). \qquad (7.2)$$

In Eq. (7.1), (z_i, μ_i) is the ith observation of the simulated catalog. In order to make the analysis more realistic, we have attributed to each data point an observational error bar $\Delta \mu_i$ estimated by comparison with the SNLS 3 data set [77]. Besides, $\mu_{\rm FL}(z | \bar{\Omega}_{\rm m}, \bar{\Omega}_\Lambda)$ is the theoretical distance modulus of a source at redshift z, in a FL universe with cosmological parameters $\bar{\Omega}_{\rm m}$, $\bar{\Omega}_\Lambda$, $\bar{\Omega}_K = 1 - \bar{\Omega}_{\rm m} - \bar{\Omega}_\Lambda$.

The results of this analysis for two mock Hubble diagrams are shown in Fig. 19. An EdS background leads to apparent parameters $(\bar{\Omega}_{\rm m}, \bar{\Omega}_K, \bar{\Omega}_\Lambda) = (0.5, 0.8, -0.3)$, which are very different from (1,0,0). Thus, the positive shift of $D_{\rm L}(z)$—clearly displayed in Fig. 18—turns out to be mostly associated to an apparent spatial curvature, rather than to an apparent cosmological constant. In this case the apparent curvature is necessary to obtain a good fit ($\bar{\Omega}_K = 0$ is out of the 2σ confidence contour), because a spatially flat FL model does not allow us to reproduce both the low-z and high-z behaviors of the diagram. The effect is weaker for a background with $(\Omega_{\rm m}, \Omega_\Lambda) = (0.3, 0.7)$, which leads to $(\bar{\Omega}_{\rm m}, \bar{\Omega}_K, \bar{\Omega}_\Lambda) = (0.2, 0.2, 0.6)$.

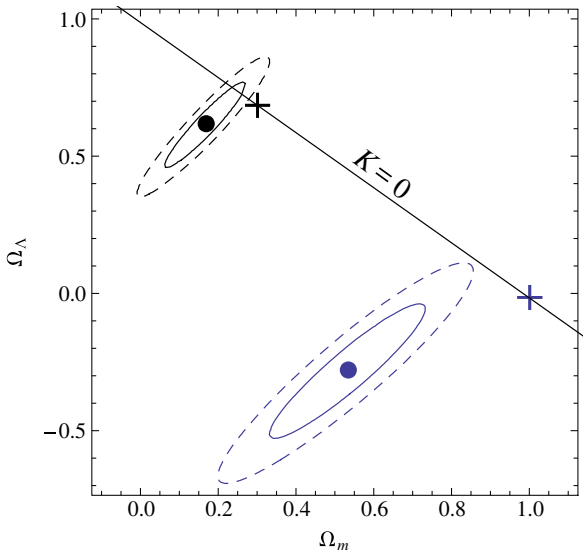

FIG. 19 (color online). Comparison between background parameters (crosses) and apparent parameters (disks) for two Swiss-cheese models with $f = f_{\rm min}$ and $M = 10^{15} M_\odot$. In blue, $(\Omega_{\rm m}, \Omega_\Lambda) = (1, 0)$ leads to $(\bar{\Omega}_{\rm m}, \bar{\Omega}_\Lambda) = (0.5, -0.3)$. In black, $(\Omega_{\rm m}, \Omega_\Lambda) = (0.3, 0.7)$ leads to $(\bar{\Omega}_{\rm m}, \bar{\Omega}_\Lambda) = (0.2, 0.6)$. The 1σ and 2σ contours are respectively the solid and dashed ellipses. The solid straight line indicates the configurations with zero spatial curvature.

[3] Recall that in the practical implementation of the theoretical results (see Sec. IV C), we assumed that $K = 0$, so that the background cosmology of our Swiss-cheese models is completely determined by $\Omega_{\rm m}$ or Ω_Λ. Nevertheless, the *apparent* curvature parameter $\bar{\Omega}_K$ is *a priori* nonzero.

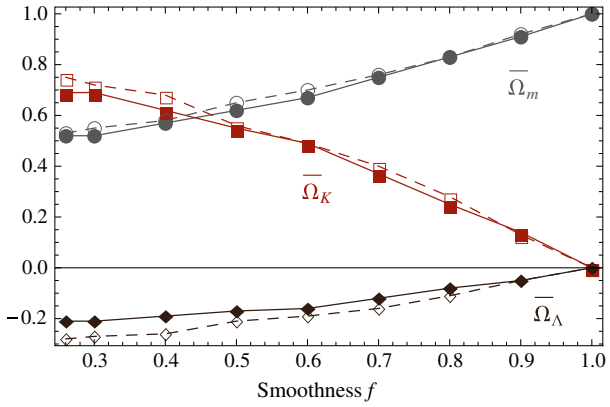

FIG. 20 (color online). Apparent cosmic parameters $\bar{\Omega}_{\rm m}$ (gray disks), $\bar{\Omega}_K$ (red squares) and $\bar{\Omega}_{\rm m}$ (black diamonds) versus smoothness parameter f, for a Swiss-cheese universe with EdS background $(\Omega_{\rm m}, \Omega_K, \Omega_\Lambda) = (1, 0, 0)$. Solid lines and filled markers correspond to $M = 10^{11} M_\odot$, dashed lines and empty markers to $M = 10^{15} M_\odot$.

C. Quantitative results

1. Influence of the smoothness parameter

Consider a Swiss-cheese model with EdS background cosmology. Figure 20 shows the evolution of the apparent cosmological parameters with smoothness f. As expected, we recover $\bar{\Omega}_i = \Omega_i$ when $f = 1$, the discrepancy between background and apparent cosmological parameters being maximal when $f = f_{\rm min}$. Surprisingly, a Swiss-cheese universe seems progressively dominated by a negative spatial curvature for small values of f.

The apparent deceleration parameter $\bar{q} = \bar{\Omega}_{\rm m}/2 - \bar{\Omega}_\Lambda$ is plotted in Fig. 21 as a function of f. Interestingly, even for $f = f_{\rm min}$, $\bar{q}$ remains almost equal to its background value $q = 1/2$. Therefore, though the apparent cosmological parameters can strongly differ from the background ones, the apparent expansion history is almost the same—at second order—as the background one.

Note that the results displayed in Figs. 20 and 21 are consistent with each other. The apparent cosmological constant $\bar{\Omega}_\Lambda$ is slightly smaller for $M = 10^{15} M_\odot$ than for $M = 10^{11} M_\odot$, so that $\bar{q}$ is slightly larger.

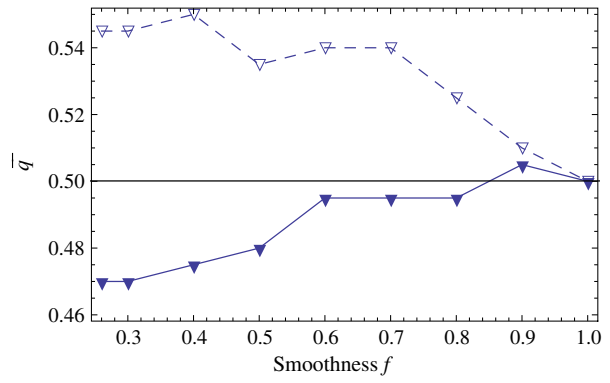

FIG. 21 (color online). Apparent deceleration parameter $\bar{q}$ as a function of smoothness parameter f, for Swiss-cheese models with EdS background ($q = 1/2$). Solid lines and filled markers correspond to $M = 10^{11} M_\odot$, dashed lines and empty markers to $M = 10^{15} M_\odot$.

2. Influence of the background cosmological constant

Now consider a Swiss-cheese model with $f = f_{\rm min}$ and change its background cosmology. Figure 22 shows the evolution of the apparent cosmological parameters versus the background cosmological constant Ω_Λ. As it could have already been suspected from Fig. 19, the difference between apparent and background parameters decreases with Ω_Λ, and vanishes in a de Sitter universe. This can be understood as follows. The construction of a Swiss-cheese universe consists in changing the spatial distribution of the pressureless matter, while the cosmological constant remains purely homogeneous. Thus, the geometry of spacetime is less affected by the presence of inhomogeneities if $\Omega_\Lambda/\Omega_{\rm m}$ is greater. In the extreme case $(\Omega_{\rm m}, \Omega_\Lambda) = (0, 1)$, any Swiss cheese is identical to its background, since there is no matter to be reorganized.

We also plot in Fig. 23 the difference between the apparent deceleration parameter $\bar{q}$ and the background one $q = \Omega_{\rm m}/2 - \Omega_\Lambda$, as a function of q. Again, $\bar{q}$ does not significantly differ from q. This result must be compared with Fig. 11 of Ref. [53], where $(\bar{q} - q)/q \approx 100\%$.

3. Comparison with other recent studies

The impact of a modified luminosity-redshift relation—due to inhomogeneities—on the cosmological parameters has already been investigated by several authors. In Ref. [55], it has been suggested that a Swiss-cheese model

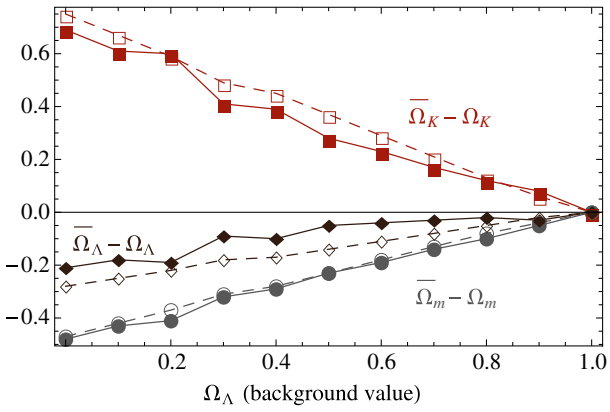

FIG. 22 (color online). Difference between apparent and background cosmological parameters $\bar{\Omega}_{\rm m} - \Omega_{\rm m}$ (gray disks), $\bar{\Omega}_K - \Omega_K$ (red squares) and $\bar{\Omega}_\Lambda - \Omega_\Lambda$ (black diamonds) versus background Ω_Λ, for Swiss-cheese models with $f = f_{\rm min}$. Solid lines and filled markers correspond to $M = 10^{11} M_\odot$, dashed lines and empty markers to $M = 10^{15} M_\odot$.

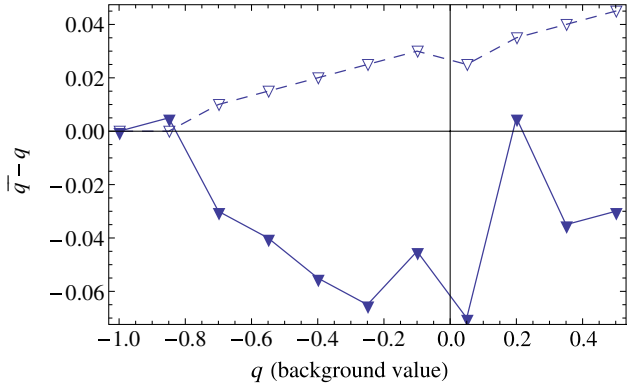

FIG. 23 (color online). Difference between apparent and background deceleration parameters $\bar{q} - q$ as a function of q, for Swiss-cheese models with $f = f_{\min}$. Solid lines and filled markers correspond to $M = 10^{11} M_\odot$, dashed lines and empty markers to $M = 10^{15} M_\odot$.

with LTB holes and EdS background displays an apparent cosmological constant $\bar{\Omega}_\Lambda = 0.4$; but as already mentioned in Sec. VI D, such a claim was proven to be inaccurate in Refs. [57,58,62], because it relies on observations along a peculiar line of sight. When many random directions of observation are taken into account, the mean magnification goes back to 1. Hence, contrary to our results, the apparent cosmological parameters of a Swiss-cheese model with LTB holes are identical to the background ones. This conclusion is in agreement with Ref. [78], where similar studies are performed in various cosmological toy models; and also with Ref. [31] in the framework of perturbation theory.

However, it is crucial to distinguish those approaches (LTB Swiss-cheese models and perturbation theory) from the one adopted in this article, because they do not address the same issue. The former share the purpose of evaluating the influence of inhomogeneities smoothed on large scales, while we focused on smaller scales for which matter cannot be considered smoothly distributed. Thus, our results must not be considered different, but rather complementary.

D. An alternative way to fit the Hubble diagram

Let us now address the converse problem, and determine the background cosmological parameters of the Swiss-cheese model that best reproduces the actual observations. For that purpose, the simplest method would be to fit our observed Hubble diagram using the theoretical luminosity-redshift relation $D_{\rm L}^{\rm SC}(z)$ of a Swiss-cheese universe. Hence, we need to derive such a relation in order to proceed.

1. Analytical estimation of the distance-redshift relation of a Swiss-cheese universe

As argued in Sec. V, any observationally relevant light beam which crosses a Kottler region has an impact parameter b much larger than the Schwarzschild radius $r_{\rm S}$ of the central object. Moreover, since the cosmological constant has no effect on light focusing, we conclude that inside a hole, the evolution of the cross-sectional area of a light beam behaves essentially as in Minkowski spacetime. This conclusion is supported by the perturbative calculation of the Wronski matrix $\mathcal{W}_{\rm K}$ performed in Sec. IV B 6.

If both the observer and the source are located on the surface of a hole, their angular distance is therefore $D_{\rm A}^{\rm hole} = \sqrt{\det \mathcal{D}} \approx \upsilon_{\rm out} - \upsilon_{\rm in}$, where υ denotes the affine parameter. More generally, for a beam which crosses N contiguous holes, we get

$$D_{\rm A}^{\rm holes} \approx \sum_{i=1}^{N} \Delta\upsilon_i, \tag{7.3}$$

where $\Delta\upsilon_i \equiv \upsilon_{{\rm out},i} - \upsilon_{{\rm in},i}$ is the variation of the affine parameter between entrance into and exit from the i th hole. Let us now evaluate $\Delta\upsilon_i$. The time part of the geodesic equation in Kottler geometry yields

$$k^t \equiv \frac{{\rm d}t}{{\rm d}\upsilon} = \frac{E}{A(r)} \overset{r \gg r_{\rm S}}{\approx} E = \text{constant}, \tag{7.4}$$

where E is the usual constant of motion. We conclude that $\Delta\upsilon_i \approx k^t_{{\rm out},i} \Delta t_i$. Besides, the relations (2.16) and (4.11) between FL and Kottler coordinates on the junction hypersurface, together with $A(r_{\rm h}) \approx 1$, lead to $\Delta t_i \approx \Delta T_i$ and $k^t_{\rm out} \approx a_{\rm out}/a_0$. Finally,

$$D_{\rm A}^{\rm holes} \approx \sum_{i=1}^{N} \frac{a_{{\rm out},i}}{a_0} \Delta T_i \approx \int_T^{T_{\rm obs}} \frac{a(T')}{a_0}\, {\rm d}T', \tag{7.5}$$

where we approximated the sum over i by an integral. This operation is valid as far as ΔT_i remains small compared to the Hubble time. In terms of redshifts, we have

$$D_{\rm A}^{\rm holes}(z) = \int_0^z \frac{{\rm d}z'}{(1+z')^2 H(z')}. \tag{7.6}$$

By construction, this formula describes the behavior of the angular distance when light only travels through Kottler regions. In order to take the FL regions into account, we write the distance-redshift relation $D_{\rm A}^{\rm SC}(z)$ of the Swiss cheese as the following (heuristic) linear combination

$$D_{\rm A}^{\rm SC}(z) = (1-f) D_{\rm A}^{\rm holes}(z) + f D_{\rm A}^{\rm FL}(z), \tag{7.7}$$

where f still denotes the smoothness parameter defined in Sec. VI A 1, and $D_{\rm A}^{\rm FL}(z)$ is the distance-redshift relation in a FL universe, given by Eq. (4.10).

A comparison between the above analytical estimation and the numerical results is plotted in Fig. 24. The agreement is qualitatively good, especially as it is obtained without any fitting procedure. Moreover, it is straightforward to show that $D_{\rm A}^{\rm SC}(z)$ and $D_{\rm A}^{\rm FL}(z)$ are identical up to second order in z. This is in agreement with—and somehow explains—the numerical results of Secs. VII C 1 and

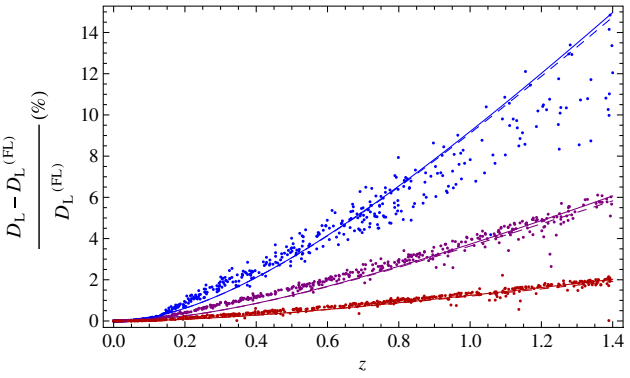

FIG. 24 (color online). Comparison between the approximate luminosity-redshift relation $D_L^{SC}(z) = (1+z)^2 D_A^{SC}(z)$ in a Swiss-cheese universe (solid lines), simulated observations (dots), and the Dyer-Roeder model $D_L^{DR}(z)$ with $\alpha(z) = f$ (dashed lines). Three different values of the smoothness parameter are tested, from top to bottom: $f = f_{min} \approx 0.26$, $f = 0.7$, $f = 0.9$.

VII C 2, where we showed that the apparent deceleration parameter $\bar{q}$ is the same as the background one q.

Note finally that the general tendency of our analytical relation is to overestimate δD_L at high redshifts. The main reason is that its derivation uses the behavior of $\mathcal{W}_K$ at zeroth order in r_S/b; that is, it neglects the effect of the central mass in the Kottler region. The first-order term in $\mathcal{W}_K$—taken into account in the numerical results—tends to lower the associated luminosity distance.

2. Comparison with the Dyer-Roeder approach

Another widely used approximation to model the propagation of light in underdense regions was proposed by Dyer and Roeder [10] in 1972. It assumes that (1) the Sachs equation and the relation $\upsilon(z)$ are the same as in a FL spacetime—in particular, the null shear vanishes—and (2) the optical parameter Φ_{00} (see Sec. III B 2) is replaced by $\alpha(z)\Phi_{00}$, where $\alpha(z)$ represents the fraction of matter intercepted by the geodesic bundle. In brief, the DR model encodes that light propagates mostly in underdense regions by reducing the Ricci focusing, while still neglecting the Weyl focusing. Under such conditions, the DR expression of the angular distance $D_A^{DR}(z)$ is determined by

$$\frac{d^2 D_A^{DR}}{dz^2} + \left(\frac{d\ln H}{dz} + \frac{2}{1+z}\right)\frac{dD_A^{DR}}{dz} = -\frac{3\Omega_m}{2}\left(\frac{H_0}{H}\right)^2 (1+z)\alpha(z) D_A^{DR}(z). \quad (7.8)$$

This attempt to model the average effect of inhomogeneities, while assuming that the Universe is isotropic and homogeneous, has been widely questioned [79–82] and recently argued to be mathematically inconsistent [8].

Interestingly, our estimation $D_A^{SC}(z)$ of the distance-redshift relation in a Swiss-cheese universe reads

$$\frac{d^2 D_A^{SC}}{dz^2} + \left(\frac{d\ln H}{dz} + \frac{2}{1+z}\right)\frac{dD_A^{SC}}{dz} = -\frac{3\Omega_m}{2}\left(\frac{H_0}{H}\right)^2 (1+z) f D_A^{FL}(z), \quad (7.9)$$

which is similar to Eq. (7.8) with $\alpha(z) = f$, except that the right-hand side is proportional to D_A^{FL} instead of D_A^{SC}. Nevertheless, it turns out that such a difference has only a very weak impact, in the sense that

$$D_A^{SC}(z) \approx D_A^{DR}(z), \text{ i.e. } D_L^{SC}(z) \approx D_L^{DR}(z), \quad (7.10)$$

if $\alpha(z) = f$. This appears clearly in Fig. 24, where the dashed and solid lines are almost superimposed. In fact, it is not really surprising, since both approaches rely on the same assumptions: no backreaction, no Weyl focusing and an effective reduction of the Ricci focusing.

Note however that this approach models the effect of the inhomogeneities on the mean value of the luminosity distance but does not address the dispersion of the data.

3. Fitting real data with $D_L^{SC}(z)$

The modified luminosity-redshift relation $D_L^{SC}(z)$ derived in the previous paragraph can be used to fit the observed Hubble diagram. We apply the same χ^2 method as described in Sec. VII B, except that now (1) the triplets $(z_i, \mu_i, \Delta\mu_i)$ are observations of the SNLS 3 catalog [77], and (2) $\mu_{FL}(z|\bar{\Omega}_m, \bar{\Omega}_\Lambda)$ is replaced by $\mu_{SC}(z|\Omega_m, f)$, where the background curvature Ω_K is fixed to 0 (so that $\Omega_\Lambda = 1 - \Omega_m$). Hence, we are looking for the smoothness parameter f, and the background cosmological parameters, of the spatially Euclidean Swiss-cheese model which best fits the actual SN observations.

The results of the χ^2 fit are displayed in Fig. 25. First of all, we note that the confidence areas are very stretched

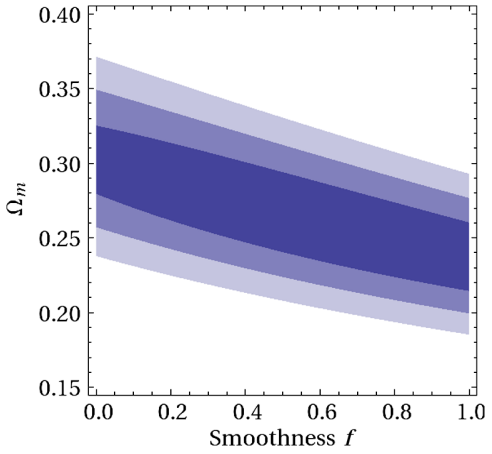

FIG. 25 (color online). Fit of the Hubble diagram constructed from the SNLS 3 data set [77], by using the luminosity-redshift relation $D_L^{SC}(z|\Omega_m, f)$ of a spatially Euclidean Swiss-cheese model. The colored areas indicate (from the darkest to the lightest) the 1σ, 2σ and 3σ confidence levels.

horizontally, so that the smoothness parameter f cannot be reasonably constrained by the Hubble diagram. There are two reasons for this. On the one hand, we know from Sec. VII C 2 that f has only a weak influence on the luminosity-redshift relation in a universe dominated by the cosmological constant, which is the case here ($\Omega_\Lambda \sim 0.7$–0.8). On the other hand, since $D_L^{SC}(z)$ and $D_L^{FL}(z)$ only differ by terms of order z^3 and higher, one would need more high-redshift observations to discriminate them. However, all the current SNe catalogs—including the SNLS 3 data set—contain mostly low-redshift SNe.

Besides, Fig. 25 shows that fixing a given value of f changes the best-fit value of Ω_m. In the extreme case of a Swiss cheese only made of clumps ($f = 0$) we get $\Omega_m = 0.3$, while in the FL case ($f = 1$) the best value is $\Omega_m = 0.24$, in agreement with Ref. [77]. Such a discrepancy, of order 20%, is significant in the era of precision cosmology, where one aims at determining the cosmological parameters at the percent level.

Let us finally emphasize that such a fit is only indicative, because it relies on an approximation of the luminosity-redshift relation in a Swiss-cheese universe.

VIII. CONCLUSION

In this article, we have investigated the effect of the distribution of matter on the Hubble diagram, and on the resulting inference of the cosmological parameters. For that purpose, we have studied light propagation in Swiss-cheese models. This class of exact solutions of the Einstein field equations is indeed very suitable, because it can describe a strongly inhomogeneous distribution of matter which does not backreact on the global cosmic expansion. The latter is entirely governed by the background cosmological parameters Ω_m, Ω_Λ characterizing the FL regions of the model. The inhomogeneities are clumps of mass M, while the fraction of remaining fluid matter is f—called smoothness parameter. The Swiss-cheese models are therefore defined by two ''dynamical'' parameters (Ω_m, Ω_Λ), and two ''structural'' parameters (f, M).

The laws of light propagation in a Swiss-cheese universe have been determined by solving the geodesic equation and the Sachs equation. For the latter, we have introduced a new technique—based on the Wronski matrix—in order to deal more easily with a patchwork of spacetimes. Our results, mostly analytical, have been included in a Mathematica program, and used to compute the impact of the Swiss-cheese holes on the redshift and on the luminosity distance. For a light beam which crosses many holes, we have shown that the effect on the redshift remains negligible, while the luminosity distance increases significantly with respect to the one observed in a FL universe ($\delta D_L \sim 10\%$ for sources at $z \sim 1$), inducing a bias in the Hubble diagram.

The consequences of the bias on the inference of the cosmological parameters have been investigated by simulating Hubble diagrams for various Swiss-cheese models, and by fitting them with the usual FL luminosity-redshift relation. In general, the resulting ''apparent'' cosmological parameters are very different from the ''background'' ones which govern the cosmic expansion, but in a way that leaves the deceleration parameter unchanged. Moreover, the discrepancy between apparent and background cosmological parameters turns out to decrease with Λ, and is therefore small for a universe dominated by the cosmological constant. Finally, we have derived an approximate luminosity-redshift relation for Swiss-cheese models, which is similar to the one obtained following the Dyer-Roeder approach. Using this relation to fit the Hubble diagram constructed from the SNLS 3 data set, we have found that the smoothness parameter cannot be constrained by such observations. However, turning arbitrarily $f = 1$ into $f = 0$ has an impact of order 20% on the best-fit value of Ω_m, which is significant in the era of precision cosmology (see Ref. [83] for further discussion).

Of course, our model is oversimplifying for various reasons. First, it does not take into account either the complex distribution of the large scale structures, or the presence of diffuse matter on small scales—such as gas and possibly dark matter. Second, it does not take strong lensing effects into account, assuming that clumps are ''opaque.'' We can conjecture that this overestimates the actual effect of the inhomogeneities. Nevertheless, it shows that their imprint on the Hubble diagram cannot be neglected, and should be modeled beyond the perturbation regime. Note finally that several extensions are allowed by our formalism. For instance, we could introduce different kinds of inhomogeneities, in order to construct fractal structures for which the smoothness parameter is arbitrarily close to zero. Additionally to the Hubble diagrams, we could also generate the shear maps of Swiss-cheese models, and determine whether their combination allows for better constraints on the various parameters.

This work explicitly raises the question of the meaning of the cosmological parameters, and of whether the values we measure under the hypothesis of a pure FL background represent their ''true'' or some ''dressed'' values. Similar ideas have actually been held in other contexts [84,85], and in particular regarding the spatial curvature [86,87]. We claim that the simplest Swiss-cheese models are good models to address such questions—as well as the Ricci-Weyl problem and the fluid approximation—with their own use, between the perturbation theory and N-body simulations.

ACKNOWLEDGMENTS

We thank Francis Bernardeau, Thomas Buchert, Nathalie Palanque-Delabrouille, Peter Dunsby, George Ellis, Yannick Mellier, Shinji Mukohyama, Cyril Pitrou, Carlo Schimd, and Markus Werner for discussions. We also thank Julian Adamek, Krzysztof Bolejko, Alan Coley,

Pedro Ferreira, Giovanni Marozzi and Zdenek Stuchlík for comments. P. F. thanks the École Normale Supérieure de Lyon for funding during his master and first year of Ph.D. H. D. thanks the Institut Lagrange de Paris for funding during her master's and the Institut d'Astrophysique de Paris for hospitality during the later phase of this work. This work was supported by French state funds managed by the ANR within the Investissements d'Avenir programme under reference ANR-11-IDEX-0004-02 and the Programme National Cosmologie et Galaxies.

[1] P. Peter and J.-P. Uzan, *Primordial Cosmology* (Oxford University, New York, 2009).
[2] G. F. R. Ellis and T. Buchert, Phys. Lett. A **347**, 38 (2005).
[3] G. F. R. Ellis and W. Stoeger, Classical Quantum Gravity **4**, 1697 (1987).
[4] T. Buchert, Gen. Relativ. Gravit. **32**, 105 (2000); **33**, 1381 (2001); S. Räsänen, J. Cosmol. Astropart. Phys. 02 (2004) 003; E. Barausse, S. Matarrese, and A. Riotto, Phys. Rev. D **71**, 063537 (2005); E. W. Kolb, S. Matarrese, and A. Riotto, New J. Phys. **8**, 322 (2006); S. Rasanen, J. Cosmol. Astropart. Phys. 11 (2006) 003; M. Kasai, Prog. Theor. Phys. **117**, 1067 (2007).
[5] A. Ishibashi and R. M. Wald, Classical Quantum Gravity **23**, 235 (2006); E. E. Flanagan, Phys. Rev. D **71**, 103521 (2005); C. M. Hirata and U. Seljak, Phys. Rev. D **72**, 083501 (2005); S. R. Green and R. M. Wald, Phys. Rev. D **83**, 084020 (2011).
[6] E. W. Kolb, S. Matarrese, A. Notari, and A. Riotto, Phys. Rev. D **71**, 023524 (2005); N. Li and D. J. Schwarz, Phys. Rev. D **76**, 083011 (2007); **78**, 083531 (2008); C. Clarkson, K. Ananda, and J. Larena, Phys. Rev. D **80**, 083525 (2009); O. Umeh, J. Larena, and C. Clarkson, J. Cosmol. Astropart. Phys. 03 (2011) 029; G. Marozzi and J.-P. Uzan, Phys. Rev. D **86**, 063528 (2012).
[7] C. Clarkson, G. Ellis, J. Larena, and O. Umeh, Rep. Prog. Phys. **74**, 112901 (2011).
[8] C. Clarkson, G. F. R. Ellis, A. Faltenbacher, R. Maartens, O. Umeh, and J.-P. Uzan, Mon. Not. R. Astron. Soc. **426**, 1121 (2012).
[9] Ya. B. Zel'dovich, Astron. Zh. **41**, 19 (1964) [Sov. Astron. **8**, 13 (1964)].
[10] C. C. Dyer and R. C. Roeder, Astrophys. J. **174**, L115 (1972); **180**, L31 (1973).
[11] V. M. Dashevskii and V. I. Slysh, Astron. Zh. **42**, 863 (1965) [Sov. Astron. **9**, 671 (1966)].
[12] B. Bertotti, Proc. R. Soc. A **294**, 195 (1966).
[13] J. E. Gunn, Astrophys. J. **147**, 61 (1967); **150**, 737 (1967).
[14] S. Refsdal, Astrophys. J. **159**, 357 (1970).
[15] S. Weinberg, Astrophys. J. **208**, L1 (1976).
[16] C. C. Dyer and R. C. Roeder, Gen. Relativ. Gravit. **13**, 1157 (1981).
[17] L. Fang and X. Wu, Chin. Phys. Lett. **6**, 233 (1989); X. Wu, Astron. Astrophys. **239**, 29 (1990).
[18] H. G. Rose, Astrophys. J. **560**, L15 (2001).
[19] T. W. B. Kibble and R. Lieu, Astrophys. J. **632**, 718 (2005).
[20] V. Kostov, J. Cosmol. Astropart. Phys. 04 (2010) 001.
[21] E. V. Linder, Astron. Astrophys. **206**, 190 (1988).
[22] K. Tomita, Prog. Theor. Phys. **100**, 79 (1998).
[23] E. Mortsell, arXiv:astro-ph/0109197.
[24] K. Bolejko, Mon. Not. R. Astron. Soc. **412**, 1937 (2011).
[25] R. Takahashi, M. Oguri, M. Sato, and T. Hamana, arXiv:1106.3823.
[26] U. Seljak and D. E. Holz, Astron. Astrophys. **351**, L10 (1999).
[27] R. B. Metcalf and J. Silk, Astrophys. J. **519**, L1 (1999).
[28] R. B. Metcalf and J. Silk, Phys. Rev. Lett. **98**, 071302 (2007).
[29] R. Kantowski, T. Vaughan, and D. Branch, Astrophys. J. **447**, 35 (1995); J. A. Frieman, Commun. Astrophys. **18**, 323 (1996); Y. Wang, Astrophys. J. **531**, 676 (2000); **536**, 531 (2000); J. Cosmol. Astropart. Phys. 03 (2005) 005.
[30] C. Bonvin, R. Durrer, and M. A. Gasparini, Phys. Rev. D **73**, 023523 (2006).
[31] P. Valageas, Astron. Astrophys. **354**, 767 (2000).
[32] N. Meures and M. Bruni, Mon. Not. R. Astron. Soc. **419**, 1937 (2012).
[33] I. Ben-Dayan, M. Gasperini, G. Marozzi, F. Nugier, and G. Veneziano, Phys. Rev. Lett. **110**, 021301 (2013).
[34] E. Di Dio and R. Durrer, Phys. Rev. D **86**, 023510 (2012).
[35] I. Ben-Dayan, M. Gasperini, G. Marozzi, F. Nugier, and G. Veneziano, arXiv:1302.0740.
[36] D. E. Holz and E. V. Linder, Astrophys. J. **631**, 678 (2005).
[37] A. Cooray, D. Holz, and D. Huterer, Astrophys. J. **637**, L77 (2006); S. Dodelson and A. Vallinotto, Phys. Rev. D **74**, 063515 (2006).
[38] A. Cooray, D. Huterer, and D. Holz, Phys. Rev. Lett. **96**, 021301 (2006).
[39] D. Sarkar, A. Amblard, D. E. Holz, and A. Cooray, arXiv:0710.4143.
[40] A. R. Cooray, D. E. Holz, and R. Caldwell, J. Cosmol. Astropart. Phys. 11 (2010) 015.
[41] A. Vallinotto, S. Dodelson, and P. Zhang, arXiv:1009.5590.
[42] B. Ménard, T. Hamana, M. Bartelmann, and N. Yoshida, Astron. Astrophys. **403**, 817 (2003).
[43] N. Dalal, D. E. Holz, X. Chen, and J. A. Frieman, Astrophys. J. **585**, L11 (2003).
[44] K. P. Rauch, Astrophys. J. **374**, 83 (1991).
[45] D. E. Holz and R. M. Wald, Phys. Rev. D **58**, 063501 (1998).
[46] R. W. Lindquist and J. A. Wheeler, Rev. Mod. Phys. **29**, 432 (1957).
[47] E. Gausmann, R. Lehoucq, J.-P. Luminet, J.-P. Uzan, and J. Weeks, Classical Quantum Gravity **18**, 5155 (2001); R. Lehoucq, J. Weeks, J.-P. Uzan, E. Gausmann, and J.-P. Luminet, Classical Quantum Gravity **19**, 4683 (2002);

J. Weeks, R. Lehoucq, and J.-P. Uzan, Classical Quantum Gravity **20**, 1529 (2003); J.-P. Uzan, A. Riazuelo, R. Lehoucq, and J. Weeks, Phys. Rev. D **69**, 043003 (2004).
[48] T. Clifton and P. G. Ferreira, Phys. Rev. D **80**, 103503 (2009); J. Cosmol. Astropart. Phys. 10 (2009) 026.
[49] J.-P. Bruneton and J. Larena, Classical Quantum Gravity **29**, 155001 (2012); **30**, 025002 (2013).
[50] K. Kainulainen and V. Marra, Phys. Rev. D **80**, 127301 (2009); **83**, 023009 (2011).
[51] A. Einstein and E. G. Straus, Rev. Mod. Phys. **17**, 120 (1945); **18**, 148 (1946).
[52] R. Kantowski, Astrophys. J. **155**, 89 (1969).
[53] C. C. Dyer and R. C. Roeder, Astrophys. J. **189**, 167 (1974).
[54] N. Brouzakis, N. Tetradis, and E. Tzavara, J. Cosmol. Astropart. Phys. 02 (2007) 013.
[55] V. Marra, E. W. Kolb, S. Matarrese, and A. Riotto, Phys. Rev. D **76**, 123004 (2007).
[56] T. Biswas and A. Notari, J. Cosmol. Astropart. Phys. 06 (2008) 021.
[57] R. A. Vanderveld, E. E. Flanagan, and I. Wasserman, Phys. Rev. D **78**, 083511 (2008).
[58] N. Brouzakis, N. Tetradis, and E. Tzavara, J. Cosmol. Astropart. Phys. 04 (2008) 008.
[59] T. Clifton and J. Zuntz, Mon. Not. R. Astron. Soc. **400**, 2185 (2009).
[60] W. Valkenburg, J. Cosmol. Astropart. Phys. 06 (2009) 010.
[61] S. J. Szybka, Phys. Rev. D **84**, 044011 (2011).
[62] E. E. Flanagan, N. Kumar, I. Wasserman, and R. A. Vanderveld, Phys. Rev. D **85**, 023510 (2012).
[63] F. Kottler, Ann. Phys. (Berlin) **361**, 401 (1918).
[64] H. Weyl, Phys. Z. **20**, 31 (1919).
[65] V. Perlick, Living Rev. Relativity **7**, 9 (2004).
[66] W. Israel, Nuovo Cimento B **44**, 1 (1966).
[67] W. Israel, Nuovo Cimento B **48**, 463 (1967).
[68] R. Sachs, Proc. R. Soc. A **264**, 309 (1961).
[69] P. Schneider, J. Ehlers, and E. E. Falco, *Gravitational Lenses* (Springer, New York, 1992).
[70] Z. Stuchlík, Bull. Astron. Inst. Czech. **34**, 129 (1983).
[71] Z. Stuchlík, Bull. Astron. Inst. Czech. **35**, 205 (1984).
[72] I. S. Gradshteyn and I. M. Ryzhik, *Table of Integrals, Series, and Products* (Academic, New York, 2007).
[73] F. Combes, P. Boissé, A. Mazure, and A. Blanchard, *Galaxies et cosmologie* (CNRS, Paris, 2003).
[74] N. Suzuki *et al.* (The Supernova Cosmology Project), Astrophys. J. **746**, 85 (2012).
[75] S. Perlmutter *et al.*, Astrophys. J. **517**, 565 (1999); A. G. Riess *et al.*, Astron. J. **116**, 1009 (1998); J. L. Tonry *et al.*, Astrophys. J. **594**, 1 (2003); R. A. Knop *et al.*, Astrophys. J. **598**, 102 (2003); A. G. Riess *et al.*, Astrophys. J. **607**, 665 (2004).
[76] K. Bolejko, C. Clarkson, R. Maartens, D. Bacon, N. Meures, and E. Beynon, Phys. Rev. Lett. **110**, 021302 (2013).
[77] A. Conley *et al.*, Astrophys. J., Suppl. Ser. **192**, 1 (2011).
[78] K. Bolejko and P. Ferreira, J. Cosmol. Astropart. Phys. 05 (2012) 003.
[79] J. Ehlers and P. Schneider, Astron. Astrophys. **168**, 57 (1986).
[80] M. Sasaki, Prog. Theor. Phys. **90**, 753 (1993).
[81] K. Tomita, H. Asada, and T. Hamana, Prog. Theor. Phys. Suppl. **133**, 155 (1999).
[82] S. Rasanen, J. Cosmol. Astropart. Phys. 02 (2009) 011.
[83] P. Fleury, H. Dupuy, and J.-P. Uzan, arXiv:1304.7791.
[84] T. Buchert and M. Carfora, Phys. Rev. Lett. **90**, 031101 (2003).
[85] D. L. Wiltshire, New J. Phys. **9**, 377 (2007); Int. J. Mod. Phys. D **17**, 641 (2008); P. R. Smale and D. L. Wiltshire, Mon. Not. R. Astron. Soc. **413**, 367 (2011).
[86] C. Clarkson, T. Clifton, A. Coley, and R. Sung, arXiv:1111.2214.
[87] A. A. Coley, N. Pelavas, and R. M. Zalaletdinov, Phys. Rev. Lett. **95**, 151102 (2005).

1.6 Article "Can all observations be accurately interpreted with a unique geometry?"

Can All Cosmological Observations Be Accurately Interpreted with a Unique Geometry?

Pierre Fleury,[1,2,*] Hélène Dupuy,[1,2,3,†] and Jean-Philippe Uzan[1,2,‡]

[1]*Institut d'Astrophysique de Paris, UMR-7095 du CNRS, Université Pierre et Marie Curie, 98 bis boulevard Arago, 75014 Paris, France*

[2]*Sorbonne Universités, Institut Lagrange de Paris, 98 bis boulevard Arago, 75014 Paris, France*

[3]*Institut de Physique Théorique, CEA, IPhT, URA 2306 CNRS, F-91191 Gif-sur-Yvette, France*

(Received 3 June 2013; published 29 August 2013)

The recent analysis of the Planck results reveals a tension between the best fits for (Ω_{m0}, H_0) derived from the cosmic microwave background or baryonic acoustic oscillations on the one hand, and the Hubble diagram on the other hand. These observations probe the Universe on very different scales since they involve light beams of very different angular sizes; hence, the tension between them may indicate that they should not be interpreted the same way. More precisely, this Letter questions the accuracy of using only the (perturbed) Friedmann-Lemaître geometry to interpret all the cosmological observations, regardless of their angular or spatial resolution. We show that using an inhomogeneous "Swiss-cheese" model to interpret the Hubble diagram allows us to reconcile the inferred value of Ω_{m0} with the Planck results. Such an approach does not require us to invoke new physics nor to violate the Copernican principle.

DOI: 10.1103/PhysRevLett.111.091302 PACS numbers: 98.80.Es, 98.62.Py, 98.70.Vc, 98.80.Jk

The standard interpretation of cosmological data relies on the description of the Universe by a spatially homogeneous and isotropic spacetime with a Friedmann-Lemaître (FL) geometry, allowing for perturbations [1]. The emergence of a dark sector, including dark matter and dark energy, emphasizes the need for extra degrees of freedom, either physical (new fundamental fields or interactions) or geometrical (e.g., a cosmological solution with lower symmetry). This has driven a lot of activity to test the hypotheses [2] of the cosmological model, such as general relativity or the Copernican principle.

The recent Planck data were analyzed in such a framework [3] in which the cosmic microwave background (CMB) anisotropies are treated as perturbations around a FL universe, with most of the analysis performed at linear order. Nonlinear effects remain small [4] and below the constraints on non-Gaussianity derived by Planck [5]. The results nicely confirm the standard cosmological model of a spatially Euclidean FL universe with a cosmological constant, dark matter, and initial perturbations compatible with the predictions of inflation.

Among the constraints derived from the CMB, the Hubble parameter H_0 and the matter density parameter Ω_{m0} are mostly constrained through the combination $\Omega_{m0}h^3$, where $H_0 = h \times 100$ km/s/Mpc. It is set by the acoustic scale $\theta_* = r_s/D_A$, defined as the ratio between the sound horizon and the angular distance at the time of last scattering. The measurement of seven acoustic peaks enables one to determine θ_* with a precision better than 0.1%. The constraints on the plane (Ω_{m0}, H_0) are presented in Fig. 3 of Ref. [3] and clearly show this degeneracy. The marginalized constraints on the two parameters were then derived [3] to be

$$H_0 = (67.3 \pm 1.2)\ \text{km/s/Mpc},$$
$$\Omega_{m0} = 0.315 \pm 0.017 \quad (1)$$

at a 68% confidence level. It was pointed out (see Secs. 5.2–5.4 of Ref. [3]) that the values of H_0 and Ω_{m0} are, respectively, low and high compared with their values inferred from the Hubble diagram. Such a trend was already indicated by WMAP-9 [6] which concluded $H_0 = (70 \pm 2.2)$ km/s/Mpc.

Regarding the Hubble constant, two astrophysical measurements are in remarkable agreement. First, the estimation based on the distance ladder calibrated by three different techniques (masers, Milky Way cepheids, and Large Magellanic Cloud cepheids) gives [7] $H_0 = (74.3 \pm 1.5 \pm 2.1)$ km/s/Mpc, respectively, with statistical and systematic errors. This improves the earlier constraint obtained by the Hubble Space Telescope (HST) Key program [8], $H_0 = (72 \pm 8)$ km/s/Mpc. Second, the Hubble diagram of type Ia supernovae (SNe Ia) calibrated with the HST observations of cepheids leads [9] to $H_0 = (73.8 \pm 2.4)$ km/s/Mpc. Other determinations of the Hubble constant, e.g., from very-long-baseline interferometry observations [10] or from the combination of Sunyaev-Zel'dovich effect and X-ray observations [11], have larger error bars and are compatible with both the CMB and distance measurements.

Additionally, the analysis of the Hubble diagram of SNe Ia leads to a lower value of Ω_{m0}—e.g., 0.222 ± 0.034 with the SNLS 3 data set [12]—compared to the constraint (1) by Planck. As concluded in Ref. [3], there is no direct inconsistency, and it was pointed out that there could be residual systematics not properly accounted for in the SN data. Still, it was stated that "the tension between

CMB-based estimates and the astrophysical measurements of H_0 is intriguing and merits further discussion."

Interestingly, the CMB constraints on (Ω_{m0}, H_0) are in excellent agreement with baryon acoustic oscillation (BAO) measurements [13], which allow one to determine the angular distance up to redshifts of order 0.7. The common point between the CMB and BAO measurements is that they involve light beams much larger than those involved in astronomical observations. Indeed, a pixel of Planck's high-resolution CMB maps corresponds to 5 arc min [14], while the typical angular size of a SN is 10^{-7} arc sec. This means that the two kinds of observations probe the Universe at very different scales. Moreover, for both the CMB and BAO measurements the crucial information is encoded in correlations, while SN observations rely on "1-point measurements" (we are interested in the luminosity and redshift of each SN, not in the correlations between several SNe). Because of such distinctions one can expect the two classes of cosmological observations to be affected differently by the inhomogeneity of the Universe, through gravitational lensing.

The effect of lensing on CMB measurements is essentially due to the large-scale structure, and it can be taken into account in the framework of cosmological perturbation theory at linear order [15] (see, however, Ref. [16] for a discussion about the impact of strong inhomogeneities). We refer to Ref. [17] for a description of the lensing effects on BAO measurements. Regarding the Hubble diagram, the influence of lensing has also been widely investigated [18]. The propagation of light in an inhomogeneous universe gives rise to both distortion and magnification. Most images are expected to be demagnified because their lines of sight probe underdense regions, while some are amplified due to strong lensing. It shall thus induce a dispersion of the luminosities of the sources, that is, an extra scatter in the Hubble diagram [19]. Its amplitude can be determined from the perturbation theory [20] and subtracted [21]. However, a considerable fraction of the lensing effects arises from sub-arc-min scales, which are not probed by shear maps smoothed on arc min scales [22].

The tension on (Ω_{m0}, H_0) may indicate that, given the accuracy of the observations achieved today, the use of a (perturbed) FL geometry to interpret the astrophysical data is no longer adapted. More precisely, the question that we want to raise is whether the use of a unique spacetime geometry is relevant for interpreting all the cosmological observations, regardless of their angular or spatial resolution and of their location (redshift). Indeed, each observation is expected to probe the Universe smoothed on a typical scale related to its resolution, and this can lead to fundamentally different geometrical situations. In a universe with a discrete distribution of matter, the Riemann curvature experienced by a beam of test particles or photons is dominated by the Weyl tensor. Conversely, in a (statistically spatially isotropic) universe smoothed on large scales, it is dominated by the Ricci tensor. Both situations correspond to distinct optical properties [23].

In the framework of geometric optics, a light beam is described by a bundle of null geodesics. All the information about the size and the shape of a beam can be encoded in a 2×2 matrix $\mathcal{D}^a{}_b$ called the Jacobi map (see Ref. [24] for further details). In particular, the angular and luminosity distances read, respectively,

$$D_A = \sqrt{|\det \mathcal{D}^a{}_b|}, \qquad D_L = (1+z)^2 D_A, \tag{2}$$

where z denotes the redshift. The evolution of the Jacobi map with light propagation is governed by the Sachs equation [25,26]

$$\frac{d^2}{dv^2}\mathcal{D}^a{}_b = \mathcal{R}^a{}_c \mathcal{D}^c{}_b, \tag{3}$$

where v is an affine parameter along the geodesic bundle. The term $\mathcal{R}_{ab}$, which controls the evolution of $\mathcal{D}^a{}_b$, is a projection of the Riemann tensor called the optical tidal matrix. It is defined by $\mathcal{R}_{ab} \equiv R_{\mu\nu\alpha\beta} k^\nu k^\alpha s_a^\mu s_b^\beta$, where k^μ is the wave vector of an arbitrary ray, and the Sachs basis $\{s_a^\mu\}_{a=1,2}$ spans a screen on which the observer projects the light beam. Because the Riemann tensor can be split into a Ricci part $R_{\mu\nu}$ and a Weyl part $C_{\mu\nu\alpha\beta}$, the optical tidal matrix can also be decomposed as

$$(\mathcal{R}_{ab}) = \underbrace{\begin{pmatrix} \Phi_{00} & 0 \\ 0 & \Phi_{00} \end{pmatrix}}_{\text{Ricci lensing}} + \underbrace{\begin{pmatrix} -\mathrm{Re}\,\Psi_0 & \mathrm{Im}\,\Psi_0 \\ \mathrm{Im}\,\Psi_0 & \mathrm{Re}\,\Psi_0 \end{pmatrix}}_{\text{Weyl lensing}}, \tag{4}$$

with $\Phi_{00} \equiv -(1/2) R_{\mu\nu} k^\mu k^\nu$ and $\Psi_0 \equiv -(1/2) C_{\mu\nu\alpha\beta} (s_1^\mu - i s_2^\mu) k^\nu (s_1^\beta - i s_2^\beta) k^\alpha$. It clearly appears in Eq. (4) that the Ricci term tends to isotropically focus the light beam, while the Weyl term tends to shear and rotate it. The behavior of a light beam is thus different whether it experiences Ricci-dominated lensing (large beams, e.g., CMB measurements) or Weyl-dominated lensing (narrow beams, e.g., SN observations).

This Ricci-Weyl problem can be addressed with different methods. One possibility, a representative of which is the Dyer-Roeder approximation [27], is to construct a general distance-redshift relation which would take into account the effect of inhomogeneities in some average way. However, such approaches are in general difficult to control [18] because they rely on approximations whose domain of applicability is unknown. An alternative possibility consists in constructing inhomogeneous cosmological models, with a discrete distribution of matter, and studying the impact on light propagation. Several models exist in the literature: the Schwarzschild-cell method [28] or the lattice universe [29], which are both approximate solutions of the Einstein equations, and the Swiss-cheese models [30], which are constructed by matching together patches of exact solutions of the Einstein equations.

This last approach is the one that we shall follow in this Letter.

Consider a Swiss-cheese model in which clumps of matter (modeling, e.g., galaxies), each of them lying at the center of a spherical void, are embedded in a FL spacetime. The interior region of a void is described by the Kottler geometry—i.e., Schwarzschild with a cosmological constant—while the exterior geometry is the FL one. By construction, such inhomogeneities do not modify the expansion dynamics of the embedding FL universe, thus avoiding any discussion regarding backreaction. The resulting spacetime is well defined, because the Darmois-Israel junction conditions are satisfied on the boundary of every void. Compared to a strictly homogeneous universe, a Swiss-cheese model is therefore characterized by two additional parameters: the size of the voids (or equivalently the mass of their central bodies) and the volumic fraction of the remaining FL regions, which encodes the smoothness of the distribution of matter. It is naturally quantified by the smoothness parameter

$$f \equiv \lim_{V\to\infty} \frac{V_{\mathrm{FL}}}{V}, \tag{5}$$

where V_{FL} is the volume occupied by the FL region within a volume V of the Swiss cheese. With the definition (5), $f = 1$ corresponds to a model with no hole (i.e., a FL universe), while $f = 0$ corresponds to the case where matter is exclusively under the form of clumps inside voids.

Of course such a model cannot be considered realistic, but neither does the exact FL geometry, used to interpret the Hubble diagram. Both spacetimes describe a spatially statistically homogeneous and isotropic universe, and the former permits additionally the investigation of the effect of a discrete distribution of matter. Since the FL universe is a particular Swiss-cheese model, this family of spacetimes therefore allows us to estimate how good the hypothesis of strict spatial homogeneity—with a continuous matter distribution at *all* scales—is.

The propagation of light in a Swiss-cheese model has been comprehensively investigated in Ref. [24], generalizing earlier works [31], with the key assumption that light never crosses the clumps. This "opacity assumption" can be observationally justified in the case of SN observations if the clumps represent galaxies (see Ref. [24] for a discussion). Compared to the strictly homogeneous case, any light signal traveling through a Swiss-cheese model then experiences a reduced Ricci focusing. This leads [see Eqs. (2)–(4)] to an increase of the observed luminosity distance D_L. The effect of Weyl lensing—i.e., here shear—is relatively small.

This systematic effect, due to inhomogeneities, tends to bias the Hubble diagram in a way that mimics the contribution of a negative spatial curvature or a positive cosmological constant. In other words, if one interprets the Hubble diagram of a Swiss-cheese universe by wrongly assuming that it is strictly homogeneous, then one underestimates the value of Ω_{m0}. The error reaches a few percent, which is comparable to other estimates in similar contexts [32]. Note, however, that in the case of Swiss-cheese models with Lemaître-Tolman-Bondi patches instead of Kottler voids, the effect of inhomogeneities has a much smaller impact on the Hubble diagram [33]. Thus, the systematic effect exhibited in Ref. [24] must be attributed to the discreteness of the distribution of matter.

Simulating the mock Hubble diagrams for Swiss-cheese universes with various values of its parameters, we inferred a phenomenological expression for the luminosity distance $D_L(z; \Omega_{m0}, \Omega_{\Lambda 0}, H_0, f)$, which is very close to the Dyer-Roeder one. This expression was then used to fit the Hubble diagram constructed from the SNLS 3 catalog [12]. Figure 25 of Ref. [24] shows that f influences the result of the best fit on Ω_{m0} that can shift from 0.22 for $f = 1$ (in agreement with the standard FL analysis performed in Ref. [12]) to 0.3 for $f = 0$.

Figure 1 shows the constraints in the plane (h, Ω_{m0}) imposed by Planck on the one hand, and by the Hubble diagram on the other hand, whether it is interpreted in a spatially flat FL universe ($f = 1$) or in a spatially flat Swiss-cheese model for which matter is entirely clumped ($f = 0$). The agreement between the CMB and the Hubble diagram is clearly improved for small values of f, especially regarding Ω_{m0}, while h is almost unaffected.

Note that SN observations *alone* cannot constrain H_0, because of the degeneracy with the (unknown) absolute magnitude M of the SNe. For the results of Fig. 1 the degeneracy was broken by fixing $M = -19.21$, according to the best-fit value obtained by Ref. [12] with a fiducial Hubble constant $h = 0.7$. Thus, the horizontal positions of the SN contours in Fig. 1 are only *indicative*.

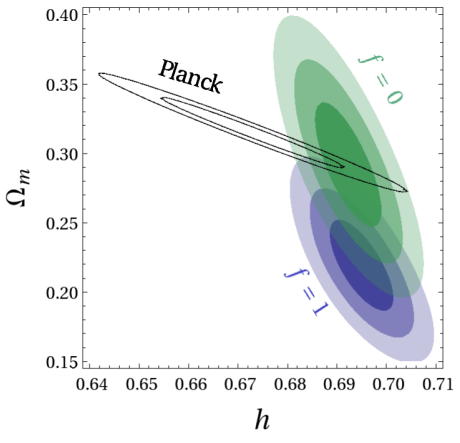

FIG. 1 (color online). Comparison of the constraints obtained by Planck on (Ω_{m0}, h) [3] and from the analysis of the Hubble diagram constructed from the SNLS 3 catalog [12]. The shaded contour plots correspond to two different smoothness parameters. For $f = 1$, the geometry used to fit the data is the FL one.

Alleviating the tension on H_0 remains an open issue. Because inferring its value from SNe is a *local* measurement, a promising approach consists in taking into account the impact of our close environment. It has been suggested [34] that cosmic variance increases the uncertainty on $H_0^{\rm local}$ and thus reduces the tension with $H_0^{\rm CMB}$. More speculatively, $H_0^{\rm local} > H_0^{\rm CMB}$ may be a hint that our local environment is underdense [35]. Our conclusions on Ω_{m0} remain, however, unaffected by this issue.

Our analysis, though relying on a particular class of models, indicates that the FL geometry is probably too simplistic to describe the Universe for certain types of observations, given the accuracy reached today. In the end, a single metric may not be sufficient to describe all the cosmological observations, just as Lilliputians and Brobdingnag's giants [36] cannot use a map with the same resolution to travel. A better cosmological model probably requires an atlas of maps with various smoothing scales, determined by the observations at hand.

Other observations, such as lensing [37], may help to characterize the distribution and the geometry of voids [38], in order to construct a better geometrical model. For the first time, the standard FL background geometry may be showing its limits to interpret the cosmological data with the accuracy they require.

We thank Francis Bernardeau, Yannick Mellier, Alice Pisani, Cyril Pitrou, Joe Silk, and Benjamin Wandelt for discussions. This work was supported by French state funds managed by the ANR within the Investissements d'Avenir programme under reference ANR-11-IDEX-0004-02, the Programme National Cosmologie et Galaxies, and the ANR THALES (ANR-10-BLAN-0507-01-02).

*fleury@iap.fr
†helene.dupuy@cea.fr
‡uzan@iap.fr

[1] P. Peter and J.-P. Uzan, *Primordial Cosmology* (Oxford University Press, Oxford, England, 2009).
[2] J.-P. Uzan, Gen. Relativ. Gravit. **39**, 307 (2007); arXiv:0912.5452; Living Rev. Relativity **14**, 2 (2011).
[3] P. A. R. Ade *et al.* (Planck Collaboration), arXiv:1303.5076.
[4] C. Pitrou, J.-P. Uzan, and F. Bernardeau, Phys. Rev. D **78**, 063526 (2008); C. Pitrou, J.-P. Uzan, and F. Bernardeau, J. Cosmol. Astropart. Phys. 07 (2010) 003; Z. Huang and F. Vernizzi, Phys. Rev. Lett. **110**, 101303 (2013).
[5] P. A. R. Ade *et al.* (Planck Collaboration), arXiv:1303.5084.
[6] G. Hinshaw *et al.*, arXiv:1212.5226.
[7] W. L. Freedman, B. F. Madore, V. Scowcroft, C. Burns, A. Monson, S. Eric Persson, M. Seibert, and J. Rigby, Astrophys. J. **758**, 24 (2012).
[8] W. L. Freedman *et al.*, Astrophys. J. **553**, 47 (2001).
[9] A. G. Riess, L. Macri, S. Casertano, H. Lampeitl, H. C. Ferguson, A. V. Filippenko, S. W. Jha, W. Li, and R. Chornock, Astrophys. J. **730**, 119 (2011).
[10] M. J. Reid *et al.*, arXiv:1207.7292.
[11] M. Bonamente, M. K. Joy, S. J. LaRoque, J. E. Carlstrom, E. D. Reese, and K. S. Dawson, Astrophys. J. **647**, 25 (2006).
[12] J. Guy *et al.*, Astron. Astrophys. **523**, A7 (2010).
[13] S. Cole *et al.*, Mon. Not. R. Astron. Soc. **362**, 505 (2005); D. J. Eisenstein *et al.*, Astrophys. J. **633**, 560 (2005); W. J. Percival *et al.*, Mon. Not. R. Astron. Soc. **401**, 2148 (2010); N. Padmanabhan, X. Xu, D. J. Eisenstein, R. Scalzo, A. J. Cuesta, K. T. Mehta, and E. Kazin, Mon. Not. R. Astron. Soc. **427**, 2132 (2012).
[14] P. A. R. Ade *et al.* (Planck Collaboration), arXiv:1303.5062.
[15] P. A. R. Ade *et al.* (Planck Collaboration), arXiv:1303.5077.
[16] K. Bolejko, J. Cosmol. Astropart. Phys. 02 (2011) 025.
[17] A. Vallinotto, S. Dodelson, C. Schimd, and J.-P. Uzan, Phys. Rev. D **75**, 103509 (2007).
[18] C. Clarkson, G. F. R. Ellis, A. Faltenbacher, R. Maartens, O. Umeh, and J.-P. Uzan, Mon. Not. R. Astron. Soc. **426**, 1121 (2012).
[19] R. Kantowski, T. Vaughan, and D. Branch, Astrophys. J. **447**, 35 (1995); J. A. Frieman, Commun. Astrophys. **18**, 323 (1996); Y. Wang, Astrophys. J. **531**, 676 (2000).
[20] C. Bonvin, R. Durrer, and M. A. Gasparini, Phys. Rev. D **73**, 023523 (2006); N. Meures and M. Bruni, Mon. Not. R. Astron. Soc. **419**, 1937 (2012); P. Valageas, Astron. Astrophys. **354**, 767 (2000).
[21] A. Cooray, D. Holz, and D. Huterer, Astrophys. J. **637**, L77 (2006); S. Dodelson and A. Vallinotto, Phys. Rev. D **74**, 063515 (2006); A. Cooray, D. Huterer, and D. E. Holz, Phys. Rev. Lett. **96**, 021301 (2006); D. Sarkar, A. Amblard, D. E. Holz, and A. Cooray, Astrophys. J. **678**, 1 (2008); A. R. Cooray, D. E. Holz, and R. Caldwell, J. Cosmol. Astropart. Phys. 11 (2010) 015; A. Vallinotto, S. Dodelson, and P. Zhang, Phys. Rev. D **84**, 103004 (2011); B. Ménard, T. Hamana, M. Bartelmann, and N. Yoshida, Astron. Astrophys. **403**, 817 (2003).
[22] N. Dalal, D. E. Holz, X. Chen, and J. A. Frieman, Astrophys. J. **585**, L11 (2003).
[23] C. C. Dyer and R. C. Roeder, Gen. Relativ. Gravit. **13**, 1157 (1981).
[24] P. Fleury, H. Dupuy, and J.-P. Uzan, Phys. Rev. D **87**, 123526 (2013).
[25] R. Sachs, Proc. R. Soc. A **264**, 309 (1961).
[26] P. Schneider, J. Ehlers, and E. E. Falco, *Gravitational Lenses* (Springer, New York, 1992).
[27] C. C. Dyer and R. C. Roeder, Astrophys. J. **174**, L115 (1972); C. C. Dyer and R. C. Roeder, Astrophys. J. **180**, L31 (1973).
[28] R. W. Lindquist and J. A. Wheeler, Rev. Mod. Phys. **29**, 432 (1957); T. Clifton and P. G. Ferreira, Phys. Rev. D **80**, 103503 (2009); J. Cosmol. Astropart. Phys. 10 (2009) 026.
[29] D. E. Holz and R. M. Wald, Phys. Rev. D **58**, 063501 (1998); J.-P. Bruneton and J. Larena, Classical Quantum Gravity **29**, 155001 (2012); J.-P. Bruneton and J. Larena, Classical Quantum Gravity **30**, 025002 (2013); K. Kainulainen and V. Marra, Phys. Rev. D **80**, 127301 (2009).
[30] A. Einstein and E. G. Straus, Rev. Mod. Phys. **17**, 120 (1945); A. Einstein and E. G. Straus, Rev. Mod. Phys. **18**, 148 (1946).

[31] R. Kantowski, Astrophys. J. **155**, 89 (1969); C. C. Dyer and R. C. Roeder, Astrophys. J. **189**, 167 (1974).

[32] K. Bolejko and P. G. Ferreira, J. Cosmol. Astropart. Phys. 05 (2012) 003.

[33] N. Brouzakis, N. Tetradis, and E. Tzavara, J. Cosmol. Astropart. Phys. 02 (2007) 013; V. Marra, E. W. Kolb, S. Matarrese, and A. Riotto, Phys. Rev. D **76**, 123004 (2007); T. Biswas and A. Notari, J. Cosmol. Astropart. Phys. 06 (2008) 021; R. A. Vanderveld, E. E. Flanagan, and I. Wasserman, Phys. Rev. D **78**, 083511 (2008); N. Brouzakis, N. Tetradis, and E. Tzavara, J. Cosmol. Astropart. Phys. 04 (2008) 008; T. Clifton and J. Zuntz, Mon. Not. R. Astron. Soc. **400**, 2185 (2009); W. Valkenburg, J. Cosmol. Astropart. Phys. 06 (2009) 010; S. J. Szybka, Phys. Rev. D **84**, 044011 (2011); E. E. Flanagan, N. Kumar, I. Wasserman, and R. A. Vanderveld, Phys. Rev. D **85**, 023510 (2012).

[34] V. Marra, L. Amendola, I. Sawicki, and W. Valkenburg, Phys. Rev. Lett. **110**, 241305 (2013).

[35] S. Jha, A. Riess, and R. Kirshner, Astrophys. J. **659**, 122 (2007).

[36] J. Swift, *Travels into Several Remote Nations of the World. In Four Parts* (Benjamin Motte, London, 1726).

[37] K. Bolejko, C. Clarkson, R. Maartens, D. Bacon, N. Meures, and E. Beynon, Phys. Rev. Lett. **110**, 021302 (2013).

[38] G. Lavaux and B. D. Wandelt, Mon. Not. R. Astron. Soc. **403**, 1392 (2010).

1.7 Continuation of this work

Several improvements could be brought to this work, which is a mere manipulation of a toy model. For example, to be more realistic, it would be useful to study in detail the space distribution of the structures of the universe. What are the relevant masses? What fraction of the total volume do these structures represent? How lumpy the universe is? Introducing holes with different sizes could in particular be relevant. We could also envisage a similar study in which light is replaced by gravitational waves (playing the role of "standard sirens") to check that conclusions about cosmology do not depend on the observables considered.

In the continuity of our project, my collaborators P. Fleury and J. P. Uzan have realized several studies. For instance, in [78], they propose a comprehensive analysis of light propagation in a spatially anisotropic and homogeneous spacetime and in [75] P.Fleury compares the distance-redshift relation of a certain class of Swiss-cheese models to the one predicted by the so-called Dyer-Roeder approach ([61]).

This kind of study is an illustration of what precision cosmology means because it is the description of the very fine structure of the universe that is questioned. Such approaches do not aim at proposing new models but rather at adding a level of description to the existing ones. In the present case, the novelty would consist in adapting the mapping of the universe to the scale considered instead of using homogeneous and isotropic descriptions smoothed on large scales. Precision cosmology can also be developed by considering the large-scale structure of the universe. In the framework of perturbation theory, a common effort is indeed realized in order to go beyond the linear regime and to account for cosmic components that had been neglected so far. This is exactly the type of issues addressed in the remainder of this manuscript.

Chapter 2

A glimpse of neutrino cosmology

Neutrino phenomenology is extremely rich. Rather than getting into the details, details which are nevertheless captivating, I confine this chapter to elements that I consider relevant for familiarizing with neutrino cosmology and understanding what is at stake in the part of this thesis oriented towards neutrinos. A clear and comprehensive review of the role of neutrinos in cosmology can be found in [104].

2.1 Basic knowledge about neutrinos

In December 1930, Wolfgang Pauli suggested the existence of an unknown particle. This was motivated by the observation that, if it did not exist, conservation laws would be violated in β decay. For energy, momentum and angular momentum to be conserved, this particle had to be electrically neutral, extremely light and with a spin 1/2. Besides, to explain why it had never been detected, it has been postulated that it should interact very weakly with matter. At that time, its existence was purely hypothetical. Pauli's idea was even considered by many as a desperate theorist's attempt to keep up appearances.

However, Enrico Fermi took it seriously and incorporated the new particle, that he named neutrino, in his theory of β decay in 1934. This theory was to become the theory of the weak interaction.

Between 1953 and 1956, Clyde Cowan and Frederick Reines achieved the first neutrino detections thanks to a nuclear reactor of the Savannah River site ([41]).

For this finding, they received the Nobel Prize in 1995.

Then it has been demonstrated that neutrinos are of several types, or flavors, i.e. one can distinguish between "electron neutrinos" (the firsts to be discovered), "muon neutrinos" (discovered in 1962 by Leon M. Lederman, Melvin Schwartz and Jack Steinberger, winners of the Nobel Prize for their research on neutrinos in 1988) and "tau neutrinos" (whose detection has been announced in 2000 by the DONUT collaboration at Fermilab).

A remarkable fact is that, even before muon neutrinos were discovered, Bruno Pontecorvo suggested that, provided they are massive, neutrinos can change in nature during their time evolution (see his paper [138], which dates from 1957). Assuming a non-zero mass is a modification of the standard model of particle physics[1], in which neutrinos are massless leptons. On the other hand, the absence of mass is a mere assertion, which is not justified theoretically by the model. Naturally, the detection of a second neutrino flavor strengthened B. Pontecorvo's intuition ([139]). The existence of flavor neutrino oscillations, i.e. of transitions from one flavor to another, has been confirmed by the Homestake experiment thirty years later ([34]). It is a thrilling point since its theoretical justification demands to go beyond the standard model of particle physics, that is to say to invoke new physics. At the present time, thanks to experiments involving atmospheric and solar neutrinos, there is no doubt that at least two of the three neutrino species are massive. Planetary atmospheres (when excited by cosmic rays) and stars are indeed powerful natural sources[2] of neutrinos.

2.2 Why are cosmologists interested in neutrinos?

At ordinary energies, neutrinos interact so weakly with matter that they can go through a planet with no consequence. Such an insensitiveness is annoying for particle physicists. It makes the detection of neutrinos and the study of their properties very challenging. But the universe is an amazing laboratory in which highly energetic phenomena occur naturally. By looking far into space, one accesses to the extreme physical conditions that characterized the young universe. Observational astrophysics offers therefore an opportunity to get unhoped constraints on

[1] The standard model of particle physics is a scientific theory describing interactions between the elementary particles that constitute matter. It was developed throughout the latter half of the twentieth century.

[2] Among such sources, one can cite supernovae too.

particles and fundamental interactions. This is what justifies the existence of the research field called astroparticle physics. In particular, when the observed object is the observable universe and the studied particles are neutrinos, it is referred to as neutrino cosmology.

For the game to be fair, cosmologists too should enjoy the benefits of testing neutrino properties. And they definitely do! Indeed, the ambitions of precision cosmology require to develop a solid knowledge of the properties of each cosmic component involved in the dynamical evolution of the universe. As will be sketched in the next sections, neutrinos truly had a role to play in this evolution, their means of action being weak interaction and gravitation.

2.2.1 An equilibrium that does not last long

At the beginning, the particles of the universe are all maintained in equilibrium by processes involving very high energies. At that time, neutrinos are relativistic and interact continuously with the rest of the cosmic plasma. In the meantime the universe cools, which lowers the rate at which neutrinos interact. This decrease is faster than the one of the Hubble rate. Hence, there is a moment at which weak interactions are beaten by expansion: neutrinos decouple from electrons, positrons and photons and then propagate freely. So, in the same way as there exists a cosmic microwave background, there exists a cosmic neutrino background. Unfortunately, there is little chance for the latter to be detected directly someday because neutrinos interact very weakly, which is worsened by the fact that their interaction rate is largely suppressed by the cooling of the universe. However, some imprints left by neutrinos during different cosmological eras are present in several observables. As we will see, the role played by neutrinos is especially significant at late times, i.e. during the formation of the large-scale structure of the universe.

Neutrino decoupling takes place much earlier than photon decoupling, when the universe is at most few-minute-old[3] and has a temperature in the MeV range[4]. At this temperature, neutrinos are still relativistic, whence the appellation “hot relics” which is sometimes used.

[3]There is no single decoupling time because decoupling is not an instantaneous phenomenon. It is nevertheless possible to obtain a correct order of magnitude in the “instantaneous decoupling limit”. Neutrino decoupling is estimated to start about one-tenth of a second after the Big Bang.

[4]The typical temperature of neutrino decoupling is thus almost seven orders of magnitude higher than the one of photon decoupling (photon decoupling marks the start of the CMB propagation).

Thermodynamical considerations show that, when equilibrium is broken, the neutrino-to-photon temperature ratio, which used to be 1, becomes[5]

$$\frac{T_\nu}{T_\gamma} = \left(\frac{4}{11}\right)^{1/3}. \tag{2.1}$$

Note that, as well as photons, neutrinos are exceptionally cold today. Indeed, the measurement of the present CMB temperature gives $T_{\gamma,0} = 2.725$ K, whence $T_{\nu,0} = 1.945$ K ($\sim 10^{-4}$ eV). As explained in [104], it means in particular that at least two of the three neutrino species are non-relativistic today.

2.2.2 The effective number of neutrino species, a parameter relevant for precision cosmology

Definition

After decoupling and as long as neutrinos are relativistic, the total energy density of relativistic species can be written (see also [104])

$$\rho_{\mathrm{R}} = \rho_\gamma \left[1 + \frac{7}{8}\left(\frac{4}{11}\right)^{4/3} N_{\mathrm{eff}}\right]. \tag{2.2}$$

ρ_γ is the photon energy density. N_{eff} is called effective number of neutrino species. It characterizes the neutrino abundance in the early universe, plus possibly extra relativistic species. In the instantaneous decoupling limit, provided that neutrinos are well described by Fermi-Dirac distribution functions with no chemical potential[6] and that the only relativistic components of the universe are photons plus three neutrino species, N_{eff} is equal to 3. So, as a first approximation, any deviation from $N_{\mathrm{eff}} = 3$ would be indicative of a need for a refinement of the cosmological model, hence the importance of measuring this parameter. Actually, the standard model of cosmology predicts $N_{\mathrm{eff}} = 3.046$, the difference from three being due to a small amount of entropy inherited by neutrinos from the electron/positron annihilation process (see [114]). The latest observational constraint, obtained by combining Planck data with other surveys, is $N_{\mathrm{eff}} = 3.15 \pm 0.23$ ([137]). As the rest of the Planck results, this estimation confers credibility to the cosmological scenario currently adopted.

[5] It is valid only when $T \ll m_e$, m_e being the electron mass. See e.g. [104] for a demonstration.

[6] See section 2.3.2 for discussions on the form of the phase-space distribution function of neutrinos.

Impact of N_{eff} on primordial abundances

It is also at a temperature of the order of 1 MeV that neutrons are trapped by protons for the first time, producing deuterium,

$$n + p \leftrightarrow {}^2\text{H} + \gamma, \tag{2.3}$$

and initiating subsequent formations of light elements, mainly ^{3}He, ^{4}He and ^{7}Li. This key period of the history of the universe is called primordial nucleosynthesis, or Big Bang nucleosynthesis (see e.g. [156, 124, 174, 95, 140] for reviews on Big Bang nucleosynthesis).

So, do neutrinos intervene in this? Equation (2.2) tells one that extra relativistic species (with respect to photons) enhance the primordial radiation energy density. Consequently, they affect the expansion rate of the universe before and during the Big Bang nucleosynthesis (see the Friedmann equations (1.9) and (1.10)). It changes in particular the freezing temperature of the neutron-to-proton ratio, and thus the primordial abundance of ^{4}He. More precisely, the larger N_{eff} is, the quicker the universe expands so the earlier the neutron-to-proton ratio is frozen. It leads to a larger relic neutron abundance and eventually to a higher production of ^{4}He. The theoretical impact of N_{eff} on primordial abundances is depicted in figure 2.1. Y_p characterizes the ^{4}He abundance[7]. It is this abundance that is the most impacted but one can see that all primordial abundances of light elements are influenced by the effective number of neutrino species.

The measurement of such abundances is an investigation tool widely exploited in precision cosmology. It is also part of the elements that favored historically the Big Bang model. One can find a recent update of the predictions related to primordial nucleosynthesis, based on the results of the Planck mission, in [36]. The dependence of primordial abundances on N_{eff} illustrates the importance of including neutrinos in modern cosmological models.

Impact of N_{eff} on the anisotropies of the cosmic microwave background

Given the richness of the information contained in CMB anisotropies, it seems crucial to determine if the presence of neutrinos makes a difference.

Recombination marks the end of thermal equilibrium between baryons, elec-

[7] $Y_p = 4\frac{n_{^4\text{He}}}{n_{\text{B}}}$, n standing for number densities and B for baryons.

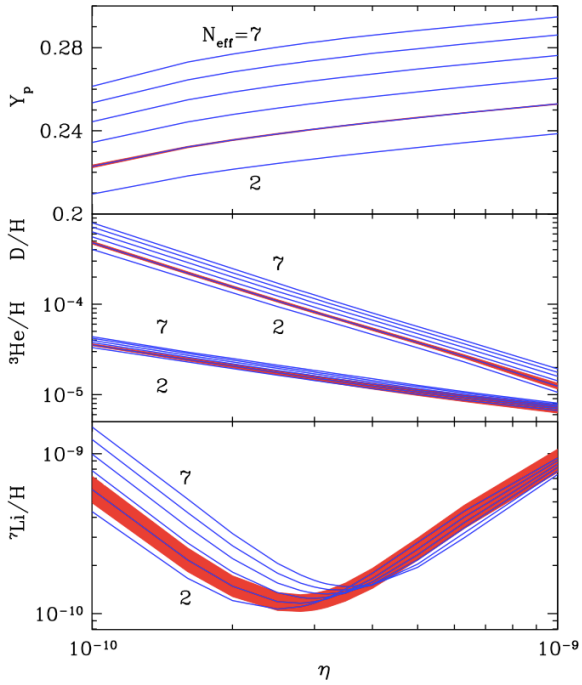

Figure 2.1: Big Bang nucleosynthesis abundance predictions as a function of the baryon-to-photon ratio η, for $N_{\rm eff} = 2$ to 7. The bands show the 1σ error bars. All bands are centered on $N_{\rm eff} = 3$. Authors: Cyburt *et al.*, [47].

trons and photons. From this time, photons propagate freely and carry with them physical characteristics of their last scattering point. In particular, after decoupling, each photon can be associated with a local temperature $\overline{T} + \delta T(\eta, \vec{x}, \hat{n})$, where $\hat{n}$ gives the direction of propagation. It is therefore possible to construct a CMB temperature map. The relevant information is contained in the angular scale, shape and amplitude of its angular correlation function.

To be more precise, temperature anisotropies on the last scattering surface are usually expanded in the following way,

$$\frac{\delta T}{T}(\hat{n}) = \sum_{lm} a_{lm} Y_{lm}(\hat{n}). \tag{2.4}$$

Then one defines the harmonic power spectrum C_l as

$$C_l = \langle a_{lm} a^*_{lm} \rangle \quad \forall m. \tag{2.5}$$

This power spectrum is isotropic, i.e. it depends on l but not on m. Here, and throughout the manuscript, the symbol "$\langle\ \rangle$" denotes ensemble averages of variables X depending on scalar stochastic[8] fields, $s(\mathbf{x})$. Those fields are random variables: they can be described with the help of distribution functions, which determine the probability for them to have given values at given positions. Explicitly,

$$\langle X \rangle \equiv \int X(s_1, s_2, ...)\mathcal{P}(s_1, s_2, ...)\mathrm{d}s_1\mathrm{d}s_2..., \tag{2.6}$$

with $\mathcal{P}(s_1, s_2, ...)\mathrm{d}s_1\mathrm{d}s_2...$ the probability for s to have a value between s_1 and $s_1+\mathrm{d}s_1$ at position x_1, between s_2 and $s_2+\mathrm{d}s_2$ at position x_2, etc. When the number of variables is sufficient (which is usually not restrictive in cosmology, especially given the richness of the latest observation surveys), it is commonly assumed that ensemble averages are equivalent to space averages (ergodic hypothesis).

Isolating the theoretical impact of N_{eff} on this power spectrum is a subtle task, described in full detail in [104]. The difficulty arises from the fact that a large variety of effects, originating from several species, are entangled in the C_l's. On the one hand, at the background level, each cosmic component affects the time evolution of the scale factor and, on the other hand, perturbations of decoupled species disturb the growth of metric perturbations. Depending on the effect that one wants to bring to light, one decides to fix one or another set of parameters of the model. As an illustration, figure 2.2 highlights the effect of N_{eff} for three different settings. The tuning of the parameters has been done so that the features of the upper curve can entirely be interpreted in terms of direct effects due to neutrino perturbations, whereas the lower curve is more realistic but mixes background and perturbative effects. More precisely, the rapid decrease at high l's visible on the lower curve is a background effect due to diffusion damping, or Silk damping ([166]). Indeed, varying N_{eff} affects the typical length of the random walk that characterizes interactions between photons and electrons. In multipole space, this length is hidden in the parameter l_{D}[9] and the envelope of the curve is controlled by a factor $\exp[-(l/l_{\mathrm{D}})^2]$. Concerning the perturbative level, basically, metric fluctuations are reduced on scales at which neutrinos free-stream because they do not cluster

[8] The reason why statistics occupies inevitably a place in cosmology is briefly addressed in the item "Impact of N_{eff} on the matter power spectrum" of the present subsection.

[9] $l_{\mathrm{D}} \sim k_{\mathrm{D}}(\eta_0 - \eta_{\mathrm{LS}})$, where k_{D} is the wavenumber associated with the comoving distance traveled by a photon during Thomson diffusion, η_0 is the present comoving time and η_{LS} is the last scattering comoving time.

while free-streaming. One can refer to e.g. [93, 9, 104] for analytic interpretations of the patterns of the curves. In the plot 2.2, neutrino masses have been fixed to zero for the contribution of the mass not to mix with the one of $N_{\rm eff}$ (see section 2.2.3 for discussions on mass effects). Note chiefly that the suppression of the C_l's that appears when one switches from a neutrinoless model to a model with three neutrino species is close to 20% in the case represented by the upper curve, which is non-negligible in precision cosmology.

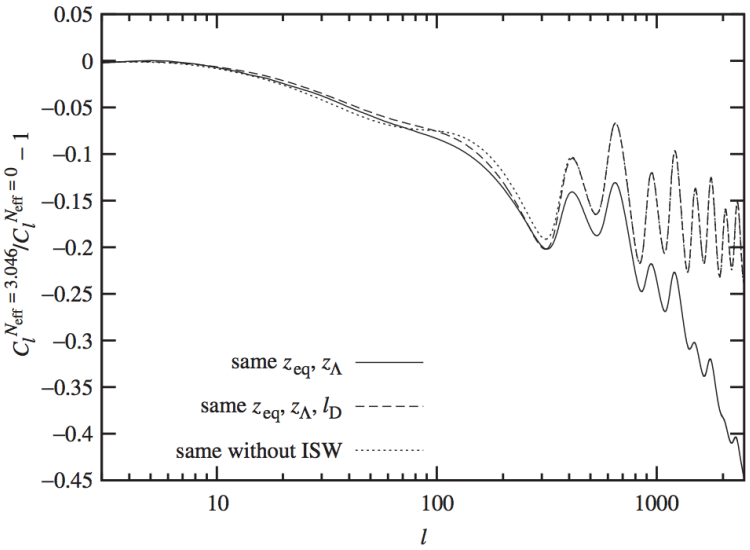

Figure 2.2: CMB temperature spectrum for models with $N_{\rm eff} = 3.046$ divided by the spectrum of a model with $N_{\rm eff} = 0$. $z_{\rm eq}$ is the redshift of equality between matter and radiation. z_Λ is the redshift of equality between matter and dark energy. $l_{\rm D}$ is a multipole parameter which characterizes diffusion damping. It has been fixed in the second case in order to get rid of diffusion damping effects. ISW stands for Integrated Sachs-Wolfe effect, whose contribution is tiny in this context. Authors: Lesgourgues *et al.*, [104].

Impact of $N_{\rm eff}$ on the matter power spectrum

Strictly speaking, density perturbations are realizations of stochastic fields. According to the inflation theory, stochasticity is present from the beginning because inhomogeneities originate from quantum fluctuations, whose evolution is not deterministic. Furthermore, the ignorance of the initial conditions and the existence of unobservable regions confirm the necessity of a statistical approach in cosmology.

Besides, it is very common to describe the observable universe in terms of variables belonging to the reciprocal space (in particular when it comes to compute correlation functions). As usual, one switches from real space to reciprocal space with the help of Fourier transforms. In this thesis, the convention that we use is (for any field X)

$$X(\mathbf{x}) = \int \frac{\mathrm{d}^3\mathbf{k}}{(2\pi)^{3/2}} X(\mathbf{k}) \exp(\mathrm{i}\mathbf{k}.\mathbf{x}), \tag{2.7}$$

$$X(\mathbf{k}) = \int \frac{\mathrm{d}^3\mathbf{x}}{(2\pi)^{3/2}} X(\mathbf{x}) \exp(-\mathrm{i}\mathbf{k}.\mathbf{x}). \tag{2.8}$$

Since initial fluctuations of density emerge from a field which is free in the sense of quantum mechanics, they are usually assumed to be Gaussianly distributed (which is in very good agreement with the latest results of the Planck mission, [136]). In this context, all the needed information regarding initial time derives from two-point correlation functions (but the observables that one uses to study large-scale structures at a later time are in general multi-point correlation functions). It is a consequence of Wick's theorem. More precisely, cosmologists introduced a quantity $P(k)$, omnipresent in studies of large-scale structure formation and defined so that

$$\langle \delta_{\mathrm{m}}(\vec{k}) \delta_{\mathrm{m}}(\vec{k}') \rangle = P(k) \delta_{\mathrm{D}}(\vec{k} + \vec{k}'), \tag{2.9}$$

where δ_{D} is the Dirac delta function and δ_{m} is the matter density contrast, i.e. $\delta_{\mathrm{m}} = \dfrac{\rho_{\mathrm{m}}}{\bar{\rho}_{\mathrm{m}}} - 1$ with $\bar{\rho}_{\mathrm{m}}$ the spatial average of the matter density ρ_{m}. $P(k)$ is called matter power spectrum. According to Wick's theorem, higher order initial-time correlations are zero if they involve an odd number of fields. In contrast, in case of an even number $2N$ of fields, then $(2N-1)!!$ terms contribute to the correlators. Those terms correspond to all different pairings of the $2N$ fields:

$$\langle \delta^1_{\mathrm{m}}(\vec{k}_1) ... \delta^{2N}_{\mathrm{m}}(\vec{k}_{2N}) \rangle = \sum_{\text{all pair associations}} \prod_{\text{pairs (i,j)}} \langle \delta^i_{\mathrm{m}}(\vec{k}_i) ... \delta^j_{\mathrm{m}}(\vec{k}_j) \rangle. \tag{2.10}$$

If one assumes, in addition, that initial conditions are adiabatic, all species share initially the same density contrast (with only a known species-dependent factor in front of it). It means that primordial power spectra of photons and neutrinos (and of any hypothetical other species, like dark energy) are proportional to the

primordial matter power spectrum. More details about the meaning of adiabaticity will be given in section 4.3.3. We will see that it can generally be considered as a reasonable assumption.

As in the case of the power spectrum of CMB anisotropies, it is not possible to disentangle totally the contributions of the various parameters to the matter power spectrum (again, I refer the reader to [104] for a thorough analysis). Illustratively, figure 2.3 shows how the phase and amplitude of BAO, imprinted in the matter power spectrum, are altered by the presence of massless neutrinos. The lower curve mixes neutrino perturbation effects with a background effect due to the fact that the baryon density $\omega_{\rm B}$[10] is not fixed: a non-zero value of $N_{\rm eff}$ increases $\omega_{\rm B}$, leading to an earlier release of baryons. On the contrary, $\omega_{\rm B}$ is fixed in the case corresponding to the upper curve whereas the baryon-to-cold dark matter ratio varies, this latter variation altering the BAO amplitude. In both cases, neutrino perturbations damp the BAO amplitude and induce a phase shift in it.

All these examples prove that even massless neutrinos would contribute to the development of the universe. Yet, to be in tune with reality, neutrino masses should not be ignored.

2.2.3 Neutrino masses: small but decisive

Current estimates

It is thanks to neutrino oscillation experiments that neutrino masses have been revealed. Such experiments are in fact interference experiments, which can only detect differences between squares of neutrino masses (see [119, 66, 21, 8, 118, 130, 71] for precisions). The absolute neutrino mass scale being still out of reach[11], many efforts realized in order to constrain neutrino masses consist in putting bounds on the total neutrino mass $M_\nu = \sum_i m_{\nu_i}$, where each value of i denotes a neutrino species. The number of studies carried out for that purpose is phenomenal. Predictions vary from one study to another, depending on the selected data and on the cosmological assumptions made to interpret them. Table 2.1 presents few examples of mass constraints (including the estimation from the 2015 release of the Planck

[10] $\omega_{\rm B}$ is part of the six parameters of the standard model of cosmology. It is defined as $\omega_{\rm B} = \Omega_{\rm B} h^2$, with $\Omega_{\rm B} = \dfrac{8\pi G}{3H_0^2} m_{\rm N} n_{\rm B}$, $m_{\rm N}$ being the average nucleon mass.

[11] It is nevertheless reasonable to hope that, in the near future, large-scale structure surveys will unveil the absolute neutrino mass scale.

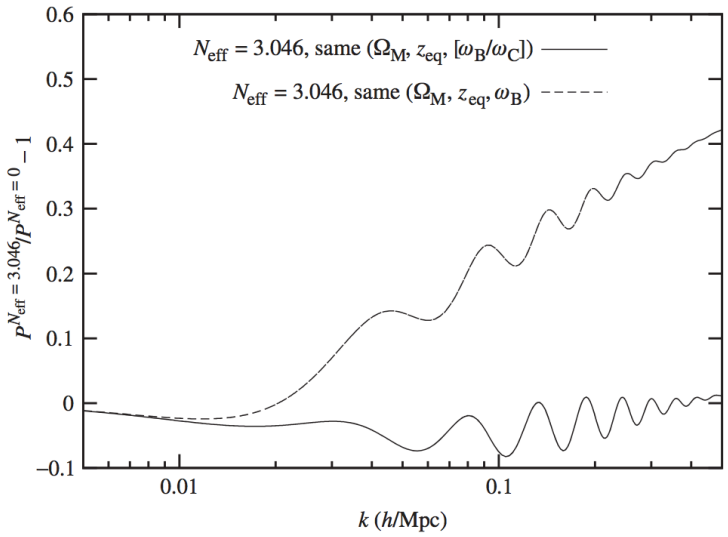

Figure 2.3: Matter power spectra for models with $N_{\rm eff} = 3.046$ divided by the power spectrum of a model with $N_{\rm eff} = 0$. $\Omega_{\rm M} = \dfrac{8\pi G}{3H_0^2}\rho_{\rm m,0}$, with $\rho_{\rm m,0}$ the present energy density of the matter fluid. $\omega_{\rm C}$ is the cold dark matter density and $\omega_{\rm B}$ is the baryon density. Authors: Lesgourgues *et al.*, [104].

mission, [137]) among many others.

Observables	Year and reference	Result
CMB+BAO	2015, [137]	$M_\nu < 0.23$ eV
CMB+BAO+Lyman-α forest	2014, [125]	$M_\nu < 0.14$ eV
CMB+BAO	2014, [135]	$M_\nu < 0.23$ eV
Galaxy survey+CMB+BAO	2014, [147]	$M_\nu < 0.18$ eV
Galaxy survey+CMB+BAO+Supernovae	2010, [115]	$M_\nu < 0.33$ eV

Table 2.1: Some 2σ-upper bounds on the total neutrino mass.

What cosmological repercussions can one expect from sub-eV masses?

Impact of M_ν on the anisotropies of the cosmic microwave background

Assuming the existence of three equal-mass neutrino species and adjusting judiciously the other parameters, the authors of [104] highlight the impact of non-zero neutrino masses on the CMB temperature spectrum. It is presented in figure 2.4.

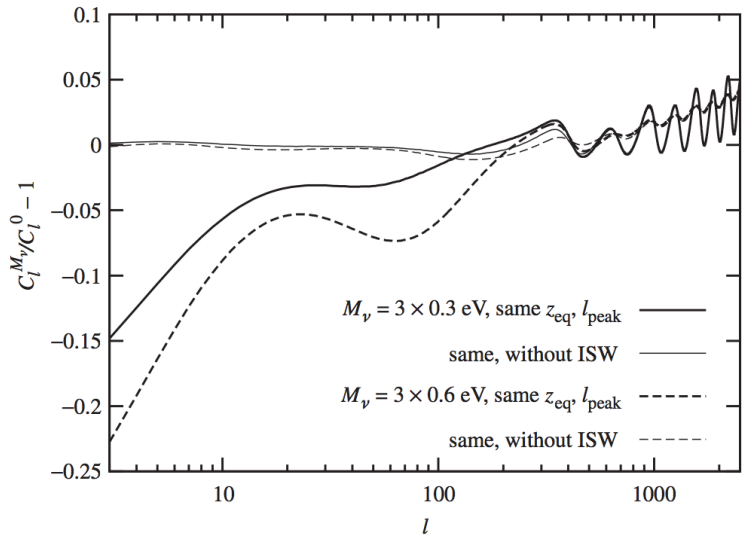

Figure 2.4: CMB temperature spectra for models with either $M_\nu = 3 \times 0.3$ eV or $M_\nu = 3 \times 0.6$ eV divided by the spectrum of a model with three massless neutrinos sharing the same temperature. l_{peak}, which is kept constant here, is a parameter fixing the l's at which acoustic oscillations peak. Authors: Lesgourgues *et al.*, [104].

The leading effect, impacting the multipoles for which $l < 20$, is a background effect. At late times, dark energy becomes predominant, which makes metric fluctuations decay and therefore disturbs photons in their path between the last scattering surface and observers. This phenomenon, known as late integrated Sachs-Wolfe effect[12], is affected by massive neutrinos because the time of equality between matter and dark energy depends on neutrino masses. In figure 2.4, the integrated Sachs-Wolfe effect is controlled by the parameter ISW, which has been fixed on the upper curves to differentiate ISW from other phenomena.

The rise visible at $l > 500$ is also a background effect, corresponding to the Silk damping induced by the neutrinos that are already non-relativistic at decoupling.

Between $l = 20$ and $l = 500$, features of the two lower curves are mainly attributed to the early integrated Sachs-Wolfe effect, which is simply the disclosure of the impact of neutrino masses on metric perturbations after decoupling. This perturbation effect, in the order of 3% for 0.3 eV masses, can seem tiny but it is

[12]The Sachs of the Sachs-Wolfe effect, Rainer K. Sachs, is the same as the Sachs of the Sachs equation discussed in chapter 1.

within the range of precision targetted today in cosmology.

Impact of M_ν on the matter power spectrum

As already mentioned, in cosmological models, one usually assumes that initial conditions are adiabatic. So, as long as free-streaming can be neglected, assigning a mass to neutrinos does not affect the matter power spectrum[13] because such massive particles behave as cold dark matter. However, the free-streaming of massive neutrinos can not be mimicked by any other species. During free-streaming, massive neutrinos increase the expansion rate of the universe without clustering under the influence of gravitational instability. Such a behavior slows down the growth of structure, or equivalently damps the matter power spectrum on small scales. This is well illustrated in figure 2.5.

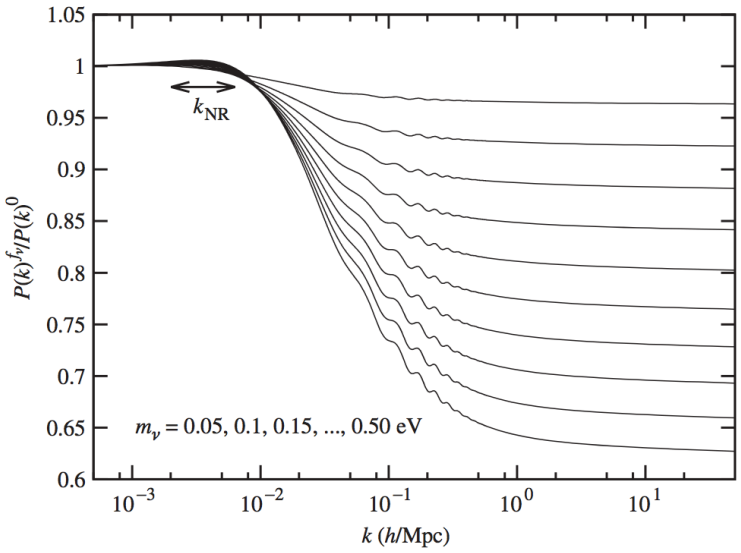

Figure 2.5: Steplike suppression of the matter power spectrum due to neutrino mass. The power spectrum of a standard cosmological model with two massless and one massive species has been divided by that of a massless model, for several values of m_ν between 0.05 eV and 0.50 eV, spaced by 0.05 eV. All spectra have the same primordial power spectrum and the same parameters $(\Omega_\mathrm{m}, \omega_\mathrm{m}, \omega_\mathrm{B})$. k_NR is the free-streaming wavenumber at the non-relativistic transition ($k_\mathrm{NR} \sim 5.10^{-3} h/\mathrm{Mpc}$). Authors: Lesgourgues *et al.*, [104].

[13] It is true provided that the total matter density and the primordial power spectrum are unchanged.

An analytic justification, based on linear perturbation theory, can be found in [104] (see also references herein). In fact, while particularly enriching, adopting a linear approach to model this kind of phenomenon is not sufficient. Indeed, on small scales and at small redshifts, the evolution of cosmological perturbations is not linear[14]. Actually, the scales that are the most sensitive to neutrino masses (roughly $k > 0.1h/\mathrm{Mpc}$) correspond to the nonlinear part of the matter power spectrum. Hence the importance of modeling the behavior of massive neutrinos beyond the linear regime when trying to describe the formation of the large-scale structure of the universe. Another argument along this is that a large amount of cosmological data would be wasted if the absence of theoretical counterpart made one skip the observations corresponding to nonlinear scales. Besides, it has been shown in several studies that neglecting the nonlinear corrections induces a spurious behavior on small wavenumbers due to a violation of momentum conservation (see [82, 91, 126, 27]). So a common effort is currently carried out to investigate the nonlinear regime (see section 2.3.2), in particular in the field of numerical simulations. Achieving this objective is to a large extent what motivates the work undertaken for my PhD thesis, during which I developed a new analytic description of the nonlinear evolution of massive neutrinos (see chapters 4, 5 and 6).

2.3 How cosmic neutrinos are studied

2.3.1 Observation

It is fortunate that there exists a great variety of astrophysical sources because all are not sensitive to the same properties. The recent explosion in the number of high precision observational projects allows to multiply the possible combinations of data, increasing dramatically the relevance of the constraints. CMB, BAO and large galaxy surveys have already been mentioned as observables useful for neutrino cosmology but the list can be extended.

One can cite for instance quasars, which are objects particularly luminous and distant. In a range of frequencies called Lyman-α forest, their spectra are good tracers of hydrogen density fluctuations on mildly nonlinear scales, and thus indirectly of the matter perturbations that govern the matter power spectrum (see e.g.

[14] Density perturbations grow with time and only extremely small perturbations can be treated at linear level (see chapter 3 for precisions).

[186, 188, 152] for recent studies in which the Lyman-α forest is put at the service of neutrino cosmology).

Gravitational lensing, i.e. distortion of galaxy images due to density fluctuations along the line of sight, is also useful in this context ([187, 178]). Note that the upcoming Euclid mission will give particular importance to the examination of gravitational lensing.

Even cosmic voids contribute to the exploration of neutrino properties ([188]).

Giving an exhaustive list and dissecting the advantages and drawbacks of each kind of observation is not the purpose here (an enlightening overview adapted to neutrino cosmology is nevertheless given in [104]). The intent was rather to exemplify the richness of observational cosmology, which is a direct gateway between infinitely large and infinitely small.

2.3.2 Modeling

The Boltzmann hierarchy

The standard way of modeling massive neutrinos is to consider them as a non-cold fluid, i.e. a fluid made of particles that are still relativistic when they decouple. As soon as the fluid is out of equilibrium, a kinetic approach is necessary to depict what happens. It is therefore convenient to describe the fluid with its phase-space distribution function, $f(x^\mu, p_\mu)$, where x^μ is a space coordinate and p_μ is the conjugate[15] momentum of x^μ, i.e.

$$p_\mu = m u_\mu \quad \text{with} \quad u_\mu = g_{\mu\nu} \mathrm{d}x^\nu / \sqrt{-\mathrm{d}s^2}. \tag{2.11}$$

m is the particle mass so, if neutrino masses are not degenerate, m is different for each species. Using standard results of general relativity, it is straightforward to show that p_μ satisfies the mass-shell condition $p^\mu p_\mu = -m^2$.

The starting point is that, in the absence of interactions, the Liouville operator,

$$\mathcal{L}(f) \equiv \frac{\mathrm{d}f}{\mathrm{d}\lambda}\left(x^\mu(\lambda), p_\mu(\lambda)\right), \tag{2.12}$$

is zero[16]. In this equation, λ is an arbitrary parameter. Note that the possibility

[15] Actually, there are several ways to define a phase-space momentum but only the conjugate momentum is defined so that $\mathrm{d}^3x^i\mathrm{d}^3p_i$ is the phase-space unit volume and that the number of particles in it is $\mathrm{d}^6N = f(x^i, p_i)\mathrm{d}^3x^i\mathrm{d}^3p_i$ (see the reference paper [111]).

[16] To demonstrate it, one can e.g. write the geodesic equation for u_μ and use the fact that f is

of interacting neutrinos has been explored in many non-standard models (see the references given in [104]) and that the eventuality of self-interacting neutrino fluids is disfavored by observations ([51, 4]). The time evolution of f is then governed by an equation called collisionless Boltzmann equation or Vlasov equation. In terms of the conformal time η, it reads:

$$\frac{\partial f}{\partial \eta} + \frac{\mathrm{d}x^i}{\mathrm{d}\eta}\frac{\partial f}{\partial x^i} + \frac{\mathrm{d}p_i}{\mathrm{d}\eta}\frac{\partial f}{\partial p_i} = 0. \tag{2.13}$$

During the equilibrium stage, neutrinos are expected to be characterized by a relativistic Fermi-Dirac distribution in which the chemical potential is negligible,

$$f(q) = \left(1 + \exp\frac{q}{aT}\right)^{-1}, \tag{2.14}$$

where T is the temperature and q is the physical momentum[17]. The absence of chemical potential is justified theoretically, thanks to quantum field theory considerations, in [104]. Besides, this assertion can be tested experimentally.

When equilibrium breaks down, the previous description is not valid anymore. However, the Boltzmann equation can be studied perturbatively. To that aim, f is decomposed into a homogeneous part f_0 (given by equation (2.14)) and a perturbation $f_0\Psi$,

$$f\left(x^i, q\right) = f_0\left(q\right)\left[1 + \Psi\left(x^i, q\right)\right]. \tag{2.15}$$

Note that, in the relativistic regime, the expression of Ψ is known. Indeed one can show that[18], before the non-relativistic transition, f keeps a Fermi-Dirac form except that it exhibits local fluctuations of temperature:

$$f\left(x^i, q\right) = \left[1 + \exp\frac{q}{a\left(T + \delta T(x^i)\right)}\right]^{-1} \text{ in the relativistic regime.} \tag{2.16}$$

conserved along geodesics when particles do not interact.

[17]The physical momentum is defined so that the energy ϵ measured by a comoving observer is $\epsilon^2 = m^2 + (q/a)^2$. Explicit relations between p_i and q^i (in different metrics) are given in the papers presented in sections 4.4 and 5.4.

[18]The theoretical argument is the writing of the geodesic equation for q_i. Indeed, provided that $q \gg m$, the momentum shift induced by metric perturbations does not depend on the momentum itself (see [104]).

Hence, one has

$$\Psi\left(x^i, q\right) = -\frac{\delta T(x^i)}{T}\frac{\mathrm{d}\ln f_0}{\mathrm{d}\ln q} \text{ in the relativistic regime.} \tag{2.17}$$

More generally, one can derive an equation governing the time evolution of Ψ. Its form depends on the gauge which is chosen, i.e. on the form of the metric. As will be explained in chapter 3, a convenient way to take inhomogeneities into account is to add spatial perturbations in the homogeneous and isotropic Friedmann-Lemaître metric (1.4). In the gauge called conformal Newtonian gauge, those perturbations are denoted ϕ and ψ and the metric reads (assuming a flat universe)

$$\mathrm{d}s^2 = a^2(\eta)\left[-(1+2\psi)\,\mathrm{d}\eta^2 + (1-2\phi)\,\mathrm{d}x^i\mathrm{d}x^j\delta_{ij}\right]. \tag{2.18}$$

Calculations are usually made *in the linear regime*, which means that all couplings between any perturbations are neglected. In this framework, $q^i = a^2(1-\phi)p^i$ (see [57]). Noticing that $\dfrac{\mathrm{d}x^i}{\mathrm{d}\eta} = \dfrac{p^i}{p^0}$ and writing the geodesic equation in the metric (2.18) to compute $\dfrac{\mathrm{d}p_i}{\mathrm{d}\eta}$, one gets from equation (2.13),

$$\partial_\eta\Psi + \frac{q}{a\epsilon}\hat{n}^i\partial_i\Psi + \frac{\mathrm{d}\ln f_0(q)}{\mathrm{d}\ln q}\left(\partial_\eta\phi - \frac{a\epsilon}{q}\hat{n}^i\partial_i\psi\right) = 0, \tag{2.19}$$

where $\hat{n}$ gives the direction of the physical momentum.

Besides, in momentum space, the only dependence on $\mathbf{k}$ is through its angle with $\hat{n}$. Hence, one can define $\alpha \equiv \hat{k}.\hat{n}$ and rewrite the linearized Boltzmann equation as

$$\partial_\eta\tilde{\Psi} + \mathrm{i}\alpha k\frac{q}{a\epsilon}\tilde{\Psi} + \left(\partial_\eta\phi - \mathrm{i}\alpha k\frac{a\epsilon}{q}\psi\right) = 0, \tag{2.20}$$

where $\tilde{\Psi} \equiv \left(\dfrac{\mathrm{d}\log f_0(q)}{\mathrm{d}\log q}\right)^{-1}\Psi$.

The standard treatment is then to expand $\tilde{\Psi}$ in Legendre polynomials,

$$\tilde{\Psi} = \sum_\ell (-\mathrm{i})^\ell\tilde{\Psi}_\ell\,P_\ell(\alpha), \tag{2.21}$$

where $P_\ell(\alpha)$ is the Legendre polynomial of order ℓ. By plugging this expansion into

the Boltzmann equation (2.20), one obtains the Boltzmann hierarchy,

$$\partial_\eta \tilde{\Psi}_0(\eta,q) = -\frac{qk}{3a\epsilon}\tilde{\Psi}_1(\eta,q) - \partial_\eta\phi(\eta) \tag{2.22}$$

$$\partial_\eta \tilde{\Psi}_1(\eta,q) = \frac{qk}{a\epsilon}\left(\tilde{\Psi}_0(\eta,q) - \frac{2}{5}\tilde{\Psi}_2(\eta,q)\right) - \frac{a\epsilon k}{q}\psi(\eta), \tag{2.23}$$

$$\partial_\eta \tilde{\Psi}_\ell(\eta,q) = \frac{qk}{a\epsilon}\left[\frac{\ell}{2\ell-1}\tilde{\Psi}_{\ell-1}(\eta,q) - \frac{\ell+1}{2\ell+3}\tilde{\Psi}_{\ell+1}(\eta,q)\right] (\ell \geq 2). \tag{2.24}$$

It should be mentioned that the Boltzmann hierarchy is often written in a slightly different form, obtained by replacing the decomposition (2.21) by $\tilde{\Psi} = \sum_\ell (-\mathrm{i})^\ell (2l+1)\tilde{\Psi}_\ell\, P_\ell(\alpha)$. As highlighted in [111], the interest of the introduction of a factor $(2l+1)$ is that it makes more natural the writing of the harmonic coefficients $\tilde{\Psi}_\ell$'s in terms of spherical Bessel functions when neutrinos free stream. It is useful in particular for the formulation of truncation schemes (see the next section).

It is from the integration of the Boltzmann hierarchy that the relevant physical quantities are computed. Note that this approach is very general. In particular, it applies to photons provided that the Fermi-Dirac distribution is replaced by the Bose-Einstein one. It means that there exists a CMB Boltzmann hierarchy too. Codes dedicated to the numerical integration of such hierarchies are called Boltzmann codes (see below). The Boltzmann approach is very powerful. However, the fact that it is a linear theory is too restrictive to be considered totally satisfactory.

Boltzmann codes

The Boltzmann hierarchy is infinite. It can nevertheless be handled by numerical codes since it is convergent. The first scheme that comes to mind to integrate it numerically consists in finding theoretical arguments to perform a sharp truncation at a given $l_{\rm max}$, i.e. to set a $\tilde{\Psi}_{l_{\rm max}}$ brutally to zero. In this context, the multipoles of interest must be i) of a lower order and ii) sufficiently far from $\tilde{\Psi}_{l_{\rm max}}$ in the hierarchy for their evolution not to be impacted by the truncation. In practice, the only multipoles whose integration over phase-space momenta gives macroscopic quantities useful for cosmology correspond to $l = 0, 1, 2$. They allow to compute respectively the linear density perturbation ${\rho_\nu}^{(1)}$, velocity divergence ${\theta_\nu}^{(1)}$ and shear stress ${\sigma_\nu}^{(1)}$:

$$\rho_\nu{}^{(1)}(\eta) = 4\pi \int q^2 \mathrm{d}q \frac{\epsilon f_0(q)}{a^3} \frac{\mathrm{d}\log f_0(q)}{\mathrm{d}\log q} \tilde{\Psi}_0(\eta, q), \tag{2.25}$$

$$(\rho_\nu{}^{(0)} + P_\nu{}^{(0)})\theta_\nu{}^{(1)}(\eta) = \frac{4\pi}{3} \int q^2 \mathrm{d}q \frac{\epsilon f_0(q)}{a^3} \frac{\mathrm{d}\log f_0(q)}{\mathrm{d}\log q} \frac{q}{a\epsilon} \tilde{\Psi}_1(\eta, q), \tag{2.26}$$

$$(\rho_\nu{}^{(0)} + P_\nu{}^{(0)})\sigma_\nu{}^{(1)}(\eta) = \frac{8\pi}{15} \int q^2 \mathrm{d}q \frac{\epsilon f_0(q)}{a^3} \frac{\mathrm{d}\log f_0(q)}{\mathrm{d}\log q} \frac{q^2}{a^2\epsilon^2} \tilde{\Psi}_2(\eta, q), \tag{2.27}$$

where superscripts $^{(0)}$ denote background quantities and P stands for pressure. As explained in [104], the "sharp truncation method" has proven to be accurate when l_{max} is sufficiently large. The problem is that, despite the truncation, the number of equations that one needs to integrate is huge. Indeed, l_{max} must be chosen well above[19] 2 and the hierarchy is coupled to other equations describing baryons and dark matter. Moreover, each calculation should be performed for a large number of wavenumbers and, in the case of neutrinos, several momenta. In practice, the resulting numerical cost is prohibitive.

A more subtle procedure is proposed in [111]. The authors show in particular that, for free-streaming species, the harmonic coefficients of the Boltzmann hierarchy are easily expressible in terms of the spherical Bessel functions (especially when a factor $(2l + 1)$ has previously been introduced in the harmonic decomposition (2.21)). Recurrence relations can thus be used to relate $\tilde{\Psi}_{l+1}$ to $\tilde{\Psi}_l$ and $\tilde{\Psi}_{l-1}$, which allows to control the impact of a truncation down to $l_{\mathrm{max}} - 2$. In usual Boltzmann codes, it is this strategy that is adopted. In this framework, experience shows that choosing $l_{\mathrm{max}} \sim 10$ has very little impact on the three first multipoles. Typically, depending on the desired level of precision, l_{max} is at most 20 in usual codes. For instance, in the numerical tests performed in the study that I will present in chapter 4, we truncated the Boltzmann hierarchy at $l_{\mathrm{max}} = 6$.

The main reference Boltzmann codes are `CMBFAST` ([162]), `CAMB` ([107]), `CMBEASY` ([55]) and `CLASS` ([28]). Note that, for codes which include massive neutrinos, it is the integration of massive neutrino equations that is the most time-consuming part because of the need to sum over momenta (see [106] for the presentation of a method, called quadrature approach, allowing to keep the number of momenta reasonable).

[19] In [104], the authors give $k\eta_{\mathrm{nr}}$ as typical value of l_{max} for massive neutrinos, η_{nr} being the conformal time at the non-relativistic transition.

Modeling the nonlinear evolution of neutrinos

So far, most descriptions of the nonlinear evolution of neutrinos rely on N-body simulations. One can find a presentation of the algorithms at play in such simulations in [104]. In this context, one of the most powerful code is the one called `GADGET` ([170]).

Interestingly, the numerical works [29, 186, 23, 88, 189] conclude that, in the nonlinear regime, the steplike suppression induced by massive neutrinos on the matter power spectrum is replaced by a "spoon-shaped" suppression, see figure 2.6. Since the total matter density is fixed in figure 2.6, it is not surprising that non-zero neutrino masses induce an extra suppression of the nonlinear matter power spectrum. Indeed, in that case, the density perturbations of cold dark matter evolve more gently, which postpones the nonlinear clustering that enhances the matter power spectrum. Upcoming large-scale surveys should exhibit features of this subtle scale dependence of the suppression of the matter power spectrum.

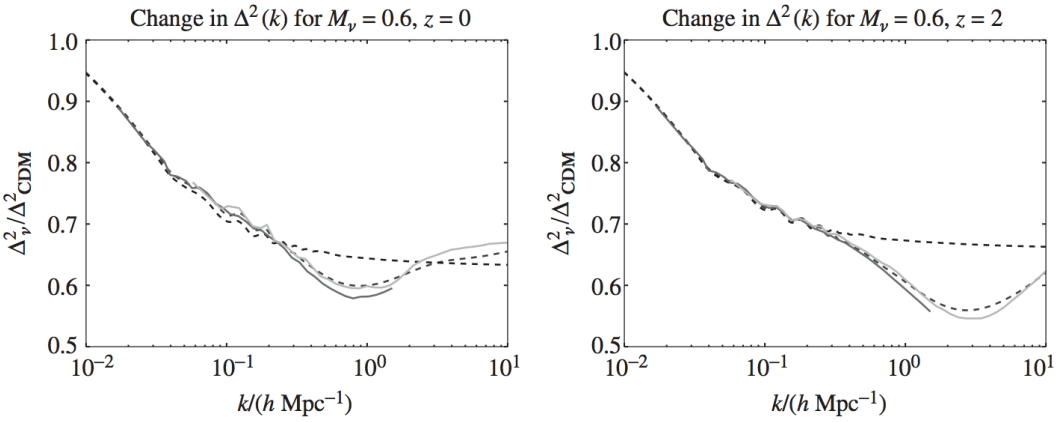

Figure 2.6: Spoon-shaped suppression of the matter power spectrum due to neutrino masses. The solid lines show the power spectrum of a standard model with three massive species of total mass $M_\nu = 0.6$ eV, divided by that of a massless model with the same parameters $(\Omega_{\rm m}, \omega_{\rm m})$. Baryons have been neglected in these simulations. In each plot, the two solid lines correspond to two different N-body simulations with different resolution scales. The step-shaped dashed line shows the linear predictions whereas the spoon-shaped dashed curve represents the nonlinear prediction accounting for massive neutrino effects. Authors: Bird *et al.*, [23].

Such results, obtained from N-body simulations, are reliable and very enlight-

ening. However, the successes of numerical cosmology do not exclude the need for analytic models, in particular to avoid heavy calculations and to be able to explore a wider variety of cosmological parameters and scales. Note that the recent theoretical study [27] manages to explicitly predict an extra suppression of the matter power spectrum due to nonlinearities thanks to nonlinear cosmological perturbation theory.

Still on the analytic side, a natural idea is to extend the Boltzmann hierarchy to the nonlinear regime. It has been done in [184], in which the moments of f,

$$A^{ij...k} \equiv \int \mathrm{d}^3\mathbf{q} \left[\frac{q^i}{a\epsilon}\frac{q^j}{a\epsilon}...\frac{q^k}{a\epsilon}\right]\frac{\epsilon f}{a^3}, \tag{2.28}$$

are studied without performing any linearization. In the conformal Newtonian gauge (2.18), the nonlinear hierarchy resulting from the collisionless Boltzmann equation is

$$\begin{aligned}
&\partial_\eta A^{i_1...i_n} + (\mathcal{H} - \partial_\eta\phi)\left[(n+3)A^{i_1...i_n} - (n-1)A^{i_1...i_njj}\right] \\
&+\sum_{m=1}^{n}(\partial_{i_m}\psi)A^{i_1...i_{m-1}i_{m+1}...i_n} + \sum_{m=1}^{n}(\partial_{i_m}\phi)A^{i_1...i_{m-1}i_{m+1}...i_njj} \\
&+(1+\phi+\psi)\partial_j A^{i_1...i_nj} + \left[(2-n)\partial_j\psi - (2+n)\partial_j\phi\right]A^{i_1...i_nj} = 0.
\end{aligned} \tag{2.29}$$

For physical interpretation, a non-trivial mapping between the $A^{ij...k}$'s and the Ψ_l's is provided in [184]:

$$A = 4\pi\int q^2\mathrm{d}q\frac{\epsilon f_0}{a^3}(1+\Psi_0), \tag{2.30}$$

$$A^{ii} = 4\pi\int q^2\mathrm{d}q\frac{q^2}{a^2\epsilon^2}\frac{\epsilon f_0}{a^3}(1+\Psi_0), \tag{2.31}$$

$$ik_iA^i = \frac{4\pi}{3}\int q^2\mathrm{d}q\frac{q}{a\epsilon}\frac{\epsilon f_0}{a^3}\Psi_1, \tag{2.32}$$

$$\left[\frac{1}{3}k^2\delta_ij + (ik_i)(ik_j)\right]A^{ij} = k^2\frac{8\pi}{15}\int q^2\mathrm{d}q\frac{q^2}{a^2\epsilon^2}\frac{\epsilon f_0}{a^3}\Psi_2, \tag{2.33}$$

$$\left[\frac{1}{3}k^2\delta_ij + (ik_i)(ik_j)\right]A^{ijkk} = k^2\frac{8\pi}{15}\int q^2\mathrm{d}q\frac{q^4}{a^4\epsilon^4}\frac{\epsilon f_0}{a^3}\Psi_2, \tag{2.34}$$

$$\left[\frac{1}{3}k^2\delta_ij + (ik_i)(ik_j)\right](ik_k)A^{ijk} = -k^3\frac{16\pi}{45}\int q^2\mathrm{d}q\frac{q^3}{a^3\epsilon^3}\frac{\epsilon f_0}{a^3}\Psi_1... \tag{2.35}$$

One can see in particular from (2.25) that $A = \rho_\nu$, from (2.26) that $ik_i A^i = ({\rho_\nu}^{(0)} + {P_\nu}^{(0)})\theta_\nu$ and from (2.27) that $\left[\frac{1}{3}k^2\delta_i j + (ik_i)(ik_j)\right] A^{ij} = k^2\left[{\rho_\nu}^{(0)} + {P_\nu}^{(0)}\right]\sigma_\nu$. Besides, A^{ii} is nothing but three times the pressure. Unfortunately, the fact that the nonlinear hierarchy (2.29) is multi-dimensional makes its numerical integration cumbersome, especially because developing a satisfying truncation scheme is extremely difficult.

Independently on this attempt, and as will be explained in chapter 3, there exist robust analytic approaches that study the behavior of the nonlinear power spectrum. Originally, neutrinos were not included in such works. Then some extensions have been proposed to account for a neutrino component (see in particular [198, 154, 105]). The limitation is that massive neutrinos are treated at the linear level in those studies, which are furthermore valid in a very small range of scales (up to $k \sim 0.2h/\mathrm{Mpc}$ for $z > 2$ and $k \sim 0.15h/\mathrm{Mpc}$ for $z = 1$). Some recent improvements will also be presented in chapter 3. One can cite in particular the studies [27] and [81].

Chapter 3

Refining perturbation theory to refine the description of the growth of structure

I included a glimpse of neutrino cosmology in my manuscript because, to understand the interest of my work, one has to be aware of the crucial role played by neutrino cosmology in precision cosmology. However, studying neutrino phenomenology was not the objective of my thesis. My everyday task consisted rather in very general thoughts regarding cosmological perturbation theory beyond the linear regime and beyond the Newtonian approximation. The link with neutrinos is that such considerations suit perfectly for the study of the impact of neutrinos on the nonlinear matter power spectrum. In this chapter, I introduce all the tools of nonlinear cosmological perturbation theory that I used in the studies presented in the three following chapters.

Since physical conditions evolve drastically over the cosmological eras, the simplifying hypotheses that can be formulated in the models evolve accordingly. Some stages of the history of the universe are thus more difficult to describe than others. In particular, modeling analytically the late-time evolution of perturbations (during which the large-scale structure emerges) is very challenging. In this context, numerical cosmology is very helpful. Indeed, advanced numerical simulations such as the `Horizon-AGN` simulation ([56]) or the `Millennium` simulation ([171]) provide insightful pictures of the construction of the cosmic web.

On the theoretical side, important advances have been realized since the 2000s.

The initiating element has been standard perturbation theory then several refinements have followed. A review of standard perturbation theory is given in [13] and an outline of the subsequent developments can be found in [12]. In this chapter, I introduce the concepts of perturbation theory on which I based my work on neutrinos. The approach that I present in the next chapters is indeed a relativistic extension of the standard formalism, which had originally been designed to describe the emergence of gravitational instabilities in the cold dark matter component.

3.1 A brief presentation of cosmological perturbation theory

Cosmological perturbation theory is based on the observation that, on very large scales, the universe is quasi-homogeneous. More precisely, maps obtained by probing all the directions of the sky exhibit relative spatial fluctuations in the order of 10^{-5}. This is certified by the CMB temperature maps obtained by the Planck satellite, as illustrated in figure 3.1. Consequently, strictly speaking, the geometry of the universe can not be characterized by the Friedmann-Lemaître metric (1.8), even on large scales. However, it seems reasonable to assume that, on appropriate scales, the real metric differs little from the homogeneous and isotropic one. This is the reason why cosmologists usually consider perturbed Friedmann-Lemaître metrics, that is to say metrics in which inhomogeneous quantities, assumed to be small compared with the background values, have been introduced (see the pioneer work [108], reviewed in [109, 193, 126, 101, 123, 63] and standardly used since then). A generic form of a perturbed Friedmann-Lemaître metric is

$$\mathrm{d}s^2 = a^2(\eta)\left[-\left(1+2A\right)\mathrm{d}\eta^2 + 2B_i\mathrm{d}x^i\mathrm{d}\eta + \left(\gamma_{ij}+h_{ij}\right)\mathrm{d}x^i\mathrm{d}x^j\right], \tag{3.1}$$

where the metric perturbations are A, B_i and h_{ij}.

As expected in general relativity, a given phenomenon can be described by different equations, their forms depending on the point of view adopted. In this context it is the form chosen for the metric perturbations, usually called choice of gauge, which is determining. The conformal Newtonian gauge, given by (2.18), is an example of gauge widely used in cosmology. It is characterized by the absence of time-space perturbations and by a diagonal space-space perturbation. Many studies have also been carried out using the Synchronous gauge, characterized by

the absence of time-time and time-space perturbations (i.e. by $A = 0$ and $B_i = 0$). The predictions of cosmological perturbation theory in those two gauges have been studied in full detail in [111]. Besides, a presentation of the most common gauges and of the transformations laws allowing to switch from one to another is given in [131]. In cosmology, a particular effort is devoted to the identification of quantities that are gauge-independent (see [6, 60]). Note that the quantities that can be observed, called observables, naturally satisfy this property.

As described by the Einstein equations, such metric perturbations generate density perturbations, which in turn affect the geometry of the spacetime, and so forth. Understanding the time evolution of density perturbations under the influence of gravity in an expanding universe is precisely the purpose of cosmological perturbation theory.

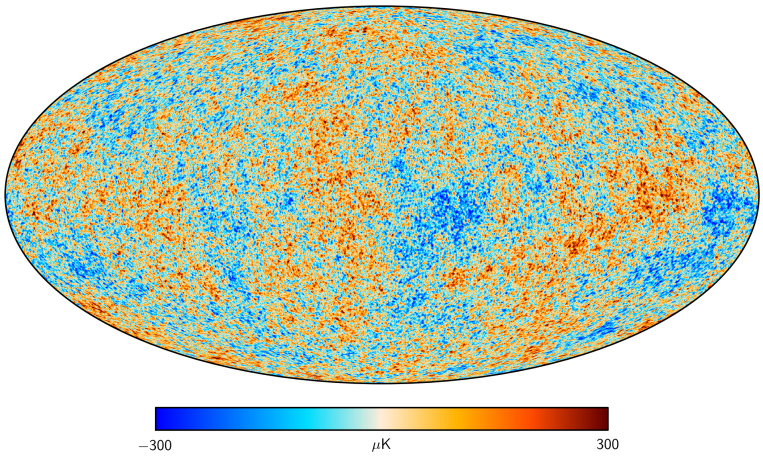

Figure 3.1: CMB temperature map obtained from the SMICA pipeline of the Planck satellite (February 2015). © EUROPEAN SPACE AGENCY - PLANCK COLLABORATION.

3.2 The Vlasov-Poisson system, cornerstone of standard perturbation theory

In standard perturbation theory, the large-scale structures observed in galaxy surveys are interpreted as the result of the clustering of collisionless cold dark matter, represented by a non-relativistic pressureless fluid. The particles of the fluid undergo gravitational interaction only and have a mass m. In this framework, the

starting point of the description is again the Vlasov equation[1]

$$\frac{\partial f}{\partial T} + \frac{\mathrm{d}x^i}{\mathrm{d}T}\frac{\partial f}{\partial x^i} + \frac{\mathrm{d}p_i}{\mathrm{d}T}\frac{\partial f}{\partial p_i} = 0, \tag{3.2}$$

where T denotes here the cosmic time.

Because of the expansion of the universe, a distinction should be made between comoving distances $\vec{x}$ and physical distances $\vec{r} = a(T)\vec{x}$. The same distinction applies to velocities: peculiar velocities $\vec{u}$ must not be confused with physical velocities $\vec{v} = \vec{u} + \vec{v}_{\mathrm{H}}$, where $\vec{v}_{\mathrm{H}}$ is the velocity associated with the Hubble flow[2]. For $\vec{p}$ to be the conjugate momentum of $\vec{x}$ in the Lagrangian describing the dynamics, it has to be defined as

$$\vec{p} = ma\vec{u}. \tag{3.3}$$

Besides, the study is much simplified by the fact that cold species can be studied in the Newtonian approximation. In this context, it is straightforward to notice that

$$\frac{\mathrm{d}\vec{x}}{\mathrm{d}T} = \frac{\vec{p}}{ma^2} \tag{3.4}$$

and

$$\frac{\mathrm{d}\vec{p}}{\mathrm{d}T} = -m\vec{\nabla}\Phi, \tag{3.5}$$

Φ being the gravitational potential.

It is convenient to define macroscopic fields from f and to derive their time evolution from the first moments of the Vlasov equation. Since the phase-space variables have been chosen so that $\mathrm{d}^3\vec{x}\ \mathrm{d}^3\vec{p}\ f$ is the number of particles contained in a phase-space *comoving* unit volume, the density ρ of the cold dark matter fluid, i.e. the total mass contained in a *physical* unit volume, is given by

$$\rho(\vec{x}, T) = \frac{m}{a^3}\int f(\vec{x}, \vec{p}, T)\mathrm{d}^3\vec{p}. \tag{3.6}$$

[1] The Vlasov equation can be applied because two-point interactions are neglected and the number of particles is conserved.

[2] $\vec{u} = a\dfrac{\mathrm{d}\vec{x}}{\mathrm{d}T}$ and $\vec{v} = \vec{u} + \dfrac{\mathrm{d}a}{\mathrm{d}T}\vec{x}$.

The velocity field is defined as the average of the phase-space velocities:

$$u_i(\vec{x},T) = \frac{1}{\int f(\vec{x},\vec{p},T)\mathrm{d}^3\vec{p}} \int \frac{p_i}{ma} f(\vec{x},\vec{p},T)\mathrm{d}^3\vec{p}. \tag{3.7}$$

The velocity dispersion field $\sigma_{ij}(\vec{x},T)$ is defined so that

$$u_i(\vec{x},T)u_j(\vec{x},T) + \sigma_{ij}(\vec{x},T) = \frac{1}{\int f(\vec{x},\vec{p},T)\mathrm{d}^3\vec{p}} \int \frac{p_i}{ma}\frac{p_j}{ma} f(\vec{x},\vec{p},T)\mathrm{d}^3\vec{p}. \tag{3.8}$$

Finally, one introduces the density contrast field $\delta(\vec{x},t)$:

$$\delta(\vec{x},T) = \frac{\rho(\vec{x},T)}{\bar{\rho}} - 1, \tag{3.9}$$

where $\bar{\rho}$ is the spatial average of the density field.

In the Newtonian approximation, the Poisson equation then imposes[3]

$$\Delta\Phi = 4\pi G a^2 \bar{\rho}\delta. \tag{3.10}$$

Equations (3.2) and (3.10) form the Vlasov-Poisson system. They are the basis on which all the calculations of standard perturbation theory rely.

From the Vlasov equation, it is easy to show that the fields previously defined satisfy the continuity and Euler equations[4]

$$\frac{\partial\delta(\vec{x},T)}{\partial T} + \frac{1}{a}\partial_i\left[(1+\delta(\vec{x},T))\, u_i(\vec{x},T)\right] = 0, \tag{3.11}$$

$$\frac{\partial u_i(\vec{x},T)}{\partial T} + \frac{1}{a}\frac{\mathrm{d}a}{\mathrm{d}T}u_i(\vec{x},T) + \frac{1}{a}u_j(\vec{x},T)\partial_j u_i(\vec{x},T) = -\frac{1}{a}\partial_i\Phi(\vec{x},T) - \frac{\partial_j\left[\rho(\vec{x},T)\sigma_{ij}(\vec{x},T)\right]}{a\rho(\vec{x},T)}. \tag{3.12}$$

3.3 The single-flow approximation and its consequences

Cold fluids do not experience much thermal motion. Consequently, in the early stages of gravitational instability, one expects velocity dispersion to be small compared with the velocity gradients induced by density fluctuations. It is only at more

[3] Here, it is assumed that the gravitational effect of other cosmic components is negligible.
[4] The Einstein convention applies in those equations.

advanced stages that velocity dispersion becomes effective. Indeed, gravity guides the different flows in the same direction so there is a time at which they cross. This phenomenon, called shell crossing, is illustrated in figure 3.2.

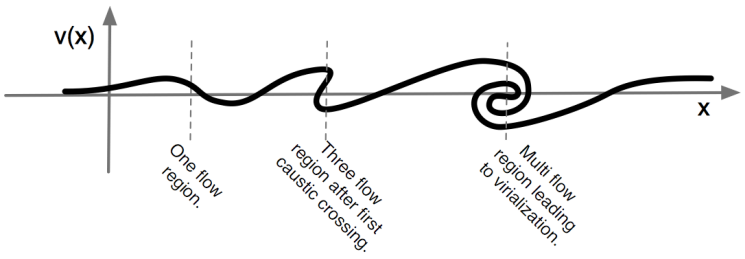

Figure 3.2: Schematic illustration of the emergence of multi-flow regions under the influence of gravity. Distances and velocities are represented as one-dimensional quantities. Author: Bernardeau, [12].

It is during the late phase of virialization that astrophysical objects such as galaxies begin to form (see [22]). Unfortunately, as soon as shell crossing starts, the physical processes at play become very difficult to model analytically (there exist nevertheless attempts of post-shell-crossing modeling, see e.g. [87, 180, 37]). So far, what is known about this epoch relies mostly on N-body simulations.

On the contrary, before shell crossing, analytic developments are possible because velocity dispersion is negligible. More precisely, one can impose $\sigma_{ij} = 0$ in the Euler equation, which makes the second term of the right hand side vanish. This approximation is known as the single-flow approximation. It means that, at given time and position, all the particles of the fluid have the same velocity.

In the single-flow approximation, the Euler equation reads[5]

$$\frac{\mathrm{d}\left[a u_i(\vec{x}, T)\right]}{\mathrm{d}T} = -\partial_i \Phi(\vec{x}, T). \tag{3.13}$$

One can see from this equation that the velocity field $u_i(\vec{x}, T)$ is a gradient (plus possibly a homogeneous function of time). Consequently, no vorticity can appear in the fluid in the absence of shell crossing (see [132, 182, 142] for more details). In this context, the behavior of the velocity field can entirely be described in terms of

[5]For any field $X(\vec{x}, T)$, $\dfrac{\mathrm{d}X}{\mathrm{d}T} = \partial_T X + \partial_i X \partial_T x^i = \partial_T X + \dfrac{1}{a} u^i \partial_i X$.

its divergence $\theta(\vec{x},T)$, defined as

$$\theta(\vec{x},T)=\frac{1}{aH}\partial_i u_i(\vec{x},T). \tag{3.14}$$

This property is very useful. In particular, it allows to rewrite the system of equations on a compact form, much easier to manipulate.

To that aim, it is convenient to move to reciprocal space, to use the conformal time as time variable and to introduce the doublet[6]

$$\Psi_b(\mathbf{k},\eta)\equiv(\delta(\mathbf{k},\eta),-\theta(\mathbf{k},\eta))^{\mathrm{T}}. \tag{3.15}$$

In this framework, after taking the divergence of the Euler equation to make the quantity θ appear[7], the equations of motion can be grouped into a single equation[8] (the convention that repeated Fourier arguments are integrated over applies here),

$$a(\eta)\partial_a\Psi_b(\mathbf{k},\eta)+\Omega_b{}^c(\eta)\Psi_c(\mathbf{k},\eta)=\gamma_b{}^{cd}(\mathbf{k}_1,\mathbf{k}_2)\Psi_c(\mathbf{k}_1,\eta)\Psi_d(\mathbf{k}_2,\eta). \tag{3.16}$$

The left-hand side is linear (i.e. there is no mode coupling at play in it) and the right hand side contains all nonlinear interactions between the fields. Note in particular that those couplings are quadratic without adding any approximation.

The explicit expression of $\Omega_b{}^c(\eta)$ is

$$\Omega_b{}^c(\eta)=\begin{pmatrix}0 & -1\\ -\frac{3}{2}\Omega_{\mathrm{m}} & 1+a\frac{\partial_a\mathcal{H}}{\mathcal{H}}\end{pmatrix}, \tag{3.17}$$

where $\Omega_{\mathrm{m}}=\dfrac{8\pi G\bar{\rho}a^2}{3\mathcal{H}^2}$. Note in particular that this matrix is scale-independent. Besides, the non-zero elements of the symmetrized coupling matrix $\gamma_b{}^{cd}(\mathbf{k}_1,\mathbf{k}_2)$ are given by

$$\gamma_2{}^{22}(\mathbf{k}_1,\mathbf{k}_2)=\delta_{\mathrm{D}}(\mathbf{k}-\mathbf{k}_1-\mathbf{k}_2)\frac{|\mathbf{k}_1+\mathbf{k}_2|^2(\mathbf{k}_1.\mathbf{k}_2)}{2k_1^2k_2^2}, \tag{3.18}$$

[6]The index b is either 1 ($\Psi_1=\delta$) or 2 ($\Psi_2=-\theta$).

[7]Note that, in reciprocal space, $u_i(\mathbf{k},\eta)=-\mathrm{i}\dfrac{aH}{k^2}k_i\theta(\mathbf{k},\eta)$.

[8]By definition, $\partial_a=\dfrac{1}{aH}\partial_T$.

$$\gamma_1{}^{12}(\mathbf{k}_1,\mathbf{k}_2) = \delta_{\mathrm{D}}(\mathbf{k}-\mathbf{k}_1-\mathbf{k}_2)\frac{(\mathbf{k}_1+\mathbf{k}_2).\mathbf{k}_2}{2k_2^2}, \tag{3.19}$$

$$\gamma_1{}^{21}(\mathbf{k}_1,\mathbf{k}_2) = \delta_{\mathrm{D}}(\mathbf{k}-\mathbf{k}_1-\mathbf{k}_2)\frac{(\mathbf{k}_1+\mathbf{k}_2).\mathbf{k}_1}{2k_1^2}. \tag{3.20}$$

Note that, in this approach, this matrix does not depend on time.

The compact equation presents the benefit of making possible the writing of a formal solution:

$$\Psi_b(\mathbf{k},\eta) = g_b{}^c(\eta)\Psi_c(\mathbf{k},\eta_0) + \int_{\eta_0}^{\eta} \mathrm{d}\eta' g_b{}^c(\eta,\eta')\gamma_c{}^{de}(\mathbf{k}_1,\mathbf{k}_2)\Psi_d(\mathbf{k}_1,\eta')\Psi_e(\mathbf{k}_2,\eta'), \tag{3.21}$$

η_0 being the initial time and $g_b{}^c$ the Green function of the equation (3.16) (see the reference articles [159, 160, 45]). The first term of the right hand side of (3.21) is the linear solution, i.e. the solution of the linear equation

$$a(\eta)\partial_a\Psi_b(\mathbf{k},\eta) + \Omega_b{}^c(\eta)\Psi_c(\mathbf{k},\eta) = 0. \tag{3.22}$$

Studying the properties of this linear limit is not problematic in standard perturbation theory (see [13]). However, dealing with the nonlinear terms is more challenging. Several approaches aiming at going beyond the linear regime have nevertheless been proposed in order to gain accuracy.

3.4 Perturbation theory at NLO and NNLO

In nonlinear perturbation theory, many achievements rely on the use of diagrammatic representations. Indeed, the form of the solution (3.21) quite naturally incites one to describe couplings in terms of diagrams (analogs of the Feynman diagrams of quantum field theory). As can be seen clearly in (3.21), the time evolution of a given field $\Psi_b(\mathbf{k},\eta)$ is determined by the initial values of all fields. The statistical quantities that are relevant for cosmology are thus the correlation functions involving those initial (Gaussian) fields. The simplest one is of course the one involving only two fields, i.e. the linear power spectrum

$$\langle\Psi_a(\mathbf{k},\eta)\Psi_b(\mathbf{k}',\eta)\rangle = P_{ab}(\mathbf{k},\eta)\delta_{\mathrm{D}}(\mathbf{k}+\mathbf{k}'). \tag{3.23}$$

Its diagrammatic representation is in accordance with it, simple and linear. This level of description is called tree-level.

Obviously, one can increase accuracy by increasing the number of contributing initial fields taken into account. Diagrammatically, it simply means adding loops in linear diagrams, those loops symbolizing pair associations[9]. Indeed, one can introduce l-order power spectra $P_{ab}^{(l)}$ (l being also the number of loops) so that

$$P_{ab}(\mathbf{k},\eta) = \sum_{l=0}^{\infty} P_{ab}^{(l)}(\mathbf{k},\eta), \tag{3.24}$$

with

$$\delta_{\mathrm{D}}(\mathbf{k}+\mathbf{k}')P_{ab}^{(l)}(\mathbf{k},\eta) = \sum_{m=1}^{2l+1} \langle \Psi_a^{(m)}(\mathbf{k},\eta)\Psi_b^{(2l+2-m)}(\mathbf{k}',\eta)\rangle. \tag{3.25}$$

The exponents in brackets are the numbers of interacting modes $\mathbf{k}_1$, $\mathbf{k}_2$, ... (satisfying $\mathbf{k} = \mathbf{k}_1 + \mathbf{k}_2 + ...$) taken into account in $\Psi_a^{(\ )}(\mathbf{k},\eta)$.

Usually, one-loop corrections are called next-to-leading-order (NLO) corrections and two-loop corrections are called next-to-next-to-leading-order (NNLO) corrections. The first calculations of loop corrections were performed in the nineties ([112, 97, 161]). More recent studies allow to reach the two-loop level ([15, 177]) or even the three-loop level ([26]).

I do not present in more detail the associated formalism because it would be cumbersome and not particularly helpful to understand the work I did as a PhD student. Indeed, I did not directly use diagrammatic representations and renormalization techniques. Besides, all the needed information can be found in very detailed references. The two leading methods that make a fruitful use of diagrammatic representations thanks to renormalization group techniques are [45][10] and [117]. A particular formulation of such developments is the so-called time-flow equation approach ([133]). Several improvements of such approaches have been achieved since then. One can cite e.g. the MPT`BREEZE` ([46]) or RegPT ([177]) approaches. Such enhancements of standard perturbation theory involving resummation techniques are necessary because the expansion of standard perturbation theory, order by order, is not convergent (see [15] and [26]).

[9] Again, only pair associations matter in virtue of Wick's theorem. See section 2.2.2.

[10] This reference also explains in detail the procedure to be followed to draw diagrams and to interpret them.

What is important here is rather to stress on the fact that all those developments, which are the cornerstones of the understanding of the nonlinear growth of structure, rely on the equation (3.16). For this reason, when starting my work on neutrinos, it was precisely in the relativistic generalization of this equation that I was interested. Succeeding in it would indeed mean that, in the long term, one could hope for comparable predictions without the need to restrict the studied cosmic fluid to cold dark matter.

3.5 Eikonal approximation and invariance properties

In the standard case of a cold pressureless fluid, a strategy has been developed to better understand how couplings between modes of very different wavelengths contribute to the nonlinear growth of structure. This strategy relies on the eikonal approximation, which in this context can be associated with the invariance properties of the equation of motion (3.16). I will briefly present the principle of the reasoning in this section. Then it will be convenient to expose in the next chapters the way in which I started to extend those results to relativistic flows. Full details concerning the standard approach are to be found in [14] and [16]. Besides, the role of the so-called extended Galilean invariance is examined carefully in [25, 127, 100, 44, 43, 42].

3.5.1 Eikonal approximation

The notion of eikonal approximation intervenes in various fields of theoretical physics. The way it is used in cosmology is very similar to the method described in the quantum electrodynamics paper [1], i.e. highlighting the impact of given modes (in the QED case, those of soft photons) on the propagation of other modes (in the QED case, those of electrons).

The starting point to apply the eikonal approximation to the equation of motion (3.16) is the fact that the amplitudes of the coupling terms (3.18), (3.19) and (3.20) vary a lot with the wavenumber ratio $\frac{k_1}{k_2}$. Hence, it is convenient to split the right hand side of equation (3.16) into two integration domains. The hard domain (characterized in the following by an index $\mathcal{H}$) contains all modes whose wavelengths are of the same order and the soft domain (characterized in the following by an index $\mathcal{S}$) encompasses modes of very different wavelengths.

Assuming that the soft domain is obtained for $k_2 \ll k_1$, $\mathbf{k}_1 \approx \mathbf{k}$ so that the contribution corresponding to the soft domain appears simply as a corrective term in the linear equation of motion of the mode $\mathbf{k}$, (3.22). Indeed, in this context, equation (3.16) can be rewritten

$$a\partial_a \Psi_b(\mathbf{k},\eta) + \Omega_b{}^c(\eta)\Psi_c(\mathbf{k},\eta) - \Xi_b{}^c(\mathbf{k},\eta)\Psi_c(\mathbf{k},\eta) = \Big[\gamma_b{}^{cd}(\mathbf{k}_1,\mathbf{k}_2)\ \Psi_c(\mathbf{k}_1,\eta)\ \Psi_d(\mathbf{k}_2,\eta)\Big]_{\mathcal{H}}, \quad (3.26)$$

with

$$\Xi_b{}^c(\mathbf{k},\eta) \equiv 2\int_{\mathcal{S}} \mathrm{d}^3\mathbf{q}\ {}^{\text{eik.}}\gamma_b{}^{cd}(\mathbf{k},\mathbf{q})\Psi_d(\mathbf{q},\eta)\ . \quad (3.27)$$

The soft momenta q (i.e. $q \ll k$) at play in equation (3.27) being integrated over, $\Xi_b{}^c(\mathbf{k},\eta)$ is a mere field, not a coupling matrix. When the contribution of the hard domain is negligible, the equation of motion reads

$$a\partial_a \Psi_b(\mathbf{k},\eta) + \Omega_b{}^c(\eta)\Psi_c(\mathbf{k},\eta) - \Xi_b{}^c(\mathbf{k},\eta)\Psi_c(\mathbf{k},\eta) = 0. \quad (3.28)$$

It can be interpreted as the equation of motion of the mode $\mathbf{k}$ evolving in a medium perturbed by large-scale modes. It is particularly interesting for cosmologists because it is much simpler than the full equation while encoding the way in which long-wave modes alter the growth of structure.

In the eikonal limit (i.e. when $k_2 \ll k_1$), $\mathbf{k}_1 \approx \mathbf{k}$ and $\mathbf{k}_2 \approx \mathbf{q}$ so the predominant elements of the coupling matrix are

$${\gamma_2}^{22}(\mathbf{k},\mathbf{q}) = {\gamma_1}^{12}(\mathbf{k},\mathbf{q}) \approx \frac{\mathbf{k}.\mathbf{q}}{2q^2}. \quad (3.29)$$

One neglects ${\gamma_1}^{21}(\mathbf{k},\mathbf{q})$ because

$${\gamma_1}^{21}(\mathbf{k},\mathbf{q}) \approx \frac{1}{2} \ll \frac{\mathbf{k}.\mathbf{q}}{2q^2}. \quad (3.30)$$

In this context, the NLO correction $\Xi_b{}^c(\mathbf{k},\eta)$ simply reads

$$\Xi_b{}^c(\mathbf{k},\eta) \equiv -\delta_b{}^c \int_{\mathcal{S}} \mathrm{d}^3\mathbf{q}\ \frac{\mathbf{k}.\mathbf{q}}{q^2}\theta(\mathbf{q},\eta) = \delta_b{}^c\ \Xi(\mathbf{k},\eta). \quad (3.31)$$

Note in particular that it does not directly depend on the density contrast field

$\delta(\mathbf{k},\eta)$. Besides, it is a purely imaginary quantity because the velocity divergence is real and $\theta(\mathbf{q},\eta)=\theta^*(-\mathbf{q},\eta)$ implies $\Xi_b{}^c(\mathbf{k},\eta)=-\Xi_b{}^{c*}(-\mathbf{k},\eta)$.

The advantage of the equation of motion (3.28) is that it can easily be solved. Indeed, its Green functions $\xi_a{}^b(\mathbf{k},\eta,\eta_0)$ are related to the Green functions $g_a{}^b(\eta,\eta_0)$ of the zeroth order equation (3.22) simply by

$$\xi_b{}^c(\mathbf{k},\eta,\eta_0)=g_b{}^c(\eta,\eta_0)\exp\left[\int_{\eta_0}^{\eta}\mathrm{d}\eta'\Xi(\mathbf{k},\eta')\right]. \tag{3.32}$$

Given the definition (3.31), the time integration of $\Xi(\mathbf{k},\eta)$ is nothing but a displacement $\mathbf{d}$ projected along the direction $\mathbf{k}$,

$$\xi_b{}^c(\mathbf{k},\eta,\eta')=g_b{}^c(\eta,\eta')\exp\left[\mathrm{i}\mathbf{k}.\mathbf{d}(\eta,\eta')\right]. \tag{3.33}$$

More precisely, the quantity $\mathbf{d}(\eta,\eta')$ should be interpreted as the total displacement induced by the long-wave modes between times η and η'. Expression (3.33) shows that the only impact of long-wave modes is to shift the phase of the propagator of the background equation.

Renormalized perturbation theory comes into play when one decides to construct nonlinear propagators associated with the general nonlinear equation of motion (3.16). Such propagators, denoted $G_b{}^c$, are defined so that

$$G_b{}^c(k,\eta)\delta_{\mathrm{D}}(\mathbf{k}-\mathbf{k}')\equiv\left\langle\frac{\Psi_b(\mathbf{k},\eta)-\Psi_b^{(0)}(\mathbf{k},\eta)}{\Psi_c(\mathbf{k}',\eta_0)-\Psi_c^{(0)}(\mathbf{k}',\eta_0)}\right\rangle. \tag{3.34}$$

They must in particular take into account the perturbations induced by the soft domain, that is to say that one needs to compute (among others) the quantities

$$\left\langle\xi_b{}^c(\mathbf{k},\eta,\eta')\right\rangle=g_b{}^c(\eta,\eta')\exp\left[-\frac{1}{2}k^2\sigma_{\mathrm{d}}^2(\eta,\eta')\right], \tag{3.35}$$

with $\sigma_{\mathrm{d}}^2(\eta,\eta')=\frac{1}{3}\left\langle\mathbf{d}^2(\eta,\eta')\right\rangle$. The idea developed in [45] is that, in diagrammatic representation, one-loop contributions to nonlinear propagators (then called renormalized propagators) can be divided into sub-diagrams, whose resummations are connectable to physical quantities. For instance, the authors showed that

$$\sigma_{\mathrm{d}}^2(\eta,\eta')=\left(e^{\eta}-e^{\eta'}\right)^2\int\mathrm{d}^3\mathbf{q}\frac{1}{3q^2}P^{\mathrm{lin}}(q), \tag{3.36}$$

where P^{lin} is the two-point correlation function of initial linear fields. This key

result is the starting point of the computation of resummed propagators at NLO (see [45] for the "RPT method", [46] for the "MPTBREEZE method" and [177] for the "RegPT method"). In this context, perturbative expansions of the nonlinear power spectrum contain renormalized propagators plus terms describing mode couplings.

Interestingly (and independently on renormalized perturbation theory), one can show that introducing an eikonal correction in the linear equation of motion has no impact on the power spectra, provided that they involve fields evaluated at the same time. The reason is that the different phase shifts appearing in the corrected propagators (3.33) exactly cancel each other out. We will see now that it is directly related to the invariance properties of the equations of motion.

3.5.2 Invariance properties

It is easy to check that, in the single-flow approximation, the system of equations (3.11)-(3.12) is invariant under the change of coordinates (written here in terms of conformal time)

$$\begin{aligned}
\tilde{x}^i &= x^i + D_i(\eta), \\
\tilde{\eta} &= \eta, \\
\tilde{\delta} &= \delta, \\
\tilde{u}_i &= u_i + \frac{\mathrm{d}D_i(\eta)}{\mathrm{d}\eta}, \\
\tilde{\Phi} &= \Phi - \frac{1}{a}\frac{\mathrm{d}a}{\mathrm{d}\eta}\frac{\mathrm{d}D_i(\eta)}{\mathrm{d}\eta}x^i - \frac{\mathrm{d}^2 D_i(\eta)}{\mathrm{d}\eta^2}x^i,
\end{aligned} \tag{3.37}$$

where $D_i(\eta)$ is an arbitrarily time-dependent uniform field. The relative motion between the two frames depending on time, this invariance is sometimes called *extended* Galilean invariance. As shown in [44], it actually derives from the equivalence principle. It is a powerful property since it states that any acceleration of a given area of the universe does not affect the development of gravitational instabilities in it.

The striking point is that such a change of frame affects the linear propagator precisely in the same way as the eikonal correction $\Xi_b{}^c(\mathbf{k}, \eta)$ does. Indeed, according

to (2.8), transformations (3.37) impose

$$\tilde{g}_b{}^c(\tilde{\eta},\tilde{\eta}') = g_b{}^c(\eta,\eta')\exp\{-\mathrm{i}\mathbf{k}.\left[\mathbf{D}(\eta)-\mathbf{D}(\eta')\right]\}. \tag{3.38}$$

So the displacement D_i at play in the transformations (3.37) can be related to the eikonal displacement d_i in such a way that

$$\tilde{g}_b{}^c(\tilde{\eta},\tilde{\eta}') = g_b{}^c(\eta,\eta')\exp\left[\mathrm{i}\mathbf{k}.\mathbf{d}(\eta,\eta')\right]. \tag{3.39}$$

In other words, the perturbation of the linear propagator generated by long-wave modes, (3.33), can be wiped out by a mere change of coordinates. It explains why equal-time statistical quantities such as power spectra are not sensitive to $\Xi_b{}^c(\mathbf{k},\eta)$.

Regarding unequal-time correlation functions, it is possible to derive consistency relations involving them. We have seen that velocity divergences (or equivalently density contrasts according to the continuity equation (3.11)) involving soft modes perturb the medium by generating displacement fields in the form

$$\mathbf{d}(\eta,\eta') = \mathrm{i}\int \mathrm{d}^3\mathbf{q}\frac{1}{q^2}\mathbf{q}\int_{\eta'}^{\eta}\mathrm{d}\eta''\ \theta(\mathbf{q},\eta''). \tag{3.40}$$

Hence, taking the effect of a soft mode $\mathbf{q}$ into account is equivalent to considering that all other modes evolve in a perturbed medium, the perturbed fields being here nothing but the original fields transformed according to (3.37):

$$\langle\delta(\mathbf{x}_1,\eta_1)...\delta(\mathbf{x}_n,\eta_n)\rangle_{\text{p.m.}} = \left\langle\tilde{\delta}(\tilde{\mathbf{x}}_1,\tilde{\eta}_1)...\tilde{\delta}(\tilde{\mathbf{x}}_n,\tilde{\eta}_n)\right\rangle_{\text{u.m.}}, \tag{3.41}$$

where "p.m." stands for "perturbed medium" and "u.m." for "unperturbed medium". In reciprocal space, to compute a correlation function involving a field evaluated at $\mathbf{q}$, one can therefore compute the correlation function of all other fields (in the perturbed medium) and then correlate it with the disturber field:

$$\langle\delta(\mathbf{q},\eta)\delta(\mathbf{k}_1,\eta_1)...\delta(\mathbf{k}_n,\eta_n)\rangle_{q\to 0,\ \text{u.m.}} = \left\langle\delta(\mathbf{q},\eta)\,\langle\delta(\mathbf{k}_1,\eta_1)...\delta(\mathbf{k}_n,\eta_n)\rangle_{\text{p.m.}}\right\rangle_{\text{u.m.}}. \tag{3.42}$$

In general, the form of the consistency relations (also called Ward identities) that can be derived from such considerations depends on the assumptions made to express the perturbed density contrasts. Examples can be found in [100]. In the case of perturbations corresponding to "extended Galilean" transformations (3.37), one

finds as a first approximation for the three-point correlator

$$\begin{aligned}&\langle\delta(\mathbf{q},\eta)\delta(\mathbf{k}_1,\eta_1)\delta(\mathbf{k}_2,\eta_2)\rangle_{q\to 0} \\ &\quad = -\frac{\mathbf{q}.(\mathbf{k}_1+\mathbf{k}_2)}{q^2}P^{\rm lin}(q;\eta)\,\langle\delta(\mathbf{k}_1,\eta_1)\delta(\mathbf{k}_2,\eta_2)\rangle\left(e^{\eta_1-\eta}-e^{\eta_2-\eta}\right),\end{aligned} \tag{3.43}$$

where $P^{\rm lin}(q;\eta)$ is the linear power spectrum defined in (3.23).

Note that, at equal times, $\langle\delta(\mathbf{k}_1,\eta_1)\delta(\mathbf{k}_2,\eta_1)\rangle \propto \delta_{\rm D}(\mathbf{k}_1+\mathbf{k}_2)$ so that the right-hand side of (5.29) is zero. In theory, consistency relations such as (5.29) are particularly interesting because they allow to gain one order in the knowledge of correlation functions. However, the fact that it involves unequal-time correlators only makes the measurement of such observables very challenging.

3.6 Perturbation theory applied to the study of massive neutrinos

The formalism described in the previous sections is valid only for cold fluids in which the velocity dispersion is negligible. It is tempting to extend it to other species than cold dark matter. For instance, multi-fluid approaches involving cold dark matter and baryons ([169, 17]) or dark energy ([155, 49, 3]) have been realized. Including neutrinos is challenging because it is a hot species so neglecting velocity dispersion would not be realistic. Other simplifying assumptions are thus necessary.

In [153, 198, 105, 181], mixtures of baryons, cold dark matter and massive neutrinos are considered at NLO but neutrino perturbations (whose effect is assumed to be particularly small) are kept at linear order. In [164, 106, 163], it is the time-dependence of the free-streaming length of neutrinos that is neglected. [27] proposes a hybrid approach: the fluid approach based on the Vlasov-Poisson system is applied at NLO at small redshifts and, at high redshifts, neutrinos are described using the linear Boltzmann hierarchy. Indeed, at small redshifts, a simple expression can be found for the velocity dispersion and the Newtonian approximation holds whereas nonlinearities can be neglected at high redshifts. Note that [81] also recommends the use of hybrid approaches. Besides, it warns against the use of approximation schemes, invoking the emergence of spurious behaviors due to unrealistic assumptions.

The work that I present in the next chapters is based on the idea that considering neutrinos as a collection of single-flow fluids instead of a single multi-flow fluid could allow one to get rid of velocity dispersion.

Chapter 4

A new way of dealing with the neutrino component in cosmology

We have seen that there exist two standard ways to account for neutrinos in cosmological models. In the one based on the Vlasov-Poisson system, the main difficulty arises from the velocity dispersion term present in the Euler equation. Regarding the Boltzmann approach, it is rather the treatment of nonlinearities that appears challenging. As discussed in section 3.6, considering a hybrid approach that mixes those two methods might be a solution to get a satisfactory description of massive neutrinos beyond the linear regime.

In this thesis, I propose an alternative which consists in decomposing neutrinos into several fluids labeled by their initial velocities and exploiting the nonlinear continuity and Euler equations of each flow. To extend its scope of application, this approach does not rely on the Newtonian approximation.

4.1 Principle of the method

It is clear that the single-flow approximation is decisive in the analytic modeling of the development of inhomogeneities, responsible for the formation of the large-scale structure, in cold pressureless fluids. The idea behind the article presented in section 4.4 is that one can take advantage of the single-flow approximation for a greater variety of species simply by splitting non-cold fluids into collections of flows.

To be more precise, instead of considering a unique neutrino fluid with a continuous phase space, one can discretize the momentum space at initial time and consider N fluids corresponding to the N initial momenta. This is illustrated in figure 4.1 for $N = 11$. Note that initial momenta are characterized not only by a norm but also by a sense and, in multi-dimensional spaces, by a direction. Furthermore, by construction, such a description applies to one mass eigenstate at a time. What makes the decomposition possible is the fact that, after decoupling, neutrinos free-stream. In other words, provided that initial conditions are chosen after neutrino decoupling, no interactions between cosmic fluids need to be taken into account. In the picture, variations of thickness represent fluctuations of density. It should be noticed that, at given positions, densities differ from one fluid to another on this snapshot. It is not surprising since we know that the number of particles will not be the same in each flow (we have seen in section 2.3.2 that phase-space distribution functions depend on p). However, one expects usual global quantities, which depend only on time and position, to be recovered after summing over all the flows (explicit summation formulae are given later in this chapter).

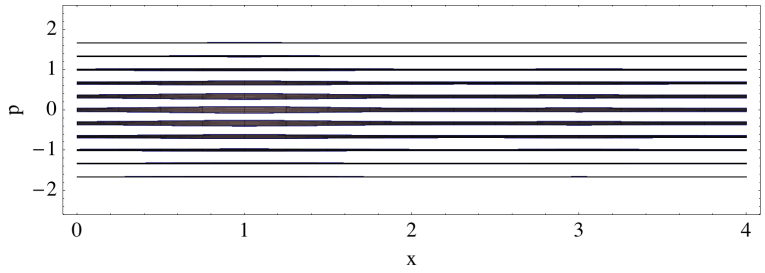

Figure 4.1: Discretized phase space at initial time for a collection of eleven flows. In each flow, momenta are initially homogeneous. Variations of thickness represent fluctuations of density. For simplicity, momenta and positions have been represented as one-dimensional quantities.

Although momenta are initially homogeneous, the unavoidable presence of fluctuations of density makes momentum gradients develop over time in each flow. Note that, for a given mass, flows of neutrinos are all the more sensitive to density fluctuations that the norm of their initial momentum is small because, in that case, they fall easily into potential wells. In particular, a fluid characterized by a zero initial momentum is expected to behave as cold dark matter. The development of spatial variations in momentum space is illustrated in figure 6. Momentum gradients

are located on an inclined axis, characterizing the direction of the initial momenta (which is unique here since it is a one-dimensional representation). In the same way as for the cold dark matter component, one expects multi-flow regions to emerge eventually. It is clear in figure 6 that it will occur much earlier in fluids with low initial velocities. However, before shell crossing starts, it is reasonable to assume that each fluid of neutrinos can be studied in the single-flow approximation. As for cold dark matter, describing shell crossing is beyond the scope of the study. Besides, it is worth noting that shell crossing occurs likely only after neutrinos have become sufficiently slow to be rightly considered as cold species.

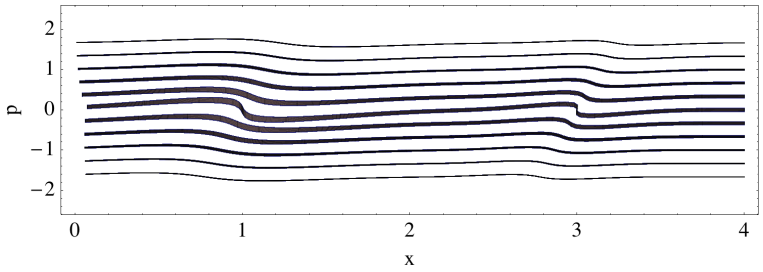

Figure 4.2: Development of momentum gradients in the discretized phase space for a collection of eleven flows. This phenomenon is due to fluctuations of density, represented by variations of thickness.

As already mentioned, in this kind of description, the global behavior of neutrinos should be recovered after summing results over all the single-flow fluids, provided that the number of flows is sufficient for the sample to be representative. Each flow being characterized by an initial momentum that I will denote $\vec{\tau}$, the total phase-space distribution function is given for instance by

$$f^{\mathrm{tot}}(\eta, \mathbf{x}, \mathbf{p}) = \sum_{\vec{\tau}} f_{\vec{\tau}}(\eta, \mathbf{x}, \mathbf{p}) \tag{4.1}$$

or, in the three-dimensional continuous limit,

$$f^{\mathrm{tot}}(\eta, \mathbf{x}, \mathbf{p}) = \int \mathrm{d}^3\tau f_{\vec{\tau}}(\eta, \mathbf{x}, \mathbf{p}), \tag{4.2}$$

where $f_{\vec{\tau}}$ is the phase-space distribution function of the fluid labeled by $\vec{\tau}$.

Symbolically, the choice of labeling fluids by their initial momenta and then deriving equations of motion specific to each of them can be seen as an analog of

the choice of adopting a Lagrangian point of view to describe a flow. The difference is that, in a Lagrangian description, it is the initial position that is used as a label. Conversely, the standard description of neutrinos relying on the study of $f^{\rm tot}(\eta, \mathbf{x}, \mathbf{p})$ is more similar to an Eulerian approach.

4.2 Derivation of the equations of motion

Our first study concerning neutrinos (section 4.4), whose main goal was to test the reliability of the method described above, has been performed in the conformal Newtonian gauge (2.18). General relativity is indeed relevant to capture the effect of neutrino perturbations from the local universe to super-Hubble scales. The gauge has been chosen to facilitate comparison with the Newtonian equations of motion presented in chapter 3. To be in tune with this formalism, we wished to derive nonlinear equations of motion governing the behavior of a density contrast field and of a velocity divergence field. This ambition maintains some freedom regarding the choice of variables. As we will see, the desired equations can be obtained from basic conservation laws. For simplicity, couplings between the metric perturbations ϕ and ψ are neglected throughout the analysis. It is important to have in mind that this action does not prevent one to depict the nonlinear growth of structure. Indeed, couplings involving density contrasts and/or velocity divergences are untouched and it is these nonlinear interactions that are relevant for the modeling of the formation of the large-scale structure of the universe.

4.2.1 Conservation of the number of particles

Once the flows have been defined at initial time, the number of neutrinos contained in each of them is constant. Indeed, only the initial momentum determines the flow to which each neutrino is assigned. The way in which one chooses the number of neutrinos assumed to have a given initial momentum will be discussed in section 4.3.3. Mathematically, the conservation of the number of particles is encoded in the continuity equation. In general relativity, it is given by the conservation of a quantity J^μ called particle four-current[1],

$$J^\mu_{\ ;\mu} = 0. \tag{4.3}$$

[1]I recall that the symbol " ; " stands for the covariant derivative defined in section 1.3.3.

The four-current is the four-dimensional analog of the current density of classical physics, i.e. of a flow rate. It can thus be expressed in terms of a density and a velocity or momentum. Several possibilities concerning the choice of variables are explored in the article presented in section 4.4 and a continuity equation is given for each doublet. With hindsight, the variables that I retain are:

- the comoving number density $n_c(\eta, \mathbf{x})$, defined as the number of particles per comoving unit volume d^3x^i,
- the comoving momentum field[2] $P_i(\eta, \mathbf{x})$.

The latter choice will be argued in section 4.3.1 and definitively justified in chapter 5. In terms of the phase-space distribution function, the comoving number density is given by

$$n_c(\eta, \mathbf{x}) = \int \mathrm{d}^3p_i \; f(\eta, x^i, p_i) \tag{4.4}$$

and $P_i(\eta, \mathbf{x})$ is nothing but the average of the phase-space comoving momenta

$$P_i(\eta, \mathbf{x}) = \frac{\int \mathrm{d}^3p_i \; f(\eta, x^i, p_i) p_i}{\int \mathrm{d}^3p_i \; f(\eta, x^i, p_i)}. \tag{4.5}$$

Besides, the four-current satisfies (see e.g. [18])

$$J^\mu(\eta, \mathbf{x}) = -\int \mathrm{d}^3p_i (-g)^{-1/2} \frac{p^\mu}{p^0} f(\eta, x^i, p_i), \tag{4.6}$$

where g is the determinant of the metric tensor[3] .

The single-flow approximation is particularly helpful in this context. Indeed, at given time η and position $\mathbf{x}$, all the particles of the fluid have the same momentum $P_i(\eta, \mathbf{x})$ whence

$$f(\eta, x^i, p_i) = n_c(\eta, \mathbf{x}) \delta_{\mathrm{D}}(p_i - P_i(\eta, \mathbf{x})). \tag{4.7}$$

It imposes directly

$$J^\mu = -a^{-4}(1 - \psi + 3\phi) \frac{P^\mu}{P^0} n_c. \tag{4.8}$$

[2] As the comoving phase-space momentum defined in (2.11), it satisfies the mass-shell condition $P^\mu P_\mu = -m^2$.

[3] I recall that the metric tensor $g_{\alpha\beta}$ is defined so that $\mathrm{d}s^2 = g_{\alpha\beta}\mathrm{d}x^\alpha \mathrm{d}x^\beta$. In the conformal Newtonian gauge, $\mathrm{d}s^2$ is given by (2.18) whence $(-g)^{-1/2} = a^{-4}(1 - \psi + 3\phi)$.

Putting this into the conservation equation (4.3), one finds eventually (ϕ and ψ being kept at linear order in the calculation) the succinct equation

$$\partial_\eta n_c + \partial_i \left(\frac{P^i}{P^0} n_c \right) = 0. \tag{4.9}$$

This equation of motion contains two independent variables only because P^0 and P^i are related via the mass-shell condition (the explicit relation is given in the article of section 4.4). Note that $\dfrac{P^i}{P^0}$ is simply $\dfrac{\mathrm{d}x^i}{\mathrm{d}\eta}$ (see (2.11)). The form of the continuity equation (4.9) is thus particularly reminiscent of the continuity equation (3.11) of the cold pressureless fluid. It should be supplemented by a relativistic equivalent of the Euler equation (3.12).

4.2.2 Conservation of the energy-momentum tensor

In the single-flow approximation, deriving the equation of motion of the momentum field is straightforward. Indeed, in that case, the energy-momentum tensor is simply[4] (see again [18])

$$T^{\mu\nu} = -P^\mu J^\nu. \tag{4.10}$$

Given the conservation of the four-current, the conservation of the energy-momentum tensor,

$$T^{\mu\nu}{}_{;\nu} = 0, \tag{4.11}$$

reduces to

$$P^\mu{}_{;\nu} J^\nu = 0. \tag{4.12}$$

When applied to the spatial part of P^μ, it results in

$$\partial_\eta P_i - (1 + 2\phi + 2\psi) \frac{P_j}{P_0} \partial_j P_i = P_0 \partial_i \psi + \frac{P_j P_j}{P_0} \partial_i \phi. \tag{4.13}$$

It should be compared with the Newtonian Euler equation (3.12) taken in the single-flow approximation. In the article presented in section 4.4, variants of equation

[4] In the article presented in section 4.4, we omitted the minus sign. Fortunately, it is a harmless mistake.

(4.13) are proposed. They involve more concrete variables such as the physical velocity field or the energy field.

Encoding the time evolution of neutrino perturbations in a system such as (4.9)-(4.13) is a novel point of view. It has been made possible thanks to the trick consisting in splitting the overall neutrino fluid into several flows. Those equations are very general because they have been derived from general relativity without neglecting field couplings. We will see in chapter 5 that even more general equations of this type can be found if one decides not to specify the gauge. Concrete applications will be presented in the next chapters. In the present one, the focus is placed on the comparison with the standard Boltzmann approach presented in section 2.3.2.

4.2.3 An alternative: derivation from the Boltzmann and geodesic equations

In the case of a cold pressureless fluid, the continuity and Euler equations had been obtained from the first moments of the collisionless Boltzmann equation combined with Newton's second law. The phase-space distribution functions of the different flows of neutrinos satisfying also the Vlasov equation, one expects the equations of motion of neutrinos to be re-derivable from comparable manipulations. It is useful to ensure that it is true. Indeed, recovering our equations from an alternative method would confer credibility to our results.

So let's write again the Vlasov equation:

$$\frac{\partial}{\partial\eta}f + \partial_i\left(\frac{\mathrm{d}x^i}{\mathrm{d}\eta}f\right) + \frac{\partial}{\partial p_i}\left(\frac{\mathrm{d}p_i}{\mathrm{d}\eta}f\right) = 0. \tag{4.14}$$

Note that this form is more general than the one given in section 2.3.2. It is thanks to the Hamiltonian evolution of the system that both formulations are valid. In the non-relativistic case, $\dfrac{\mathrm{d}x^i}{\mathrm{d}\eta}$ had been expressed in terms of the phase-space variables thanks to the classic definition (3.4) and $\dfrac{\mathrm{d}p_i}{\mathrm{d}\eta}$ had been related to the gravitational potential thanks to Newton's second law (3.5).

In general relativity, those relations are replaced respectively by

$$\frac{\mathrm{d}x^i}{\mathrm{d}\eta} = \frac{p^i}{p^0}, \tag{4.15}$$

which derives from the very definition (2.11) of the momentum p^i, and by the

geodesic equation

$$\frac{\mathrm{d}p_i}{\mathrm{d}\eta} = p_0 \partial_i \psi + \frac{p_j p_j}{p_0} \partial_i \phi. \tag{4.16}$$

Note that the definition of the macroscopic momentum field, (4.5), is equivalent to

$$P_i(\eta, \mathbf{x}) n_c(\eta, \mathbf{x}) = \int \mathrm{d}^3 p_i \; f(\eta, x^i, p_i) p_i. \tag{4.17}$$

More generally, in the single-flow approximation, (4.7) imposes to any macroscopic field $\mathcal{F}$ depending on $P_i(\eta, \mathbf{x})$ the relation

$$\mathcal{F}\left[P_i(\eta, \mathbf{x})\right] n_c(\eta, \mathbf{x}) = \int \mathrm{d}^3 p_i \; f(\eta, x^i, p_i) \; \mathcal{F}\left[p_i\right], \tag{4.18}$$

which gives a direct mapping between phase-space variables and macroscopic fields. In this framework, it is easy to show that the integration of equation (4.14) over phase-space momenta leads to

$$\partial_\eta n_c + \partial_i \left(\frac{P^i}{P^0} n_c \right) = 0, \tag{4.19}$$

which is precisely our first equation of motion (4.9). Besides, by combining the geodesic equation (4.16) with (4.18), one finds[5]

$$\partial_\eta P_i - (1 + 2\phi + 2\psi) \frac{P_j}{P_0} \partial_j P_i = P_0 \partial_i \psi + \frac{P_j P_j}{P_0} \partial_i \phi, \tag{4.20}$$

which is actually our second equation of motion (4.13). The system (4.9)-(4.13) appears as a true relativistic generalization of the system (3.11)-(3.12). Indicatively, we also showed in our article that our approach allows to re-derive the nonlinear Boltzmann hierarchy (2.29). Finally, to close the system of equations, metric perturbations should be related to the fields chosen as variables. In general relativity, such relations are given by the Einstein equations, which generalize the Poisson equation (3.10) of the Vlasov-Poisson system.

[5]It requires to notice that $\frac{\mathrm{d}p_i}{\mathrm{d}\eta} = \partial_\eta p_i + \frac{p^j}{p^0} \partial_j p_i = \partial_\eta p_i - (1 + 2\phi + 2\psi) \frac{p_j}{p_0} \partial_j p_i$.

4.3 Comparison with standard results

We have seen in section 2.3.2 that it is in the linear regime that the Boltzmann hierarchy is concretely exploitable. Indeed, the linearized Boltzmann hierarchy (2.22)-(2.23)-(2.24) allows to compute the linear perturbations of the first multipoles of the energy distribution (2.25)-(2.26)-(2.27) whereas the nonlinear Boltzmann hierarchy (2.29) is fruitless. To make a preliminary test of the accuracy of our approach, we thus expressed the linearized energy multipoles in terms of our fields and derived their time evolution from our equations of motion taken in the linear limit.

4.3.1 Linearized equations of motion

The equation of motion (4.13) shows that the zeroth order of the momentum field, $P_i^{(0)}$, is constant. Besides, since the momentum field is initially homogeneous, $P_i\left(\eta_{\rm in}\right) = P_i^{(0)}\left(\eta_{\rm in}\right)$ ($\eta_{\rm in}$ being the initial time). The label of each flow $\tau_i \equiv P_i\left(\eta_{\rm in}\right)$ is thus not only the initial momentum but also the homogeneous part of the momentum at any time, i.e.

$$\tau_i \equiv P_i^{(0)}. \tag{4.21}$$

Once linearized, the Euler equation (4.13) can thus be rewritten

$$\frac{{\rm d}P_i^{(1)}}{{\rm d}\eta} = \partial_i \left[\tau_0 \psi + \frac{\tau^2}{\tau_0}\phi\right], \tag{4.22}$$

where

$$\tau = \sqrt{\delta_{ij}\tau_i\tau_j} \tag{4.23}$$

and

$$\tau_0(\eta) = -\sqrt{\tau^2 + m^2 a^2(\eta)}. \tag{4.24}$$

The form of the equation (4.22) is pleasant because it is reminiscent of the form (3.13), according to which the relevant characteristics of the velocity field u_i are all contained in its divergence. This gives a first incitement to choose the momentum field P_i as one of our variables. In our second study (see chapter 5), we showed that P_i keeps this attractive property in any gauge and at any order in perturbation theory. One can therefore definitely consider it as "the good variable", especially

since none of the other fields that we tested presents this particularity.

It is legitimate to wonder what differentiates inherently P_i from P^i for instance. A first clue may be the fact that $P_i^{(1)}$ is a gradient in terms of its canonically conjugate space coordinates x^i so one can expect $P^{i(1)}$ to be a gradient in terms of the space coordinates x_i. Note moreover that it was already pointed out in [104] that lowering the momentum indices to work with the conjugate momenta of the comoving space coordinates is useful since the geodesic equation written in a homogeneous universe shows that $P^{i(0)} \propto a^{-2}$ whereas $P_i^{(0)}$ is constant.

After moving to Fourier space and introducing, in the spirit of the study of the cold pressureless fluid, a density constrast field

$$\delta_n(\eta, \mathbf{x}) = \frac{n_c^{(1)}(\mathbf{x}, \eta)}{n_c^{(0)}}, \tag{4.25}$$

and a divergence field

$$\theta_P(\mathbf{x}) = \partial_i P_i^{(1)}, \tag{4.26}$$

the linearized equations of motion take the form

$$\partial_\eta \delta_n = \mathrm{i}\mu k \frac{\tau}{\tau_0} \left[\delta_n + \psi + \phi \left(2 - \frac{\tau^2}{\tau_0^2} \right) \right] + \frac{\theta_P}{\tau_0} \left(1 - \frac{\mu^2 \tau^2}{{\tau_0}^2} \right) \tag{4.27}$$

and

$$\partial_\eta \theta_P = \mathrm{i}\mu k \frac{\tau}{\tau_0} \theta_P - k^2 \left(\tau_0 \psi + \frac{\tau^2}{\tau_0} \phi \right), \tag{4.28}$$

with μ the Cosine of the angle between the wave vector $\mathbf{k}$ and the initial momentum direction,

$$\mu = \frac{k_i \tau_i}{k\tau}. \tag{4.29}$$

In general, μ runs from -1 to 1 since the other number that characterizes the initial momentum, τ, is defined in (4.23) as a positive quantity. Note nevertheless that the equations of motion impose

$$\delta_n(-\mu, k, \tau) = \delta_n(\mu, -k, \tau) = \delta_n^*(\mu, k, \tau) \tag{4.30}$$

and the same for θ_P. Such relations would reduce the number of equations if one assumed that the real and imaginary parts of the fields are not independent.

In the large mass limit, i.e. when $\tau \to 0$ (and thus $\tau_0 \to -ma$), one recovers the standard linear equations of cold dark matter (3.22)[6]. The additional terms, all proportional to $\dfrac{\tau}{\tau_0}$, reflect the influence of a non-zero initial velocity. Their presence in the equations of motion affects the time evolution of the perturbations δ_n and θ_P (in a different way for each flow). Such contributions characterize the free-streaming of neutrinos, i.e. they add in solutions a transitory period before the fall into potential wells. Usually, free-streaming is taken into account by assuming a non-zero (but approximate and hence valid only at given scales) velocity dispersion in the Euler equation and by taking the contribution of neutrinos into account in the Poisson equation (valid only on scales at which relativistic effects are negligible). The point of view adopted here is therefore less restrictive.

4.3.2 Linearized multipole energy distribution

Our study allows to track individually the behavior of each flow of neutrinos but what is of most interest for cosmology is of course the global effect of neutrinos. We were thus interested in reconstructing the global multipole energy distribution from individual features.

In terms of the global energy-momentum tensor of neutrinos, the first global multipoles ρ_ν, θ_ν and σ_ν read in Fourier space and in the linear regime (see [111]):

$$\rho_\nu{}^{(1)} \equiv -T^0{}_0{}^{(1)}, \tag{4.31}$$

$$\left(\rho_\nu{}^{(0)} + P_\nu^{(0)}\right)\theta_\nu{}^{(1)} \equiv \mathrm{i}k^i T^0{}_i{}^{(1)}, \tag{4.32}$$

$$\left(\rho_\nu{}^{(0)} + P_\nu{}^{(0)}\right)\sigma_\nu{}^{(1)} \equiv -\left(\frac{k^i k^j}{k^2} - \frac{1}{3}\delta_{ij}\right)\left(T^i{}_j{}^{(1)} - \frac{1}{3}\delta^i_j T^k{}_k{}^{(1)}\right), \tag{4.33}$$

with ([18])

$$T^{\mu\nu}(\eta, \mathbf{x}) = \int \mathrm{d}^3 p_i (-g)^{-1/2} \frac{p^\mu p^\nu}{p^0} f(\eta, x^i, p_i). \tag{4.34}$$

A distinctive sign of our approach is that integrations over phase-space momenta are replaced by integrations over all the flows of the collection, or equivalently over

[6] Indeed, in the non-relativistic regime, $\delta_n = \Psi_1$, $\theta_P = -ma\mathcal{H}\Psi_2$ and ψ is the gravitational potential Φ.

all the initial momenta $\vec{\tau}$. More explicitly, since (4.2) and (4.7) impose

$$f^{\rm tot}(\eta, x^i, p_i) = \int {\rm d}^3\tau_i \, n_c(\eta, \mathbf{x}; \vec{\tau}) \delta_{\rm D}(p_i - P_i(\eta, \mathbf{x}; \vec{\tau})), \tag{4.35}$$

the mapping between the two approaches reads

$$\int {\rm d}^3 p_i \, f^{\rm tot}(\eta, x^i, p_i) \; \mathcal{F}(p_i) = \int {\rm d}^3\tau_i \, n_c(\eta, \mathbf{x}; \vec{\tau}) \; \mathcal{F}(P_i(\eta, \mathbf{x}; \vec{\tau})). \tag{4.36}$$

Eventually, in terms of our fields, the linearized multipole energy distribution is therefore given by

$$\rho_\nu{}^{(1)} = -\frac{4\pi}{a^4}\mathcal{R}e \int_0^{\tau_{\rm max}} \tau^2 {\rm d}\tau \int_{-1}^{1} {\rm d}\mu \; \tau_0 \; n_c{}^{(0)}(\mu, \tau) \times \tag{4.37}$$
$$\left[\delta_n(\mu, \tau) + \phi\left(3 + \frac{\tau^2}{\tau_0^2}\right) - {\rm i}\frac{\mu\tau}{k\tau_0^2}\theta_P(\mu, \tau)\right],$$

$$\left(\rho_\nu{}^{(0)} + P_\nu^{(0)}\right)\theta_\nu{}^{(1)} = \frac{4\pi}{a^4}\mathcal{R}e \int_0^{\tau_{\rm max}} \tau^2 {\rm d}\tau \int_{-1}^{1} {\rm d}\mu \; n_c{}^{(0)}(\mu, \tau) \left\{{\rm i}\mu k\tau \left[\delta_n(\mu, \tau) + 4\phi\right] + \theta_P(\mu, \tau)\right\}, \tag{4.38}$$

$$\left(\rho_\nu{}^{(0)} + P_\nu{}^{(0)}\right)\sigma_\nu{}^{(1)} = \frac{4\pi}{a^4}\mathcal{R}e \int_0^{\tau_{\rm max}} \tau^2 {\rm d}\tau \int_{-1}^{1} {\rm d}\mu \; \tau_0 \; n_c{}^{(0)}(\mu, \tau) \times \tag{4.39}$$
$$\left\{\frac{\tau^2}{\tau_0^2}\left(\mu^2 - \frac{1}{3}\right)\left[\delta_n(\mu, \tau) + \phi\left(5 - \frac{\tau^2}{\tau_0^2}\right) + {\rm i}\frac{\mu\tau}{k\tau_0^2}\theta_P(\mu, \tau)\right] - \frac{4}{3}{\rm i}\frac{\mu\tau}{k\tau_0^2}\theta_P(\mu, \tau)\right\},$$

where the "$\mathcal{R}e$" operator takes the real part of the quantity it precedes. We give alternative expressions, involving other fields, in our article. This is precisely in the comparison between this way of calculating the energy distribution and the standard one, (2.25)-(2.26)-(2.27), that we were interested.

4.3.3 Initial conditions

When the initial time is assumed to lie between the time of neutrino decoupling and the moment at which neutrinos become non-relativistic, an analytic expression of the global phase-space distribution function is known. It is given by equation (2.16):

$$f^{\rm tot}\left(x^i, q\right) = \left[1 + \exp\frac{q}{a\left(T + \delta T(x^i)\right)}\right]^{-1} \quad \text{at initial time,} \tag{4.40}$$

where $q^i = a^2(1-\phi)p^i$ in the conformal Newtonian gauge (see [111]).

The mechanisms at play in the emergence of inhomogeneities (such as the local fluctuations of temperature δT) are complex[7]. To simplify the description, a common practice is to assume that initial conditions are linear combinations of adiabatic (also called isentropic) and isocurvature modes. The former are the two solutions (a growing one and a decaying one) obtained by assuming that all species have been perturbed in the same way when homogeneity ended (see more details in [196]). It means in particular that relative entropies between flows, which are in general non zero after a thermodynamic process has occurred, have been neglected. The latter encompass all the combinations for which the spatial curvature remains homogeneous while two (and only two) cosmic fluids undergo density fluctuations.

Hence, when considering N fluids (each characterized by two equations of motion), solutions are *a priori* a superposition of one growing adiabatic mode, $(N-1)$ growing isocurvature modes and N decaying modes. Neglecting decaying modes is natural because they have become too small to be observable today. Besides, for simplicity, isocurvature modes are also neglected in most studies (see nevertheless [113] for an illustration of how to deal with isocurvature modes). Fortunately, the second simplifying hypothesis (that might appear arbitrary) is strongly supported by observations[8].

Following this trend, we assumed initial conditions to be purely adiabatic in our study. Actually, this option was really lucky for us. Indeed, our approach would have made the description of isocurvature solutions particularly heavy since we consider an increased number of fluids (see the next section for discussions concerning the requisite number of neutrino flows). As explained in our paper (and following some standard results), in the conformal Newtonian gauge, the adiabaticity hypothesis leads to (on appropriate scales)

$$\frac{\delta T\left(\eta_{\rm in}, x^i\right)}{T} = -\frac{\psi\left(\eta_{\rm in}, x^i\right)}{2}. \tag{4.41}$$

The physical meaning of equation (4.35) is that all the flows whose time evolution is such that, at time η and location x^i, the particles have a momentum equal to p_i contribute to $f^{\rm tot}\left(\eta, x^i, p_i\right)$. However, at initial time, the only flow that con-

[7] The most robust theories describing this phenomenon are inflationary paradigms and models describing topological defects.

[8] For example, according to the 2015 Planck results [137], the isocurvature contribution represents less than about 3% of the adiabatic contribution.

tributes to $f^{\rm tot}\left(\eta=\eta_{\rm in},x^i,p_i\right)$ is the one labeled by $\tau_i=p_i$, whence a perfect match between the global initial distribution functions $f^{\rm tot}\left(\eta_{\rm in},x^i,p_i=\tau_i\right)$ and the initial comoving number densities $n_c\left(\eta_{\rm in},x^i;\vec{\tau}\right)$.

As demonstrated in the article of section 4.4, one finds eventually[9]

$$\delta_n(\eta_{\rm in},x^i;\vec{\tau})=\left(\frac{\psi\left(\eta_{\rm in},x^i\right)}{2}+\phi(\eta_{\rm in},x^i)\right)\frac{{\rm d}f_0(\tau)}{{\rm d}\log\tau}, \tag{4.42}$$

where f_0 is the background distribution function given by (2.14).

Besides, the definition

$$P_i(\eta_{\rm in},x^i;\vec{\tau})=\tau_i \tag{4.43}$$

dictates in each flow the initial condition

$$\theta_P(\eta_{\rm in},x^i;\vec{\tau})=0. \tag{4.44}$$

The expressions (4.42) and (4.44) give the leading behavior of the fields at initial time. They depend on τ but not on μ, which means that they describe isotropic fields. To be able to depict the early development of anisotropic pressure in the neutrino streams, we computed also the first early-time corrections obtained by expanding the fields in one-dimensional[10] Legendre polynomials (whose variable is μ). The procedure is described in our article. In practice, the initial conditions that we implemented in our code are

$${\delta_n}^{\rm init}(\mu,\tau)=\delta_0+\left(\frac{1}{3}-\mu^2\right)\left[\frac{\theta_1}{2\mathcal{H}\tau_0}+\frac{k^2}{2\mathcal{H}^2}\left(\delta_0+\phi+\psi\right)\right]-{\rm i}\frac{\mu k}{\mathcal{H}}\left(\delta_0+\phi+\psi\right) \tag{4.45}$$

and

$${\theta_P}^{\rm init}(\mu,\tau)=\theta_1-{\rm i}\frac{\mu k}{2\mathcal{H}}\theta_1, \tag{4.46}$$

where $\delta_0=\left(\frac{\psi}{2}+\phi\right)\frac{{\rm d}\log f_0}{{\rm d}\log\tau}$ and $\theta_1=-k^2\frac{\tau_0}{\mathcal{H}}\left(\phi+\psi\right)$.

[9] Note that, in our article, initial conditions are presented in terms of the proper number density whereas I consider here the comoving number density.

[10] It is possible to express the angular dependence with one-dimensional polynomials because the only variable that characterizes the direction of the initial momentum in the equations is μ.

Note that the symmetries previously mentioned are preserved in those initial fields.

4.3.4 Numerical tests and discussion on the appropriateness of the multi-fluid approach

Once the analytic expression of the linearized multipole energy density distribution, the equations of motion of the fields and the initial conditions are known, it is easy to check that the perspective we propose is consistent with the standard description. The principle of the integration scheme, as well as the numerical results, are presented in the article of section 4.4. The main conclusions we drew are the followings.

- For small wavenumbers, the most influential parameters are the numbers of momenta taken into account in the discretized sums involved in the two formulations of the energy multipoles. On the contrary, the number of discrete values of μ, N_μ, and the order at which the Boltzmann hierarchy is truncated, $l_{\max}$, are not determining at those scales. For example, with $N_\mu = 12$, $\ell_{\max} = 6$, $k = 0.002h/\text{Mpc}$ and $m = 0.05$ eV, the mean relative errors decrease from 10^{-2} to 10^{-4} when the number of discrete momenta (in each approach) is increased from 16 to 100. For the number of equations to remain reasonable in our study, one can thus keep N_μ small as long as $k \lesssim 0.01h/\text{Mpc}$.

- For larger wavenumbers, the numerical integration is more demanding because the fields undergo rapid oscillations and also depend more significantly on τ and μ (which is visible on the equations (4.27) and (4.28) and is reminiscent from the fact that the pulsation of acoustic oscillations is expected to be proportional to k in neutrino fluids, see [104]). Illustratively, it is necessary to go up to $N_\mu = 100$ to get a percent accuracy for $k = 0.1h/\text{Mpc}$. Clearly, a concrete numerical exploitation of our results would therefore require to search for strategies allowing to reduce the numerical cost. It is something that we have not done yet.

- Considering smaller masses also requires to improve the discretization scheme since, in that case, the dependence on $\vec{\tau}$ is increased.

- At late times, all the flows behave as cold dark matter. Unsurprisingly, the convergence towards this regime strongly depends on μ, τ and m. During the

oscillatory phase, neutrino and cold-dark-matter fields are generally out of phase so, before the integration over μ has been performed, some velocity and density perturbations of neutrinos have a larger real part than the fluctuations experienced by the cold-dark-matter fluid. This can be misleading at first glance but global perturbations have actually the expected behavior.

Those numerical tests show unequivocally that both approaches are consistent in the linear regime. We have proven it up to a 10^{-5} accuracy. Illustratively, a 10^{-3} accuracy (obtained for $k = 0.01h/\text{Mpc}$ and $m = 0.3$ eV) is presented in figure 4.3, which shows the comparison of the behaviors of the first energy multipoles. The main drawback of our method is that, for the agreement to be satisfying, our number of equations must generally be larger than the one required in the Boltzmann approach. However, our analytic model is valid beyond the linear regime. Besides, as will be illustrated in the next chapters, the great similarities that exist between our study and the study of the cold pressureless component inspire further developments.

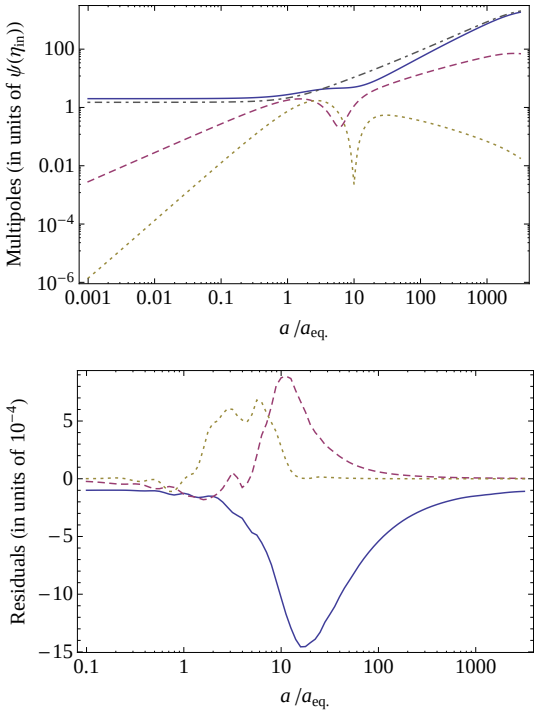

Figure 4.3: Time evolution of the energy density contrast (solid line), velocity divergence (dashed line) and shear stress (dotted line) of the neutrinos. The dot-dashed line is presented for comparison and corresponds to the density contrast of the cold-dark-matter component. Top panel: the quantities are computed with our multi-fluid approach. Bottom panel: residuals (defined as the relative differences) when the two methods are compared. Numerical integration has been done with 40 values of τ and q and 12 values of μ. k is set to $0.01h$/Mpc, m is set to 0.3 eV and $l_{\rm max}$ is set to 6. The resulting relative differences are of the order of 10^{-3}.

4.4 Article "Describing massive neutrinos in cosmology as a collection of independent flows"

Journal of Cosmology and Astroparticle Physics
An IOP and SISSA journal

Describing massive neutrinos in cosmology as a collection of independent flows

Hélène Dupuy and Francis Bernardeau

Institut de Physique Théorique, CEA, IPhT, F-91191 Gif-sur-Yvette, CNRS, URA 2306, F-91191 Gif-sur-Yvette, France

E-mail: helene.dupuy@cea.fr, francis.bernardeau@cea.fr

Received November 29, 2013
Accepted January 9, 2014
Published January 17, 2014

Abstract. A new analytical approach allowing to account for massive neutrinos in the non-linear description of the growth of the large-scale structure of the universe is proposed. Unlike the standard approach in which neutrinos are described as a unique hot fluid, it is shown that the overall neutrino fluid can be equivalently decomposed into a collection of independent flows. Starting either from elementary conservation equations or from the evolution equation of the phase-space distribution function and assuming that there is no shell-crossing, we derive the two non-linear motion equations that each of these flows satisfies. Those fluid equations describe the evolution of macroscopic fields. We explain in detail the connection between the collection of flows we defined and the standard massive neutrino fluid. Then, in the particular case of adiabatic initial conditions, we explicitly check that, at linear order, the resolution of this new system of equations reproduces the results obtained in the standard approach based on the collisionless Boltzmann hierarchy. Besides, the approach advocated in this paper allows to show how each neutrino flow settles into the cold dark matter flow depending on initial velocities. Although valid up to shell-crossing only, it is a further step towards a fully non-linear treatment of the dynamical evolution of neutrinos in the framework of large-scale structure growth.

Keywords: cosmological neutrinos, neutrino masses from cosmology

ArXiv ePrint: 1311.5487

doi:10.1088/1475-7516/2014/01/030

JCAP01(2014)030

Contents

1 Introduction

The recent results of the Planck mission [1, 2] crown three decades of observational and theoretical investigations on the origin, evolution and statistical properties of cosmological perturbations. Those properties are governed not only by the mechanisms that produced cosmological perturbations — inflation is the most commonly referred explanation — but also by matter itself. In addition to the information they give regarding inflationary parameters, observations of the Cosmic Microwave Background (CMB) temperature anisotropies and polarization are thus a very precious probe of the matter content of the universe. Although

JCAP01(2014)030

this observational window is confined to the time of recombination, in a regime where the metric or density perturbations are all deeply rooted in the linear regime,[1] it allows an exquisite determination of several fundamental cosmological parameters. However, some of them remain elusive. This is in particular the case of the neutrino masses if they are too small to leave an imprint on the recombination physics.

The experiments on neutrino flavor oscillations demonstrating that neutrinos are indeed massive are thus of crucial importance and it is necessary to examine minutely the impact of those masses on various cosmological observables. Understandably, such a discovery has triggered a considerable effort in theoretical, numerical and observational cosmology to infer the consequences on the cosmic structure growth. The first study in which massive neutrinos are properly treated in the linear theory of gravitational perturbations dates back from ref. [3] (see also its companion paper ref. [4]). The consequences of these results are thoroughly presented in ref. [5], where the connection between neutrino masses and cosmology - in the standard case of three neutrino species - is investigated in full detail. It is shown that CMB anisotropies are indirectly sensitive to massive neutrinos whereas the late-time large-scale structure growth rate, via its time and scale dependences, offers a much more direct probe of the neutrino mass spectrum. To a large extent current and future cosmology projects aim at exploiting these dependences to put constraints on the neutrino masses. Indeed, the impact of massive neutrinos on the structure growth has proved to be significative enough to make such constraints possible, as shown for instance in [6–11]. These physical interpretations are based on numerical experiments, the early incarnations dating back from the work of ref. [12], which have witnessed a renewed interest in the last years [13–16], and also on theoretical investigations such as [17–20], where the effect of massive neutrinos in the non-linear regime is investigated with the help of Perturbation Theory. An important point is that it is potentially possible to get better constraints than what the predictions of linear theory offer. Observations of the large-scale structure within the local universe are indeed sensitive to the non-linear growth of structure and thus also to the impact of mode-coupling effects on this growth. Such a coupling is expected to strengthen the role played by the matter and energy content of the universe on cosmological perturbation properties. This is true for instance for the dark energy equation of state [21] or for the masses, even if small, of the neutrino species, as shown in numerical experiments [14].

One can mention another alternative that has been proposed to study the effect of neutrinos on the large-scale structure growth, [22], where the neutrino fluid is tentatively described as a perfect fluid. In the present study we are more particularly interested in designing tools to explore the impact of massive neutrinos within the non-linear regime of the density perturbation growth. Little has been obtained in this context in presence of massive neutrinos. One of the reasons for such a limitation is that the non-linear evolution equations of the neutrino species are a priori cumbersome and difficult to handle (the most thorough investigations of the non-linear hierarchy equations are to be found in [23]). On the other hand Perturbation Theory applied to pure dark matter systems has proved very valuable and robust (see [24] for a recent review on the subject). The aim of this paper is thus to set the stage for further theoretical analyses by presenting a complete set of equations describing the neutrino perturbation growth, from super-Hubble perturbations of relativistic species to those of non-relativistic species within the local universe. In particular we are interested in deriving equations from which the connection with the standard non-linear system describing dark matter particles is convenient.

[1] Except the effects of lensing, which reveal non-linear line-of-sight effects.

JCAP01(2014)030

The strategy usually adopted to describe neutrinos, massive or not, is calqued from that used to describe the radiation fluid (see e.g. refs. [3–5]): neutrinos are considered as a single hot multi-stream fluid whose evolution is dictated by the behavior of its distribution function in phase-space f. Calculations are performed in a perturbed Friedmann-Lemaître spacetime. The key equation is the Boltzmann equation. For neutrinos, contrary to radiation, it is taken in the collisionless limit since neutrinos do not interact with ordinary matter (neither at the time of recombination nor after). It leads to the Vlasov equation, which derives from the conservation of the number of particles applied to a Hamiltonian system, $\frac{\mathrm{d}f}{\mathrm{d}\eta} = 0$, where η is a time coordinate. The different terms participating in the expanded form of this equation are computed in particular with the help of the geodesic equation. In practice, whether at super or sub-Hubble scales, the motion equations are derived at linear order with respect to the metric fluctuations. We will here also restrict ourselves to this approximation as the late-time non-linearity of the large-scale structure growth is not due to direct metric-metric couplings but to the non-linear growth of the density contrasts and velocity divergences.

The possibility we explore in the present work is that neutrinos[2] could be considered as a collection of single-flow fluids instead of a single multi-flow fluid. We take advantage here of the fact that neutrinos are actually free streaming: they do not interact with one another and they do not interact with matter particles. We will see in particular that it is possible to distinguish the fluid elements of the collection by labeling each of them with an initial velocity. The complete neutrino fluid behavior is then naturally obtained by summing the contributions of each fluid element over the initial velocity distribution. As we will see, this description is actually very similar to that of dark matter from the very beginning. It also breaks down for the same reason: an initially single-flow fluid can form multiple streams after shell crossings. But this regime corresponds to the late-time evolution of the fields, which is beyond the scope of Standard Perturbation Theory calculations so no shell-crossing is taken into account in the following.

The paper is organized as follows. In section 2, the geometric context in which the calculations are performed is specified as well as some physical quantities of interest. We then derive the non-linear equations of motion associated with each fluid of neutrinos and we make the comparison with the first moments of the Boltzmann hierarchy. In section 3, we describe the linearized system. Section 4 is devoted to the description of the specific construction of a multi-fluid system of single flows. We present in particular the initial and early-time number density and velocity fields corresponding to adiabatic initial conditions. This section ends by the presentation of the results given by the numerical integration of the system of equations, when the whole neutrino fluid is discretized into a finite sum of independent fluids. Results are explicitly compared to those obtained from the standard integration scheme based on the Boltzmann hierarchy. Finally we give some hints on how each flow settles into the cold dark matter component.

2 Equations of motion

In this section we present the derivation of the non-linear equations of motion for a single-flow fluid of particles, relativistic or not. A confrontation of our findings with those of a more standard approach based on the use of the Vlasov equation is presented in the last part of the present section.

[2] As a matter of fact, neutrinos of each mass eigenstate.

JCAP01(2014)030

2.1 Spacetime geometry, momenta and energy

In order to describe the impact of massive neutrinos on the evolution of inhomogeneities, we consider a spatially flat Friedmann-Lemaître spacetime with scalar metric perturbations only. Units are chosen so that the speed of light in vacuum is equal to unity. We adopt in this work the conformal Newtonian gauge, which makes the comparison with the standard motion equations of non-relativistic species, the Vlasov-Poisson system, easier. The metric is given by

$$\mathrm{d}s^2 = a^2(\eta)\left[-(1+2\psi)\,\mathrm{d}\eta^2 + (1-2\phi)\,\mathrm{d}x^i\mathrm{d}x^j\delta_{ij}\right], \tag{2.1}$$

where η is the conformal time, x^i $(i=1,2,3)$ are the Cartesian spatial comoving coordinates, $a(\eta)$ is the scale factor , δ_{ij} is the Kronecker symbol and ψ and ϕ are the metric perturbations. The expansion history of the universe, encoded in the time dependence of a, is driven by the overall matter and energy content of the universe. It is supposed to be known and for practical calculations we adopt the numerical values of the concordance model.

Following the same idea, in the rest of the paper metric perturbations will be considered as known, determined by the Einstein equations. Furthermore, following the framework presented in the introduction, only linear terms in ψ and ϕ will be taken into account in all the derivations that follow, in particular in the motion equations we will derive.

We will consider massive particles, relativistic or not, freely moving in space-time (2.1). Their kinematic properties are given by their momenta so we introduce the quadri-vector p_μ as the conjugate momentum of x^μ, i.e.

$$p_\mu = m u_\mu \quad \text{where} \quad u_\mu = g_{\mu\nu}\mathrm{d}x^\nu/\sqrt{-\mathrm{d}s^2}. \tag{2.2}$$

It obviously implies $p^\mu p_\mu = -m^2$. In the following we will also make use of the momentum q^i, defined as

$$q^i = a^2(1-\phi)p^i \tag{2.3}$$

in such a way that

$$p_i p^i = g_{ij}p^i p^j = \delta_{ij}\frac{q^i q^j}{a^2}. \tag{2.4}$$

Another useful quantity is the energy ϵ measured by an observer at rest in metric (2.1), which is such that

$$p^0 p_0 = g_{00}p^0 p^0 \equiv -\epsilon^2. \tag{2.5}$$

It satisfies

$$\epsilon^2 = m^2 + (q/a)^2. \tag{2.6}$$

2.2 The single-flow equations from conservation equations

We now proceed to the derivation of the motion equations satisfied by a single-flow fluid starting from elementary conservation equations. Such a fluid is entirely characterized by two fields, its local numerical density field $n(\eta,\mathbf{x})$ and its momentum[3] field $P^i(\eta,\mathbf{x})$(the zero component can be deduced from the spatial ones using the on-shell mass constraint). This approach contrasts with a description of the complete neutrino fluid for which one has to introduce the whole velocity distribution.

[3]We use an uppercase to distinguish it from a phase-space variable and we use sometimes in this paper the velocity field $V^i(\eta,\mathbf{x})$ rather than the momentum field.

JCAP01(2014)030

2.2.1 Evolution equation of the proper number density n

The key idea is to consider a set of neutrinos that form a single flow, i.e. a fluid in which there is only one velocity (one modulus and one direction) at a given position. If a fluid initially satisfies this condition, it will continue to do so afterwards since the neutrinos it contains evolve in the same gravitational potential. Thus in the following we consider fluids in which all the neutrinos have initially the same velocity. In such physical systems, neutrinos are neither created nor annihilated nor diffused through collision processes so neutrinos contained in each flow obey an elementary conservation law,

$$J^{\mu}_{\ ;\mu} = 0, \tag{2.7}$$

where J^μ is the particle four-current and where we adopt the standard notation; to indicate a covariant derivative. It is easy to show that, in the metric we chose, this relation leads to,

$$\partial_\eta J^0 + \partial_i J^i + (4\mathcal{H} + \partial_\eta\psi - 3\partial_\eta\phi)J^0 + (\partial_i\psi - 3\partial_i\phi)J^i = 0, \tag{2.8}$$

where $\mathcal{H}$ is the conformal Hubble constant, $\mathcal{H} = \partial_\eta a/a$.

The four-current is related to the number density of neutrinos as measured by an observer at rest in metric (2.1), $n(\eta, \mathbf{x})$, by $n = J^\mu U_\mu$, where U_μ is a vector tangent to the worldline of this observer. The latter satisfies $U^\mu U_\mu = -1$ and $U^i = 0$. Thus $n = J^0 U_0 = -a\,(1+\psi)\,J^0$. Given that $J^i = J^0 \frac{P^i}{P^0}$, eq. (2.8) can thereby be rewritten

$$\partial_\eta n + \partial_i\left(\frac{P^i}{P^0}n\right) = 3n\left(\partial_\eta\phi - \mathcal{H} + \partial_i\phi\frac{P^i}{P^0}\right). \tag{2.9}$$

We signal here that this number density is the proper number density, not to be confused with the comoving number density that we will define later (eq. (2.29)). The fact that the right-hand side of its evolution equation is non-zero is thus not surprising. It simply reflects the expansion of the universe. This relation can alternatively be written with the help of the momentum P_i, expressed with covariant indices, thanks to the relations $P_i = a^2\,(1-2\phi)\,P^i$ and $P_0 = -a^2\,(1+2\psi)\,P^0$. It leads to,

$$\partial_\eta n - (1+2\phi+2\psi)\partial_i\left(\frac{P_i}{P_0}n\right) = 3n(\partial_\eta\phi - \mathcal{H}) + n(2\partial_i\psi - \partial_i\phi)\frac{P_i}{P_0}, \tag{2.10}$$

where a summation is still implied on repeated indices. Note that in all these transformations we consistently keep all contributions to linear order in the metric perturbations.[4]

2.2.2 Evolution equation of the momentum P_i

The second motion equation expresses the momentum conservation. It is obtained from the observation that, for a single-flow fluid, all particles located at the same position have the same momentum so that the energy momentum tensor $T^{\mu\nu}$ is given by $T^{\mu\nu} = P^\mu J^\nu$. The conservation of this tensor then gives

$$T^{\mu\nu}_{\ \ ;\nu} = P^{\mu}_{\ ;\nu}J^\nu + P^\mu J^{\nu}_{\ ;\nu} = 0, \tag{2.11}$$

[4] We note however that the factor $(1+2\phi+2\psi)$ that appears in the second term of this equation could be dropped as it is multiplied by a gradient term that vanishes at homogeneous level. For the sake of consistency we however keep such factor here and in similar situations in the following.

JCAP01(2014)030

which combined with equation (2.7) leads to

$$T^{\mu\nu}{}_{;\nu} = P^{\mu}{}_{;\nu} J^{\nu} = 0. \tag{2.12}$$

This relation should be valid in particular for spatial indices, $P^{i}{}_{;\nu} J^{\nu} = 0$. It eventually imposes,

$$\partial_\eta P_i - (1 + 2\phi + 2\psi)\frac{P_j}{P_0}\partial_j P_i = P_0 \partial_i \psi + \frac{P_j P_j}{P_0}\partial_i \phi \tag{2.13}$$

on the covariant coordinates of the momentum. Eq. (2.13) is our second non-linear equation of motion. At this stage the fact that we choose covariant coordinates P_i instead of contravariant P^i or a combination of both such as q_i is arbitrary but we will see that it is crucial when it comes to actually solve this system in the linear regime, see section 3.

We have now completed the derivation of our system of equations. It is a generalization of the standard single-flow equations of a pressureless fluid composed of non-relativistic particles. The latter is obtained simply by imposing to the velocity to be small compared to unity (while keeping its gradient large). To see it more easily, let us express the motion equations in terms of the proper velocity field.

2.2.3 Other formulations of the momentum conservation

An alternative representation of eq. (2.13) can be obtained by introducing the physical velocity field $V^i(\eta, \mathbf{x})$ (expressed in units of the speed of light). This velocity is along the momentum P^i and is such that $V^2 = -P_i P^i/(P_0 P^0)$. We can easily show that,

$$V^i = -\frac{P_i}{P_0}(1 + \phi + \psi). \tag{2.14}$$

Note that V^i can entirely be expressed in terms of P_i with the help of the relation

$$P_0^2 = P_i^2(1 + 2\phi + 2\psi) + m^2 a^2 (1 + 2\psi). \tag{2.15}$$

Its evolution equation derives from eq. (2.13) and reads

$$\partial_\eta V^i + V^i(\mathcal{H} - \partial_\eta \phi)(1 - V^2) + \partial_i \psi + V^2 \partial_i \phi + (1 + \phi + \psi) V^j \partial_j V^i - V^i V^j \partial_j (\phi + \psi) = 0. \tag{2.16}$$

From this equation, it is straightforward to recover the standard Euler equation in the limit of non-relativistic particles.

Similarly, the evolution equation of the energy field $\epsilon(\eta, \mathbf{x})$, defined by[5]

$$\epsilon(\eta, \mathbf{x}) = \frac{m}{\sqrt{1 - V(\eta, \mathbf{x})^2}} = -\frac{(1 - \psi)}{a} P_0(\eta, \mathbf{x}), \tag{2.17}$$

can be deduced from eq. (2.13),

$$\partial_\eta \epsilon + (1 + \phi + \psi) V^i \partial_i \epsilon + \epsilon V^i \partial_i \psi + \epsilon V^2 (\mathcal{H} - \partial_\eta \phi) = 0. \tag{2.18}$$

We will now compare these field equations to those obtained from the Boltzmann approach, which is based on the evolution equation of the phase-space distribution function.

[5] $P_0 = -a(1 + \psi)\epsilon$ is a sign convention that we use in all this paper.

JCAP01(2014)030

2.3 The single-flow equations from the evolution of the phase-space distribution function

2.3.1 The non-linear moments of the Boltzmann equation

The Boltzmann approach consists in studying the evolution of the phase-space distribution function $f(\eta, x^i, p_i)$, defined as the number of particles per differential volume $\mathrm{d}^3x^i\mathrm{d}^3p_i$ of the phase-space, with respect to the conformal time η, the comoving positions x^i and the conjugate momenta p_i. The particle conservation implies that

$$\frac{\partial}{\partial\eta}f + \partial_i\left(\frac{\mathrm{d}x^i}{\mathrm{d}\eta}f\right) + \frac{\partial}{\partial p_i}\left(\frac{\mathrm{d}p_i}{\mathrm{d}\eta}f\right) = 0, \tag{2.19}$$

where $\mathrm{d}x^i/\mathrm{d}\eta$ and $\mathrm{d}p_i/\mathrm{d}\eta$ are a priori space and momentum dependent functions. Because of the Hamiltonian evolution of the system, eq. (2.19) can be simplified into,

$$\frac{\partial}{\partial\eta}f + \frac{\mathrm{d}x^i}{\mathrm{d}\eta}\partial_i f + \frac{\mathrm{d}p_i}{\mathrm{d}\eta}\frac{\partial}{\partial p_i}f = 0. \tag{2.20}$$

In other words, f satisfies a Liouville equation, $\mathrm{d}f/\mathrm{d}\eta$=0. To compute this total derivative, there is some freedom about the choice of the momentum variable (but this choice does not affect the physical interpretation of f, which remains in any case the number of particles per $\mathrm{d}^3x^i\mathrm{d}^3p_i$). On the basis of previous work, we adopt here the variable q^i defined in eq. (2.3). In this context, the chain rule gives for the Liouville equation,

$$\frac{\partial f}{\partial\eta} + \frac{\mathrm{d}x^i}{\mathrm{d}\eta}\frac{\partial f}{\partial x^i} + \frac{\mathrm{d}q^i}{\mathrm{d}\eta}\frac{\partial f}{\partial q^i} = 0. \tag{2.21}$$

We are not interested in deriving a multipole hierarchy at this stage so we keep here a Cartesian coordinate description. From the very definition of q^i we have,

$$\frac{\mathrm{d}x^i}{\mathrm{d}\eta} = \frac{p^i}{p^0} = \frac{q^i}{a\epsilon}(1+\phi+\psi). \tag{2.22}$$

On the other hand the geodesic equation leads to,

$$\frac{\mathrm{d}q^i}{\mathrm{d}\eta} = -a\epsilon\,\partial_i\psi + q^i\partial_\eta\phi + (\hat{n}^i\hat{n}^j - \delta^{ij})\frac{q^2}{a\epsilon}\partial_j\phi, \tag{2.23}$$

where $q^2 = \delta_{ij}q^iq^j$ and $\hat{n}^i$ is the unit vector along the direction q^i,

$$\hat{n}^i = \frac{q^i}{q}. \tag{2.24}$$

The resulting Vlasov (or Liouville) equation takes the form,

$$\frac{\partial f}{\partial\eta} + (1+\phi+\psi)\,\frac{q^i}{a\epsilon}\partial_i f + a\epsilon\frac{\partial f}{\partial q^i}\left[-\partial_i\psi + \frac{q^i}{a\epsilon}\partial_\eta\phi + \left(\hat{n^i}\hat{n^j} - \delta^{ij}\right)\frac{q^2}{a^2\epsilon^2}\partial_j\phi\right] = 0. \tag{2.25}$$

By definition, the proper energy density ρ and the energy-momentum tensor are related by $\rho = -T^0_0$. As demonstrated in [4], ρ can thereby be expressed in terms of the distribution function,

$$\rho(\eta, \mathbf{x}) = \int \mathrm{d}^3q^i\,\frac{\epsilon f}{a^3}. \tag{2.26}$$

JCAP01(2014)030

Its evolution equation is obtained by integrating equation (2.25) with respect to d^3q^i with proper weight,

$$\partial_\eta\rho + (\mathcal{H} - \partial_\eta\phi)(3\rho + A^{ii}) + (1+\phi+\psi)\partial_i A^i + 2A^i\partial_i(\psi-\phi) = 0, \tag{2.27}$$

where the quantities $A^{ij\ldots k}$ are defined as,

$$A^{ij\ldots k}(\eta,\mathbf{x}) \equiv \int \mathrm{d}^3q^i \left[\frac{q^i}{a\epsilon}\frac{q^j}{a\epsilon}\ldots\frac{q^k}{a\epsilon}\right]\frac{\epsilon f}{a^3}. \tag{2.28}$$

As explicitly shown in appendix A, a complete hierarchy giving the evolution equations of $A^{ij\ldots k}$ can be obtained following the same idea.

2.3.2 The single-flow equations from the moments of the Boltzmann equation

The aim of this paragraph is to show that the motion equations we derived previously, (2.10) and (2.13), can alternatively be obtained from the Vlasov equation (2.25). This comparison requires to precise the physical meaning of the quantities defined in both approaches in order to explicitly relate them.

Let us start with the number density of particles. By definition, for any fluid, the *comoving* number density $n_c(\eta,\mathbf{x})$, i.e. the number of particles per comoving unit volume d^3x^i, is related to the distribution function f associated with this fluid thanks to

$$n_c(\eta,\mathbf{x}) = \int \mathrm{d}^3p_i\ f(\eta,x^i,p_i). \tag{2.29}$$

On the other hand, the *proper* number density $n(\eta,\mathbf{x})$, which is such that the proper energy density is given by $\rho(\eta,\mathbf{x}) = n(\eta,\mathbf{x})\epsilon(\eta,\mathbf{x})$, reads

$$n(\eta,\mathbf{x}) = \int \mathrm{d}^3q^i\ \frac{f(\eta,x^i,p_i)}{a^3} \tag{2.30}$$

to be in agreement with eq. (2.26). Given that $\mathrm{d}^3q^i = (1+3\phi)\mathrm{d}^3p_i$, the relation between $n_c(\eta,\mathbf{x})$ and $n(\eta,\mathbf{x})$ is therefore

$$n(\eta,\mathbf{x}) = \frac{1+3\phi(\eta,\mathbf{x})}{a^3}n_c(\eta,\mathbf{x}). \tag{2.31}$$

Similarly, the momentum field $P_i(\eta,\mathbf{x})$ can be defined as the average of the phase-space comoving momenta p_i. Using the distribution function to compute this mean value, one thus has

$$P_i(\eta,\mathbf{x})n_c(\eta,\mathbf{x}) = \int \mathrm{d}^3p_i\ f(\eta,x^i,p_i)p_i \quad\text{or}\quad P_i(\eta,\mathbf{x})n(\eta,\mathbf{x}) = \int \mathrm{d}^3q^i\ \frac{f(\eta,x^i,p_i)}{a^3}p_i. \tag{2.32}$$

In the particular case explored in this section, fluids are single flows so, for each of them,

$$f(\eta,x^i,p_i) = f^{\mathrm{one-flow}}(\eta,x^i,p_i) = n_c(\eta,\mathbf{x})\delta_{\mathrm{D}}(p_i - P_i(\eta,\mathbf{x})), \tag{2.33}$$

where δ_{D} is the Dirac distribution function. As a result we have, for any macroscopic field depending on $P_i(\eta,\mathbf{x})$, $\mathcal{F}[P_i(\eta,\mathbf{x})]$,

$$\mathcal{F}\left[P_i(\eta,\mathbf{x})\right]n_c(\eta,\mathbf{x}) = \int \mathrm{d}^3p_i\ f(\eta,x^i,p_i)\ \mathcal{F}\left[p_i\right]. \tag{2.34}$$

JCAP01(2014)030

Taking advantage of this, we proceed to show that the Vlasov and geodesic equations together with the relations (2.29), (2.32) and (2.34) allow to recover the equations of motion we derived previously. We first note that the field $P_0(\eta, \mathbf{x})$ defined previously as a function of $P_i(\eta, \mathbf{x})$ is nothing but

$$P_0(\eta, \mathbf{x}) n(\eta, \mathbf{x}) = \int \mathrm{d}^3 q^i \; \frac{f(\eta, x^i, p_i)}{a^3} p_0. \tag{2.35}$$

It is then easy to see that integration over $\mathrm{d}^3 p_i$ of the equation (2.19) gives

$$\partial_\eta n_c + \partial_i \left(\frac{P^i}{P^0} n_c \right) = 0, \tag{2.36}$$

which is exactly the first equation of motion, (2.9), after n_c is expressed in terms of n following eq. (2.31). Finally, it is also straightforward to show that the average (as defined by eq. (2.34)) of the geodesic equation (2.23) directly gives the second equation of motion when expressed in terms of P_i, eq. (2.13).

Note that conversely, it is possible to derive the hierarchy (A.3)–(A.5) from our equations of motion. For instance, the combination of eqs. (2.9) and (2.18) gives the following evolution equation for $\rho(\eta, \mathbf{x}) = n(\eta, \mathbf{x}) \epsilon(\eta, \mathbf{x})$,[6]

$$\partial_\eta \rho + \rho(\mathcal{H} - \partial_\eta \phi)(3 + V^2) + (1 + \phi + \psi) \partial_i (\rho V^i) + 2 \rho V^i \partial_i (\psi - \phi) = 0. \tag{2.37}$$

Given that $A(\eta, \mathbf{x}) = \rho(\eta, \mathbf{x})$ and that, for a single-flow fluid, the fields $A^{i_1 \cdots i_n}(\eta, \mathbf{x})$ are related to $A(\eta, \mathbf{x})$ by

$$A^i(\eta, \mathbf{x}) = V^i(\eta, \mathbf{x}) \, A(\eta, \mathbf{x}), \quad A^{ij}(\eta, \mathbf{x}) = V^i(\eta, \mathbf{x}) V^j(\eta, \mathbf{x}) \, A(\eta, \mathbf{x}), \quad \text{etc.}, \tag{2.38}$$

eq. (2.37) is exactly the average of eq. (2.27), i.e. eq. (2.27) multiplied by f/a^3, integrated over $\mathrm{d}^3 q^i$ and divided by n. It is then a simple exercise to check that the subsequent equations of the hierarchy can be similarly recovered with successive uses of eq. (2.16).

3 The single-flow equations in the linear regime

In this section we explore the system of motion equations (2.10)–(2.13) in the linear regime. It is useful in particular in order to properly set the initial conditions required to solve the system.

3.1 The zeroth order behavior

Let us start with the homogeneous quantities. It is straightforward to see that the zeroth order contribution of (2.10) is

$$\partial_\eta n^{(0)} = -3 \mathcal{H} n^{(0)}, \tag{3.1}$$

and that the unperturbed equation for P_i is (see eq. (2.13)),

$$\partial_\eta P_i^{(0)} = 0. \tag{3.2}$$

As a result the number density of particles is simply decreasing as $1/a^3$ and $P_i^{(0)}$ is constant. This latter result is attractive as it makes $P_i^{(0)}$ a good variable to label each flow. To take advantage of this property, we introduce a new variable, τ_i, defined as

$$\tau_i \equiv P_i^{(0)}(\eta) = P_i^{(0)}(\eta_{\mathrm{in}}), \tag{3.3}$$

[6] The energy field $\epsilon(\eta, \mathbf{x})$ satisfies $\epsilon(\eta, \mathbf{x}) n(\eta, \mathbf{x}) = \int \mathrm{d}^3 q^i \; \frac{f(\eta, \mathbf{x}, \mathbf{q})}{a^3} \epsilon(q)$.

JCAP01(2014)030

where $\eta_{\rm in}$ is the initial time. We also introduce the norm of τ_i, τ, given by

$$\tau = \sqrt{\delta_{ij}\tau_i\tau_j}. \tag{3.4}$$

Similarly, we define τ_0 as ${P_0}^{(0)}$. Note that this quantity is not constant over time. Given the sign convention for P_0 adopted in this paper, it satisfies

$$\tau_0 = -\sqrt{\tau^2 + m^2a^2}. \tag{3.5}$$

By definition, P_i is the comoving momentum so the fact that ${P_i}^{(0)}$ is constant does not conflict with the fact that the physical velocities of neutrinos - as well as the velocities of any other massive particles - are smoothed with time because of the expansion of the universe. At this stage, we can already note that,[7]

$${P_i}^{(0)} \sim \text{constant} \quad \text{and} \quad {P^i}^{(0)} \sim a^{-2}. \tag{3.6}$$

To be more comprehensive regarding notations, let us mention that the flows can alternatively be labeled by the zeroth order velocity, denoted v^i,

$$v^i = {V^i}^{(0)}. \tag{3.7}$$

It satisfies

$$v^i = \frac{\tau_i}{(m^2a^2+\tau^2)^{1/2}} = -\frac{\tau_i}{\tau_0}, \quad v^2 = \delta_{ij}v^iv^j \tag{3.8}$$

or alternatively,

$$\frac{\tau_i}{a} = \frac{mv^i}{\sqrt{1-v^2}}. \tag{3.9}$$

3.2 The first order behavior

We focus now on the first order system. In order to simplify the notations, we introduce the total first order derivative operator as,

$$\frac{\mathrm{d}X^{(1)}}{\mathrm{d}\eta} = \partial_\eta X^{(1)} + \frac{{P^i}^{(0)}}{{P^0}^{(0)}}\partial_i X^{(1)}. \tag{3.10}$$

It can be written alternatively,

$$\frac{\mathrm{d}X^{(1)}}{\mathrm{d}\eta} = \partial_\eta X^{(1)} - \frac{\tau_i}{\tau_0}\partial_i X^{(1)} = \partial_\eta X^{(1)} + v^i\partial_i X^{(1)}. \tag{3.11}$$

With this notation the first order equation of the number density reads,

$$\frac{\mathrm{d}n^{(1)}}{\mathrm{d}\eta} = 3\partial_\eta\phi n^{(0)} - 3\mathcal{H}n^{(1)} + (2\partial_i\psi - \partial_i\phi)\frac{\tau_i}{\tau_0}n^{(0)} + \left(\frac{\partial_i {P_i}^{(1)}}{\tau_0} - \frac{\tau_i\partial_i {P_0}^{(1)}}{\tau_0^2}\right)n^{(0)} \tag{3.12}$$

and that for the momentum is given by,

$$\frac{\mathrm{d}{P_i}^{(1)}}{\mathrm{d}\eta} = \tau_0\partial_i\psi + \frac{\tau^2}{\tau_0}\partial_i\phi. \tag{3.13}$$

[7] The behavior of the momentum variables with respect to the scale factor can also be deduced from the geodesic equation (see e.g. ref. [25]).

JCAP01(2014)030

The latter equation exhibits a crucial property: it shows that the source terms of the evolution of $P_i^{(1)}$ form a gradient field. As a consequence, although one cannot mathematically exclude the existence of a curl mode in $P_i^{(1)}$, such a mode is expected to be diluted by the expansion so that $P_i^{(1)}$ remains effectively potential. At linear order, this property should be rigorously exact for adiabatic initial conditions.[8]

As a consequence, the $P_i^{(1)}$ behavior is dictated by the gradient of $\tau_0\psi + \tau^2/\tau_0\phi$. It is not the case of other variables such as $P^{i(1)}$, which is a combination of $P_i^{(1)}$ and v^i. This is the reason we preferably write the motion equations in terms of this variable.

We close the system thanks to the on-shell normalization condition of P_μ, which gives the expression of P_0 at first order,

$$P_0^{(1)} = \frac{\tau_i P_i^{(1)}}{\tau_0} + \frac{\tau^2}{\tau_0}\,\phi + \tau_0\,\psi. \tag{3.14}$$

Eqs. (3.12) and (3.13) associated with relation (3.14) form a closed set of equations describing the first order evolution of a fluid of relativistic or non-relativistic particles.

3.3 The system in Fourier space

To explore the properties of the solution of the system (3.12)–(3.13)–(3.14), let us move to Fourier space. Each field is decomposed into Fourier modes using the following convention for the Fourier transform,

$$F(\mathbf{x}) = \int \frac{\mathrm{d}^3\mathbf{k}}{(2\pi)^{3/2}} F(\mathbf{k})\exp(\mathrm{i}\mathbf{k}.\mathbf{x}). \tag{3.15}$$

We will consider the Fourier transforms of the density contrast field $\delta_n(\mathbf{x})$

$$\delta_n(\mathbf{x}) = \frac{1}{n^{(0)}} n^{(1)}(\mathbf{x}), \tag{3.16}$$

of the divergence field,

$$\theta_P(\mathbf{x}) = \partial_i P_i^{(1)}, \tag{3.17}$$

and of the potentials. We can here take full advantage of the fact that P_i is potential at linear order. It indeed implies that ${P_i}^{(1)}$ is entirely characterized by its divergence,

$$P_i^{(1)}(\mathbf{k}) = \frac{-\mathrm{i}k_i}{k^2}\theta_P(\mathbf{k}). \tag{3.18}$$

After replacing equation (3.13) by its divergence, one finally obtains from equations (3.12) and (3.13)

$$\partial_\eta\delta_n = \mathrm{i}\mu k\frac{\tau}{\tau_0}\delta_n + 3\,\partial_\eta\phi + \frac{\theta_P}{\tau_0}\left(1 - \frac{\tau^2}{\tau_0^2}\mu^2\right) - \mathrm{i}\mu k\frac{\tau}{\tau_0}\left[\left(1 + \frac{\tau^2}{\tau_0^2}\right)\phi - \psi\right] \tag{3.19}$$

and

$$\partial_\eta\theta_P = \mathrm{i}\mu k\frac{\tau}{\tau_0}\theta_P - \tau_0 k^2\psi - \frac{\tau^2}{\tau_0}k^2\phi, \tag{3.20}$$

[8] But there is no guarantee it remains true to all orders in Perturbation Theory.

JCAP01(2014)030

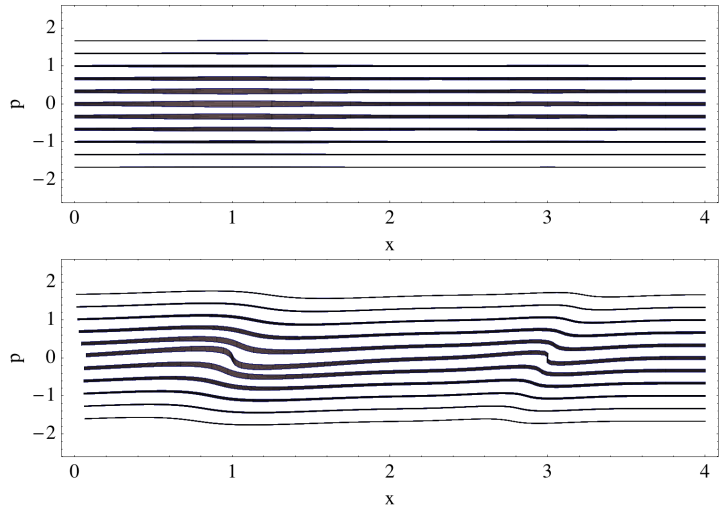

Figure 1. Sketch of 1D phase-space evolution. The top panel shows flows with initially no velocity gradients but density fluctuations (illustrated by the thickness variation of the lines). The bottom panel shows how the flows develop velocity gradients at later times. They can ultimately form multi-flow regions after they experience shell-crossing, in a way similar to what happens to dark matter flows. It is expected to happen preferably to flows with low initial velocities. Note that a flow with no initial velocity would behave exactly like a cold dark matter component.

where μ gives the relative angle between $\mathbf{k}$ and τ or alternatively between $\mathbf{k}$ and v,

$$\mu = \frac{\mathbf{k}.\tau}{k\tau} = \frac{\mathbf{k}.v}{k\,v}. \tag{3.21}$$

These equations can alternatively be written in terms of the zeroth order physical velocity v,

$$\partial_\eta \delta_n = -\mathrm{i}\mu k v\,\delta_n + 3\,\partial_\eta\phi - \sqrt{1-v^2}\left(1-v^2\mu^2\right)\frac{\theta_P}{ma} + \mathrm{i}\mu k v\left[\left(1+v^2\right)\phi - \psi\right], \tag{3.22}$$

$$\partial_\eta \theta_P = -\mathrm{i}\mu k v\,\theta_P + \frac{ma}{\sqrt{1-v^2}}k^2\left(v^2\phi + \psi\right). \tag{3.23}$$

This is this system that we encode in practice. As we will see, it provides a valid representation of a fluid of initially relativistic species. In the following, we explicitly show how it can be implemented numerically.

4 A multi-fluid description of neutrinos

In this section, we explain how one can define a collection of flows to describe the whole fluid of neutrinos. Note that this construction is valid for any given mass eigenstate of the neutrino fluid. If the masses are not degenerate, it should therefore be repeated for each three eigenstates.

4.1 Specificities of the multi-fluid description

In a multi-fluid approach, the overall distribution function is obtained taking several fluids into account (see figure 1 for illustration purpose). More precisely, the overall distribution

JCAP01(2014)030

function $f^{\rm tot}$ has to be reconstructed from the single flows labeled by τ_i,

$$f^{\rm tot}(\eta, x^i, p_i) = \sum_{\tau_i} f^{\rm one-flow}(\eta, x^i, p_i; \tau_i) = \sum_{\tau_i} n_c(\eta, \mathbf{x}; \tau_i)\delta_{\rm D}(p_i - P_i(\eta, \mathbf{x}; \tau_i)). \tag{4.1}$$

In the continuous limit, we thus have

$$f^{\rm tot}(\eta, x^i, p_i) = \int \mathrm{d}^3\tau_i \, n_c(\eta, \mathbf{x}; \tau_i)\delta_{\rm D}(p_i - P_i(\eta, \mathbf{x}; \tau_i)), \tag{4.2}$$

the parameter τ_i being assumed to describe a 3D continuous field.

It means in particular that the momentum integrations in phase-space used in the standard description (i.e. for a single multi-flow fluid) to compute global physical quantities should be replaced in our description by a sum over the τ_i-fluids (i.e. a sum over all the possible initial momenta or velocities),

$$\int \mathrm{d}^3 p_i \, f^{\rm tot}(\eta, x^i, p_i) \; \mathcal{F}(p_i) = \int \mathrm{d}^3\tau_i \, n_c(\eta, \mathbf{x}; \tau_i) \; \mathcal{F}(P_i(\eta, \mathbf{x}; \tau_i)) \tag{4.3}$$

or equivalently

$$\int \mathrm{d}^3 q^i \, \frac{f^{\rm tot}(\eta, x^i, q^i)}{a^3} \; \mathcal{F}(p_i) = \int \mathrm{d}^3\tau_i \, n(\eta, \mathbf{x}; \tau_i) \; \mathcal{F}(P_i(\eta, \mathbf{x}; \tau_i)) \tag{4.4}$$

for any function $\mathcal{F}$. For each flow, the evolution equations are known but we still have to set the initial conditions to be able to use them in practice, see 4.3. Before doing this, we will compute the multipole energy distribution associated with our description.

4.2 The multipole energy distribution in the linear regime

Of particular interest to compare our results to those of the Boltzmann approach is the computation of the overall multipole energy distribution. We will focus on the total energy density ρ_ν, the total energy flux dipole θ_ν and the total shear stress σ_ν. These quantities are directly related to the phase-space distribution function thanks to the following relations (see [4]),

$$\rho_\nu = -T^0{}_0 = \int \mathrm{d}^3 q^i \, \frac{\epsilon(q^i)}{a^3} f, \tag{4.5}$$

$$\left(\rho_\nu{}^{(0)} + P_\nu^{(0)}\right)\theta_\nu = \mathrm{i}k^i \Delta T^0{}_i = \mathrm{i}\Delta\left[\int \mathrm{d}^3 q^i \, \frac{k^j q^j}{a^4} f\right], \tag{4.6}$$

$$\begin{aligned}\left(\rho_\nu{}^{(0)} + P_\nu{}^{(0)}\right)\sigma_\nu &= -\left(\frac{k^i k^j}{k^2} - \frac{1}{3}\delta_{ij}\right)\left(\Delta T^i{}_j - \frac{1}{3}\delta^i_j \Delta T^k{}_k\right) \\ &= \frac{1}{3}\Delta\left[\int \mathrm{d}^3 q^i \, \frac{q^i q^j}{a^5 \epsilon(q^i)}\left(\delta^{ij} - 3\frac{k^i k^j}{k^2}\right) f\right],\end{aligned} \tag{4.7}$$

where $\rho_\nu^{(0)}$ and $P_\nu^{(0)}$ are the density and pressure of the neutrino fluid at background level and Δ stands for the perturbed part of the quantity it precedes.

JCAP01(2014)030

At linear order these quantities can be expressed with the help of the linear fields introduced in our description. More precisely, eq. (4.4) yields

$$\rho_\nu^{(1)} = 4\pi \int \tau^2 \mathrm{d}\tau \int_{-1}^{1} \mathrm{d}\mu \rho^{(1)}(\tau,\mu), \tag{4.8}$$

$$\left(\rho_\nu{}^{(0)} + P_\nu^{(0)}\right)\theta_\nu^{(1)} = 4\pi \mathrm{i} \int \tau^2 \mathrm{d}\tau \int_{-1}^{1} \mathrm{d}\mu \left[\rho^{(1)}(\tau,\mu) v(\tau,\mu)\mu k + \rho_\nu^{(0)}(\tau,\mu) k^i V^{i(1)}(\tau,\mu)\right], \tag{4.9}$$

$$\begin{aligned}\left(\rho_\nu{}^{(0)} + P_\nu{}^{(0)}\right)\sigma_\nu^{(1)} = &-4\pi \int \tau^2 \mathrm{d}\tau \int_{-1}^{1} \mathrm{d}\mu \left[\rho^{(1)}(\tau,\mu) v^2(\tau,\mu)\left(\mu^2 - \frac{1}{3}\right)\right] \\ &- 8\pi \int \tau^2 \mathrm{d}\tau \int_{-1}^{1} \mathrm{d}\mu \left[\rho^{(0)}(\tau,\mu) v(\tau,\mu)\left(\frac{\mu k^i V^{i(1)}(\tau,\mu)}{k} - \frac{V^{(1)}(\tau,\mu)}{3}\right)\right].\end{aligned} \tag{4.10}$$

For explicit calculation, note that $\rho^{(1)}(\tau,\mu) = n^{(1)}(\tau,\mu)\epsilon^{(0)}(\tau,\mu) + n^{(0)}(\tau,\mu)\epsilon^{(1)}(\tau,\mu)$, where

$$\epsilon^{(1)}(\tau,\mu) = \frac{m v^2(\tau,\mu)}{\sqrt{1 - v^2(\tau,\mu)}}\phi - \frac{\mathrm{i}\mu v(\tau,\mu)}{ak}\theta_P(\tau,\mu) \tag{4.11}$$

and that

$$V^{i(1)}(\tau,\mu) = (1 - v^2)v^i\phi - \frac{\mathrm{i}}{k^2}\frac{\sqrt{1-v^2}}{ma}\left(k^i - k^j v^j v^i\right)\theta_P(\tau,\mu). \tag{4.12}$$

The physical quantities $\rho_\nu^{(1)}$, $\theta_\nu^{(1)}$ and $\sigma_\nu^{(1)}$ are source terms generating the metric fluctuations involved in the growth of the large-scale structure of the universe. We use them to compare the predictions of the multi-fluid approach with those of the standard Boltzmann approach in section 4.4.

4.3 Initial conditions

The initial time $\eta_{\rm in}$ is chosen so that the neutrino decoupling occurs at a time $\eta < \eta_{\rm in}$ and neutrinos become non-relativistic at a time $\eta > \eta_{\rm in}$. The initial conditions depend obviously on the cosmological model adopted. In this paper, we describe solutions corresponding to adiabatic initial conditions. It imposes to the quantities $\theta_\nu^{(1)}$ and $\sigma_\nu^{(1)}$, defined by eqs. (4.9)–(4.10), to be zero but we still have some freedom in the way we assign each neutrino to one flow or to another. The initial conditions we present in the following correspond to a simple choice respecting the adiabaticity constraint.

4.3.1 Initial momentum field $P_i(\eta_{\rm in}, \mathbf{x}; \tau_i)$

The description we adopt is the following: at initial time we assign to the flow labeled by τ_i all the neutrinos whose momentum P_i is equal to τ_i within $\mathrm{d}^3\tau_i$. It obviously imposes

$$P_i(\eta_{\rm in}, \mathbf{x}; \tau_i) = \tau_i. \tag{4.13}$$

It implies in particular that $P_i^{(1)}(\mathbf{x}, \eta_{\rm in}; \tau_i) = 0$ and consequently that $\theta_P(\mathbf{x}, \eta_{\rm in}; \tau_i) = 0$.

JCAP01(2014)030

4.3.2 Initial number density field $n(\eta_{\rm in}, \mathbf{x}; \tau_i)$

Although the velocity fields are initially uniform, it is not the case of the individual numerical density fields as we expect the total numerical density field to depend on space coordinates at linear order.

Initial number densities are obviously strongly related to initial distribution functions in phase-space f. Before decoupling, the background distribution of neutrinos is expected to follow a Fermi-Dirac law f_0 with a temperature T and no chemical potential (see e.g. refs. [3–5, 25] for a physical justification of this assumption),

$$f_0\left(q\right) \propto \frac{1}{1+\exp\left[q/(ak_BT)\right]}, \tag{4.14}$$

where k_B is the Boltzmann constant and q is the norm - previously defined, see the geodesic equation (2.23) - of the phase-space variable q^i. As explained in ref. [25], after neutrino decoupling, the phase-space distribution function of relativistic neutrinos is still a Fermi-Dirac distribution but modified by local fluctuations of temperature, whence

$$f\left(\eta_{\rm in}, \mathbf{x}, q\right) \propto \frac{1}{1+\exp\left[q/(ak_B(T+\delta T(\eta_{\rm in}, \mathbf{x}))\right]}. \tag{4.15}$$

In terms of the variable p_i, it can be rewritten

$$f\left(\eta_{\rm in}, \mathbf{x}, p_i\right) \propto \frac{1}{1+\exp\left[p(1+\phi(\mathbf{x}, \eta_{\rm in}))/(ak_B(T+\delta T(\mathbf{x}, \eta_{\rm in})))\right]}. \tag{4.16}$$

Given eqs. (2.29) and (2.31) and recalling that f is non zero only for $p_i = \tau_i$ at initial time, the initial numerical density contrast follows directly,

$$\delta_n(\eta_{\rm in}, x^i; \tau_i) = \frac{f^{(1)}(\eta_{\rm in}, x^i, \tau_i)}{f^{(0)}(\eta_{\rm in}, x^i, \tau_i)} + 3\phi(\eta_{\rm in}, x^i). \tag{4.17}$$

The expression of $f^{(1)}(\eta, x^i, p_i)$ can be easily computed. It reads

$$f^{(1)}(\eta_{\rm in}, x^i, p) = \frac{p}{ak_BT}\left(\frac{\delta T(\eta_{\rm in}, x^i)}{T} - \phi(\eta_{\rm in}, x^i)\right)\frac{\exp[p/(ak_BT)]}{1+\exp[p/(ak_BT)]}\, f_0(p), \tag{4.18}$$

which can be reexpressed in the form,

$$f^{(1)}(\eta_{\rm in}, x^i, p) = -\left(\frac{\delta T(\eta_{\rm in}, x^i)}{T} - \phi(\eta_{\rm in}, x^i)\right)\frac{\mathrm{d}f_0(p)}{\mathrm{d}\log p}. \tag{4.19}$$

The last step of the calculation consists in relating the local initial temperature fluctuations to the metric fluctuations for adiabatic modes. As mentioned in [5], on super-Hubble scales, the temperature perturbation of the neutrino fluid is proportional to its density constrast: $4\delta T(\mathbf{x}, \eta_{\rm in})/T(\eta_{\rm in}) = \rho^{(1)}(\mathbf{x}, \eta_{\rm in})/\rho^{(0)}(\eta_{\rm in})$. Besides, the adiabaticity hypothesis imposes equality between the initial density contrasts of all species. Using the standard result that, for photons, $\rho_\gamma^{(1)}(\mathbf{x}, \eta_{\rm in})/\rho_\gamma^{(0)}(\eta_{\rm in}) = -2\psi(\mathbf{x}, \eta_{\rm in})$, one thus finds $\delta T(\mathbf{x}, \eta_{\rm in})/T(\eta_{\rm in}) = -\psi(\mathbf{x}, \eta_{\rm in})/2$. Besides, at super-Hubble scales, the neutrino distribution is static (see e.g. [4]). We finally get the following expression for the linearized initial number density fluctuations,

$$\delta_n(\eta_{\rm in}, \mathbf{x}; \tau_i) = 3\phi(\mathbf{x}, \eta_{\rm in}) + \left(\frac{\psi(\eta_{\rm in}, \mathbf{x})}{2} + \phi(\eta_{\rm in}, \mathbf{x})\right)\frac{\mathrm{d}\log f_0(\tau)}{\mathrm{d}\log\tau}. \tag{4.20}$$

It can then easily be checked from eqs. (4.8)–(4.10) that θ_ν and σ_ν both vanish at initial time with this choice of initial conditions.

JCAP01(2014)030

4.3.3 Early-time behavior

A remarkable property of the initial fields we just computed is that they are isotropic, i.e. they do not depend on μ. We know however that neutrinos develop an anisotropic pressure which is a source term of the Einstein equations. For practical purpose, e.g. to implement these calculations in a numerical code, it is therefore useful to examine in more detail the sub-leading behavior at initial time. To that aim, we study how higher order multipoles arise at early time by decomposing the μ dependence of the fields δ_n and θ_P into Legendre polynomials,

$$\delta_n(\eta, \mathbf{k}; \tau, \mu) = \sum_\ell \delta_{n,\ell}(\eta, \mathbf{k}; \tau)\ (-\mathrm{i})^\ell P_\ell(\mu) \tag{4.21}$$

and

$$\theta_P(\eta, \mathbf{k}; \tau, \mu) = \sum_\ell \theta_{P,\ell}(\eta, \mathbf{k}; \tau)\ (-\mathrm{i})^\ell P_\ell(\mu). \tag{4.22}$$

In order to properly compute the source terms of the Einstein equations, one needs to know the expression of the number density multipoles up to $\ell = 2$ and the one of the momentum divergence multipoles up to $\ell = 1$. The leading order behavior corresponding to these terms can be obtained easily from the motion equations (3.22)–(3.23) noting that ϕ and ψ are constant, $\mathcal{H}$ scales like $1/a$ and $\sqrt{1-v^2}$ scales like a at superhorizon scales for adiabatic initial conditions.

Once the equations of motion are decomposed into Legendre polynomials, one gets successively,

$$\theta_{P,0} = \frac{a}{\mathcal{H}} \frac{m}{\sqrt{1-v^2}} k^2\, (\phi + \psi) \tag{4.23}$$

$$\theta_{P,1} = \frac{k}{2\mathcal{H}}\ \theta_{P,0} \tag{4.24}$$

$$\delta_{n,0} = 3\phi + \left(\frac{\psi}{2} + \phi\right) \frac{\mathrm{d}\log f_0(\tau)}{\mathrm{d}\log\tau} \tag{4.25}$$

$$\delta_{n,1} = \frac{k}{\mathcal{H}}\left[\delta_{n,0} - \psi + 2\phi)\right] \tag{4.26}$$

$$\delta_{n,2} = -\frac{k}{3\mathcal{H}}\delta_{n,1} - (1-v^2)^{1/2}\frac{\theta_{P,0}}{3am\mathcal{H}}, \tag{4.27}$$

where $\theta_{P,\ell}$ scales like $a^{\ell+1}$ and $\delta_{n,\ell}$ scales like a^ℓ at leading order.

4.4 Numerical integration

This section aims at describing the numerical integration scheme developed to deal with a multi-fluid description and to compare its efficiency with that of the standard integration of the Boltzmann hierarchy. All the plots we will present to illustrate our findings are made using the WMAP5 cosmological parameters. In the following, the wave number values k are expressed in units of $k_{\mathrm{eq.}}$, where $k_{\mathrm{eq.}} \approx 0.01\, h/\mathrm{Mpc}$ is the horizon crossing wave number at matter-radiation equality. Similarly, the time dependence will be expressed in units of $a_{\mathrm{eq.}}$. Besides, convergence tests are realized for a neutrino mass of 0.05 eV or 0.3 eV.

4.4.1 Method

The equations of motion in Fourier space (3.22) and (3.23) are numerically integrated with the help of a Mathematica program in which the time evolution of the metric perturbations

JCAP01(2014)030

N_q (↓) and N_τ(→)	16	40	100
16	10^{-2}	$5\,10^{-3}$	$5\,10^{-3}$
40	10^{-2}	10^{-3}	$2\,10^{-4}$
100	10^{-2}	10^{-3}	10^{-4}

Table 1. Relative errors (averaged in time between $a/a_{\rm eq} = 10^{-2}$ and $a/a_{\rm eq} = 10^3$) between the results obtained with the Boltzmann hierarchy and those obtained with the multi-fluid approach. For each value of N_q and N_τ, the largest magnitude of the relative error on either the density, the dipole or the shear is given. Calculations are made with $N_\mu = 12$, $\ell_{\rm max} = 6$, $k = 0.2\,k_{\rm eq.}$ and $m = 0.05\,{\rm eV}$.

is given. It is as usual determined by the Einstein equations but in practice simply extracted from a standard Boltzmann code (the code presented in [26]). The initial conditions we implement correspond to the adiabatic expressions appearing in eqs. (4.23)–(4.27). The main objective of this numerical experiment is to check that the multipole energy distributions are identical when computed from the resolution of the Boltzmann hierarchy or from the equations of the multi-fluid description. In appendix A, we succinctly review the construction of the Boltzmann hierarchy. In this approach, energy multipoles are computed thanks to eqs. (A.10)–(A.15). The angular dependence of q^i is taken into account via the Legendre polynomials used to decompose the distribution function in phase-space. Of course, because of the integration on d^3q^i necessary to compute the multipoles, the amplitude of q has to be discretized for numerical integration.

In the multi-fluid description, integrals that appear in the distribution energy (4.8)–(4.10) also involve a discretization on momentum directions, i.e. a discretization on μ. In both approaches, all integrals are estimated using the third degree Newton-Cotes formula (Boole's rule) which consists in approximating $\int_{x_1}^{x_5} \mathrm{d}x$ by,

$$\int_{x_1}^{x_5} f(x)\mathrm{d}x \approx \frac{2h}{45}[7f(x_1) + 32f(x_2) + 12f(x_3) + 32f(x_4) + 7f(x_5)], \tag{4.28}$$

that is to say in using five discrete values regularly spaced, i.e. $x_{1+n} = x_1 + nh$, $h = (x_5 - x_1)/4$, to compute the integral. In such a scheme, which gives exact results when integrating polynomials of order less than 6, the error term is proportional to h^7. In practice, we divide the τ, q and μ ranges into respectively N_τ, N_q and N_μ intervals - where N_τ, N_q and N_μ are multiples of four - and we apply the integration scheme $N_\tau/4$, $N_q/4$ and $N_\mu/4$ times. Besides, since the Fourier modes computed for μ and $-\mu$ are conjugate complex numbers when the initial gravitational potentials are real, we can restrict our calculations to the range $[0, 1]$ for μ.

4.4.2 Results

We first compare the consistency of the two approaches by varying N_τ and N_μ on one side and N_q and $\ell_{\rm max}$ on the other side, where $\ell_{\rm max}$ is the order at which the Boltzmann hierarchy is truncated. Preliminary results are presented on table 1 and on figure 2.

They show that the values computed in both descriptions can reach an extremely good agreement. For example, $N_q = N_\tau = 40$, $N_\mu = 12$ and $\ell_{\rm max} = 6$ give for $k = 0.2\,k_{\rm eq.}$ and $m = 0.05\,{\rm eV}$ a 10^{-3} accuracy. However, the relative performances of the two methods actually depend on wave numbers. Indeed, table 1 and figure 2 correspond to particular cases for which there are no or very few oscillations in the neutrino fluid (due to the relatively small

JCAP01(2014)030

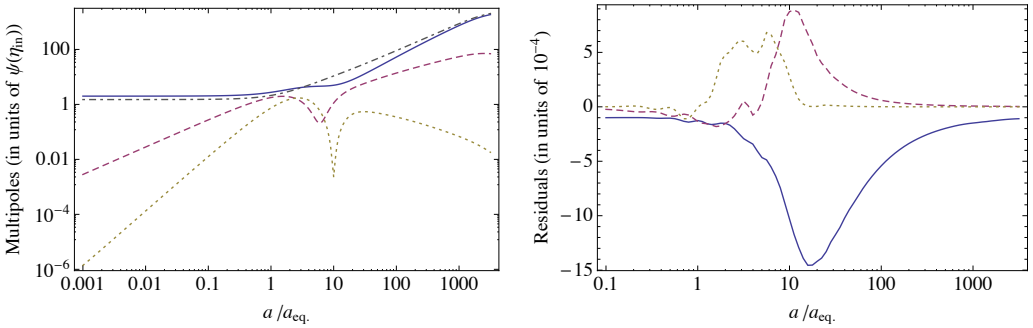

Figure 2. Time evolution of the energy density contrast (solid line), velocity divergence (dashed line) and shear stress (dotted line) of the neutrinos. The dot-dashed line is presented for comparison and corresponds to the density contrast of the dark matter component. Left panel: the quantities are computed with the multi-fluid approach. Right panel: residuals (defined as the relative differences) when the two methods are compared. Numerical integration has been done with 40 values of τ and q, k is set to $k_{\rm eq.}$ and m is set to 0.3 eV. The resulting relative differences are of the order of 10^{-3}.

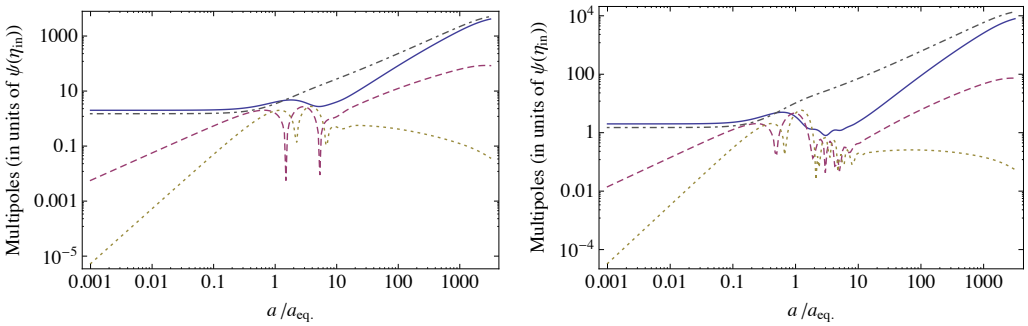

Figure 3. Same as left panel of figure 2 (with adapted values of N_τ and N_q) for $k = 2\,k_{\rm eq.}$ and $k = 5\,k_{\rm eq.}$.

value of the wave number and, for figure 2, to the quite large value of the neutrino mass). In such a situation, the main limitation in the relative precision is the number of points we put in the τ or q intervals. With 16 values for each, only percent accuracy is reached for $k = 0.2\,k_{\rm eq.}$ and $m = 0.05\,$eV (see table 1 for more details regarding the relative precision one can get). Meanwhile, the parameters N_μ and $\ell_{\rm max}$ do not appear as critical limiting factors in the accuracy of the numerical integration, provided of course that they are not too small. For instance, with $N_\mu = 12$, the numerical scheme (4.28) allows to reach an exquisite accuracy and with $N_\mu = 8$, it is still possible to reach 10^{-3}. These tests show that the extra cost of the use of our representation, where neutrinos are described by a set of $2 \times N_\mu \times N_\tau$ equations instead of $\ell_{\rm max} \times N_q$, is not dramatically large if $k \lesssim k_{\rm eq.}$.

For larger values of k (or smaller neutrino masses), the field values experience rapid oscillations during a significant time interval (as seen on figure 3). Time integrations become then particularly long as the system is becoming stiffer. Furthermore, at fixed times, the field amplitudes depend more significantly on the momentum, both on its amplitude and on its direction, making necessary the improvement of the discretization scheme resolution. This

JCAP01(2014)030

phenomenon is illustrated on figure 4, where the μ dependence of the total energy density is presented[9] at fixed times $a/a_{\rm eq.} = 10$ and $a/a_{\rm eq.} = 100$. Clearly, as k increases, a better resolution in μ is required (up to $N_\mu = 100$ for a percent resolution if $k \approx 10\, k_{\rm eq.}$). Similarly a better resolution in q is necessary (for both schemes). We leave for further studies a more thorough analysis of the numerical requirements.

To finish, we illustrate the fact that the multi-fluid approach, by its specificity, allows to show the convergence of the number density contrast and of the velocity divergence of each flow to the ones of the Cold Dark Matter (CDM) component. Let us remind that each flow is characterized by two parameters: its initial momentum modulus τ and μ, the cosine of the angle between its initial velocity vector v^i and the wave vector k^i. Unsurprisingly, for a fixed mass, the smaller the initial momentum τ is, the quicker the convergence takes place. This is illustrated on the left panels of figures 5 and 6, which show the convergence of the fluctuation amplitudes of several neutrino flows to those of the dark matter component when μ is set to zero.[10] The convergence is also more rapid when, for a fixed momentum, the neutrino mass is larger, as illustrated by the difference between the solid and the dashed lines of these figures. Concurrently, the right panels show that the way this convergence takes place is strongly dependent on the value of μ, this convergence exhibiting non trivial patterns when $\mu \neq 0$. In that case, the fluctuations of the neutrino flows and of the CDM component are indeed expected to be out of phase, in particular during the oscillatory periods. This phenomenon is particularly important for $\mu \neq 0$, but only partially visible on these plots as they give only the real values of complex Fourier modes. A consequence of this complex dependence is that, after integration over μ, the resulting number density and velocity divergence are largely suppressed compared to those of the CDM component (as can be seen on the left panel of figure 2 and on figure 3, to be compared e.g. to figure 11 of [5]). Finally, let us remark that the convergence of the velocity divergence is more rapid than the one of the number density. It simply illustrates the fact that the former acts as a source term of the latter in the motion equations.

5 Conclusions

We have developed an alternative approach to the method based on the Boltzmann hierarchy to account for massive neutrinos in non-linear cosmological calculations. In this new description, neutrinos are treated as a collection of single-flow fluids and their behavior is encoded in fluid equations derived from conservation laws or from the evolution of the phase-space distribution function. The resulting fluid equations, (2.10) and (2.13), are derived at linear level with respect to the metric perturbations but at full non-linear level with respect to the density fluctuations and velocity divergences. They can easily be compared to the equations resulting from the standard study of the distribution function of a single hot fluid of dark matter particles. In both cases, equations describe single-flow fluids so shell-crossing is beyond the scope of this kind of study. After having considered in detail these equations in the linear regime, we have shown precisely how a proper choice of the single-flow fluids and a proper choice of the initial conditions allow to recover the physical behavior of the overall neutrino fluid. These initial conditions are given explicitly in the case of initially adiabatic metric perturbations.

[9] More precisely, it corresponds to $\rho^{(1)}(\mu) = 4\pi \int \tau^2 {\rm d}\tau \rho^{(1)}(\tau, \mu)$.

[10] The velocity divergence that appears on figure 5 is related to the momentum divergence by eq. (4.12).

JCAP01(2014)030

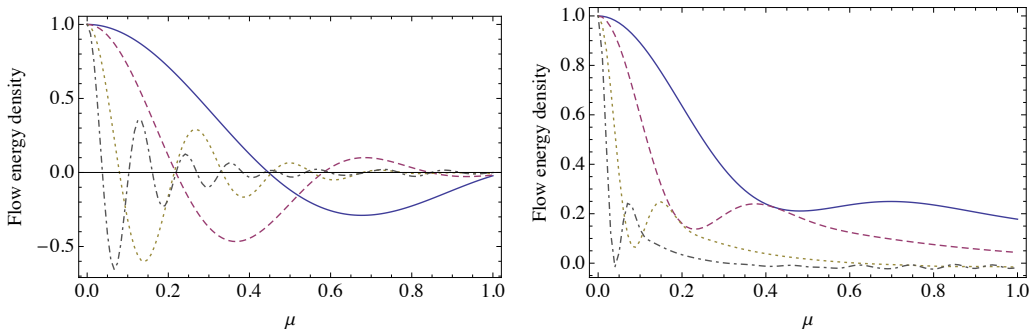

Figure 4. Angular dependence of the neutrino energy fluctuations. The amplitude is arbitrarily set to unity for $\mu = 0$. It is computed for a neutrino mass $m = 0.3\,\mathrm{eV}$. The left panel corresponds to a time where $a/a_{\mathrm{eq.}} = 10$ and the right panel to $a/a_{\mathrm{eq.}} = 100$. The wave numbers associated with the solid, dashed, dotted and dot-dashed lines are respectively $k = k_{\mathrm{eq.}}$, $k = 2\,k_{\mathrm{eq.}}$, $k = 5\,k_{\mathrm{eq.}}$ and $k = 10\,k_{\mathrm{eq.}}$.

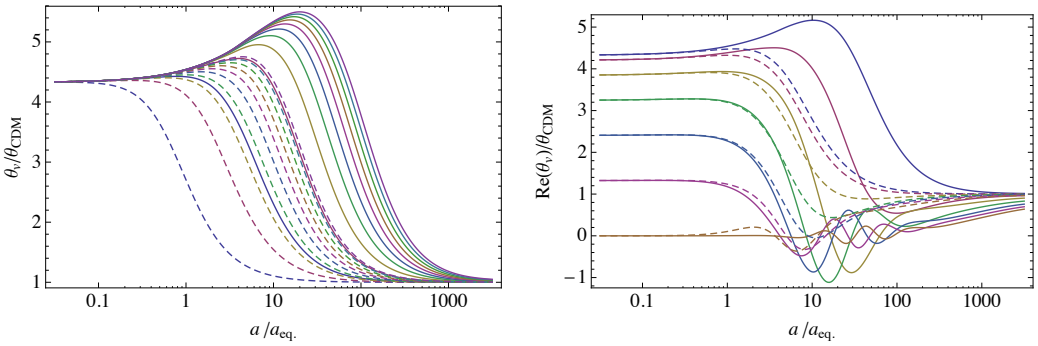

Figure 5. Time evolution of the velocity divergence. Left panel: values of τ range from $0.45\,k_B T_0$ (bottom lines) to $9\,k_B T_0$ (top lines) with $\mu = 0$. Right panel is for $\tau = 3.6\,k_B T_0$ and μ ranging from $\mu = 0$ (top lines) to $\mu = 1$ (bottom lines). The time evolution of the velocity divergence of each flow is plotted in units of the dark matter velocity divergence. The wave number is set to $k = k_{\mathrm{eq.}}$, the solid lines correspond to a 0.05 eV neutrino mass and the dashed lines to a 0.3 eV neutrino mass.

We then check that the two descriptions are equivalent at linear level through numerical experiments. The conclusion is that the whole macroscopic properties of the neutrino fluid can actually be accounted for by studying such a collection of flows with an arbitrary precision (in practice we reached a 10^{-5} relative precision). An additional information exists in our approach since it also describes the physics of each flow separately. We illustrate this point by showing how individual neutrino flows converge to the CDM component as a function of their initial momentum and of the neutrino mass at play.

This representation opens the way to a genuine and fully non-linear treatment of the neutrino fluid during the late stage of the large-scale structure growth - as long as shell-crossing can be neglected - since the two evolution equations satisfied by each flow can be incorporated separately into the equations describing the non-linear dynamics of this growth. In particular, it should be possible to apply resummation techniques such as those introduced in [27–29] or to incorporate the neutrino component at non-linear level in approaches such as [30, 31]. We leave for future work the examination of the importance of non-linear effects on observables such as power spectra.

JCAP01(2014)030

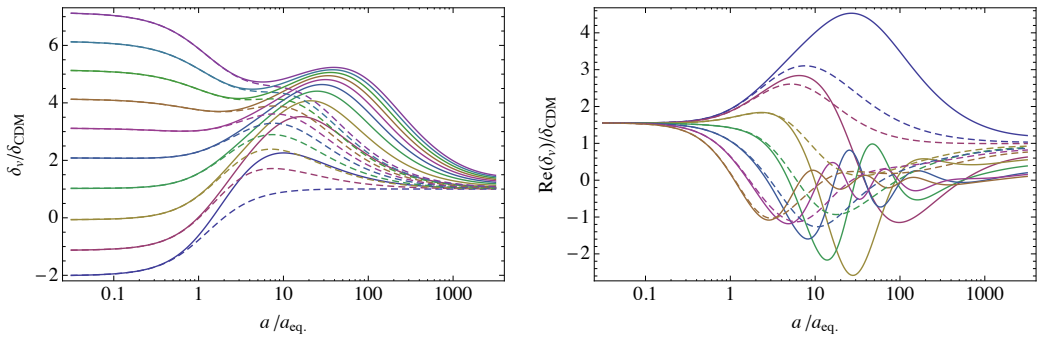

Figure 6. Same as the previous plot for the *number* density contrast.

Acknowledgments

The authors are grateful to Cyril Pitrou, Jean-Philippe Uzan, Pierre Fleury, Romain Teyssier and Atsushi Taruya for insightful discussions and encouragements. FB also thanks the YITP of the university of Kyoto and the RESCUE of the university of Tokyo for hospitality during the completion of this manuscript. This work is partially supported by the grant ANR-12-BS05-0002 of the French Agence Nationale de la Recherche.

A The Boltzmann hierarchies

Starting from the Vlasov equation (2.25), one can build hierarchies to describe the evolution of the moments of the phase-space distribution function. There are several ways to do this.

A.1 A Boltzmann hierarchy from tensor field expansion

A first hierarchy can be built by integrating equation (2.25) with respect to $\mathrm{d}^3\mathbf{q}$, weighted by products of $\frac{q^i}{a\epsilon}$. To that end, it is useful to introduce the tensorial fields A, A^i, A^{ij},... defined as (see [23])

$$A \equiv \rho, \tag{A.1}$$

$$A^{ij\ldots k} \equiv \int \mathrm{d}^3\mathbf{q} \left[\frac{q^i}{a\epsilon}\frac{q^j}{a\epsilon}\ldots\frac{q^k}{a\epsilon}\right]\frac{\epsilon f}{a^3}. \tag{A.2}$$

After multiplying eq. (2.25) by adequate factors such as ϵ/a^3, $\epsilon/a^3\, q^i/(a\epsilon)$ and in general $\epsilon/a^3\, q^{i_1}/(a\epsilon)\ldots q^{i_n}/(a\epsilon)$, integrations by parts directly give the desired hierarchy of equations. For A it leads to

$$\partial_\eta A + (\mathcal{H} - \partial_\eta\phi)(3A + A^{ii}) + (1+\phi+\psi)\partial_i A^i + 2A^i\partial_i(\psi-\phi) = 0, \tag{A.3}$$

for A^i it leads to,

$$\partial_\eta A^i + 4(\mathcal{H} - \partial_\eta\phi)A^i + (1+\phi+\psi)\partial_j A^{ij} + A\partial_i\psi + A^{ij}\partial_j\psi - 3A^{ij}\partial_j\phi + A^{jj}\partial_i\phi = 0, \tag{A.4}$$

JCAP01(2014)030

and in general it leads to the following equation,

$$\partial_\eta A^{i_1\dots i_n} + (\mathcal{H} - \partial_\eta\phi)\left[(n+3)A^{i_1\dots i_n} - (n-1)A^{i_1\dots i_n jj}\right] + \sum_{m=1}^{n}(\partial_{i_m}\psi)A^{i_1\dots i_{m-1}i_{m+1}\dots i_n} + \sum_{m=1}^{n}(\partial_{i_m}\phi)A^{i_1\dots i_{m-1}i_{m+1}\dots i_n jj} + (1+\phi+\psi)\partial_j A^{i_1\dots i_n j} + \left[(2-n)\partial_j\psi - (2+n)\partial_j\phi\right]A^{i_1\dots i_n j} = 0 \tag{A.5}$$

Note that this hierarchy of coupled equations retains the same level of non-linearities as eqs. (2.10) and (2.13). Once linearized, it is equivalent to the standard hierarchy of equations describing the multipole decomposition of the distribution function perturbation as given below.

A.2 A Boltzmann hierarchy from harmonic expansion

We recall here the standard construction of the Boltzmann hierarchy, i.e. of the hierarchy that Boltzmann codes usually implement (see refs. [3–5, 23] for more details). It is based on a decomposition of the phase-space distribution function $f(\mathbf{x},\mathbf{q})$ into a homogeneous part and an inhomogeneous contribution,

$$f(\mathbf{x},\mathbf{q}) = f_0(q)\left[1+\Psi(\mathbf{x},\mathbf{q})\right] \tag{A.6}$$

and a decomposition of the latter into harmonic functions. At linear order, the Vlasov equation for f (2.25) leads to the following equation for Ψ,

$$\partial_\eta\Psi + \frac{q}{a\epsilon}\hat{n}^i\partial_i\Psi + \frac{\mathrm{d}\log f_0(q)}{\mathrm{d}\log q}\left(\partial_\eta\phi - \frac{a\epsilon}{q}\hat{n}^i\partial_i\psi\right) = 0, \tag{A.7}$$

where the local momentum is defined trough its norm q and its direction $\hat{n}$. In momentum space, the only dependence on $\mathbf{k}$ is through its angle with $\hat{n}$, so we define $\alpha \equiv \hat{k}.\hat{n}$ and rewrite the linearized Boltzmann equation as

$$\partial_\eta\tilde{\Psi} + \mathrm{i}\alpha k\frac{q}{a\epsilon}\tilde{\Psi} + \left(\partial_\eta\phi - \mathrm{i}\alpha k\frac{a\epsilon}{q}\psi\right) = 0, \tag{A.8}$$

where $\tilde{\Psi} \equiv \left(\frac{\mathrm{d}\log f_0(q)}{\mathrm{d}\log q}\right)^{-1}\Psi$. The next step is to expand $\tilde{\Psi}$ using Legendre polynomials thus we introduce the moments $\tilde{\Psi}_\ell$,

$$\tilde{\Psi} = \sum_\ell(-\mathrm{i})^\ell\tilde{\Psi}_\ell\,P_\ell(\alpha), \tag{A.9}$$

where $P_\ell(\alpha)$ is the Legendre polynomial of order ℓ. By plugging this expansion into the Boltzmann equation (A.8), one obtains the standard hierarchy,

$$\partial_\eta\tilde{\Psi}_0(\eta,q) = -\frac{qk}{3a\epsilon}\tilde{\Psi}_1(\eta,q) - \partial_\eta\phi(\eta) \tag{A.10}$$

$$\partial_\eta\tilde{\Psi}_1(\eta,q) = \frac{qk}{a\epsilon}\left(\tilde{\Psi}_0(\eta,q) - \frac{2}{5}\tilde{\Psi}_2(\eta,q)\right) - \frac{a\epsilon k}{q}\psi(\eta), \tag{A.11}$$

$$\partial_\eta\tilde{\Psi}_\ell(\eta,q) = \frac{qk}{a\epsilon}\left[\frac{\ell}{2\ell-1}\tilde{\Psi}_{\ell-1}(\eta,q) - \frac{\ell+1}{2\ell+3}\tilde{\Psi}_{\ell+1}(\eta,q)\right] \quad (\ell \geq 2). \tag{A.12}$$

JCAP01(2014)030

Since this hierarchy is infinite, it is of course necessary to truncate it at a given order for practical implementation. Finally, relevant physical quantities can be built out of the coefficients $\tilde{\Psi}_\ell(\eta, q)$,

$$\rho_\nu^{(1)}(\eta) = 4\pi \int q^2 \mathrm{d}q \frac{\epsilon f_0(q)}{a^3} \frac{\mathrm{d}\log f_0(q)}{\mathrm{d}\log q} \tilde{\Psi}_0(\eta, q) \tag{A.13}$$

$$(\rho_\nu^{(0)} + P_\nu^{(0)})\theta_\nu^{(1)}(\eta) = \frac{4\pi}{3} \int q^2 \mathrm{d}q \frac{\epsilon f_0(q)}{a^3} \frac{\mathrm{d}\log f_0(q)}{\mathrm{d}\log q} \frac{q}{a\epsilon} \tilde{\Psi}_1(\eta, q) \tag{A.14}$$

$$(\rho_\nu^{(0)} + P_\nu^{(0)})\sigma_\nu^{(1)}(\eta) = \frac{8\pi}{15} \int q^2 \mathrm{d}q \frac{\epsilon f_0(q)}{a^3} \frac{\mathrm{d}\log f_0(q)}{\mathrm{d}\log q} \left(\frac{q}{a\epsilon}\right)^2 \tilde{\Psi}_2(\eta, q). \tag{A.15}$$

Note that as the numerical integration of the Boltzmann hierarchy gives access to $\tilde{\Psi}_\ell$, expressions of $\rho^{(1)}(\eta)$, $\theta_\nu^{(1)}$ and $\sigma_\nu^{(1)}$ are computed from eqs. (A.13)–(A.15).

References

[1] Planck collaboration, P.A.R. Ade et al., *Planck 2013 results. I. Overview of products and scientific results*, arXiv:1303.5062 [INSPIRE].

[2] Planck collaboration, P.A.R. Ade et al., *Planck 2013 results. XVI. Cosmological parameters*, arXiv:1303.5076 [INSPIRE].

[3] C.-P. Ma and E. Bertschinger, *A Calculation of the full neutrino phase space in cold + hot dark matter models*, *Astrophys. J.* **429** (1994) 22 [astro-ph/9308006] [INSPIRE].

[4] C.-P. Ma and E. Bertschinger, *Cosmological perturbation theory in the synchronous and conformal Newtonian gauges*, *Astrophys. J.* **455** (1995) 7 [astro-ph/9506072] [INSPIRE].

[5] J. Lesgourgues and S. Pastor, *Massive neutrinos and cosmology*, *Phys. Rept.* **429** (2006) 307 [astro-ph/0603494] [INSPIRE].

[6] S. Saito, M. Takada and A. Taruya, *Neutrino mass constraint with the Sloan Digital Sky Survey power spectrum of luminous red galaxies and perturbation theory*, *Phys. Rev.* **D 83** (2011) 043529 [arXiv:1006.4845] [INSPIRE].

[7] S. Riemer-Sørensen et al., *The WiggleZ Dark Energy Survey: Cosmological neutrino mass constraint from blue high-redshift galaxies*, *Phys. Rev.* **D 85** (2012) 081101 [arXiv:1112.4940] [INSPIRE].

[8] B. Audren, J. Lesgourgues, S. Bird, M.G. Haehnelt and M. Viel, *Neutrino masses and cosmological parameters from a Euclid-like survey: Markov Chain Monte Carlo forecasts including theoretical errors*, *JCAP* **01** (2013) 026 [arXiv:1210.2194] [INSPIRE].

[9] C. Carbone, L. Verde, Y. Wang and A. Cimatti, *Neutrino constraints from future nearly all-sky spectroscopic galaxy surveys*, *JCAP* **03** (2011) 030 [arXiv:1012.2868] [INSPIRE].

[10] EUCLID collaboration, R. Laureijs et al., *Euclid Definition Study Report*, arXiv:1110.3193 [INSPIRE].

[11] I. Tereno, C. Schimd, J.-P. Uzan, M. Kilbinger, F.H. Vincent and L. Fu, *CFHTLS weak-lensing constraints on the neutrino masses*, *Astron. Astrophys.* **500** (2009) 657 [arXiv:0810.0555] [INSPIRE].

[12] L. Kofman, A. Klypin, D. Pogosian and J.P. Henry, *Mixed dark matter in halos of clusters*, *Astrophys. J.* **470** (1996) 102 [astro-ph/9509145] [INSPIRE].

[13] J. Brandbyge, S. Hannestad, T. Haugbølle and Y.Y.Y. Wong, *Neutrinos in Non-linear Structure Formation - The Effect on Halo Properties*, *JCAP* **09** (2010) 014 [arXiv:1004.4105] [INSPIRE].

JCAP01(2014)030

[14] S. Bird, M. Viel and M.G. Haehnelt, *Massive Neutrinos and the Non-linear Matter Power Spectrum*, *Mon. Not. Roy. Astron. Soc.* **420** (2012) 2551 [arXiv:1109.4416] [INSPIRE].

[15] S. Hannestad, T. Haugbølle and C. Schultz, *Neutrinos in Non-linear Structure Formation - a Simple SPH Approach*, *JCAP* **02** (2012) 045 [arXiv:1110.1257] [INSPIRE].

[16] Y. Ali-Haimoud and S. Bird, *An efficient implementation of massive neutrinos in non-linear structure formation simulations*, *Mon. Not. Roy. Astron. Soc.* **428** (2013) 3375 [arXiv:1209.0461] [INSPIRE].

[17] J. Lesgourgues, S. Matarrese, M. Pietroni and A. Riotto, *Non-linear Power Spectrum including Massive Neutrinos: the Time-RG Flow Approach*, *JCAP* **06** (2009) 017 [arXiv:0901.4550] [INSPIRE].

[18] S. Saito, M. Takada and A. Taruya, *Nonlinear power spectrum in the presence of massive neutrinos: perturbation theory approach, galaxy bias and parameter forecasts*, *Phys. Rev.* **D 80** (2009) 083528 [arXiv:0907.2922] [INSPIRE].

[19] Y.Y.Y. Wong, *Higher order corrections to the large scale matter power spectrum in the presence of massive neutrinos*, *JCAP* **10** (2008) 035 [arXiv:0809.0693] [INSPIRE].

[20] S. Saito, M. Takada and A. Taruya, *Impact of massive neutrinos on nonlinear matter power spectrum*, *Phys. Rev. Lett.* **100** (2008) 191301 [arXiv:0801.0607] [INSPIRE].

[21] K. Benabed and F. Bernardeau, *Testing quintessence models with large scale structure growth*, *Phys. Rev.* **D 64** (2001) 083501 [astro-ph/0104371] [INSPIRE].

[22] M. Shoji and E. Komatsu, *Massive Neutrinos in Cosmology: Analytic Solutions and Fluid Approximation*, *Phys. Rev.* **D 81** (2010) 123516 [*Erratum ibid.* **D 82** (2010) 089901] [arXiv:1003.0942] [INSPIRE].

[23] N. Van de Rijt, Signatures of the primordial universe in large-scale structure surveys, Ph.D thesis, École Polytechnique & Institut de Physique Théorique, CEA Saclay, Gif-sur-Yvette Cedex France (2012).

[24] F. Bernardeau, *The evolution of the large-scale structure of the universe: beyond the linear regime*, arXiv:1311.2724 [INSPIRE].

[25] J. Lesgourgues, G. Mangano, G. Miele and S. Pastor, *Neutrino Cosmology*, Cambridge University Press (2013).

[26] C. Pitrou, *CMBquick: Spectrum and Bispectrum of Cosmic Microwave Background (CMB)*, Astrophysics Source Code Library ascl:1109.009.

[27] M. Crocce and R. Scoccimarro, *Renormalized cosmological perturbation theory*, *Phys. Rev.* **D 73** (2006) 063519 [astro-ph/0509418] [INSPIRE].

[28] F. Bernardeau, N. Van de Rijt and F. Vernizzi, *Resummed propagators in multi-component cosmic fluids with the eikonal approximation*, *Phys. Rev.* **D 85** (2012) 063509 [arXiv:1109.3400] [INSPIRE].

[29] F. Bernardeau, N. Van de Rijt and F. Vernizzi, *Power spectra in the eikonal approximation with adiabatic and non-adiabatic modes*, *Phys. Rev.* **D 87** (2013) 043530 [arXiv:1209.3662] [INSPIRE].

[30] M. Pietroni, *Flowing with Time: a New Approach to Nonlinear Cosmological Perturbations*, *JCAP* **10** (2008) 036 [arXiv:0806.0971] [INSPIRE].

[31] A. Taruya and T. Hiramatsu, *A Closure Theory for Non-linear Evolution of Cosmological Power Spectra*, *Astrophys. J.* **674** (2008) 617 [arXiv:0708.1367] [INSPIRE].

JCAP01(2014)030

Chapter 5

Towards a relativistic generalization of nonlinear perturbation theory

In this chapter, the previously described multi-fluid approach is used to extend the scope of application of some standard results of nonlinear perturbation theory. In particular, I highlight analogies between the subhorizon limit of our nonlinear equations of motion and the equations describing cold pressureless fluids. I also show that it is possible to take inspiration of the Newtonian approach to identify and exploit invariance properties. Full details are given in the article of section 5.4.

5.1 Generic form of the relativistic equations of motion

In section 4.2.3, the equation reflecting the conservation of the number of particles in each flow, (4.19), has been derived without writing explicitly the metric. It is thus valid in any gauge. Besides, it does not rely on any approximation.

Similarly, the method presented in section 4.2.2 is valid in any metric $g_{\alpha\beta}$. It is then easy to show that the universal equation of motion of the comoving momentum is

$$P^\nu \partial_\nu P_i = \frac{1}{2} P^\sigma P^\nu \partial_i g_{\sigma\nu}. \tag{5.1}$$

The system {(4.19), (5.1)} is actually an exact representation of the time evolution of a single-flow fluid, relativistic or not, provided that it interacts only grav-

itationally. In cosmology, it can thus describe the time evolution of any decoupled species as long as shell crossing can be neglected (whence the necessity of defining several neutrino species in our approach). It must be supplemented, on the one hand, with general initial conditions (the ones adapted to flows of massive neutrinos are given in the paper of section 5.4) and, on the other hand, with the Einstein equations, which read in this context (in the absence of a cosmological constant, see the demonstration in section 5.4)

$$G_{\mu\nu}(\eta, x^i) = 8\pi G \sum_{\text{species and flows}} \frac{P_\mu P_\nu}{(-g)^{1/2} P^0} n_c, \tag{5.2}$$

where $G_{\mu\nu}$ is the Einstein tensor[1].

5.2 Useful properties in the subhorizon limit

Equations (4.19) and (5.1) have the advantage of being very general. Yet, they contain many coupling terms. In order to make them easier to manipulate (in the light of the handy equation (3.16)), we decided to eliminate the coupling terms that are not indispensable for the description of structure formation. More precisely, we used the Hubble radius[2] as characteristic scale and focused on subhorizon scales, i.e. on scales smaller than the Hubble radius. Indeed, the nonlinear growth of structure being a late-time event, the terms that become evanescent on subhorizon scales are *a priori* not determining in this context. Those terms are easy to identify in reciprocal space by putting conditions on the highest power of $k_{\mathcal{H}}/k$ taken into account, $k_{\mathcal{H}}$ being the inverse of the Hubble radius (see more details in our paper). When calculations are performed in a generic perturbed Friedmann-Lemaître metric (3.1), the subhorizon limit of the equations of motion eventually takes the form[3]

[1] $G_{\mu\nu} = R_{\mu\nu} - \frac{1}{2} R g_{\mu\nu}$, with $R_{\mu\nu}$ the Ricci tensor (i.e. $R_{\mu\nu} = R^{\alpha}{}_{\mu\alpha\nu}$, with $R^{\alpha}{}_{\mu\alpha\nu}$ the Riemann tensor defined in section 1.3.4) and R the scalar curvature, also called Ricci scalar (i.e. $R = R_{\mu\nu} g^{\mu\nu}$).

[2] The Hubble radius is defined as the inverse of Hubble's constant. It gives the order of magnitude of the radius of the observable universe (whose boundary is called cosmological horizon).

[3] Here again, non-linearities involving the fields of interest are taken into account whereas couplings between metric perturbations are neglected.

$$\mathcal{D}_\eta n_c + \partial_i(V_i n_c) = 0, \tag{5.3}$$

$$\mathcal{D}_\eta P_i + V_j \partial_j P_i = \tau_0 \partial_i A + \tau_j \partial_i B_j - \frac{1}{2}\frac{\tau_j \tau_k}{\tau_0}\partial_i h_{jk}, \tag{5.4}$$

with

$$\mathcal{D}_\eta = \partial_\eta - \frac{\tau_i}{\tau_0}\partial_i \qquad \text{and} \qquad V_i = -\frac{P_i - \tau_i}{\tau_0} + \frac{\tau_i}{\tau_0}\frac{\tau_j(P_j - \tau_j)}{(\tau_0)^2}. \tag{5.5}$$

Those equations are very rewarding for several reasons.

Consequences on P_i

First, they enabled us to prove that the rotational part of the momentum field P_i is zero for adiabatic initial conditions. Indeed, as demonstrated in our article, the sole source of the rotational part Ω_i of the momentum field is the rotational part itself on subhorizon scales[4], which is initially zero because of adiabaticity. It can be seen by deriving Ω_i's evolution equation from that of P_i, (5.4). It means that, on subhorizon scales, P_i can be fully described in terms of its divergence even in the nonlinear regime and independently on the gauge. This is a major result of our study given the repercussion this property has when it concerns the velocity field of cold pressureless fluids. By analogy with (3.14), it is therefore convenient to introduce the velocity divergence in units of $\mathcal{H}$,

$$\theta_{\vec{\tau}}(\eta, x^i) \equiv \frac{\partial_i P_i(\eta, x^i; \vec{\tau})}{ma\mathcal{H}}. \tag{5.6}$$

Invariance properties

The form of equations (5.3) and (5.4) is favorable to a generalization of the invariance properties given in (3.37). Indeed, one checks easily that the following transformations do not modify the system[5]

[4] Note that the general equation (5.1) shows that, in the linear regime, it is not necessary to drop any term to write P_i as a gradient.

[5] The transformation law for V_i is equivalent to $\tilde{P}_i(\tilde{\eta}, \tilde{x}^i; \vec{\tau}) = P_i(\eta, x^i; \vec{\tau}) - \tau_0 \partial_\eta D_i(\eta) - \frac{\tau_0}{\tau_0^2 - \tau_j \tau_j}\, \tau_i \tau_j \partial_\eta D_j(\eta)$.

$$\tilde{x}^i = x^i + D_i(\eta), \tag{5.7}$$

$$\tilde{\eta} = \eta, \tag{5.8}$$

$$\tilde{\delta}_{\vec{\tau}}(\tilde{\eta}, \tilde{x}^i) = \delta_{\vec{\tau}}(\eta, x^i), \tag{5.9}$$

$$\tilde{V}_i(\tilde{\eta}, \tilde{x}^i) = V_i(\eta, x^i) + \partial_\eta D_i(\eta), \tag{5.10}$$

where

$$\delta_{\vec{\tau}}(\eta, x^i) = \frac{n_c(\eta, x^i; \vec{\tau})}{n_c^{(0)}(\vec{\tau})} - 1 \tag{5.11}$$

and with τ_i and τ_0 left unchanged. Note that the metric perturbations A, B_i and $h_{i,j}$ are not affected by such a transformation since the metric $\mathrm{d}s^2$ is an invariant in general relativity. Hence, the transformation of Φ (in the system (3.37)) is not the non-relativistic limit of our transformations of metric perturbations written in the conformal Newtonian gauge[6]. It is due to the fact that equations (3.11) and (3.12) contain additional terms compared to the non-relativistic limit of the relativistic equations when the latter are taken in the subhorizon limit. The momentum divergence, $\partial_i P_i$, is also preserved. We used this relativistic version of the extended Galilean invariance to derive consistency relations (see section 5.3) and to exploit the eikonal approximation in a study involving non-cold species (see chapter 6). The existence of invariance properties was predictable according to the equivalence principle. As a matter of fact, we also identified transformation laws keeping the general equations (4.19) and (5.1) invariant (see the paper of section 5.4). I do not present them here because, in practice, it is the subhorizon limit of the equations that we handled.

Generalization of the standard compact equation

Universality is the principal interest of the system {(5.3)-(5.4)}. After decoupling, it distinguishes between baryons, cold dark matter and neutrinos only via their initial velocities (which set τ_i) and masses (which set τ_0). Hence, introducing the

[6]It is possible to find transformations of A, B_i and $h_{i,j}$ which have this property but they depend on $\vec{\tau}$, which does not make sense.

$2N$-uplet

$$\Psi_b(\mathbf{k}) = (\delta_{\vec{\tau}_1}(\mathbf{k}), -\theta_{\vec{\tau}_1}(\mathbf{k}), \ldots, \delta_{\vec{\tau}_N}(\mathbf{k}), -\theta_{\vec{\tau}_N}(\mathbf{k}))^T \tag{5.12}$$

is sufficient to encode the physics of all free-streaming cosmic fluids (labeled by $\vec{\tau}_1$, ..., $\vec{\tau}_N$) in a unique equation (here again, the convention that repeated Fourier arguments are integrated over applies)

$$a(\eta)\partial_a \Psi_b(\mathbf{k},\eta) + \Omega_b{}^c(\mathbf{k},\eta)\Psi_c(\mathbf{k},\eta) = \gamma_b{}^{cd}(\mathbf{k}_1,\mathbf{k}_2,\eta)\Psi_c(\mathbf{k}_1,\eta)\Psi_d(\mathbf{k}_2,\eta), \tag{5.13}$$

which is formally identical to (3.16) except that i) b, c and d run now from 1 to $2N$, ii) $\Omega_b{}^c$ is now scale-dependent and iii) $\gamma_b{}^{cd}$ is now time-dependent. More precisely, the individual equations of motion read in Fourier space

$$\left(a\partial_a - \mathrm{i}\frac{\mu k\tau}{\mathcal{H}\tau_0}\right)\delta_{\vec{\tau}}(\mathbf{k}) - \frac{ma}{\tau_0}\left(1 - \frac{\mu^2\tau^2}{\tau_0^2}\right)\theta_{\vec{\tau}}(\mathbf{k}) = \frac{ma}{\tau_0}\int \mathrm{d}^3\mathbf{k}_1\mathrm{d}^3\mathbf{k}_2\alpha_R(\mathbf{k}_1,\mathbf{k}_2;\vec{\tau})\delta_{\vec{\tau}}(\mathbf{k}_1)\theta_{\vec{\tau}}(\mathbf{k}_2), \tag{5.14}$$

$$\left(1 + a\frac{\partial_a\mathcal{H}}{\mathcal{H}} + a\partial_a - \mathrm{i}\frac{\mu k\tau}{\mathcal{H}\tau_0}\right)\theta_{\vec{\tau}}(\mathbf{k}) + \frac{k^2}{ma\mathcal{H}^2}\mathcal{S}_{\vec{\tau}}(\mathbf{k}) = \frac{ma}{\tau_0}\int \mathrm{d}^3\mathbf{k}_1\mathrm{d}^3\mathbf{k}_2\beta_R(\mathbf{k}_1,\mathbf{k}_2;\vec{\tau})\theta_{\vec{\tau}}(\mathbf{k}_1)\theta_{\vec{\tau}}(\mathbf{k}_2), \tag{5.15}$$

where the source term $\mathcal{S}_{\vec{\tau}}(\mathbf{k})$ is given by

$$\mathcal{S}_{\vec{\tau}}(\mathbf{k}) = \tau_0 A(\mathbf{k}) + \vec{\tau}\cdot\vec{B}(\mathbf{k}) - \frac{1}{2}\frac{\tau_i\tau_j}{\tau_0}h_{ij}(\mathbf{k}) \tag{5.16}$$

and where the kernel functions (which differ from one flow to another) are defined as

$$\alpha_R(\mathbf{k}_1,\mathbf{k}_2;\vec{\tau}) = \delta_{\mathrm{D}}(\mathbf{k}-\mathbf{k}_1-\mathbf{k}_2)\frac{(\mathbf{k}_1+\mathbf{k}_2)}{k_2^2}\cdot\left[\mathbf{k}_2 - \vec{\tau}\frac{\mathbf{k}_2\cdot\vec{\tau}}{\tau_0^2}\right], \tag{5.17}$$

$$\beta_R(\mathbf{k}_1,\mathbf{k}_2;\vec{\tau}) = \delta_{\mathrm{D}}(\mathbf{k}-\mathbf{k}_1-\mathbf{k}_2)\frac{(\mathbf{k}_1+\mathbf{k}_2)^2}{2k_1^2k_2^2}\left[\mathbf{k}_1\cdot\mathbf{k}_2 - \frac{\mathbf{k}_1\cdot\vec{\tau}\mathbf{k}_2\cdot\vec{\tau}}{\tau_0^2}\right]. \tag{5.18}$$

Hence the non-zero matrix elements (for p an integer $\in [1,N]$),

$$\gamma_{2p-1}^{\ 2p-1\ 2p}(\mathbf{k}_1,\mathbf{k}_2,\eta) = -\frac{ma(\eta)}{2\tau_0^{[p]}(\eta)}\alpha_R(\mathbf{k}_1,\mathbf{k}_2;\vec{\tau}_p), \tag{5.19}$$

$$\gamma_{2p-1}^{\ 2p\ 2p-1}(\mathbf{k}_1,\mathbf{k}_2,\eta) = -\frac{ma(\eta)}{2\tau_0^{[p]}(\eta)}\alpha_R(\mathbf{k}_2,\mathbf{k}_1;\vec{\tau}_p), \tag{5.20}$$

$$\gamma_{2p}^{\ 2p\ 2p}(\mathbf{k}_1,\mathbf{k}_2,\eta) = -\frac{ma(\eta)}{\tau_0^{[p]}(\eta)}\beta_R(\mathbf{k}_1,\mathbf{k}_2;\vec{\tau}_p), \tag{5.21}$$

where an exponent $^{[p]}$ means that one refers to the fluid labeled by $\vec{\tau}_p$, and

$$\Omega_{2p-1}^{\ 2p-1} = -\mathrm{i}\mu^{[p]}\frac{k}{\mathcal{H}}\frac{\tau^{[p]}}{\tau_0^{[p]}}, \tag{5.22}$$

$$\Omega_{2p-1}^{\ 2p} = \frac{ma}{\tau_0^{[p]}}\left(1-\frac{(\mu^{[p]})^2(\tau^{[p]})^2}{(\tau_0^{[p]})^2}\right), \tag{5.23}$$

$$\Omega_{2p}^{\ 2p} = 1 + a\frac{\partial_a\mathcal{H}}{\mathcal{H}} - \mathrm{i}\mu^{[p]}\frac{k}{\mathcal{H}}\frac{\tau^{[p]}}{\tau_0^{[p]}} + ..., \tag{5.24}$$

$$\Omega_{2p}^{\ 2(p+n)-1} = ..., \tag{5.25}$$

$$\Omega_{2p}^{\ 2(p+n)}(n\neq 0) = ..., \tag{5.26}$$

where the "..." denote contributions coming from the source term (5.16), which can be estimated by taking the subhorizon limit of the Einstein equations (5.2). Note that the standard matrix elements of section 3.3, which govern the cold-dark-matter evolution, are contained in these ones. They correspond to the two fields Ψ_b labeled by $\vec{\tau}=\vec{0}$. The difference here is that all gravitational contributions (including relativistic effects) are taken into account so the source term (which relates Ψ_{2p} to all other fields of the collection) is not trivially connected to Ψ_{2p-1} via the Poisson equation.

Such a description paves the way for the implementation of resummation techniques, such as the ones enumerated in section 3.4, in the relativistic and nonlinear equation of motion (5.13). It therefore appears as a further step towards a relativistic generalization of nonlinear perturbation theory. Yet, I did not develop tools to put such an implementation into practice during my PhD thesis.

5.3 Consistency relations

The fact that the relativistic system also satisfies an extended Galilean invariance makes easy the generalization of Ward identities. Taking inspiration of the results presented in section 3.5.2, we assumed in our paper that the density contrasts evolving in the medium perturbed by $\vec{D}$ are related to the unperturbed ones by (as long as the perturbation is small enough to be treated linearly)

$$\tilde{\delta}_{\vec{\tau}}(\mathbf{k},\eta) = \exp(\mathrm{i}\mathbf{k}.\vec{D})\delta_{\vec{\tau}}(\mathbf{k},\eta) \approx (1+\mathrm{i}\mathbf{k}.\vec{D})\delta_{\vec{\tau}}(\mathbf{k},\eta). \tag{5.27}$$

Moreover, in the light of (3.40), we related those displacements to the perturbative fields that generated them via

$$\vec{D}(\eta,\mathbf{x}) = \int \mathrm{d}^3\mathbf{q}\frac{-\mathrm{i}\mathbf{q}}{q^2}e^{\mathrm{i}\mathbf{q}.\mathbf{x}}\delta_{\mathrm{adiab}}(\eta,\mathbf{q}). \tag{5.28}$$

The index "adiab" means that the modes q that generated such displacements are assumed to be adiabatic, whence a displacement identical in each flow.

Following the procedure depicted in section 3.5.2, we recovered eventually the standard consistency relations, i.e.

$$\begin{aligned}\langle\delta(\mathbf{q},\eta)\delta(\mathbf{k}_1,\eta_1)\delta(\mathbf{k}_2,\eta_2)...\delta(\mathbf{k}_n,\eta_n)\rangle_{q\to 0} \\ = -\sum_i \frac{\mathbf{q}.\mathbf{k}_i}{q^2}P^{\mathrm{lin}}(q;\eta,\eta_i)\langle\delta(\mathbf{k}_1,\eta_1)\delta(\mathbf{k}_2,\eta_2)...\delta(\mathbf{k}_n,\eta_n)\rangle,\end{aligned} \tag{5.29}$$

where the wavenumber q is much smaller than all other wavenumbers k_i and where $P^{\mathrm{lin}}(q;\eta,\eta_i)$ is the linear unequal-time power spectrum. So, in our approach, it is still possible to relate $(n+1)$-order correlation functions to n-order ones when the times at which the fields are computed are different. As already discussed, this property is in fact hardly operable. Nevertheless, it strengthens the consistency of our generalization work.

5.4 Article "Cosmological Perturbation Theory for streams of relativistic particles"

Journal of Cosmology and Astroparticle Physics
An IOP and SISSA journal

Cosmological Perturbation Theory for streams of relativistic particles

Hélène Dupuy[a,b] **and Francis Bernardeau**[b,a]

[a]Institut de Physique Théorique, CEA (CNRS: URA 2306)
Orme des merisiers 91191 Gif-sur-Yvette, France
[b]Institut d'Astrophysique de Paris, UPMC (CNRS: UMR 7095)
98 bis boulevard Arago 75014 Paris, France

E-mail: helene.dupuy@cea.fr, francis.bernardeau@iap.fr

Received December 10, 2014
Accepted February 12, 2015
Published March 17, 2015

Abstract. Motion equations describing streams of relativistic particles and their properties are explored in detail in the framework of Cosmological Perturbation Theory. Those equations, derived in any metric both in the linear and nonlinear regimes, express the matter and momentum conservation. In this context we extend the setup of adiabatic initial conditions — that was initially performed in the conformal Newtonian gauge — to the synchronous gauge. The subhorizon limit of the nonlinear motion equations written in a generic perturbed Friedmann-Lemaître metric is then derived and analyzed. We show in particular that the momentum field $P_i(x)$ is always potential in the linear regime and remains so at subhorizon scales in the nonlinear regime. Finally the equivalence principle is exploited to highlight invariance properties satisfied by such a system of equations, extending that known for streams of non-relativistic particles, namely the extended Galilean invariance.

Keywords: cosmic flows, cosmological perturbation theory

ArXiv ePrint: 1411.0428v2

JCAP03(2015)030

doi:10.1088/1475-7516/2015/03/030

Contents

JCAP03(2015)030

1 Introduction

Entering in the era of precision cosmology requires an examination of the structure growth in minute detail. So far, the impact of neutrinos on large-scale structure formation has often been overlooked, especially in the nonlinear regime, because of the difficulties encountered when accounting for the gravitational dynamics of such particles is needed (see recent attempts in [1–3]). Since neutrinos have been shown to be massive, the situation has evolved: it has become crucial to include neutrino masses in cosmological models to study their impact on the late-time growth of structure. On the one hand, one indeed needs to ensure that the estimation of the fundamental cosmological parameters is not undermined by the presence of massive neutrinos. On the other hand, doing so is an efficient way to improve our knowledge of those enigmatic particles because, as mentioned in many references [4–9], the signature of neutrino masses on cosmological observables is significant enough for those masses to be constrained observationally.

Numerical approaches are obviously a precious tool in this context and several N-body simulations have been designed to take the nonlinear effects of massive neutrinos into account

(see the recent works [10–16]). From a theoretical point of view, this kind of investigation is not straightforward. Indeed, contrary to Cold Dark Matter (CDM) particles, neutrinos are relativistic at horizon crossing so their velocity dispersion is not negligible and the Newtonian approximation does not hold. The phase-space distribution of neutrinos is therefore difficult to describe. Usually, in analytical models, this question is addressed in the linear regime only by performing a harmonic decomposition of the phase-space distribution function. As presented in some standard references (e.g. [17] and its companion paper ref. [18]), this approach leads to a hierarchy of equations called the Boltzmann hierarchy. It is possible to examine in full detail the impact of such results on cosmology, as reviewed for instance in ref. [19], but this analysis is limited to the linear regime, which is too restrictive to be in balance with the current surveys. Indeed, observational projects aiming at putting constraints on neutrino masses are all sensitive to the nonlinear growth of structure, at least in the mildly nonlinear regime. Problematically, the extension into the nonlinear regime of the phase-space harmonic decomposition has proved to be very cumbersome.[1] Note that numerical simulations and analytical studies are complementary. For instance, Perturbation Theory can be useful to test the approximation schemes (used e.g. to reduce noise or to describe velocity dispersion) at play in some N-body simulations. It allows also to reach better precisions, which makes the comparison with present and future data more relevant, and to do it faster.[2]

A new theoretical approach, which we further explore here, has been put forward recently in ref. [21]. In this study neutrinos, or more generally any non-interacting relativistic or non-relativistic particles, were described as a collection of flows evolving independently from one another. Such a study takes advantage of the fact that the particles at play are free-streaming. This is this property that allows to replace the standard study of a single multi-stream fluid by that of a collection of single-stream fluids. Somehow it takes inspiration of the CDM description (for which the single-stream approximation is an effective approximation, see e.g. [22]), the aim being to establish a similar description for neutrinos. In our first paper we demonstrated that, at linear level, the method we proposed led to the same results as the standard one. In the present article, we explore in more detail the formalism associated with the approach we developed. In particular we derive the motion equations in a more general framework, focusing on the symmetry properties of the resulting equations. Ward identities, resulting from those invariances, are also presented. What motivates this task is the fact that carrying out Perturbation Theory calculations requires a good understanding of the mode coupling structure.

The organization of the paper is the following. In section 2 we recall the specificities of a multi-fluid description. Then we derive the fully nonlinear motion equations satisfied by single-stream fluids of relativistic particles. The aim of the following section is to bring out some remarkable properties related to the linear regime. Finally, section 5 explains how to deal with relativistic streams in Perturbation Theory. In particular a global motion equation, fully nonlinear but in which the terms that are subdominant at subhorizon scales have been dropped, is presented in this section. We then present and comment the key properties of this system before concluding and discussing perspectives.

[1] The only attempt we are aware of is described in [20].

[2] The computational time is very problematic in some numerical simulations modeling the nonlinear power spectrum.

JCAP03(2015)030

2 A multi-fluid description of non-interacting relativistic particles

We recall here the method we developed to describe a fluid of non-interacting relativistic massive particles as a collection of streams or flows[3] (we will use hereafter the two terms indistinctively). This approach requires to properly define the phase-space distribution function $f(x^i, p_i, \eta)$, where x^i are the comoving positions, p_i the conjugate momenta of x^i and η the conformal time.

The key idea is to split a relativistic multi-flow fluid into several flows in order to enter in the field of application of the single-flow approximation. In the absence of shell-crossing, particles having initially the same velocity will continue to do so throughout the cosmological time. Indeed, in that case, particles that have the same velocity at the same time are particles that are located at the same place so such particles will travel through the same gravitational potentials. Those sets of particles are thus single-flow fluids. A convenient way to distinguish between the flows is to use initial momenta $p_i(\eta_{\rm in})$ as labels,[4] denoted τ_i. Each single-flow fluid considered in our multi-fluid approach is therefore defined as the collection of all the particles that have at initial time the comoving momentum τ_i. The time evolution of each flow itself is encoded in a phase-space distribution function $f^{\rm one-flow}(\eta, x^i, p_i; \tau_i)$. One also introduces the momentum field $P_i(\eta, x_i; \tau)$, which is the value of the momentum of any particle of the flow labelled by τ_i at time η and position x_i. The phase-space distribution function $f^{\rm one-flow}(\eta, x^i, p_i; \tau_i)$ then reads

$$f^{\rm one-flow}(\eta, x^i, p_i; \tau_i) = n_c(\eta, \mathbf{x}; \tau_i)\delta_{\rm D}(p_i - P_i(\eta, \mathbf{x}; \tau_i)), \tag{2.1}$$

where n_c is the comoving number density of the flow.

Finally, the overall distribution function $f(\eta, x^i, p_i)$ is computed by taking all the single-flow fluids previously defined into account:

$$f(\eta, x^i, p_i) = \sum_{\tau_i} f^{\rm one-flow}(\eta, x^i, p_i; \tau_i) = \sum_{\tau_i} n_c(\eta, \mathbf{x}; \tau_i)\delta_{\rm D}(p_i - P_i(\eta, \mathbf{x}; \tau_i)). \tag{2.2}$$

Assuming that the parameter τ_i describes a 3D continuous field, the continuous limit of this expression is naturally

$$f(\eta, x^i, p_i) = \int \mathrm{d}^3\tau_i \, n_c(\eta, \mathbf{x}; \tau_i)\delta_{\rm D}(p_i - P_i(\eta, \mathbf{x}; \tau_i)). \tag{2.3}$$

In this context, one can see that the integration over phase-space momenta usually performed to compute global physical quantities associated with a single multi-flow fluid is replaced by a sum over the single-flow fluids labelled by τ_i (i.e. a sum over all the possible initial momenta or velocities). It implies in particular that, for any functional form $\mathcal{F}(p_i)$, we have

$$\int \mathrm{d}^3 p_i \, f(\eta, x^i, p_i) \; \mathcal{F}(p_i) = \int \mathrm{d}^3\tau_i \, n_c(\eta, \mathbf{x}; \tau_i) \; \mathcal{F}(P_i(\eta, \mathbf{x}; \tau_i)). \tag{2.4}$$

Eq. (2.3) shows that, to determine the time evolution of the phase-space distribution function, one needs to study the time evolution of the comoving number densities and of the momentum fields. A derivation of the corresponding motion equations in the conformal Newtonian gauge was presented in detail in [21]. In the next section, we succinctly generalize this derivation to an arbitrary spacetime.

[3] Note that, when applied to neutrinos, this construction is valid for any given mass eigenstate. If the masses are not degenerate, it should therefore be repeated for each three eigenstates.

[4] In a homogeneous expanding universe, one can easily show that p_i is a constant.

JCAP03(2015)030

3 Derivation of the nonlinear motion equations of relativistic massive particles

3.1 Evolution equation of the comoving number densities

The comoving number density of a fluid, single-flow or not, is related to its phase-space distribution function in a very simple way,

$$n_c(\eta, x^i) = \int \mathrm{d}^3 p_i \, f(\eta, x^i, p_i). \tag{3.1}$$

Note that n_c is not necessarily the number density measured by an observer at rest in the metric (see subsection 3.4). Its evolution equation can be derived straightforwardly from the conservation equation[5] satisfied by the phase-space distribution function f,

$$\frac{\partial}{\partial \eta} f + \frac{\partial}{\partial x^i}\left(\frac{\mathrm{d}x^i}{\mathrm{d}\eta} f\right) + \frac{\partial}{\partial p_i}\left(\frac{\mathrm{d}p_i}{\mathrm{d}\eta} f\right) = 0. \tag{3.2}$$

The only assumption made here is that the particles we consider are conserved (they do not decay because no disintegration or scattering process is at play at the time of interest). Integrating over momenta leads to

$$\frac{\partial}{\partial \eta} n_c + \frac{\partial}{\partial x^i}\left(\int \mathrm{d}^3 p_i \frac{\mathrm{d}x^i}{\mathrm{d}\eta} f\right) = 0. \tag{3.3}$$

For a single-flow fluid, $\mathrm{d}x^i/\mathrm{d}\eta$ can be expressed in terms of momenta. More specifically,

$$\frac{\mathrm{d}x^i}{\mathrm{d}\eta} = \frac{\mathrm{d}x^i}{\mathrm{d}\tau}\frac{\mathrm{d}\tau}{\mathrm{d}\eta} = \frac{p^i}{p^0}, \tag{3.4}$$

where τ is the particle proper time and p^i and p^0 are related to p_i through the metric and the on-shell mass constraint. As a result, for a single-flow fluid we have

$$\frac{\partial}{\partial \eta} n_c + \frac{\partial}{\partial x^i}\left(\frac{P^i}{P^0} n_c\right) = 0, \tag{3.5}$$

with $P^\mu(\eta, x^i) = g^{\mu\nu} P_\nu(\eta, x^i)$ and $P^\mu P_\mu = -m^2$. Note that this motion equation does not rely on any perturbative expansion of the metric.

3.2 Evolution equation of the momentum fields

A fluid in which particles are neither created nor annihilated nor subjected to diffusion, as is the case with the fluids considered here, obeys general conservation laws such as

$$T^{\mu\nu}{}_{;\mu} = 0, \tag{3.6}$$

where $T^{\mu\nu}$ is the energy-momentum tensor and where we adopt the standard notation; to indicate a covariant derivative. The conservation of the particles can besides be expressed as

$$J^\mu{}_{;\mu} = 0, \tag{3.7}$$

[5]The Vlasov equation derives from this equation under the assumption that the motion equations are Hamiltonian.

JCAP03(2015)030

where J^μ is the particle four-current. Noting that, for a single-flow fluid, the energy-momentum tensor $T^{\mu\nu}$ is related to J^ν and to the momentum field P^μ by

$$T^{\mu\nu} = -P^\mu J^\nu, \tag{3.8}$$

the conservation of the energy momentum tensor combined with the conservation of the four-current imposes $P^\mu_{\ ;\nu} J^\nu = 0$. Moreover, the energy-momentum tensor being symmetric, $T^{\mu\nu} = -P^\mu J^\nu$ gives $J^i = \dfrac{P^i}{P^0} J^0$, whence

$$P^\nu P_{\mu;\nu} = 0. \tag{3.9}$$

Expressing the covariant derivative in terms of the spatial derivative finally gives the following motion equation

$$P^\nu P_{\mu,\nu} = \frac{1}{2} P^\sigma P^\nu g_{\sigma\nu,\mu}. \tag{3.10}$$

Together with eq. (3.5), it dictates the time evolution of a collection of massive relativistic particles evolving in an arbitrary metric $g_{\alpha\beta}$. Once again, this equation has been obtained without performing any perturbative expansion of the metric. Besides, the time coordinate of the momentum field being related to the spatial ones thanks to the on-shell mass constraint, one can restrict the coordinates μ to spatial coordinates i in the previous equation,

$$P^\nu P_{i,\nu} = \frac{1}{2} P^\sigma P^\nu g_{\sigma\nu,i}. \tag{3.11}$$

Eq. (3.11) can therefore be considered as the second motion equation governing the time evolution of the flow in the nonlinear regime.

3.3 Explicit form for the momentum field in a generic perturbed Friedmann-Lemaître metric

As an illustration, we present in this section the explicit form of the motion equation satisfied by the momentum field in a generic perturbed Friedmann-Lemaître metric. The metric we use reads

$$\mathrm{d}s^2 = a^2(\eta)\left[-(1+2A)\mathrm{d}\eta^2 + 2B_i \mathrm{d}x^i \mathrm{d}\eta + (\delta_{ij} + h_{ij})\mathrm{d}x^i \mathrm{d}x^j\right], \tag{3.12}$$

where η is the conformal time, x^i $(i = 1, 2, 3)$ are the Cartesian spatial comoving coordinates, $a(\eta)$ is the scale factor and A, B_i and h_{ij} are respectively the time-time, time-space and space-space metric perturbations. Units are chosen so that the speed of light in vacuum is equal to unity and the expansion history of the universe, encoded in the time dependence of a, is driven by the overall matter and energy content of the universe. The equation of motion for the momentum is then

$$\frac{\mathrm{d}P_i}{\mathrm{d}\eta} = a^2(\eta)\left[-P^0 \partial_i A + P^j \partial_i B_j + \frac{1}{2}\frac{P^j P^k}{P^0}\partial_i h_{jk}\right], \tag{3.13}$$

where we define the operator $\mathrm{d}/\mathrm{d}\eta$ as

$$\frac{\mathrm{d}}{\mathrm{d}\eta} \equiv \frac{\partial}{\partial\eta} + \frac{P^i}{P^0}\frac{\partial}{\partial x^i}. \tag{3.14}$$

JCAP03(2015)030

This equation is, on the one hand, a relativistic generalization of one of the two equations describing CDM and, on the other hand, a generalization to an arbitrary perturbed Friedmann-Lemaître metric of eq. (2.13) of [21], which corresponds to the conformal Newtonian gauge (in which, by definition, $A = \psi$, $B_i = 0$ and $h_{ij} = -2\phi\delta_{ij}$). For example, to write the motion equation in the synchronous gauge, one only has to set $A = 0$ and $B_i = 0$ in eq. (3.13). Furthermore, in the non-relativistic limit, we simply have in the synchronous and conformal Newtonian gauges $P^0 = m/a(1 - A)$ and $P^i \ll m/a$ so that eq. (3.13) simply takes the form

$$\frac{\mathrm{d}P_i}{\mathrm{d}\eta} = -am\partial_i A. \tag{3.15}$$

It is of course nothing but Newton's second law written using the conformal time.

3.4 Link with the Einstein equations

In general, the energy-momentum tensor is related to the phase-space distribution function through (see e.g. [18, 23])

$$T_{\mu\nu}(\eta, x^i) = \int \mathrm{d}^3 p_i \, (-g)^{-1/2} \frac{p_\mu p_\nu}{p^0} \, f(\eta, x^i, p_i). \tag{3.16}$$

When considering single-flow fluids, integration over momenta can be done straightforwardly and the resulting expression is

$$T^{\mathrm{one-flow}}_{\mu\nu} = \frac{P_\mu P_\nu}{(-g)^{1/2} P^0} n_c. \tag{3.17}$$

This result is important since it gives the contribution of each flow to the Einstein equations. The particle four-current J_μ can also be computed very easily,

$$J^{\mathrm{one-flow}}_{\mu} = -\frac{P_\mu}{(-g)^{1/2} P^0} n_c. \tag{3.18}$$

Besides, the expression of the particle four-current can be used to express the number density of particles as seen by an observer at rest in the metric, denoted n. If one calls the four-velocity of such an observer U^μ, one indeed has

$$n = U^\mu J_\mu. \tag{3.19}$$

Admitting that the four-velocity of such an observer satisfies $U^i = 0$, one gets $U^0 = (-g_{00})^{-1/2}$ from the constraint $U^\mu U_\mu = -1$, whence

$$n = -\frac{P_0}{(-g_{00})^{1/2}(-g)^{1/2} P^0} \, n_c. \tag{3.20}$$

In ref. [21], the evolution equation of the number density of neutrinos was formulated in terms of n rather than n_c but the two approaches are of course equivalent. Those equations allow to study explicitely the Einstein equations after recombination because, when all the cosmic components are free-streaming, one can write

$$G_{\mu\nu}(\eta, x^i) = 8\pi G \sum_{\text{species and flows}} T^{\mathrm{one-flow}}_{\mu\nu}(\eta, x^i), \tag{3.21}$$

JCAP03(2015)030

the sum being performed over all species participating in the cosmic fluid and G being Newton's constant. Indeed, the formalism we are proposing can be applied to relativistic as well as to non-relativistic species so no contribution is missing. Together with the evolution equation of n_c and P_i, these equations form a closed set of equations.

In the following we analyze this system in more detail, starting with the study of its invariance properties.

3.5 Invariance properties

In this subsection, we present transformation laws that leave the motion equations unchanged.

A priori, a whole set of transformation laws can be derived from a change of variables of the form

$$x^\mu \;\rightarrow\; \tilde{x}^\mu(x^\mu). \tag{3.22}$$

In this study, we are interested in generalizing the so-called extended Galilean invariance that the standard motion equations of non-relativistic particles (or, equivalently, the motion equations of this paper written in the non-relativistic limit) satisfy. The corresponding transformation laws are explicitly given by the following changes of coordinates and fields (see e.g. [24][6]),

$$\tilde{x}^i = x^i + d_i(\eta), \qquad \tilde{\eta} = \eta, \tag{3.23}$$

$$\tilde{V}^i = V^i + \frac{\mathrm{d}}{\mathrm{d}\eta} d_i(\eta), \qquad \tilde{\delta} = \delta, \tag{3.24}$$

$$\tilde{A} = A - \mathcal{H}\frac{\mathrm{d}}{\mathrm{d}\eta} d_i(\eta) x^i - \frac{\mathrm{d}^2}{\mathrm{d}\eta^2} d_i(\eta) x^i, \tag{3.25}$$

where we use the notations of this paper and where $d_i(\eta)$ is an arbitrarily time-dependent uniform field, V^i is the velocity field and δ is the density contrast. Such an invariance corresponds to an extension of the Galilean invariance in the sense that the displacement can depend on time. It actually derives from the equivalence principle. As pointed out in recent studies, such as [22], the extended Galilean invariance plays a significant role in the computation of correlation functions involved in the study of large-scale structure formation. To generalize it, we will explore in the following the consequences of coordinate transforms closely connected to special Lorentz transformations.

So let us consider a transformation $x^\mu \rightarrow \tilde{x}^\mu$ defined so that

$$\mathrm{d}\tilde{x}^\mu = \xi^\mu_\nu \, \mathrm{d}x^\nu. \tag{3.26}$$

It is an acceptable transformation provided that

$$\xi^\mu_{\nu,\sigma} = \xi^\mu_{\sigma,\nu}. \tag{3.27}$$

In particular, it is easy to check that

$$\xi^0_0 = 1 + x^i \frac{\partial}{\partial\eta} v_i(\eta), \qquad \xi^0_i = v_i(\eta), \tag{3.28}$$

$$\xi^i_0 = v_i(\eta) + u_i(\eta), \qquad \xi^i_j = \delta^i_j, \tag{3.29}$$

[6] In this study several particular cases, corresponding to different possible time dependencies of the spatial translation, are explored.

JCAP03(2015)030

where $v_i(\eta)$ and $u_i(\eta)$ are two arbitrarily time-dependent functions, obeys the property (3.27). More explicitly, the change of frame corresponding to (3.28)–(3.29) is given by

$$\tilde{x}^i = x^i + d_i(\eta) + g_i(\eta), \qquad \tilde{\eta} = \eta + v_i\, x^i, \tag{3.30}$$

with $v_i = \frac{\mathrm{d}}{\mathrm{d}\eta} d_i(\eta)$ and $u_i = \frac{\mathrm{d}}{\mathrm{d}\eta} g_i(\eta)$.

In the rest of the paper, we will assume that both v_i and u_i are infinitesimal quantities and we will restrict all calculations to linear order in these quantities. Besides, the differential operators associated with the new coordinates are related to the previous ones thanks to

$$\frac{\partial}{\partial\tilde{\eta}} = \left(1 - \dot{v}_i x^i\right) \frac{\partial}{\partial\eta} - \left(v_i + u_i\right) \frac{\partial}{\partial x^i} \quad \text{and} \quad \frac{\partial}{\partial\tilde{x}^i} = -v_i \frac{\partial}{\partial\eta} + \frac{\partial}{\partial x^i}. \tag{3.31}$$

The momentum components therefore transform as (once again v_i and u_i are kept at linear order)

$$\tilde{P}^0 = (1 + x^i v_{i,0}) P^0 + v_i P^i \tag{3.32}$$

$$\tilde{P}^i = (v_i + u_i) P^0 + P^i \tag{3.33}$$

$$\tilde{P}_0 = (1 - x^i v_{i,0}) P_0 - (v_i + u_i) P_i \tag{3.34}$$

$$\tilde{P}_i = -v_i P_0 + P_i, \tag{3.35}$$

the transformation of the comoving numerical density field is given by

$$\tilde{n}_c = n_c \left(1 + v_i \frac{P^i}{P^0}\right) \tag{3.36}$$

and finally the potentials transform the following way,

$$\tilde{A} = A - \mathcal{H} v_i x^i - v_{i,0} x^i, \qquad \tilde{B}_i = B_i - u_i, \qquad \tilde{h}_{ij} = h_{ij} - 2\mathcal{H}\delta_{ij} v_k x^k. \tag{3.37}$$

Interestingly, we can note that the combination $(-g)^{-1/2} n_c / P^0$ that appears in the expression of the energy-momentum tensor is invariant under such transformations.

It can then be easily checked that the motion equations (3.5)–(3.13) are invariant under the transformations (3.26)–(3.28)–(3.29)–(3.37). It is also the case for the Einstein equations but the explicit verification is more involved.

The invariance we are putting forward is clearly a generalization of the extended Galilean invariance. We leave for further studies the exploration of the consequences of such an invariance. In the last section, we will present a similar symmetry property satisfied by the motion equations written at subhorizon scales and we will explore in more detail its consequences.

4 Relativistic streams in the linear regime

This section aims at highlighting properties of relativistic streams in the linear regime. From the motion equations (3.5) and (3.11), it is straightforward to see that, in a homogeneous metric, the variables P_i and n_c do not depend on time. Considering that metric inhomogeneities are small compared to background values, we develop a perturbation scheme that consists in expanding each relevant field with respect to the metric perturbations[7],

$$P_i(\eta, x^i; \tau_i) = \tau_i + P_i^{(1)}(\eta, x^i; \tau_i) + P_i^{(2)}(\eta, x^i; \tau_i) + \dots \tag{4.1}$$

[7]By definition, $P_i^{(0)} = \tau_i$ since $P_i^{(0)}$ is a constant and $\tau_i \equiv P_i(\eta_{\rm in})$.

JCAP03(2015)030

and

$$n_c(\eta, x^i; \tau_i) = n_c^{(0)}(\tau_i) + n_c^{(1)}(\eta, x^i; \tau_i) + n_c^{(2)}(\eta, x^i; \tau_i) + \dots \,. \tag{4.2}$$

4.1 A useful property of $P_i^{(1)}$

When taking only linear perturbations into account, eq. (3.11) reads

$$\frac{\mathrm{d}P_i^{(1)}}{\mathrm{d}\eta} = \frac{1}{2}\frac{P^{(0)\mu}P^{(0)\nu}}{P^{(0)0}} g^{(1)}_{\mu\nu,i}. \tag{4.3}$$

It appears that $P_i^{(1)}$ is sourced by a gradient term. For scalar adiabatic initial conditions, $P_i^{(1)}$ will therefore remain a potential field. Note that, as already mentioned in [21], this property is a specificity of the variable $P_i^{(1)}$ only. For instance, even at linear order, the momentum field P^i does not derive from a potential[8]. In the particular case of a perturbed Friedmann-Lemaître metric, this equation takes the form

$$\frac{\mathrm{d}P_i^{(1)}}{\mathrm{d}\eta} = \partial_i \left(P_j^{(0)} B_j - \frac{1}{2}\frac{P_j^{(0)} P_k^{(0)}}{P_0^{(0)}} h_{jk} + P_0^{(0)} A \right), \tag{4.4}$$

which allows to express the source term whose $P_i^{(1)}$ is the gradient in terms of the potentials (for example in the conformal Newtonian and synchronous gauges). Note that, to get this expression, only linear terms in the metric perturbations have been taken into account. The same approximation will be used in the rest of this paper since what matters in the nonlinear regime is not metric-metric coupling but the nonlinear coupling between the fields of interest.

4.2 Linearized equations in Fourier space

In light of what is done in the study [21], we explicitly write in this section the linearized equations in Fourier space. To this end, we introduce a Fourier mode $\mathbf{k}$ and all the fields we study in Fourier space correspond to this mode. We use the same notations as in [21],[9]

$$\tau_0(\eta) \equiv P_0{}^{(0)}(\eta), \qquad \theta_P(\mathbf{x}, \eta) = \partial_i P_i^{(1)}(\mathbf{x}, \eta), \tag{4.5}$$

$$P_i^{(1)}(\mathbf{k}, \eta) = \frac{-\mathrm{i}k_i}{k^2}\theta_P(\mathbf{k}, \eta), \qquad \delta_n(\mathbf{x}, \eta) = \frac{n_c^{(1)}(\mathbf{x}, \eta)}{n_c^{(0)}}. \tag{4.6}$$

Note that here we have used the fact that $P_i^{(1)}(\eta, x^i)$ is potential at linear order. Besides, the on-shell mass constraint imposing

$$P_0^{(1)} = B_i\tau_i + A\tau_0 + \frac{\tau_i}{\tau_0}\left(P_i^{(1)} - \frac{1}{2}\tau_j h_{ij}\right), \tag{4.7}$$

one has

$$\left(\frac{P^i}{P^0}\right)^{(1)} = -\frac{P_i^{(1)}}{\tau_0} + \frac{P_j^{(1)}\tau_j\tau_i}{\tau_0^3} - \frac{\tau_i}{\tau_0}A - B_i + \frac{\tau_j h_{ij}}{\tau_0} - \frac{\tau_i}{2\tau_0}\frac{\tau_j\tau_k h_{jk}}{\tau_0^2}. \tag{4.8}$$

[8] Since $P_i^{(1)}$ is sourced by a gradient in terms of the space coordinates x^i, we expect $P^{i\,(1)}$ to be sourced by a gradient in terms of the space coordinates x_i.

[9] Except δ_n, which applies here to the *comoving* number density whereas it applied to the *proper* number density in [21].

JCAP03(2015)030

Thus, after linearizing eq. (3.5), moving to Fourier space and taking the divergence of eq. (4.4), one finally obtains

$$\dot{\delta}_n = i\mu k \frac{\tau}{\tau_0} \left(\delta_n + A - h - 4\gamma + \kappa(\tau, \tau_0, \mu, h, \gamma)\right) + ik_i B_i + \frac{\theta_P}{\tau_0}\left(1 - \frac{\mu^2\tau^2}{{\tau_0}^2}\right) \tag{4.9}$$

and

$$\dot{\theta}_P = i\mu k \frac{\tau}{\tau_0}\theta_P - k^2 \left(\tau_0 A + \tau_j B_j - \tau_0 \kappa(\tau, \tau_0, \mu, h, \gamma)\right), \tag{4.10}$$

where μ is the Cosine of the angle between the wave vector $\mathbf{k}$ and the initial momentum direction,

$$\mu = \frac{k_i \tau_i}{k\tau} \quad \text{with} \quad \tau^2 = \tau_i^2, \tag{4.11}$$

where h and γ are scalar modes defined so that (see e.g. [18])

$$h_{ij} = \frac{k_i k_j}{k^2} h + \left(\frac{k_i k_j}{k^2} - \frac{1}{3}\delta_{ij}\right) 6\gamma \tag{4.12}$$

and where

$$\kappa(\tau, \tau_0, \mu, h, \gamma) = \frac{\tau^2}{{\tau_0}^2}\left[\frac{1}{2}\mu^2 h + \gamma\left(3\mu^2 - 1\right)\right]. \tag{4.13}$$

We can see in particular that the angle between the wave vector $\mathbf{k}$ and the initial momentum vector plays a significant role in the time evolution of the considered flow.

The setting of the adiabatic initial conditions, essential to numerically solve the system (4.9)–(4.10), is explained in full detail in appendix A for the particular case of massive neutrinos.

5 Perturbation Theory with relativistic streams

The aim of this section is to show how the formalism developed to study CDM thanks to Perturbation Theory (PT) can be extended to the study of relativistic species. The regime we will investigate is the one relevant in the context of large-scale structure formation, i.e. we will focus here on subhorizon scales. This restriction will allow us to remove the subdominant coupling terms from the motion equations. It is indeed important to keep in mind that the nonlinear couplings that appear for example in the Einstein equations, in the source term of the Euler equation or in the $P^i/P^0\partial_i$ operator do not all have the same amplitude after subhorizon scales have been reached.

5.1 Coupling structure at subhorizon scales

The identification of the relevant coupling terms is made by comparing the wave number k (characterizing the scale at which the field evolution is studied) with the horizon wave number $k_{\mathcal{H}}$ (defined as the inverse of the Hubble radius). First, let us notice that metric perturbations scale like $\delta_\rho\, k_{\mathcal{H}}^2/k^2$ and that the relative velocity field $(P_i - \tau_i)$ scales like $\delta_\rho k_{\mathcal{H}}/k$, where δ_ρ is the typical energy density contrast. The latter is assumed to be small but can reach values comparable with unity. This is precisely this regime of PT calculations that we want to explore.

JCAP03(2015)030

Following the description of CDM fluids at subhorizon scales, in practice we neglect in (3.5) all the terms behaving as $k_{\mathcal{H}}\,(k_{\mathcal{H}}/k)^{\alpha}$ with $\alpha \geq 1$ and in (3.13) all the terms behaving as $k_{\mathcal{H}}\,(k_{\mathcal{H}}/k)^{\alpha}$ with $\alpha \geq 2$. In this limit, eqs. (3.5)–(3.13) take the form

$$\mathcal{D}_\eta n_c + \partial_i(V_i n_c) = 0 \tag{5.1}$$

$$\mathcal{D}_\eta P_i + V_j \partial_j P_i = \tau_0 \partial_i A + \tau_j \partial_i B_j - \frac{1}{2}\frac{\tau_j \tau_k}{\tau_0}\partial_i h_{jk}, \tag{5.2}$$

with

$$\tau_0 = -\sqrt{m^2 a^2 + \tau_i^2}, \quad \mathcal{D}_\eta = \frac{\partial}{\partial \eta} - \frac{\tau_i}{\tau_0}\frac{\partial}{\partial x^i}, \tag{5.3}$$

and

$$V_i = -\frac{P_i - \tau_i}{\tau_0} + \frac{\tau_i}{\tau_0}\frac{\tau_j (P_j - \tau_j)}{(\tau_0)^2}. \tag{5.4}$$

The metric perturbations that appear in the Euler equation are computed at linear order from the Einstein equation. Note that in the sub horizon limit, the source term of the Einstein equation is dominated by the fluctuations of the number density.

5.2 The no-curl theorem and its consequences

In this paragraph we explicitly demonstrate one of the key results on which rely the carrying out of Perturbation Theory calculations. What we show is that, similarly to the velocity fields of non-relativistic flows, the momentum field P_i remains potential to all orders in Perturbation Theory (see [22, 25] and references therein for demonstrations in the non-relativistic case).

First, let us decompose P_i into a potential and a non potential parts,

$$P_i = \Phi_{,i} + W_i, \tag{5.5}$$

with

$$W_{i,i} = 0. \tag{5.6}$$

One can then define the curl field, related to the momentum field via

$$\Omega_i = \epsilon_{ijk} P_{j,k} = \epsilon^{ijk} W_{j,k}, \tag{5.7}$$

ϵ_{ijk} being the Levi-Civita symbol, or fully antisymmetric tensor. The objective here is to derive the evolution equation of Ω_i by exploiting the relativistic Euler equation. Noticing that

$$P_{i,j} = P_{j,i} + \epsilon_{kij}\Omega_k \tag{5.8}$$

and applying the operator $\epsilon_{kij}\partial_k$ to eq. (5.2), one obtains

$$\mathcal{D}_\eta \Omega_k + \epsilon_{kij}\epsilon_{mil}\left(V_l\,\Omega_m\right)_{,j} + \epsilon_{kij}\left(V_l\,P_{l,i}\right)_{,j} = 0. \tag{5.9}$$

The last term of the left hand side of this equation eventually vanishes since $V_l P_{l,ij}$ is symmetric in (i,j) and

$$V_{l,j} P_{l,i} = -\frac{1}{\tau^0} P_{l,i} P_{l,j} + \frac{1}{(\tau^0)^3}\tau_k P_{k,j}\,\tau_l P_{l,i}, \tag{5.10}$$

which is also symmetric in those indices. So finally we have

$$\mathcal{D}_\eta \Omega_k + V_i \Omega_{k,i} + V_{i,i}\Omega_k - V_{k,i}\Omega_i = 0, \tag{5.11}$$

JCAP03(2015)030

which means in particular that the curl field is only sourced by itself. Consequently, in the absence of such source terms in the initial conditions, as is the case for adiabatic initial conditions, no curl modes will be created in the relativistic flows.

We are here confronted to a situation very similar to the case of non-relativistic fluids, in which curl modes are generated after shell-crossing only. An immediate consequence is that, in standard Perturbation Theory calculations, the evolution equations of the density and P_i-divergence fields form, together with the equations describing the scalar modes of the metric fluctuations, a complete set of equations.

It is then possible to write those equations on a form easily comparable to the one of a non-relativistic pressureless fluid. To that aim, let us introduce for each fluid labelled by τ_i the density contrast field δ_{τ_i},

$$\delta_{\tau_i}(\eta, x^i) = \frac{n_c(\eta, x^i; \tau_i)}{n_c^{(0)}(\tau_i)} - 1. \tag{5.12}$$

The evolution equations then read

$$\mathcal{D}_\eta \delta_{\tau_i} + \left(V_i(1+\delta_{\tau_i})\right)_{,i} = 0, \tag{5.13}$$

$$\mathcal{D}_\eta P_{i,i} + \left(V_j P_{i,j}\right)_{,i} - \mathcal{S}_{\tau_i,ii} = 0, \tag{5.14}$$

where V_i is related to the field P_i via (5.4) and where the source term $\mathcal{S}_{\tau_i}$ is given by

$$\mathcal{S}_{\tau_i} = \tau_0 A + \tau_j B_j - \frac{1}{2}\frac{\tau_j \tau_k}{\tau_0} h_{jk}. \tag{5.15}$$

Note that the relation (5.4) between P_i and V_i can be easily inverted,

$$P_i = \tau_i \left(1 - \frac{1}{1 - \tau_j \tau_j / \tau_0^2} \frac{\tau_j V_j}{\tau_0}\right) - \tau_0 V_i. \tag{5.16}$$

In the following we explore in further detail this system.

5.3 The extended Galilean invariance

What are the invariance properties of this system? The original system (3.5)–(3.13) was invariant under transformations that preserved the operator $P^\mu \partial_\mu$ present in the left hand side of the equation describing the time evolution of P_i. By analogy, here we would like to find transformations that preserve the operator $\mathcal{D}_\eta + V_i \partial_i$ present in the left hand side of the corresponding subhorizon equation, while preserving the time variable. Assuming that τ_i and τ_0 are unchanged, this can be obtained the following way

$$\tilde{x}^i = x^i + d_i(\eta), \tag{5.17}$$

$$\tilde{\eta} = \eta, \tag{5.18}$$

$$\tilde{\delta}_{\tau_i}(\eta, \tilde{x}^i) = \delta_{\tau_i}(\eta, x^i), \tag{5.19}$$

$$\tilde{V}_i(\eta, \tilde{x}^i) = V_i(\eta, x^i) + \partial_\eta d_i(\eta). \tag{5.20}$$

The transformation rule for the velocity field V_i can be re-expressed as a transformation rule for the momentum field P_i using (5.16),

$$\tilde{P}_i(\eta, \tilde{x}^i) = P_i(\eta, x^i) - \tau_0 \partial_\eta d_i(\eta) - \frac{\tau_0}{\tau_0^2 - \tau_j \tau_j} \tau_i \tau_j \partial_\eta d_j(\eta). \tag{5.21}$$

JCAP03(2015)030

$P_{i,i}$ and all the potentials being unchanged under such transformations, the invariance of the equation of interest is ensured. This result is an extension of the extended Galilean invariance satisfied by the CDM flow. For CDM, as it has been stressed in recent papers ([24, 26]), this property has important consequences regarding large-scale structure formation. In particular, one expects the unequal time correlation functions of fields of that type to obey Ward identities. We will derive them for relativistic species in terms of the power spectra of the Fourier modes.

5.4 Nonlinear equations in Fourier space

We complete this work by presenting a global motion equation in Fourier space, showing explicitly the coupling structure of the motion equations. So let us introduce the velocity divergence field in units of - $\mathcal{H}$, $\theta_{\tau_i}(\eta, x^i)$,[10]

$$\theta_{\tau_i}(\eta, x^i) = -\frac{P_{i,i}(\eta, x^i; \tau_i)}{ma\mathcal{H}}. \tag{5.22}$$

When written in Fourier space, eqs. (5.13)–(5.14) read[11]

$$\left(a\partial_a - \mathrm{i}\frac{\mu k\tau}{\mathcal{H}\tau_0}\right)\delta_{\tau_i}(\mathbf{k}) + \frac{ma}{\tau_0}\left(1 - \frac{\mu^2\tau^2}{\tau_0^2}\right)\theta_{\tau_i}(\mathbf{k}) = - \frac{ma}{\tau_0}\int \mathrm{d}^3\mathbf{k}_1\mathrm{d}^3\mathbf{k}_2\alpha_R(\mathbf{k}_1, \mathbf{k}_2; \tau_i)\delta_{\tau_i}(\mathbf{k}_1)\theta_{\tau_i}(\mathbf{k}_2) \tag{5.23}$$

$$\left(1 + a\frac{\partial_a\mathcal{H}}{\mathcal{H}} + a\partial_a - \mathrm{i}\frac{\mu k\tau}{\mathcal{H}\tau_0}\right)\theta_{\tau_i}(\mathbf{k}) - \frac{k^2}{ma\mathcal{H}^2}\mathcal{S}_{\tau_i}(\mathbf{k}) = - \frac{ma}{\tau_0}\int \mathrm{d}^3\mathbf{k}_1\mathrm{d}^3\mathbf{k}_2\beta_R(\mathbf{k}_1, \mathbf{k}_2; \tau_i)\theta_{\tau_i}(\mathbf{k}_1)\theta_{\tau_i}(\mathbf{k}_2), \tag{5.24}$$

where $\mathcal{S}_{\tau_i}(\mathbf{k})$ is the Fourier transform of the field $\mathcal{S}_{\tau_i}(\mathbf{x})$,

$$\mathcal{S}_{\tau_i}(\mathbf{k}) = \tau_0 A(\mathbf{k}) + \vec{\tau}\cdot\vec{B}(\mathbf{k}) - \frac{1}{2}\frac{\tau_i\tau_j}{\tau_0}h_{ij}(\mathbf{k}) \tag{5.25}$$

and where the kernel functions are defined as

$$\alpha_R(\mathbf{k}_1, \mathbf{k}_2; \tau) = \delta_{\mathrm{Dirac}}(\mathbf{k} - \mathbf{k}_1 - \mathbf{k}_2)\frac{(\mathbf{k}_1 + \mathbf{k}_2)}{k_2^2}\cdot\left[\mathbf{k}_2 - \vec{\tau}\frac{\mathbf{k}_2\cdot\vec{\tau}}{\tau_0^2}\right], \tag{5.26}$$

$$\beta_R(\mathbf{k}_1, \mathbf{k}_2; \tau) = \delta_{\mathrm{Dirac}}(\mathbf{k} - \mathbf{k}_1 - \mathbf{k}_2)\frac{(\mathbf{k}_1 + \mathbf{k}_2)^2}{2k_1^2k_2^2}\left[\mathbf{k}_1\cdot\mathbf{k}_2 - \frac{\mathbf{k}_1\cdot\vec{\tau}\mathbf{k}_2\cdot\vec{\tau}}{\tau_0^2}\right]. \tag{5.27}$$

The explicit computation of the source term $\mathcal{S}_{\tau_i}(\mathbf{k})$ would require to take the subhorizon limit of the Einstein equations and to perform a summation over all the cosmic fluids (see equation (3.21)).[12] A remarkable property is that the kernel functions α_R and β_R depend on the flow considered via the variable $\vec{\tau}$. In the non-relativistic limit (i.e. when $\tau_0 \to -ma$

[10] In the non-relativistic limit, $\partial_i P_i = -ma\partial_i V^i$.

[11] Because of the phase shifts that appear between the flows when they propagate, those equations have a non-zero imaginary part. However, the correlation functions of the fields are real since the fields are real in real space and thus $\delta_{\tau_i}(\mathbf{k}) = \delta^*_{\tau_i}(-\mathbf{k})$ and $\theta_{\tau_i}(\mathbf{k}) = \theta^*_{\tau_i}(-\mathbf{k})$.

[12] Details about the way in which the summation over the flows should be performed is given in section 4.1 of [21].

JCAP03(2015)030

and $\tau_i \to 0$), we recover the standard equations and the kernel functions that appear in the CDM flow equation (see [27]).

We are now in position to write the full equation of motion, including the scale-scale nonlinear couplings in the presence of cold and hot non-interacting dark matter. We recall that these equations are valid until the first shell-crossing occurs. Formally, we consider a collection of n streams. Each stream is single-flow. It corresponds to either a CDM component or a baryonic component or a massive neutrino component. All these fluids obey the very same motion equations so there is no point in the following to distinguish them from one another.

It means that the time-dependent $2n$-uplet,

$$\Psi_a(\mathbf{k}) = (\delta_{\tau_1}(\mathbf{k}), \theta_{\tau_1}(\mathbf{k}), \ldots, \delta_{\tau_n}(\mathbf{k}), \theta_{\tau_n}(\mathbf{k}))^T, \tag{5.28}$$

contains all the relevant field components. Note that the Einstein equations relate the potentials to those fields thus these potentials are eventually eliminated.

In this context, the motion equations (5.23) and (5.24) can formally be recast in the form

$$\partial_\eta \Psi_a(\mathbf{k}) + \Omega_a{}^b \, \Psi_b(\mathbf{k}) = \gamma_a{}^{bc}(\mathbf{k}_1, \mathbf{k}_2) \Psi_b(\mathbf{k}_1) \Psi_c(\mathbf{k}_2), \tag{5.29}$$

where the indices a and b run from 1 to $2n$.[13] In the right hand side of this equation, it is assumed that the wave modes are integrated over. The matrix elements $\Omega_a{}^b$ encode the linear theory couplings. They contain in particular the way in which the source terms $\mathcal{S}_{\tau_i}(\mathbf{k})$ can be re-expressed as a function of the $2n$-uplet elements.

Besides, the *symmetrized vertex* matrix $\gamma_a{}^{bc}(\mathbf{k}_1, \mathbf{k}_2)$ describes the nonlinear interactions between different Fourier modes. Its components are given by

$$\gamma_{2p-1}^{2p-1\,2p}(\mathbf{k}_1, \mathbf{k}_2) = -\frac{ma}{2\tau_0} \alpha_R(\mathbf{k}_1, \mathbf{k}_2, \tau_p) \tag{5.30}$$

$$\gamma_{2p}^{2p\,2p}(\mathbf{k}_1, \mathbf{k}_2) = -\frac{ma}{\tau_0} \beta_R(\mathbf{k}_1, \mathbf{k}_2, \tau_p), \tag{5.31}$$

with $\gamma_a{}^{bc}(\mathbf{k}_1, \mathbf{k}_2) = \gamma_a{}^{cb}(\mathbf{k}_2, \mathbf{k}_1)$ and $\gamma_a{}^{bc} = 0$ otherwise. Contrarily to the pure CDM case, the $\gamma_a{}^{bc}$ matrix elements depend on time (and on the background evolution) for each mode through the time evolution of τ_0. Remarkably though, they encode all the nonlinear couplings of the system, which is formally similar to that of a multi-component system of pressureless fluids.

Equation (5.29) is the main result of this paper. It encodes the evolution of streams of relativistic or non-relativistic particles in the nonlinear regime at subhorizon scales. It can in particular be used in the context of the growth of large-scale structure in presence of massive neutrinos. At this stage however we do not propose an operational procedure to implement such Perturbation Theory calculations. To do so, one could think for example about making use of the so-called Time Renormalization Group (TRG) approach introduced in [28]. Indeed, thanks to the motion equation (5.29), it is possible to compute the time derivative of products such as $\Psi_a(\mathbf{k}, \eta)\Psi_b(\mathbf{k}', \eta)$ or $\Psi_a(\mathbf{k}_1, \eta)\Psi_b(\mathbf{k}_2, \eta)\Psi_c(\mathbf{k}_3, \eta)$. Once their ensemble averages computed, one can get the coupled evolution equations for the power spectra (see [28]). Provided the truncation is properly made, such equations encompass the standard Perturbation Theory calculations but with the advantage that no explicit computation of the linear Green function is necessary. The simplicity of this approach has already been advocated in

[13] The Einstein notation for the summation over repeated indices is adopted.

JCAP03(2015)030

this context in [1], where it is used to evaluate the impact of massive neutrinos on structure growth (but restricting the neutrino fluid to its linear behavior).

5.5 The Ward identities

Let us define unequal time correlators as $\langle \delta_{\tau_1}(\eta_1, \mathbf{k}_1) \dots \delta_{\tau_n}(\eta_n, \mathbf{k}_n) \rangle$ for a collection of flows τ_i. Due to statistical homogeneity, such quantities are expected to be proportional to $\delta_{\rm Dirac}\left(\sum_i \mathbf{k}_i\right)$. One can then define the multi-point power spectra $\mathcal{P}$ so that

$$\langle \delta_{\tau_1}(\eta_1, \mathbf{k}_1) \dots \delta_{\tau_n}(\eta_n, \mathbf{k}_n) \rangle = \delta_{\rm Dirac}\left(\sum_i \mathbf{k}_i\right) \mathcal{P}_{\tau_1,\dots,\tau_n}\left(\eta_1, \mathbf{k}_1, \dots, \eta_n, \mathbf{k}_n\right). \tag{5.32}$$

Following [24, 26] and [29], one can derive Ward identities that give consistency relations between those quantities.

We denote $\tilde{\delta}(\mathbf{k}, \eta)$ the Fourier density contrast in presence of a large-scale displacement field $d_i(\eta)$ (with an arbitrary time dependence and d_i being treated linearly). It can be expressed as a function of the Fourier density contrast in absence of such displacement thanks to a simple phase shift,

$$\tilde{\delta}_{\tau_i}(\mathbf{k}, \eta) = \exp(\mathrm{i}\mathbf{k}.\mathbf{d})\delta_{\tau_i}(\mathbf{k}, \eta) \approx (1 + \mathrm{i}\mathbf{k}.\mathbf{d})\delta_{\tau_i}(\mathbf{k}, \eta). \tag{5.33}$$

This relation gives explicitly the dependence of each mode on a large-scale displacement field. The Ward identities are then obtained by relating such large displacement fields to long-wave modes. More precisely, one can define adiabatic modes inducing equal displacements in all the flows, denoted $\delta_{\rm adiab.}(\mathbf{q})$, and satisfying

$$\mathbf{d}_{\rm adiab}(\eta, \mathbf{x}) = \int \mathrm{d}^3\mathbf{q} \frac{-\mathrm{i}\mathbf{q}}{q^2} e^{\mathrm{i}\mathbf{q}.\mathbf{x}} \delta_{\rm adiab.}(\eta, \mathbf{q}). \tag{5.34}$$

This definition imposes[14]

$$\langle \delta_{\rm adiab.}(\eta, \mathbf{q}) \mathbf{d}_{\rm adiab}(\eta', \mathbf{x}) \rangle = \frac{\mathrm{i}\mathbf{q}}{q^2} \mathcal{P}_{\rm adiab.}(\eta, \eta', q), \tag{5.35}$$

$\mathcal{P}_{\rm adiab.}(\eta, \eta', q)$ being the unequal time power spectrum of adiabatic modes. Making use of eq. (5.33), the correlator reads for an adiabatic displacement

$$\langle \tilde{\delta}_{\tau_1}(\eta_1, \mathbf{k}_1) \dots \tilde{\delta}_{\tau_n}(\eta_n, \mathbf{k}_n) \rangle = \left(1 + \mathrm{i} \sum_i \mathbf{k}_i.\mathbf{d}_{\rm adiab.}(\eta_i)\right) \langle \delta_{\tau_1}(\eta_1, \mathbf{k}_1) \dots \delta_{\tau_n}(\eta_n, \mathbf{k}_n) \rangle, \tag{5.36}$$

where the ensemble average is performed over all the modes except those participating in the large-scale displacement perturbation. Finally, assuming that the only dependence with a large-scale adiabatic mode is in the displacement field, one can eventually derive the following relation,

$$\begin{aligned} \mathcal{P}_{\rm adiab.,\tau_1,\dots,\tau_n}(\eta, \mathbf{q}, \eta_1, \mathbf{k}_1, \dots, \eta_n, \mathbf{k}_n) = \\ - \sum_i \frac{\mathbf{k}_i.\mathbf{q}}{q^2} \mathcal{P}_{\rm adiab.}(\eta, \eta_i, q)\ \mathcal{P}_{\tau_1,\dots,\tau_n}(\eta_1, \mathbf{k}_1, \dots, \eta_n, \mathbf{k}_n). \end{aligned} \tag{5.37}$$

It is obtained by computing the average of the product between the quantity at play in eq. (5.36) and $\delta_{\rm adiab.}(\eta, \mathbf{q})$. This relation is valid for $q \ll k_i$. Note that the right hand side of the relation (5.37) automatically vanishes when all the time variables are equal as, in that case, one expects the result to be proportional to $\delta_{\rm Dirac}\left(\sum_i \mathbf{k}_i\right)$.

[14] To get this result, we have neglected the $e^{-\mathrm{i}\mathbf{q}.\mathbf{x}}$ term because we are interested here in large wavelenghts.

JCAP03(2015)030

6 Conclusions and perspectives

We have presented a derivation of fully nonlinear evolution equations for streams of relativistic particles in an arbitrary background. The derivation of these equations is entirely based on conservation laws. They lead to the equations (3.5) and (3.11), which form a closed system once the background is given.

The key point allowing to make this construction sensible is the fact that fluids of non-interacting particles, such as neutrinos, can be decomposed into a collection of streams, each of them obeying the independent motion equations we derived. This is the essence of eq. (2.4). It has been explicitly shown in [21] that this decomposition is effective at the level of the linear evolution of the whole neutrino fluid. The initial number density of particles in each stream can be computed once initial conditions and gauge are specified. In [21], we computed them for adiabatic initial conditions in the conformal Newtonian gauge. Here we extend the results to the synchronous gauge in order to be more exhaustive.

The last section of this study is devoted to the exploration of the coupling structure that appears once the motion equations are restricted to subhorizon scales. In this derivation, we retained only dominant nonlinear coupling terms based on a power counting argument. The resulting equations, (5.1)–(5.2), appear as a slight extension of those describing flows of cold dark matter at subhorizon scales. However, we think they capture all the relevant nonlinear couplings. The exploration of the properties of the resulting system gives very promising insights. We recall here the two most important points we noticed. The first one is that the momentum field P_i remains potential even in the nonlinear regime. It implies that, similarly to non-relativistic ones, relativistic streams can entirely be described by introducing a two-component scalar doublet containing the number density of particles and their velocity divergence. The second key element is that the couplings are only quadratic in the fields,[15] as for CDM. As a result the overall motion equation, which takes into account all the streams, can be recast in the formal form (5.29). This is the main result of this paper. It provides a starting point for the implementation of Perturbation Theory calculations involving relativistic species, such as neutrinos.

Note also that, throughout the paper, we paid attention to the invariances properties of the systems we studied. In particular, we showed that eq. (5.29) satisfies an extended Galilean invariance. Interestingly, it paves the way for a further exploration of the mode coupling structure, and particularly for a description of how the long-wave modes and the short-wave modes interact. We expect in particular that the relative motions that exist between the different streams act as a particularly efficient coupling mechanism. Indeed, as shown in [30], it is already the case for baryon-CDM mixtures. An effective way to address this issue is to exploit the eikonal approximation, as presented in refs. [27, 31]. We leave for further studies those calculations.

Acknowledgments

This work is partially supported by the grant ANR-12-BS05-0002 of the French Agence Nationale de la Recherche.

[15] This is true at subhorizon scales only.

JCAP03(2015)030

A Adiabatic initial conditions for massive neutrinos

We revisit here the setting of the initial conditions as presented in [21]: at initial time we assign to the flow labelled by τ_i all the neutrinos whose momentum P_i is equal to τ_i within $\mathrm{d}^3\tau_i$. The initial time $\eta_{\rm in}$ is chosen so that the neutrino decoupling occurs at a time $\eta < \eta_{\rm in}$ and neutrinos become non-relativistic at a time $\eta > \eta_{\rm in}$. The solutions we describe correspond to adiabatic initial conditions. We choose the simplest alternative respecting the adiabaticity constraint, i.e.

$$P_i(\eta_{\rm in}, \mathbf{x}; \tau_i) = \tau_i. \tag{A.1}$$

It implies in particular that $P_i{}^{(1)}(\mathbf{x}, \eta_{\rm in}; \tau_i) = 0$ and consequently that

$$\theta_P(\mathbf{x}, \eta_{\rm in}; \tau_i) = 0. \tag{A.2}$$

Besides, before decoupling, the background distribution of neutrinos is expected to follow a Fermi-Dirac law f_0 with a given temperature T and no chemical potential (see e.g. refs. [17–19, 32] for a physical justification of this assumption). Then, as explained in ref. [32], after neutrino decoupling the phase-space distribution function of neutrinos is still a Fermi-Dirac distribution, that we express here in terms of the momentum q defined so that the energy measured by an observer at rest in the metric, ϵ, satisfies

$$\epsilon^2 = m^2 + (q/a)^2. \tag{A.3}$$

Nonetheless, after decoupling, the temperature is expected to vary locally, whence

$$f\left(\eta_{\rm in}, \mathbf{x}, q\right) \propto \frac{1}{1 + \exp\left[q/(a k_B (T + \delta T(\eta_{\rm in}, \mathbf{x}))\right]}, \tag{A.4}$$

k_B being the Boltzmann constant. The relation between the energy (and thus q^μ) and p^μ as well as the expression of $\delta T/T$ in terms of the metric perturbations depend on the gauge chosen.

In the synchronous and conformal Newtonian gauges, the momentum variable is defined so that $\epsilon = -U^\mu p_\mu = -U^0 p_0$, U^μ being the four-velocity of the comoving observer. Thus

$$p_0 = -a\epsilon(1 + A). \tag{A.5}$$

Eq. (A.4) can thereby be re-expressed in terms of the variable p_i thanks to the relation

$$q = \tau - \frac{\tau_0^2}{\tau}\kappa(\tau, \tau_0, \mu, h, \gamma) + \frac{\tau_j}{\tau} p_j^{(1)}, \tag{A.6}$$

which gives

$$f\left(\eta_{\rm in}, \mathbf{x}, p_j\right) \propto \left(1 + \exp\left[\frac{\tau - \frac{\tau_0^2}{\tau}\kappa(\tau, \tau_0, \mu, h, \gamma) + \frac{\tau_j}{\tau} p_j^{(1)}}{a k_B (T + \delta T(\eta_{\rm in}, \mathbf{x}))}\right]\right)^{-1}. \tag{A.7}$$

One can see in particular that

$$f^{(1)}\left(\eta_{\rm in}, \mathbf{x}, p_j\right) = -\left(\frac{\delta T}{T} + \frac{\tau_0^2}{\tau^2}\kappa(\tau, \tau_0, \mu, h, \gamma)\right)\frac{\mathrm{d}f_0(p)}{\mathrm{d}\log p}. \tag{A.8}$$

JCAP03(2015)030

In the conformal Newtonian gauge, we recover of course eq. (4.19) of [21]. The second initial condition we need is therefore

$$\delta_n(\eta_{\rm in}, \mathbf{x}; \tau_i) = -\left(\frac{\delta T}{T} + \frac{\tau_0^2}{\tau^2}\kappa(\tau, \tau_0, \mu, h, \gamma)\right) \frac{\mathrm{d}\log f_0(\tau)}{\mathrm{d}\log \tau}. \tag{A.9}$$

As mentioned in [19], on super-Hubble scales, the temperature perturbation of the neutrino fluid is proportional to its density contrast: $4\delta T(\mathbf{x}, \eta_{\rm in})/T(\eta_{\rm in}) = \rho^{(1)}(\mathbf{x}, \eta_{\rm in})/\rho^{(0)}(\eta_{\rm in})$. Besides, the adiabaticity hypothesis imposes equality between the initial density contrasts of all species. Using the standard results that, for photons, $\rho_\gamma^{(1)}(\mathbf{x}, \eta_{\rm in})/\rho_\gamma^{(0)}(\eta_{\rm in}) = -2\psi(\mathbf{x}, \eta_{\rm in})$ in the conformal Newtonian gauge and $-\frac{2}{3}h_{ii}$ in the Synchronous gauge, one thus finds

$$\delta T(\mathbf{x}, \eta_{\rm in})/T(\eta_{\rm in}) = -\psi(\mathbf{x}, \eta_{\rm in})/2 \ \text{ in the conformal Newtonian gauge} \tag{A.10}$$

and

$$\delta T(\mathbf{x}, \eta_{\rm in})/T(\eta_{\rm in}) = -h_{ii}(\mathbf{x}, \eta_{\rm in})/6 \ \text{ in the Synchronous gauge .} \tag{A.11}$$

These relations are useful in order to implement the numerical resolution of the linearized motion equations, as presented in detail in [21].

References

[1] J. Lesgourgues, S. Matarrese, M. Pietroni and A. Riotto, *Non-linear Power Spectrum including Massive Neutrinos: the Time-RG Flow Approach*, *JCAP* **06** (2009) 017 [arXiv:0901.4550] [INSPIRE].

[2] M. Shoji and E. Komatsu, *Massive Neutrinos in Cosmology: Analytic Solutions and Fluid Approximation*, *Phys. Rev.* **D 81** (2010) 123516 [*Erratum ibid.* **D 82** (2010) 089901] [arXiv:1003.0942] [INSPIRE].

[3] D. Blas, M. Garny, T. Konstandin and J. Lesgourgues, *Structure formation with massive neutrinos: going beyond linear theory*, *JCAP* **11** (2014) 039 [arXiv:1408.2995] [INSPIRE].

[4] S. Saito, M. Takada and A. Taruya, *Neutrino mass constraint with the Sloan Digital Sky Survey power spectrum of luminous red galaxies and perturbation theory*, *Phys. Rev.* **D 83** (2011) 043529 [arXiv:1006.4845] [INSPIRE].

[5] S. Riemer-Sorensen et al., *The WiggleZ Dark Energy Survey: cosmological neutrino mass constraint from blue high-redshift galaxies*, *Phys. Rev.* **D 85** (2012) 081101 [arXiv:1112.4940] [INSPIRE].

[6] B. Audren, J. Lesgourgues, S. Bird, M.G. Haehnelt and M. Viel, *Neutrino masses and cosmological parameters from a Euclid-like survey: Markov Chain Monte Carlo forecasts including theoretical errors*, *JCAP* **01** (2013) 026 [arXiv:1210.2194] [INSPIRE].

[7] C. Carbone, L. Verde, Y. Wang and A. Cimatti, *Neutrino constraints from future nearly all-sky spectroscopic galaxy surveys*, *JCAP* **03** (2011) 030 [arXiv:1012.2868] [INSPIRE].

[8] EUCLID collaboration, R. Laureijs et al., *Euclid Definition Study Report*, arXiv:1110.3193 [INSPIRE].

[9] I. Tereno, C. Schimd, J.-P. Uzan, M. Kilbinger, F.H. Vincent and L. Fu, *CFHTLS weak-lensing constraints on the neutrino masses*, *Astron. Astrophys.* **500** (2009) 657 [arXiv:0810.0555] [INSPIRE].

[10] F. Villaescusa-Navarro et al., *Cosmology with massive neutrinos I: towards a realistic modeling of the relation between matter, haloes and galaxies*, *JCAP* **03** (2014) 011 [arXiv:1311.0866] [INSPIRE].

[11] S. Bird, M. Viel and M.G. Haehnelt, *Massive Neutrinos and the Non-linear Matter Power Spectrum*, *Mon. Not. Roy. Astron. Soc.* **420** (2012) 2551 [arXiv:1109.4416] [INSPIRE].

JCAP03(2015)030

[12] C. Wagner, L. Verde and R. Jimenez, *Effects of the neutrino mass splitting on the non-linear matter power spectrum*, *Astrophys. J.* **752** (2012) L31 [arXiv:1203.5342] [INSPIRE].

[13] G. Rossi et al., *Suite of Hydrodynamical Simulations for the Lyman-Alpha Forest with Massive Neutrinos*, *Astron. Astrophys.* **567** (2014) A79 [arXiv:1401.6464] [INSPIRE].

[14] S. Hannestad, T. Haugbolle and C. Schultz, *Neutrinos in Non-linear Structure Formation — a Simple SPH Approach*, *JCAP* **02** (2012) 045 [arXiv:1110.1257] [INSPIRE].

[15] F. Fontanot, F. Villaescusa-Navarro, D. Bianchi and M. Viel, *Semi-Analytic Galaxy Formation in Massive Neutrino Cosmologies*, *Mon. Not. Roy. Astron. Soc.* **447** (2015) 3361 [arXiv:1409.6309] [INSPIRE].

[16] F. Villaescusa-Navarro, *Small scales structures and neutrino masses*, arXiv:1501.04546 [INSPIRE].

[17] C.-P. Ma and E. Bertschinger, *A Calculation of the full neutrino phase space in cold + hot dark matter models*, *Astrophys. J.* **429** (1994) 22 [astro-ph/9308006] [INSPIRE].

[18] C.-P. Ma and E. Bertschinger, *Cosmological perturbation theory in the synchronous and conformal Newtonian gauges*, *Astrophys. J.* **455** (1995) 7 [astro-ph/9506072] [INSPIRE].

[19] J. Lesgourgues and S. Pastor, *Massive neutrinos and cosmology*, *Phys. Rept.* **429** (2006) 307 [astro-ph/0603494] [INSPIRE].

[20] N. Van de Rijt, *Signatures of the primordial universe in large-scale structure surveys*, Ph.D. Thesis, Ecole Polytechnique & Institut de Physique Théorique, CEA Saclay, Saclay, France (2012).

[21] H. Dupuy and F. Bernardeau, *Describing massive neutrinos in cosmology as a collection of independent flows*, *JCAP* **01** (2014) 030 [arXiv:1311.5487] [INSPIRE].

[22] F. Bernardeau, *The evolution of the large-scale structure of the universe: beyond the linear regime*, arXiv:1311.2724 [INSPIRE].

[23] J.-P. Uzan, *Dynamics of relativistic interacting gases: from a kinetic to a fluid description*, *Class. Quant. Grav.* **15** (1998) 1063 [gr-qc/9801108] [INSPIRE].

[24] A. Kehagias and A. Riotto, *Symmetries and Consistency Relations in the Large Scale Structure of the Universe*, *Nucl. Phys.* **B 873** (2013) 514 [arXiv:1302.0130] [INSPIRE].

[25] F. Bernardeau, S. Colombi, E. Gaztanaga and R. Scoccimarro, *Large scale structure of the universe and cosmological perturbation theory*, *Phys. Rept.* **367** (2002) 1 [astro-ph/0112551] [INSPIRE].

[26] M. Peloso and M. Pietroni, *Galilean invariance and the consistency relation for the nonlinear squeezed bispectrum of large scale structure*, *JCAP* **05** (2013) 031 [arXiv:1302.0223] [INSPIRE].

[27] F. Bernardeau, N. Van de Rijt and F. Vernizzi, *Resummed propagators in multi-component cosmic fluids with the eikonal approximation*, *Phys. Rev.* **D 85** (2012) 063509 [arXiv:1109.3400] [INSPIRE].

[28] M. Pietroni, *Flowing with Time: a New Approach to Nonlinear Cosmological Perturbations*, *JCAP* **10** (2008) 036 [arXiv:0806.0971] [INSPIRE].

[29] M. Peloso and M. Pietroni, *Ward identities and consistency relations for the large scale structure with multiple species*, *JCAP* **04** (2014) 011 [arXiv:1310.7915] [INSPIRE].

[30] D. Tseliakhovich and C. Hirata, *Relative velocity of dark matter and baryonic fluids and the formation of the first structures*, *Phys. Rev.* **D 82** (2010) 083520 [arXiv:1005.2416] [INSPIRE].

[31] F. Bernardeau, N. Van de Rijt and F. Vernizzi, *Power spectra in the eikonal approximation with adiabatic and nonadiabatic modes*, *Phys. Rev.* **D 87** (2013) 043530 [arXiv:1209.3662] [INSPIRE].

[32] J. Lesgourgues, G. Mangano, G. Miele and S. Pastor, *Neutrino Cosmology*, *Contemp. Phys.* **54** (2013) 1.

JCAP03(2015)030

Chapter 6

A concrete application of the multi-fluid description of neutrinos

This chapter draws attention to the interdependence between eikonal approximation, relative displacements of cosmic fluids and damping of the nonlinear matter power spectrum. Understanding it qualitatively is easy but the practical implementation requires a long-term task. As a preliminary stage, an application of our multi-fluid description, whose goal is to get a first estimate of the spatial scales at which nonlinear couplings involving neutrinos are relevant, is outlined (see section 6.3 for a full article on this topic).

6.1 Generalized definitions of displacement fields in the eikonal approximation

The compact equation of motion (3.16) having formally the same form with or without incorporating non-cold species, it is straightforward to generalize the use of the eikonal approximation.

In the multi-fluid approach, the eikonal limit of the γ matrix elements (5.19), (5.20) and (5.21) becomes (for $q \ll k$)

$$\gamma_{2p}{}^{bc}(\mathbf{k},\mathbf{q}) \approx -\delta_{2p}{}^{b}\delta_{2p}{}^{c}\,\frac{ma}{2q^2\tau_0^{[p]}}\mathbf{k}\cdot\left(\mathbf{q}-\frac{\mathbf{q}\cdot\vec{\tau}_p}{(\tau_0^{[p]})^2}\vec{\tau}_p\right), \tag{6.1}$$

$$\gamma_{2p-1}{}^{bc}_{}(\mathbf{k},\mathbf{q}) \approx -\delta_{2p-1}{}^{b}\delta_{2p}{}^{c}\,\frac{ma}{2q^2\tau_0^{[p]}}\mathbf{k}\cdot\left(\mathbf{q}-\frac{\mathbf{q}\cdot\vec{\tau}_p}{(\tau_0^{[p]})^2}\vec{\tau}_p\right), \tag{6.2}$$

which generalizes the result (3.29) obtained for a single cold-dark-matter fluid. What matters the most here is the fact that, still, all the non-zero matrix elements are identical. Their form restricts $\Xi_{2p}{}^{2p}$ and $\Xi_{2p-1}{}^{2p-1}$, defined in (3.27), to integrals of the field $\theta_{\vec{\tau}_p}(\mathbf{q},\eta)$[1]. Consequently, it is still possible to interpret the eikonal correction in terms of displacement fields $\mathbf{d}_p^{\rm eik.}$, defined so that

$$\int_{\eta'}^{\eta}\Xi_{2p}{}^{2p}(\mathbf{k},\eta'')\mathrm{d}\eta'' = \int_{\eta'}^{\eta}\Xi_{2p-1}{}^{2p-1}(\mathbf{k},\eta'')\mathrm{d}\eta'' = \mathrm{i}\,\mathbf{k}.\mathbf{d}_p^{\rm eik.}(\eta',\eta). \tag{6.3}$$

The way one constructs them from the velocity divergence field of the fluid labeled by $\vec{\tau}_p$ is necessarily

$$\mathbf{d}_p^{\rm eik.}(\eta,\eta') = -\mathrm{i}\int_{\eta'}^{\eta}\mathrm{d}\eta''\int\mathrm{d}^3\mathbf{q}\frac{ma}{q^2\tau_0^{[p]}}\left(\mathbf{q}-\frac{\mathbf{q}\cdot\vec{\tau}_p}{(\tau_0^{[p]})^2}\vec{\tau}_p\right)\theta_{\vec{\tau}_p}(\mathbf{q},\eta''). \tag{6.4}$$

For $\vec{\tau}_p=\vec{0}$, one recovers of course (3.40).

Note that a novelty of our approach is that, since the Ω matrix has become scale-dependent, one can also define background displacement fields, generated by the non-zero initial velocities. Indeed, the Ω and Ξ matrices have the same status in (3.28) when both are scale-dependent. By analogy with (6.3), such displacements contribute to the time integrals of the scale-dependent parts of $\Omega_{2p}{}^{2p}$ and $\Omega_{2p-1}{}^{2p-1}$ in the form $\mathrm{i}\,\mathbf{k}.\mathbf{d}_p^{(0)}$. According to equations (5.22) and (5.24), they read

$$\mathbf{d}_p^{(0)}(\eta,\eta') = -\int_{\eta'}^{\eta}\mathrm{d}\eta''\frac{\vec{\tau}_p}{\mathcal{H}(\eta'')\tau_0^{[p]}(\eta'')}. \tag{6.5}$$

Note that they do not impact on the time evolution of non-relativistic flows and of flows in which $\vec{\tau}_p$ is oriented in such a way that $\mathrm{i}\,\mathbf{k}.\mathbf{d}_p^{(0)}=0$. In all other cases, $\mathbf{d}_p^{(0)}$'s effect is dominant and superimposes to the perturbative one of $\mathbf{d}_p^{\rm eik.}$.

More precisely, in perturbation theory, one can write

$$\mathbf{d}_p(\eta,\eta') = \mathbf{d}_p^{(0)}(\eta,\eta') + \mathbf{d}_p^{\rm eik.\,(1)}(\eta,\eta') + \mathbf{d}_p^{\rm eik.\,(2)}(\eta,\eta') + \ldots \tag{6.6}$$

[1]Similarly to what is done in section 3.5.1, the elements $\gamma_{2p-1}{}^{2p\ 2p-1}$ are neglected since they are reduced by a factor q/k in comparison with the other non-zero matrix elements.

The role of such displacement fields with respect to structure formation is discussed in the next section.

6.2 Impact on the nonlinear growth of structure

6.2.1 Qualitative description

The case of baryons + cold dark matter

The eikonal approximation is useful when it comes to describe couplings between large-scale modes and small-scale modes. Such couplings have proven to impact noticeably on the structure-formation rate when they intervene in fluids made of baryons and cold dark matter, due to a non-zero relative velocity between those two species. Reference [179] was the first to examine this. It has then been supplemented by [17]. The relative velocity in question, $v_{\rm rel}$, emerges at recombination, when the speed of baryons starts to decline while the one of cold dark matter remains unchanged. Because of this, there is a transitory period during which baryons and cold dark matter evolve differently, which postpones the time at which baryons fall into the potential wells created by cold dark matter. Inevitably, it also postpones the time at which astrophysical objects made of baryons start to form under gravitational instability. In other words, relative motions between baryons and cold dark matter slow down the growth of structure. The scales affected by this phenomenon are the scales at which perturbations in the two fluids are advected relative to each other more rapidly than they grow, i.e. the scales at which $k > \mathcal{H}/\langle v_{\rm rel}^2\rangle^{1/2}$. In the equations of motion, it is encoded in couplings between small-scale modes and large-scale modes. In this particular context, "small scales" refers to scales at which baryonic objects begin to form, i.e. ~ 10 kpc, and "large scales" stands for the typical coherence length of the relative velocity field, i.e. few Mpc (see the calculation in [179]).

One may expect relative displacements between cold dark matter and massive neutrinos to affect the nonlinear matter power spectrum in a similar way. Verifying it is the purpose of the article presented in section 6.3. The general reasoning is sketched in the next paragraphs.

The impact of adiabatic modes in the general case

In our multi-fluid approach, it is useful to notice that several modes $\mathbf{q}$ contribute to each eikonal displacement field, whose expression is given by (6.4). Some of them are perforce adiabatic modes. The corresponding perturbations, $\theta_{\vec{\tau}_p}(\mathbf{q}_{\rm adiab}, \eta)$, contribute to the displacement field in the same manner in all flows. Hence, $\mathbf{d}_p$ can be written as

$$\mathbf{d}_p = \mathbf{d}_{\rm adiab} + \delta\mathbf{d}_p, \tag{6.7}$$

with $\mathbf{d}_{\rm adiab}$ identical in each flow[2]. Besides, as highlighted in section 3.5.1, the only effect of the eikonal correction is to shift the phase of the solution of equation (3.28). It is directly related to the extended Galilean invariance, according to which $\delta_{\vec{\tau}_p}$ and $\theta_{\vec{\tau}_p}$ are not affected by the introduction of a displacement field in the medium when they are written in real space (see section 5.2), and are thus only phase-shifted in reciprocal space. Hence, adiabatic displacement fields have no impact on equal-time power spectra because all the flows of the collection still evolve in phase when $\delta\mathbf{d}_p = \vec{0}$. Indeed, the equal-time ensemble average of adiabatically perturbed fields[3] $\tilde{\psi}_i(\mathbf{k}, \eta) = \exp[\mathrm{i}\mathbf{k}\cdot\mathbf{d}_{\rm adiab}(\eta)]\psi_i(\mathbf{k}, \eta)$ is

$$\langle\tilde{\psi}_1(\mathbf{k}_1, \eta)...\tilde{\psi}_N(\mathbf{k}_N, \eta)\rangle = \langle\psi_1(\mathbf{k}_1, \eta)...\psi_N(\mathbf{k}_N, \eta)\exp[\mathrm{i}\sum_{i=1}^{N}\mathbf{k}_i\cdot\mathbf{d}_{\rm adiab}(\eta)]\rangle, \tag{6.8}$$

whence

$$\langle\tilde{\psi}_1(\mathbf{k}_1, \eta)...\tilde{\psi}_N(\mathbf{k}_N, \eta)\rangle = \langle\psi_1(\mathbf{k}_1, \eta)...\psi_N(\mathbf{k}_N, \eta)\rangle \tag{6.9}$$

because of statistical homogeneity (according to which $\sum\mathbf{k}_i = \vec{0}$). The adiabatic contributions to the displacement fields have therefore no impact on the nonlinear matter power spectrum (at least in the standard case of a power spectrum involving equal-time fields).

For non-relativistic species, it is known that the most growing mode is adiabatic. Consequently, we know that adiabatic modes will be dominant in neutrino streams at late time. However, non-adiabatic contributions can *a priori* play a significant role before the non-relativistic transition. Equation (6.6) recalls that their effects

[2]In section 5.3, I focused on the adiabatic contribution.

[3]Those fields can be for instance $\delta_{\vec{\tau}_p}$ or $\theta_{\vec{\tau}_p}$.

are perturbative but they can take over when $\mathbf{k}.\mathbf{d}_p^{(0)}$ is small.

The impact of non-adiabatic modes in the general case

The non-adiabatic contributions, $\delta\mathbf{d}_p$, are specific to each flow. It means that, when such contributions are taken into account, the phases of the individual solutions of (3.28) vary from one flow to another. In this context, couplings between species are not effective mechanisms to enhance perturbations. The matter power spectrum is thus expected to be damped compared to what it is in the absence of $\delta\mathbf{d}_p$. This can be characterized by the statistical properties of relative motions between flows. In our study, we computed them explicitly for massive neutrinos by taking the cold pressureless fluid as benchmark.

6.2.2 Quantitative results in the case of streams of massive neutrinos

To identify the scales at which relative displacements damp the matter power spectrum, it is useful to compute the quantity

$$\sigma_p = \frac{\langle[\mathbf{k}.(\mathbf{d}_p - \mathbf{d}_{\rm CDM})]^2\rangle^{1/2}}{k}, \tag{6.10}$$

where the index "CDM" refers to the fluid labeled by $\vec{\tau} = \vec{0}$. In this context, the most impacted scales are those for which $k \gtrsim 1/\sigma_p$, i.e. the scales at which $\mathbf{k}.(\mathbf{d}_p - \mathbf{d}_{\rm CDM})$ is substantial[4].

In the conformal Newtonian gauge, we found (the full calculation is given in the article presented in the next section):

$$\langle(\mathbf{k}.\mathbf{d}_{\rm CDM})^2\rangle = 4\pi k^2 \int {\rm d}q\, P_\psi(q)\, \frac{1}{3}\, |T_{\rm CDM}(\mathbf{q})|^2 \tag{6.11}$$

and

$$\langle(\mathbf{k}.(\mathbf{d}_p - \mathbf{d}_{\rm CDM}))^2\rangle = 2\pi k^2 \int {\rm d}q\, P_\psi(q) \int_{-1}^{1} {\rm d}\alpha^{[p]} \times \tag{6.12}$$
$$\left\{\frac{1}{2}\left[1-(\mu^{[p]})^2\right]\left[1-(\alpha^{[p]})^2\right]|T_p^{(0)}(\mathbf{q}) - T_{\rm CDM}(\mathbf{q}) - T_p^{(2)}(\mathbf{q})|^2 + (\alpha^{[p]})^2(\mu^{[p]})^2|T_p^{(2)}(\mathbf{q})|^2\right\}.$$

$\alpha^{[p]}$ is the Cosine of the angle between $\vec{\tau}_p$ and $\mathbf{q}$. $T_{\rm CDM}$ and $T_p^{()}$ are transfer functions

[4] I recall that $\mathbf{k}.\delta\mathbf{d}_p$ is the non-adiabatic contribution to ${\Xi_b}^c$, see (6.3).

defined so that

$$-\int_{\eta'}^{\eta} \mathrm{d}\eta'' \frac{ma}{\tau_0^{[p]}} \left(\frac{\tau^{[p]}}{\tau_0^{[p]}}\right)^{\beta} \theta_{\vec{\tau}_p}(\mathbf{q},\eta'') = T_p^{(\beta)}(\eta,\eta',\mathbf{q})\psi_{\rm init}(\mathbf{q}), \tag{6.13}$$

$$\int_{\eta'}^{\eta} \mathrm{d}\eta''\ \theta_{\rm CDM}(\mathbf{q},\eta'') = T_{\rm CDM}(\eta,\eta',\mathbf{q})\psi_{\rm init}(\mathbf{q}), \tag{6.14}$$

with $\psi_{\rm init}$ the initial value of the metric perturbation ψ that appears in the perturbed Friedmann-Lemaître metric written in the conformal Newtonian gauge, (2.18). $P_\psi(q)$ is the initial power spectrum of ψ, i.e.

$$\langle \psi_{\rm init}(\mathbf{q})\psi_{\rm init}(\mathbf{q}')\rangle = (2\pi)^3\delta_{\rm D}(\mathbf{q}+\mathbf{q}')\ P_\psi(q). \tag{6.15}$$

One can see from (6.12) that the amplitude of σ_p strongly depends on the flow considered, both via $\alpha^{[p]}$, $\mu^{[p]}$ and $\tau^{[p]}$ (the latter being hidden in the transfer functions). We computed numerically the per mode contributions to σ_p (the setting of the cosmological parameters and initial conditions is precised in our article). Clearly, there are fluids (those with a high initial velocity) in which σ_p is comparable in amplitude with $\frac{\langle[\mathbf{k}.(\mathbf{d}_{\rm CDM})]^2\rangle^{1/2}}{k}$. This is illustrated in figure 6.1. The top panel is of particular interest since the background displacement $\mathbf{d}_p^{(0)}$ has no effect when $\mu = 0$. In this context, relative displacements are the leading contributions to the damping of the nonlinear neutrino power spectrum. Modeling their impact is therefore crucial.

As a preliminary result, we deduced from the plot 6.1 that the relevant scales correspond to wavenumbers larger than (or of the order of) about 0.2 to 0.5 h/Mpc, σ_p being of the order of 2 to 5 Mpc/h (when considering neutrinos with a 0.3 eV mass). A much more thorough analysis is necessary to make testable predictions and go one step further in precision cosmology. In this exploratory study, our aim was rather to draw attention to the way in which relative displacements between neutrino streams and other fluids affect the nonlinear growth of structure.

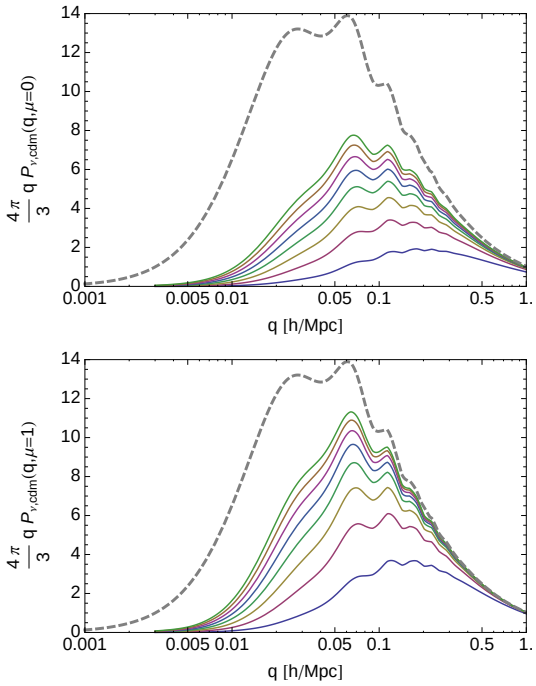

Figure 6.1: Power spectrum of the relative displacement as a function of the mode q for different neutrino flows. The quantities $P_{\nu,\mathrm{cdm}}$ are defined so that the right hand sides of eqs. (6.11) and (6.12) read $4\pi k^2/3 \int \mathrm{d}q P_{\nu,\mathrm{cdm}}(q)$. The values of τ range from 2.25 $k_B T_0$ (bottom line) to 18 $k_B T_0$ (top line). On the top panel μ is set to 0, on the bottom panel μ is set to 1 and the neutrino mass is set to 0.3 eV. The gray dashed line represents the power spectrum of the cold dark matter displacement.

6.3 Article "On the importance of nonlinear couplings in large-scale neutrino streams"

Journal of Cosmology and Astroparticle Physics
An IOP and SISSA journal

On the importance of nonlinear couplings in large-scale neutrino streams

Hélène Dupuy and Francis Bernardeau

Institut d'Astrophysique de Paris, UMR-7095 du CNRS,
Université Pierre et Marie Curie, 98 bis bd Arago, 75014 Paris, France
Institut de Physique Théorique, CEA, IPhT, F-91191 Gif-sur-Yvette,
CNRS, URA 2306, F-91191 Gif-sur-Yvette, France

E-mail: helene.dupuy@cea.fr, francis.bernardeau@iap.fr

Received March 20, 2015
Revised June 26, 2015
Accepted August 6, 2015
Published August 28, 2015

Abstract. We propose a procedure to evaluate the impact of nonlinear couplings on the evolution of massive neutrino streams in the context of large-scale structure growth. Such streams can be described by general nonlinear conservation equations, derived from a multiple-flow perspective, which generalize the conservation equations of non-relativistic pressureless fluids. The relevance of the nonlinear couplings is quantified with the help of the eikonal approximation applied to the subhorizon limit of this system. It highlights the role played by the relative displacements of different cosmic streams and it specifies, for each flow, the spatial scales at which the growth of structure is affected by nonlinear couplings. We found that, at redshift zero, such couplings can be significant for wavenumbers as small as $k = 0.2\,h/\mathrm{Mpc}$ for most of the neutrino streams.

Keywords: cosmological neutrinos, cosmic flows, neutrino theory

ArXiv ePrint: 1503.05707

doi:10.1088/1475-7516/2015/08/053

JCAP08(2015)053

Contents

JCAP08(2015)053

1 Introduction

Statistical properties of the large-scale structure of the universe have long been proposed as an efficient instrument to constrain cosmological parameters. In this context, a careful account of the role played by massive neutrinos is crucial. So far, it has often been overlooked in the nonlinear or quasilinear regime because of the technical complexity specific to the study of massive neutrinos (see recent attempts in [1–3]). This is all the more unfortunate that cosmological observations can fruitfully improve our knowledge of those particles. The signature of neutrino masses on cosmological observables is indeed expected to be significant enough for those masses to be constrained observationally [4–9].

In the linear regime, the effect of neutrinos is now well understood (see refs. [10–12]). The need for nonlinear corrections in their equations of motion has been raised because the cosmological observations that are the most sensitive to neutrinos masses, i.e. for wavenumbers in the 0.1-0.2 h/Mpc range, precisely correspond to the mildly nonlinear regime. To deal with this issue, several strategies can be adopted. Until recently, in analytic works, the neutrino fluids had always been treated in the linear regime, nonlinear couplings being introduced in the dark matter description only. This nonlinear treatment can be implemented with the help of the Renormalization Group time-flow approach [1, 13]. Improvements upon such schemes have been proposed in [3], which consists in a hybrid approach that matches the full Boltzmann hierarchy to an effective two-fluid description at an intermediate redshift. [14] is, for its part, a systematic perturbative expansion of the Vlasov equation in which high-order corrections to the neutrino density contrast are computed without the explicit need to track the perturbed neutrino momentum distribution.

Ideally, however, the fully nonlinear evolution of the neutrino fluid should be depicted. A natural way to do so would be to take inspiration of the standard linear description, which relies on the Boltzmann equation, and extend the harmonic decomposition of the phase-space distribution function to the nonlinear regime. This has been done in [15] but this method turned out to be particularly difficult to handle. In [16, 17], we proposed to describe massive neutrinos as a superposition of single-flow fluids, the equations of motion of each of them being written in the nonlinear regime.

In this paper, we are interested in exploiting those theoretical developments in order to identify the scales at which nonlinear couplings in the neutrino fluids are expected to play a

significant role. In order to do so, we apply the eikonal approximation to the nonlinear equations of motion. Note that this approximation had already been exploited in the literature to develop a Perturbation Theory approach for cold dark matter ([18]) and had proved to be able to capture the leading coupling effects.

The article is structured as follows. In section 2, we recall the form of the nonlinear equations of motion describing the time evolution of non-interacting fluids, relativistic or not, when using a multi-fluid approach. Section 3 explains in detail how the eikonal approximation can be implemented in those equations and emphasizes the key role of relative displacement fields. Finally, in section 4, power spectra of the relative displacements between neutrino fluids and the cold dark matter component are presented. The impact on the growth of large-scale structure is then discussed in a quantitative way.

2 Nonlinear equations of motion (multi-fluid description)

Following [16, 17], it is now clear that any non-interacting relativistic fluid can be divided into several flows, each of them evolving then independently until first shell-crossings. In cosmology, this approach obviously applies to massive neutrinos since they are free-streaming. In this framework, each flow can be defined as the collection of all the particles (with a mass m) having initially the same comoving momentum. They are entirely characterized by two coupled fields, namely the comoving number density n_c and momentum P_μ. Those fields obey the following general equations,

$$\frac{\partial}{\partial\eta}n_c + \frac{\partial}{\partial x^i}\left(\frac{P^i}{P^0}n_c\right) = 0, \tag{2.1}$$

with $P^\mu(\eta, x^i) = g^{\mu\nu}P_\nu(\eta, x^i)$ and $P^\mu P_\mu = -m^2$, $g_{\mu\nu}$ being the metric, and

$$P^\nu P_{\mu,\nu} = \frac{1}{2}P^\sigma P^\nu g_{\sigma\nu,\mu}. \tag{2.2}$$

These equations directly ensue from the matter and momentum conservation equations, applied to each flow. At this stage, no perturbative expansion of the metric is involved. The properties of the whole fluid are then inferred by examining an appropriate number of such flows, each of them being labeled by the initial value of its field P_i, denoted τ_i (found to be constant at zeroth order in Perturbation Theory). The initial number density of particles in each flow is constrained by the choice of initial conditions. For instance, the case of adiabatic initial conditions is described in detail in [16].

We are interested here in equations i) involving linearized metric perturbations (but non-linearized fields) and ii) rid of the coupling terms that are subdominant at subhorizon scales. They can be written in terms of the number density contrast

$$\delta_{\tau_i}(\eta, x^i) = \frac{n_c(\eta, x^i; \tau_i)}{n_c^{(0)}(\tau_i)} - 1 \tag{2.3}$$

and of the velocity divergence field (in units of $-\mathcal{H}$, $\mathcal{H}$ being the conformal Hubble constant)

$$\theta_{\tau_i}(\eta, x^i) = -\frac{\partial_i P_i(\eta, x^i; \tau_i)}{ma\mathcal{H}} \tag{2.4}$$

JCAP08(2015)053

since the field P_i has found to be potential in this regime.[1] For a generic perturbed Friedmann-Lemaître metric,[2] whose time variable is the conformal time η,

$$\mathrm{d}s^2 = a^2(\eta)\left[-(1+2A)\mathrm{d}\eta^2 + 2B_i\mathrm{d}x^i\mathrm{d}\eta + (\delta_{ij}+h_{ij})\mathrm{d}x^i\mathrm{d}x^j\right], \tag{2.5}$$

one has in Fourier space for the mode characterized by the wave vector $\mathbf{k}$ ([17])

$$\left(a\partial_a - \mathrm{i}\frac{\mu k\tau}{\mathcal{H}\tau_0}\right)\delta_{\tau_i}(\mathbf{k}) + \frac{ma}{\tau_0}\left(1-\frac{\mu^2\tau^2}{\tau_0^2}\right)\theta_{\tau_i}(\mathbf{k}) = -\frac{ma}{\tau_0}\int \mathrm{d}^3\mathbf{k}_1\mathrm{d}^3\mathbf{k}_2\alpha_R(\mathbf{k}_1,\mathbf{k}_2;\tau_i)\delta_{\tau_i}(\mathbf{k}_1)\theta_{\tau_i}(\mathbf{k}_2), \tag{2.6}$$

$$\left(1+a\frac{\partial_a\mathcal{H}}{\mathcal{H}}+a\partial_a-\mathrm{i}\frac{\mu k\tau}{\mathcal{H}\tau_0}\right)\theta_{\tau_i}(\mathbf{k}) - \frac{k^2}{ma\mathcal{H}^2}\mathcal{S}_{\tau_i}(\mathbf{k}) = -\frac{ma}{\tau_0}\int \mathrm{d}^3\mathbf{k}_1\mathrm{d}^3\mathbf{k}_2\beta_R(\mathbf{k}_1,\mathbf{k}_2;\tau_i)\theta_{\tau_i}(\mathbf{k}_1)\theta_{\tau_i}(\mathbf{k}_2). \tag{2.7}$$

We have introduced here

$$\mu = \frac{k_i\tau_i}{k\tau}, \tau^2 = \tau_i\tau_i \text{ and } \tau_0 = -\sqrt{m^2a^2+\tau_i^2}. \tag{2.8}$$

Besides, $\mathcal{S}_{\tau_i}(\mathbf{k})$ is a source term given by

$$\mathcal{S}_{\tau_i}(\mathbf{k}) = \tau_0 A(\mathbf{k}) + \vec{\tau}\cdot\vec{B}(\mathbf{k}) - \frac{1}{2}\frac{\tau_i\tau_j}{\tau_0}h_{ij}(\mathbf{k}). \tag{2.9}$$

These equations contain also the generalized kernel functions, adapted to relativistic flows,

$$\alpha_R(\mathbf{k}_1,\mathbf{k}_2;\tau) = \delta_{\mathrm{Dirac}}(\mathbf{k}-\mathbf{k}_1-\mathbf{k}_2)\frac{(\mathbf{k}_1+\mathbf{k}_2)}{k_2^2}\cdot\left[\mathbf{k}_2 - \vec{\tau}\frac{\mathbf{k}_2\cdot\vec{\tau}}{\tau_0^2}\right], \tag{2.10}$$

$$\beta_R(\mathbf{k}_1,\mathbf{k}_2;\tau) = \delta_{\mathrm{Dirac}}(\mathbf{k}-\mathbf{k}_1-\mathbf{k}_2)\frac{(\mathbf{k}_1+\mathbf{k}_2)^2}{2k_1^2k_2^2}\left[\mathbf{k}_1\cdot\mathbf{k}_2 - \frac{\mathbf{k}_1\cdot\vec{\tau}\mathbf{k}_2\cdot\vec{\tau}}{\tau_0^2}\right]. \tag{2.11}$$

As mentioned in [17], they are extensions of the kernel functions found for pressureless fluids of non-relativistic species (see [19] for details in this context.).

In any practical implementation, it is necessary to consider a collection of N streams. In that case, the general equation of motion can conveniently be written in terms of the time-dependent $2N$-uplet,

$$\Psi_a(\mathbf{k}) = (\delta_{\tau_1}(\mathbf{k}),\theta_{\tau_1}(\mathbf{k}),\ldots,\delta_{\tau_N}(\mathbf{k}),\theta_{\tau_N}(\mathbf{k}))^T. \tag{2.12}$$

Before shell-crossing, it can incorporate all the relevant species (neutrinos, dark matter, baryons) as long as they interact only via gravitation. In this context, the equations (2.6) and (2.7) of all the flows can formally be recast in the form[3]

$$\partial_z\Psi_a(\mathbf{k}) + \Omega_a{}^b\,\Psi_b(\mathbf{k}) = \gamma_a{}^{bc}(\mathbf{k}_1,\mathbf{k}_2)\Psi_b(\mathbf{k}_1)\Psi_c(\mathbf{k}_2), \tag{2.13}$$

[1] This property, rigorously demonstrated in [17], generalizes that of non-relativistic species.

[2] Units are chosen so that the speed of light in vacuum is equal to unity.

[3] The Einstein notation for the summation over repeated indices is adopted and, in the right hand side of this equation, it is assumed that the wave modes are integrated over.

JCAP08(2015)053

where $\partial/\partial z \equiv a\partial/\partial a$ and the indices a and b run from 1 to $2N$. The matrix elements $\Omega_a{}^b$ gather the linear couplings. They contain in particular the way in which the source terms $\mathcal{S}_{\tau_i}(\mathbf{k})$ can be re-expressed as a function of the $2N$-uplet elements. The left hand side of this equation is nothing but the linear field evolution. The right hand side contains the coupling terms. More precisely, the *symmetrized vertex* matrix $\gamma_a{}^{bc}(\mathbf{k}_1, \mathbf{k}_2)$ describes the nonlinear interactions between the Fourier modes. It is given by

$$\gamma_{2p-1}^{2p-1\,2p}(\mathbf{k}_1, \mathbf{k}_2) = -\frac{ma}{2(\tau_p)_0}\alpha_R(\mathbf{k}_1, \mathbf{k}_2, \tau_p), \tag{2.14}$$

$$\gamma_{2p}^{2p\,2p}(\mathbf{k}_1, \mathbf{k}_2) = -\frac{ma}{(\tau_p)_0}\beta_R(\mathbf{k}_1, \mathbf{k}_2, \tau_p), \tag{2.15}$$

with $\gamma_a{}^{bc}(\mathbf{k}_1, \mathbf{k}_2) = \gamma_a{}^{cb}(\mathbf{k}_2, \mathbf{k}_1)$ and $\gamma_a{}^{bc} = 0$ otherwise.

3 The eikonal approximation

The eikonal approximation,[4] developed in [18], is based on the observation that the amplitudes of the kernel functions describing mode couplings, α_R and β_R, significantly depend on the ratio between the wave numbers at play. This has been observed for non-relativistic fluids and we show here that it is the case for relativistic fluids too. This property leads to the idea that the right hand side of eq. (2.13) can be split into two integration domains. One is called the hard domain and encompasses modes whose wavelengths are of the same order (and for which the coupling functions are always finite). The other one is referred to as the soft domain. It is made of modes of very different wavelengths for which the coupling functions, of the order of the wavelength ratio, are large.

The main idea is that there are regimes in which the dominant coupling structure is in the soft domain. This is the case for instance in early-time fluids containing baryons and cold dark matter. At the time of recombination, the baryon velocity drops steeply whereas the velocity of cold dark matter is not affected by decoupling. It means that, at intermediate scales (i.e. between the Silk damping length and the sound horizon), the relative velocity $v_{\rm rel}$ between the baryon flow and the one of cold dark matter is substantial. Because of this, for scales at which $k > aH/\langle v_{\rm rel}^2\rangle^{1/2}$ (at decoupling), the wavelength of gravitational potential wells is too small for baryons to fall in them before being pushed towards another direction. Eventually, this phenomenon induces a damping of the matter power spectrum. The relative motion between cold dark matter and baryons and its effects on the matter power spectrum have been highlighted in [21, 22]. Such studies illustrate the relevance of couplings between large scale modes and small scale modes in the framework of structure formation. For instance, in the case of mixtures of baryons and cold dark matter, the typical coherence length of the relative velocity field is of the order of few Mpc, which is much larger than the scales at which basic baryonic objects start to form under gravitational clustering (of the order of 10 kpc). The same formalism can be used to obtain the large k behavior of the propagators in case of a single pressureless fluid, reproducing the results obtained in [23, 24]. In the same spirit, we propose here to investigate the impact of the relative motion between given neutrino streams and the cold dark matter fluid with the help the eikonal approximation. It will allow us to infer the amplitude of neutrino coupling effects.

[4] In this context, the term refers to diagram resummations performed in quantum electrodynamic field equations, [20].

JCAP08(2015)053

For convenience, let us assume that the soft domain is obtained for $k_2 \ll k_1$ in eq. (2.13). We have then $\mathbf{k} = \mathbf{k}_1$ and the contribution corresponding to the soft domain can be viewed as a mere corrective term in the *linear* equation describing the evolution of the mode $\mathbf{k}$. In other words, eq. (2.13) can be rewritten

$$\frac{\partial}{\partial z}\Psi_a(z,\mathbf{k}) + \Omega_a{}^b(z,\mathbf{k})\Psi_b(z,\mathbf{k}) - \Xi_a^b(z,\mathbf{k})\Psi_b(z,\mathbf{k}) \\ = \left[\gamma_a{}^{bc}(\mathbf{k}_1,\mathbf{k}_2)\ \Psi_b(\mathbf{k}_1,z)\ \Psi_c(\mathbf{k}_2,z)\right]_{\mathcal{H}}, \tag{3.1}$$

with

$$\Xi_a{}^b(\mathbf{k},z) \equiv 2\int_{\mathcal{S}} \mathrm{d}^3\mathbf{q}\ {}^{\mathrm{eik.}}\gamma_a{}^{bc}(\mathbf{k},\mathbf{q})\Psi_c(\mathbf{q},z)\ . \tag{3.2}$$

The soft momenta q (i.e. $q \ll k$) at play in eq. (3.2) are integrated over so that $\Xi_a{}^b(z,\mathbf{k})$ is independent on $\Psi_a(z,k)$. It is a mere time and scale dependent matrix. The fact that the integration domain is restricted to the soft wave numbers in eq. (3.2) is the key element. Conversely, in the right-hand side of eq. (3.1), the implicit convolution product excludes the soft domain (i.e. all the modes concerned have comparable wavelengths). When the contribution of the hard domain is negligible, *eq. (3.1) can then be viewed as the equation of motion of the mode* $\mathbf{k}$ *evolving in a medium perturbed by large-scale modes.* It therefore encodes the way in which long-wave modes alter the growth of structure. Once $\Xi_a^b(z,\mathbf{k})$ is given, eq. (3.1) can be solved as a linear equation. This is precisely the eikonal approximation of the global equation of motion.

In practice, applying the eikonal approximation to $\Xi_a{}^b(\mathbf{k},z)$ means that the vertex values that appear in this quantity have to be computed assuming $k_2 \ll k_1$. In this framework, one deduces from eqs. (2.10), (2.11), (2.14) and (2.15) that the eikonal limit of the vertex elements is

$${}^{\mathrm{eik.}}\gamma_{2p}^{bc}(\mathbf{k},\mathbf{k}_2) = -\delta_{2p}^b\delta_{2p}^c\ \frac{ma}{2k_2^2(\tau_p)_0}\mathbf{k}\cdot\left(\mathbf{k}_2 - \frac{\mathbf{k}_2\cdot\vec{\tau_p}}{(\tau_p)_0^2}\vec{\tau_p}\right), \tag{3.3}$$

$${}^{\mathrm{eik.}}\gamma_{2p-1}^{bc}(\mathbf{k},\mathbf{k}_2) = -\delta_{2p-1}^b\delta_{2p}^c\ \frac{ma}{2k_2^2(\tau_p)_0}\mathbf{k}\cdot\left(\mathbf{k}_2 - \frac{\mathbf{k}_2\cdot\vec{\tau_p}}{(\tau_p)_0^2}\vec{\tau_p}\right). \tag{3.4}$$

This expression depends on each flow through its initial momentum $\vec{\tau}_p$, which vanishes in the standard non-relativistic equations. Besides, $(\tau_p)_0 \to -ma$ in the non-relativistic limit so that one recovers the expected formulae in this limit (see [21, 25]).

In the following, we exploit the consequences of this approximation in order to evaluate the relevance of the coupling terms. As a first step, we can notice from eqs. (3.2), (3.3) and (3.4) that the two non-zero elements coming from the flow labeled by τ_p in the Ξ matrix, $\Xi_{2p}{}^{2p}$ and $\Xi_{2p-1}{}^{2p-1}$, are proportional to the velocity divergence of large-scale modes. Thus we can write

$$\int_{z_0}^{z}\Xi_a{}^b(z',\mathbf{k})\mathrm{d}z' = \mathrm{i}\,\mathbf{k}.\mathbf{d}_p(z_0,z)\ \delta_a{}^b, \tag{3.5}$$

where a and b are either $2p$ or $2p-1$ and where d_p is the total displacement field induced by the large-scale modes in the fluid labeled by τ_p. It reads necessarily

$$\mathbf{d}_p(z,z_0) = \mathrm{i}\int_{z_0}^{z}\mathrm{d}z'\int\mathrm{d}^3\mathbf{q}\frac{ma}{q^2(\tau_p)_0}\left(\mathbf{q} - \frac{\mathbf{q}\cdot\vec{\tau_p}}{(\tau_p)_0^2}\vec{\tau_p}\right)\Psi_{2p}(z',\mathbf{q}). \tag{3.6}$$

JCAP08(2015)053

Note that this displacement is superimposed on the zeroth order displacement field induced by the homogeneous momentum of the flow. This background displacement field is given by (see eqs. (2.6) and (2.7))

$$\mathbf{d}_p^{(0)} = -\int_{z_0}^{z} \frac{\vec{\tau}_p}{\mathcal{H}(\tau_p)_0}\,\mathrm{d}z'\,. \tag{3.7}$$

We will discuss this point in greater detail in the next section.

The impact of the eikonal correction introduced in the equation of motion depends on the way in which the various large-scale modes contribute to the displacement fields $\mathbf{d}_p$. The nature of the displacement is crucial in this context. In particular, one expects global displacement fields, which affect all species in a similar way, to induce a mere phase shift in the solution of the eikonal limit of (3.1). Remarkably, such displacements have no impact on power spectra, provided that the fields at play are evaluated at the same time (see the end of this section). Using the standard language of cosmology, we call those particular displacements "adiabatic displacements" in the following. On the contrary, relative displacements between species can induce a damping in power spectra. It is simply due to the fact that species must evolve in phase (at least during a small period of time) for couplings between them to generate a significant growth of perturbations. This phenomenon has been highlighted for the first time in [21] an reconsidered in [22]. In this paper, we show that such considerations can be extended to the study of relativistic fluids.

Knowing this, it is convenient to decompose displacement fields into

$$d_p(z, z_0) = d_{\mathrm{adiab}}(z, z_0) + \delta d_p(z, z_0), \tag{3.8}$$

where d_{adiab} denotes naturally the adiabatic part. The other part, δd_p, represents relative motions between fluids. For non-relativistic species, it is known that the most growing mode is part of the adiabatic modes. Since neutrinos become non-relativistic at late time, one expects the most growing mode of each fluid of neutrinos to become also an adiabatic mode ultimately.

When considering only the adiabatic part of the displacement field, the solution of the eikonal equation of motion is easy to find. Its form is related to the extended Galilean invariance of the equations of motion, well established for non-relativistic species and uncovered for the system (2.6)–(2.7) in [17]. Indeed, it has been shown that this system is invariant under the following transformations,

$$\tilde{x}^i = x^i + d_i(z), \tag{3.9}$$

$$\tilde{z} = z, \tag{3.10}$$

$$\tilde{\psi}_a(\tilde{z}, \tilde{\mathbf{x}}) = \psi_a(\eta, \mathbf{x}), \tag{3.11}$$

where the last transformation can equivalently be written $\tilde{\psi}_a(\tilde{\eta}, \mathbf{k}) = \exp(\mathrm{i}\mathbf{k}\cdot\mathbf{d}(\eta))\psi_a(\eta, \mathbf{k})$. It means that a homogeneous time-dependent displacement which disrupts the medium can be re-absorbed in a global phase shift of the Fourier transforms of the fields. Here, we are interested in making the large-scale adiabatic displacement fields play the role of the disturbers of the medium.

More explicitly, it is known that the solution of the standard linear system can be fully described with the help of its Green function, $g_a{}^b(z, z_0; \mathbf{k})$, defined in such a way that (see appendix A for details)

$$\Psi_a(z, \mathbf{k}) = g_a{}^b(z, z_0; \mathbf{k})\Psi_b(z_0, \mathbf{k}), \tag{3.12}$$

JCAP08(2015)053

with z and z_0 two arbitrary times. Besides, when the displacement field is purely adiabatic, the Green functions ${\xi_a}^b$ of the corrected linear system (i.e. the linear system in which an eikonal correction has been added) are related to those of the naked theory by

$$ {\xi_a}^b(z, z_0; \mathbf{k}) = {g_a}^b(z, z_0; \mathbf{k}) \exp(\mathrm{i}\mathbf{k}.\mathbf{d}_{\rm adiab}(z, z_0)). \tag{3.13} $$

A direct consequence of the symmetry property is that, after a transformation of the form (3.11), ensemble averages of any product of fields $\psi_a(z_a, \mathbf{k}_a)$ become proportional to $\exp[\mathrm{i}\sum_a \mathbf{k}_a \cdot \mathbf{d}_{\rm adiab}(z_a)]$, which is unity when the fields are computed at equal time. Indeed, statistical homogeneity imposes $\sum_a \mathbf{k}_a = 0$. This is the reason why equal time spectra or poly-spectra are not sensitive to the presence of adiabatic displacements.

Yet, we are interested in all contributions to the displacement field, including those that induce large motions between species. As already mentioned, in early-time mixtures of baryons and cold dark matter, those relative displacements (i.e. those non-adiabatic contributions that develop in the nonlinear regime) are the leading contributions to the nonlinear evolution of the power spectrum. To sketch the impact of massive neutrinos on the nonlinear growth rate, we evaluate in the next section the amplitude of the relative displacements involving them and we compute the corresponding power spectra.

4 Relative displacements and power spectra: quantitative results

As stressed in the previous section, in the eikonal approximation, the displacement fields that can cause a damping of the growth of structure are those that differ from one fluid to another. Hence, in this section, we compute on the one hand the power spectrum of the total displacement field of cold dark matter and, on the other hand, the power spectra of the relative displacement fields of relativistic flows (with respect to the a priori dominant cold dark matter component). Note that, in perturbation theory, such displacements are sums of terms of different orders (the zeroth order contribution $\mathbf{d}_p^{(0)}$ being defined in eq. (3.7)),

$$ \mathbf{d}_p(z, z_0) = \mathbf{d}_p^{(0)}(z, z_0) + \mathbf{d}_p^{(1)}(z, z_0) + \dots \tag{4.1} $$

Note also that the damping due to non-homogeneous corrections can be significant only if the considered flow is non-relativistic (since in that case $\mathbf{d}_\tau^{(0)}(z, z_0)$ is small) or if $\mathbf{k}$ is orthogonal to the zeroth order contribution (since in that case $\mathbf{k}.\mathbf{d}_\tau^{(0)}(z, z_0)$ is small compared with the other contributions). Hence, in the following, we compute the expected values of $\mathbf{k}.(\mathbf{d}_p - \mathbf{d}_{\rm cdm})$ as a function of the angle between the initial momentum $\vec{\tau}$ of the considered fluid and $\mathbf{k}$. Calculations are performed in the conformal Newtonian gauge,

$$ \mathrm{d}s^2 = a^2(\eta)\left[-(1+2\psi)\,\mathrm{d}\eta^2 + (1-2\phi)\,\mathrm{d}x^i \mathrm{d}x^j \delta_{ij}\right]. \tag{4.2} $$

This choice will allow us to take advantage of the numerical work presented in [16]. First, let us define two transfer functions $D_{\rm cdm}$ and $D_p^{(\alpha)}$ as

$$ \int_{z_0}^{z} \mathrm{d}z' \frac{ma}{-(\tau_p)_0} \left(\frac{\tau_p}{(\tau_p)_0}\right)^\alpha \theta_{\tau_p}(z', \mathbf{q}) = D_p^{(\alpha)}(z, z_0, \mathbf{q}) \psi_{\rm init}(\mathbf{q}), \tag{4.3} $$

$$ \int_{z_0}^{z} \mathrm{d}z' \; \theta_{\rm cdm}(z', \mathbf{q}) = D_{\rm cdm}(z, z_0, \mathbf{q}) \psi_{\rm init}(\mathbf{q}), \tag{4.4} $$

JCAP08(2015)053

where $\psi_{\rm init}$ is the initial value of the potential ψ. The statistical properties of those quantities are entirely encoded in their initial power spectra $P_\psi(q)$, defined so that

$$\langle \psi_{\rm init}(\mathbf{q})\psi_{\rm init}(\mathbf{q}')\rangle = (2\pi)^3\delta_{\rm Dirac}(\mathbf{q}+\mathbf{q}')\ P_\psi(q). \tag{4.5}$$

Using the expressions of the transfer functions, the contribution of each mode to the displacement field of each relativistic flow reads

$$\mathbf{d}_p(z,z_0;\mathbf{q}) = -\mathrm{i}\left(\frac{\mathbf{q}}{q^2}D_p^{(0)}(z,z_0,\mathbf{q}) - \frac{\vec{\tau}_p.\mathbf{q}}{q^2(\tau_p)^2}\vec{\tau}_p D_p^{(2)}(z,z_0,\mathbf{q})\right)\psi_{\rm init}. \tag{4.6}$$

Besides, for the cold dark matter component, one simply has

$$\mathbf{d}_{\rm cdm}(z,z_0;\mathbf{q}) = -\mathrm{i}\frac{\mathbf{q}}{q^2}\,D_{\rm cdm}(z,z_0,\mathbf{q})\psi_{\rm init}(q). \tag{4.7}$$

Furthermore, one can notice that the displacement field of a relativistic flow along an arbitrary direction $\mathbf{k}$ depends on the angles between both $\mathbf{q}$ and $\vec{\tau}$ and $\mathbf{k}$ and $\vec{\tau}$. After integration over the other angles, one finds for the variances of respectively $\mathbf{k}.\mathbf{d}_{\rm cdm}$ and $\mathbf{k}.(\mathbf{d}_p-\mathbf{d}_{\rm cdm})$,

$$\langle(\mathbf{k}.\mathbf{d}_{\rm cdm})^2\rangle = 4\pi k^2\int \mathrm{d}q\, P_\psi(q)\,\frac{1}{3}\,|D_{\rm cdm}(\mathbf{q})|^2 \tag{4.8}$$

and

$$\langle(\mathbf{k}.(\mathbf{d}_p-\mathbf{d}_{\rm cdm}))^2\rangle = 2\pi k^2\int \mathrm{d}q\, P_\psi(q)\int_{-1}^{1}\mathrm{d}\mu\left[\frac{1}{2}(1-\mu_k^2)(1-\mu^2)|D_p^{(0)}(\mathbf{q}) - D_{\rm cdm}(\mathbf{q}) - D_p^{(2)}(\mathbf{q})|^2 + \mu^2\mu_k^2|D_p^{(2)}(\mathbf{q})|^2\right], \tag{4.9}$$

where μ_k is the Cosine of the angle between the initial momentum of the flow $\vec{\tau}_p$ and $\mathbf{k}$ and where an integration is made over μ, Cosine of the angle between $\vec{\tau}_p$ and $\mathbf{q}$. In eq. (4.9), one can notice that the dependence of the r.m.s. with respect to μ_k is such that it does not vanish either for an initial momentum $\vec{\tau}_p$ orthogonal to $\mathbf{k}$ (i.e. when $\mu_k=0$) or for an initial flow momentum along $\mathbf{k}$ (i.e. when $\mu_k=1$).

On figure 1, we present the per mode contribution to the right hand side of eq. (4.9) in the particular case of neutrino fluids for $\mu_k=0$ on the left panel and $\mu_k=1$ on the right panel. The results have been computed assuming a single species of neutrinos whose mass is $m_\nu=0.3$ eV and using the cosmological parameters derived from the Five-Year Wilkinson Microwave Anisotropy Probe (WMAP 5) observations. Besides, the values of the initial power spectra have been obtained under the assumption that, in the cosmological model we adopt, metric fluctuations are initially adiabatic and characterized by the scalar spectral index $n_s\approx 0.96$. We can see that the resulting neutrino power spectra are comparable in amplitude to the cold dark matter one (represented by a thick dashed line).

Denoting $\sigma_{d_{\rm cdm}} = 1/k\langle(\mathbf{k}.\mathbf{d}_{\rm cdm})^2\rangle^{1/2}$ and $\sigma_{d_\tau} = 1/k\langle(\mathbf{k}.(\mathbf{d}_p-\mathbf{d}_{\rm cdm}))^2\rangle^{1/2}$ we find that σ_{d_τ} is of the order of 2 to about $5h^{-1}$Mpc for the cosmological modes we used for which $\sigma_{d_{\rm cdm}}\approx 6h^{-1}$Mpc,. This result depends of course on the flow considered and is actually of the order of the cold dark matter value. What does it mean? Similarly to what happens in mixtures of baryons and cold dark matter, one expects the perturbation growth to be damped for wave numbers larger than or comparable to $1/\sigma_{d_\tau}$, for which $\mathbf{k}\cdot\mathbf{d}_\tau^{(1)}$ is expected to be finite. Besides, such a non-adiabatic damping is potentially larger than the damping due to the homogeneous displacements $\mathbf{d}_p^{(0)}$ of each flow when μ_k is close to zero. A precise determination of the amplitude of these effects would require a full analysis of the nonlinear evolution of the system. We leave this for a future study.

JCAP08(2015)053

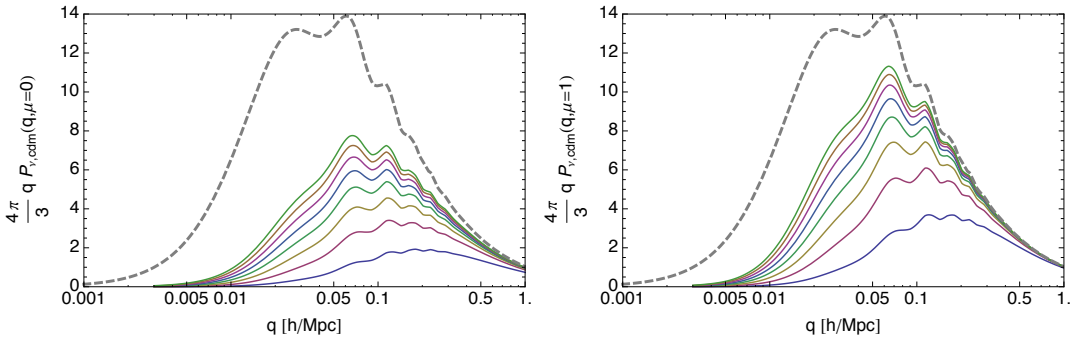

Figure 1. Power spectrum of the relative displacement as a function of the mode q for different neutrino flows. The quantities $P_{\nu,\mathrm{cdm}}$ are defined so that the right hand sides of eqs. (4.8) and (4.9) read $4\pi k^2/3 \int \mathrm{d}q P_{\nu,\mathrm{cdm}}(q)$. The values of τ range from 2.25 $k_B T_0$ (bottom line) to 18 $k_B T_0$ (top line). On the left panel μ_k is set to 0, on the right panel μ_k is set to 1 and the neutrino mass is set to 0.3 eV. The gray dashed line represents the power spectrum of the cold dark matter displacement.

5 Conclusion

Describing neutrinos as a collection of single-stream fluids is an efficient strategy to infer their impact on the growth of the cosmic structure. Using this approach, one indeed gets a complete set of equations of motion that incorporate all the nonlinear effects of relativistic or non-relativistic particles. In the subhorizon limit, the system takes the form of eq. (2.13), which can be easily handled by a formalism originally developed to depict non-relativistic species.

In this paper, we evaluated the amplitudes of the nonlinear couplings and determined for each flow the scales at which they are expected to impact significantly on the structure growth. For that purpose, we implemented the eikonal approximation into the general equation of motion. We concluded that the impact of large-scale modes on an arbitrary mode are entirely driven by large-scale displacement fields whose expressions are given in eq. (3.6). The comparison between the displacement field associated with each flow of neutrinos and the one associated with cold dark matter makes easy the comparison between the power spectra of the relative displacements between neutrinos and cold dark matter and the power spectrum of the displacement of cold dark matter alone. We found as a preliminary result that couplings involving massive neutrinos (with a 0.3 eV mass) are expected to induce a damping of the perturbation growth in neutrino flows for wave numbers larger than (or of the order of) about 0.2 to 0.5 h/Mpc. A detailed quantitative analysis of the consequences of this phenomenon is yet to be done but those findings confirm the significance of nonlinear couplings in the dynamical evolution of neutrino fluids. This sets the stage for further numerical studies beyond the linear regime.

Acknowledgments

This work is partially supported by the grant ANR-12-BS05-0002 of the French Agence Nationale de la Recherche.

A Integral form of the overall equation of motion

For a finite number of flows, the overall equation of motion (2.13) can formally be written in an integral form. It requires the use of the associated Green operator, $g_a{}^b(z, z_0; \mathbf{k})$, of the

JCAP08(2015)053

linear system. This operator satisfies

$$\Psi_a(z,\mathbf{k}) = g_a{}^b(z,z_0;\mathbf{k})\Psi_b(z_0,\mathbf{k}), \tag{A.1}$$

with z and z_0 two arbitrary times. It is besides solution of the differential equation

$$\frac{\partial}{\partial z} g_a{}^b(z,z_0;\mathbf{k}) + \Omega_a{}^c(z;\mathbf{k})\, g_c{}^b(z,z_0;\mathbf{k}) = 0 \tag{A.2}$$

with the condition

$$g_a{}^b(z_0,z_0;\mathbf{k}) = \delta_a{}^b, \tag{A.3}$$

$\delta_a{}^b$ being the identity matrix. Formally, the Green function is the ensemble of all the independent linear solutions of the system.[5] Denoting $u_a^{(\alpha)}(z,\mathbf{k})$ these solutions, g_a^b reads

$$g_a^b(z,z_0,\mathbf{k}) = \sum_\alpha u_a^{(\alpha)}(z,\mathbf{k}) c^b_{(\alpha)}(z_0,\mathbf{k}), \tag{A.4}$$

where the variables $c^b_{(\alpha)}(z_0,\mathbf{k})$ are set so that (A.3) is satisfied.

Studying in detail the Green operator of such a system is beyond the scope of this appendix. Suffice to note here that, unlike the case of a single pressureless flow, the Green operator generally depends on the wave mode k. This dependence is expected to gradually decay over time and to disappear at very late time, when all the flows have become non-relativistic. At this stage, the situation is then identical to the one of a collection of cold dark matter fluids.

As for the standard system of non-relativistic particles, the knowledge of the Green operator of the equation of motion allows to write a formal solution (see [26–28]), which is given by

$$\begin{aligned}\Psi_a(\mathbf{k},z) \;=\; & g_a{}^b(\mathbf{k},z,z_0)\;\Psi_b(\mathbf{k},z_0) \\ & + \int_{z_0}^{z} \mathrm{d}z'\; g_a{}^b(\mathbf{k},z,z')\;\gamma_b{}^{cd}(\mathbf{k}_1,\mathbf{k}_2)\Psi_c(\mathbf{k}_1,z')\Psi_d(\mathbf{k}_2,z'),\end{aligned} \tag{A.5}$$

with $\Psi_a(\mathbf{k},z_0)$ the initial conditions. Many of the approaches developed in order to improve upon standard Perturbation Theory rely on an accurate description of the Green functions beyond the linear regime. This is the purpose for instance of RPT and RegPT methods ([28–30]).

References

[1] J. Lesgourgues, S. Matarrese, M. Pietroni and A. Riotto, *Non-linear power spectrum including massive neutrinos: the time-RG flow approach*, *JCAP* **06** (2009) 017 [arXiv:0901.4550] [INSPIRE].

[2] M. Shoji and E. Komatsu, *Massive neutrinos in cosmology: analytic solutions and fluid approximation*, *Phys. Rev.* **D 81** (2010) 123516 [*Erratum ibid.* **D 82** (2010) 089901] [arXiv:1003.0942] [INSPIRE].

[3] D. Blas, M. Garny, T. Konstandin and J. Lesgourgues, *Structure formation with massive neutrinos: going beyond linear theory*, *JCAP* **11** (2014) 039 [arXiv:1408.2995] [INSPIRE].

[5] A priori the number of solutions is equal to twice the number of flows considered.

JCAP08(2015)053

[4] S. Saito, M. Takada and A. Taruya, *Neutrino mass constraint with the Sloan Digital Sky Survey power spectrum of luminous red galaxies and perturbation theory*, *Phys. Rev.* **D 83** (2011) 043529 [arXiv:1006.4845] [INSPIRE].

[5] S. Riemer-Sorensen et al., *The WiggleZ dark energy survey: cosmological neutrino mass constraint from blue high-redshift galaxies*, *Phys. Rev.* **D 85** (2012) 081101 [arXiv:1112.4940] [INSPIRE].

[6] B. Audren, J. Lesgourgues, S. Bird, M.G. Haehnelt and M. Viel, *Neutrino masses and cosmological parameters from a Euclid-like survey: Markov Chain Monte Carlo forecasts including theoretical errors*, *JCAP* **01** (2013) 026 [arXiv:1210.2194] [INSPIRE].

[7] C. Carbone, L. Verde, Y. Wang and A. Cimatti, *Neutrino constraints from future nearly all-sky spectroscopic galaxy surveys*, *JCAP* **03** (2011) 030 [arXiv:1012.2868] [INSPIRE].

[8] EUCLID collaboration, R. Laureijs et al., *Euclid definition study report*, arXiv:1110.3193 [INSPIRE].

[9] I. Tereno, C. Schimd, J.-P. Uzan, M. Kilbinger, F.H. Vincent and L. Fu, *CFHTLS weak-lensing constraints on the neutrino masses*, *Astron. Astrophys.* **500** (2009) 657 [arXiv:0810.0555] [INSPIRE].

[10] C.P. Ma and E. Bertschinger, *A calculation of the full neutrino phase space in cold + hot dark matter models*, *Astrophys. J.* **429** (1994) 22.

[11] C.-P. Ma and E. Bertschinger, *Cosmological perturbation theory in the synchronous and conformal Newtonian gauges*, *Astrophys. J.* **455** (1995) 7 [astro-ph/9506072] [INSPIRE].

[12] J. Lesgourgues and S. Pastor, *Massive neutrinos and cosmology*, *Phys. Rept.* **429** (2006) 307 [astro-ph/0603494] [INSPIRE].

[13] M. Pietroni, *Flowing with time: a new approach to nonlinear cosmological perturbations*, *JCAP* **10** (2008) 036 [arXiv:0806.0971] [INSPIRE].

[14] F. Führer and Y.Y.Y. Wong, *Higher-order massive neutrino perturbations in large-scale structure*, *JCAP* **03** (2015) 046 [arXiv:1412.2764] [INSPIRE].

[15] N. Van de Rijt, *Signatures of the primordial universe in large-scale structure surveys*, Ph.D. thesis, Ecole Polytechnique & Institut de Physique Théorique, CEA Saclay, France (2012).

[16] H. Dupuy and F. Bernardeau, *Describing massive neutrinos in cosmology as a collection of independent flows*, *JCAP* **01** (2014) 030 [arXiv:1311.5487] [INSPIRE].

[17] H. Dupuy and F. Bernardeau, *Cosmological perturbation theory for streams of relativistic particles*, *JCAP* **03** (2015) 030 [arXiv:1411.0428] [INSPIRE].

[18] F. Bernardeau, N. Van de Rijt and F. Vernizzi, *Resummed propagators in multi-component cosmic fluids with the eikonal approximation*, *Phys. Rev.* **D 85** (2012) 063509 [arXiv:1109.3400] [INSPIRE].

[19] F. Bernardeau, S. Colombi, E. Gaztañaga and R. Scoccimarro, *Large-scale structure of the Universe and cosmological perturbation theory*, *Phys. Rep.* **367** (2002) 1.

[20] H.D.I. Abarbanel and C. Itzykson, *Relativistic eikonal expansion*, *Phys. Rev. Lett.* **23** (1969) 53 [INSPIRE].

[21] D. Tseliakhovich and C. Hirata, *Relative velocity of dark matter and baryonic fluids and the formation of the first structures*, *Phys. Rev.* **D 82** (2010) 083520 [arXiv:1005.2416] [INSPIRE].

[22] F. Bernardeau, N. Van de Rijt and F. Vernizzi, *Power spectra in the eikonal approximation with adiabatic and nonadiabatic modes*, *Phys. Rev.* **D 87** (2013) 043530 [arXiv:1209.3662] [INSPIRE].

[23] M. Crocce and R. Scoccimarro, *Memory of initial conditions in gravitational clustering*, *Phys. Rev.* **D 73** (2006) 063520 [astro-ph/0509419] [INSPIRE].

JCAP08(2015)053

[24] F. Bernardeau, M. Crocce and E. Sefusatti, *Multi-point propagators for non-gaussian initial conditions*, *Phys. Rev.* **D 82** (2010) 083507 [arXiv:1006.4656] [INSPIRE].

[25] F. Bernardeau, *The evolution of the large-scale structure of the universe: beyond the linear regime*, arXiv:1311.2724.

[26] R. Scoccimarro, *Transients from initial conditions: a perturbative analysis*, *Mon. Not. Roy. Astron. Soc.* **299** (1998) 1097 [astro-ph/9711187] [INSPIRE].

[27] R. Scoccimarro, *A new angle on gravitational clustering*, in *The onset of nonlinearity in cosmology*, J.N. Fry et al. eds., New York Academy Sciences Annals volume 927, U.S.A. (2001).

[28] M. Crocce and R. Scoccimarro, *Renormalized cosmological perturbation theory*, *Phys. Rev.* **D 73** (2006) 063519 [astro-ph/0509418] [INSPIRE].

[29] F. Bernardeau, A. Taruya, and T. Nishimichi, *Cosmic propagators at two-loop order*, *Phys. Rev.* **D 89** (2014) 023502 [arXiv:1211.1571] [INSPIRE].

[30] A. Taruya, F. Bernardeau, T. Nishimichi and S. Codis, *RegPT: direct and fast calculation of regularized cosmological power spectrum at two-loop order*, *Phys. Rev.* **D 86** (2012) 103528 [arXiv:1208.1191] [INSPIRE].

JCAP08(2015)053

Conclusions and perspectives

This thesis, "Precision cosmology with the large-scale structure of the universe", provides innovative results of different types. What they have in common is the quest for precision in the description of the physical phenomena at work in the universe.

First, a toy model mimicking the propagation of light in an inhomogeneous spacetime has been presented. In this study, we chose a traditional Swiss-cheese representation. Often used in the litterature, such models offer the advantage of dealing with exact solutions of the Einstein equations, which do not affect the global dynamics of the universe while making it strongly inhomogeneous. A new method, mostly analytic, is proposed by us to investigate the impact of brutal fluctuations of density on Hubble diagrams. It relies on the introduction of Wronski matrices, which permit to determine the cumulative effect of several holes without difficulty when solving the geodesic and Sachs equations. We also derived an approximate luminosity-redshift relation for Swiss-cheese models, which turned out to be similar to the formula used in Dyer-Roeder approaches. By generating mock Hubble diagrams corresponding to the patchy spacetime, we exemplified how initial presumptions, such as the cosmological principle, can alter scientific conclusions, such as the estimation of cosmological parameters from Hubble diagrams. In general, the bias that an insertion of holes causes in Hubble diagrams can be large, due to a high sensitivity of luminosity distances with respect to the geometry of the medium. However, this effect has proven to decrease a lot with the cosmological constant, which is fortunate since observations clearly lean towards a universe content dominated by dark energy. By its extreme simplicity, our model (whose fluctuations of density are exaggeratedly abrupt), probably overestimates the bias. Indeed, large-scale structures, intergalactic gas, dark matter, etc. are likely to act as "smoothers" in the real universe. Compensation effects are undeniable. Yet

we are convinced that, in precision cosmology, it is worth examining this question minutely instead of crudely ignoring the mismatch between the scales at which the cosmological principle is valid and the scales probed by the standard candles used to build Hubble diagrams. Let us not forget that cosmological parameters are highly model-dependent so measuring them with an exquisite precision is not sufficient to attest that their values are representative of reality.

In the same spirit, I have presented in this manuscript a study in which Planck results on the one hand and observations of the SNLS 3 catalog on the other hand are interpreted assuming that the universe has a Swiss-cheese geometry. What motivated this investigation is the fact that the estimation of cosmological parameters from CMB and/or BAO (for instance observed by Planck) are not always consistent with that obtained from observational Hubble diagrams (for instance built from the SNLS 3 catalog). We have shown that, if one considers spacetimes that are particularly lumpy, the estimation of the cosmological parameter Ω_{m} from Hubble diagrams is very different from what it is when a model with a Friedmann-Lemaître spacetime is used. It can even be reconciled with the Planck estimation. Of course, such lumpy Swiss-cheese spacetimes are not realistic representations of the universe. What we wanted to point out is that the discrepancy might be due to the fact that those kinds of observations probe very different angular scales and are nevertheless interpreted with the same geometrical model. Estimations of the cosmological parameters being now very precise, a geometrical modeling which adapts to the scales considered should be opportune, or even necessary.

Our approach has scope for improvement in many ways: introducing holes with different sizes to get more liberty regarding the proportion of underdense regions, replacing photons by other particles, generating mock observations other than Hubble diagrams, making it more realistic by taking into account the real structure of the universe, etc. Actually, during my PhD, I specialized in another field of cosmology, namely the study of the large-scale structure of the universe with the help of perturbation theory. However, my collaborator Pierre Fleury devoted a major part of his PhD thesis (completed also this year) to light propagation in inhomogeneous and/or anisotropic spacetimes (see in particular [78], [75]).

The major result exposed in this thesis is the proposition of a new way of dealing with the neutrino component in cosmology. The idea is to decompose neutrinos into several single-flow fluids in order to get rid of velocity dispersion in each of them. Nonlinear equations of motion have been derived from conservation laws

in a generic perturbed Friedman-Lemaître metric, as well as formulae allowing to recover the usual physical quantities by summing over all the flows of the collection. Using those formulae to deduce the global energy density, velocity divergence and shear stress of massive neutrinos from our equations, we proved that, in the linear regime, our approach is consistent with the integration of the Boltzmann hierarchy. It required in particular to infer the individual initial conditions from the knowledge of the global initial distribution function of neutrinos. We did it explicitly for adiabatic initial conditions. Similarly to the standard approach describing the growth of perturbations in cold pressureless fluids, our method breaks down when shell crossing emerges. We argue that this phenomenon is likely to occur when neutrinos have become slow enough to be considered as cold. It means that, potentially, our work can also take advantage of the efforts realized in order to model shell crossing in cold fluids. We think that this multi-fluid description provides a more convenient basis to investigate the nonlinear behavior of neutrinos than the Boltzmann hierarchy. Moreover, it provides an additional information since the flows of neutrinos can be followed individually. It can be applied not only to massive neutrinos but, more generally, to any non-interacting species. In this context, cold dark matter appears as a mere fluid of the collection, whose particularity is to have a zero initial momentum. Any initial velocity (relativistic or not) and any mass can be handled by this formalism.

On this basis, we carried out a study devoted to the exploration of the coupling structure of our equations on subhorizon scales. The interest of this approximation is that it makes useful properties emerge while preserving the coupling terms that are relevant to depict the nonlinear growth of perturbations involved in structure formation. In particular, on subhorizon scales, the momentum fields that we chose as variables can be written as gradients in any gauge and at any order in perturbation theory. This key result is the starting point of several developments. First, taking inspiration of the description of cold dark matter, we introduced one doublet velocity divergence/density contrast per flow. It allowed us to gather in a unique nonlinear equation the growth of perturbations in all non-interacting fluids. The great advantage of this equation is that it is formally the same as the one derived from the Vlasov-Poisson system (on which most of the results of nonlinear perturbation theory rely) but with a much wider range of application. For this reason, our approach will hopefully allow to make one further step towards a relativistic generalization of nonlinear perturbation theory. We deliberately worked in arbi-

trary gauges in order to facilitate the demonstration of invariance properties. We therefore easily managed to generalize the so-called extended Galilean invariance. As for cold fluids, it has been useful to derive consistency relations and to study couplings between short-wave modes and long-wave modes with the help of the eikonal approximation.

We devoted a study specifically to the implementation of the eikonal approximation in our equations of motion. The aim was to write explicitly the eikonal corrections associated with each flow and to interpret them as sources of peculiar displacements. Taking the cold-dark-matter fluid as a benchmark, we showed that, for large wavenumbers and high initial velocities, the fields characterizing neutrinos can be phase-shifted with respect to the cold-dark-matter ones during a substantial amount of time. Eventually, this postpones the fall of neutrinos into potential wells and is therefore expected to damp the growth of structure. It would of course be interesting to examine carefully the impact it can have on the nonlinear matter power spectrum. However, doing so is a long-term project, which is still at its preliminary stage. In general, a considerable difficulty related to the study of the impact of nonlinear couplings on a given dynamics is the fact that it is not easy to forecast which couplings will cancel each other out. Thanks to our Lagrangian-like decomposition, there is no risk of missing cancellations of this type here.

The most evident perspectives offered by the multi-fluid point of view that we adopted are the following. Formally, standard resummation techniques allowing to compute the matter power spectrum at NLO can be extended to the global equation that we derived. However, the associated formalism is very heavy so replacing brutally the usual 2×2 matrices by $N\times N$ ones, which have moreover non-zero scale-dependent imaginary parts, would be prohibitive. The continuation will therefore consist in finding arguments to reduce the complexity of the problem. On the one hand, it will be crucial to examine the scales at which both nonlinearities and relativistic corrections must be taken into account. The last study presented in this manuscript is a first step to address this. In practice, since non-linearities emerge at late times whereas the highest velocities concern early times, many simplifications can be expected. On the other hand, determining the number of flows necessary for the description to be accurate (in the sense of precision cosmology), will be decisive. With Julien Lesgourgues, I started to implement the equations of motion of the multi-fluid approach in his code `CLASS`. The results we will obtain should be helpful to test efficiently the numerical requirements and to envisage well-controlled

simplifications.

Acknowledgments

Note: below, the same in French.

Working under the supervision of Francis has been a pleasure. First, I thank him for having trusted me three years ago. Beginning in research alongside him has been very insightful. In the future, I will try to take inspiration from his way of dealing with scientific issues, i.e. using intuition and not being scared by conceptual or technical difficulties. I also want to thank him for his patience towards my questions (which are frequent, especially because I often don't manage to follow him!).

Before starting my PhD, I had the privilege of having two other remarkable advisors. Alain Lecavelier des Étangs and Jean-Philippe Uzan have greatly contributed to my interest in research. Even today, they always make sure that everything goes well for me. Besides, they are available whenever I need them. I thank them warmly for that. By the way, I thank Frédéric Daigne for having suggested to Alain, and then to Jean-Philippe, to offer me an internship and for his kindness.

I am particularly grateful to Christian Frère, who has so much spoken about astrophysics when I was his student that this topic ended up really intriguing me.

I thank also the members of the astronomy group of the *Palais de la découverte*. Thanks to them, I had the opportunity to practice scientific dissemination in an amazing environment. I enjoyed preparing the talk "*An overview of modern cosmology*", presenting it and answer questions of curious people who came to listen to me.

I have the good fortune to add to the list of thanks the L'Oreal fundation. In 2014, I have indeed been awarded the *L'Oréal-UNESCO For Women in Science* prize. In addition to financial support, this made me i) meet highschool students in order to promote science amongst them, ii) have my academic carrer highlighted in the media, iii) meet Claudie Haigneré, the first French woman in space, iv) have

breakfast at the Ministry in the company of brilliant scientific... and even be elected *Picard of the year*!

I thank the people I worked with during my saty at CERN for their warm welcome, for their interest in my work and for giving me plenty of scientific avenues to be explored.

I thank the PhD students with whom I became friend (especially Lucile and Julien, of course), who made those three years even more enjoyable.

I am grateful to my very-stimulating family members. I thank especially my two brothers (who think it's fun to see their sister becoming a cosmologist), Christine and Éric (who accept to have a daughter-in-law who sometimes makes calculations while chatting with them) and my parents (who have encouraged me since the beginning, I am delighted to make them proud of me).

Out of category, Jordane. Marrying a PhD student is brave! Leaving work to follow her when she gets a postdoctoral position too. Thank you for that and for everything else.

Finally, I thank the members of the jury for having added the examination of my PhD thesis to their busy schedule.

Remerciements

Travailler sous la direction de Francis a été un plaisir. Premièrement, je le remercie de m'avoir fait confiance il y a trois ans. Débuter dans la recherche à ses côtés a été très instructif pour moi. J'essaierai par la suite de m'inspirer de sa façon d'aborder les problèmes scientifiques, à savoir faire preuve d'intuition et ne pas être effrayé par les difficultés conceptuelles ou techniques. Je tiens aussi à lui dire merci pour sa patience face à mes questions, fréquentes (notamment parce que j'ai souvent du mal à le suivre !).

Avant de débuter ma thèse, j'ai eu le privilège d'avoir deux autres remarquables encadrants. Alain Lecavelier des Étangs et Jean-Philippe Uzan ont très largement contribué à mon attraît pour la recherche. Encore aujourd'hui, ils veillent à ce que tout se passe bien pour moi et se montrent très disponibles à chaque fois que j'ai besoin d'eux. Je les en remercie chaleureusement. Merci au passage à Frédéric Daigne pour avoir suggéré à Alain puis à Jean-Philippe de me proposer un stage et aussi pour sa bienveillance.

Je suis particulièrement reconnaissante envers Christian Frère, qui m'a tellement parlé d'astrophysique lorsque j'étais son élève que cette discipline a véritablement fini par m'intriguer.

Un merci aussi pour les membres de la section d'astronomie du *Palais de la découverte*. Grâce à eux, j'ai pu m'essayer à la vulgarisation scientifique dans un cadre exceptionnel. J'ai pris énormément de plaisir à préparer l'exposé *Un aperçu de la cosmologie moderne*, à le présenter et à répondre aux questions de tous les curieux qui sont venus m'écouter.

J'ai la chance de pouvoir ajouter à la liste des remerciés la fondation L'Oréal. J'ai en effet reçu en 2014 la bourse *L'Oréal-UNESCO pour les femmes et la science*. En plus de l'aide financière, cette récompense m'a permis d'aller à la rencontre des collégiens et lycéens pour promouvoir la science auprès d'eux ; de voir mon parcours

mis en avant dans les médias ; de rencontrer Claudie Haigneré, première femme française à être allée dans l'espace ; de participer à un petit-déjeuner au ministère en compagnie de brillantes scientifiques... et même d'être élue *Picard de l'année* !

Merci aux personnes avec lesquelles j'ai eu l'occasion de travailler lors de ma visite au CERN pour leur accueil chaleureux, pour l'intérêt qu'ils portent à mon travail et pour m'avoir donné un tas de pistes de recherche à explorer.

Je remercie les doctorants avec lesquels je suis devenue amie (en particulier Lucile et Julien évidemment), qui ont rendu ces trois années encore plus agréables.

Bien sûr je suis très reconnaissante envers les très stimulants membres de ma famille. Merci notamment à mes deux frères (qui rigolent bien de voir leur sœur devenir cosmologiste), à Christine et Éric (qui acceptent d'avoir une belle-fille qui fait parfois des calculs en même temps qu'elle discute avec eux) ainsi qu'à mes parents (qui m'encouragent depuis le début et que je suis extrêmement heureuse de rendre fiers).

Hors catégorie, Jordane. Se marier avec une doctorante, c'est courageux ! Quitter son travail pour la suivre lorsqu'elle part en post-doctorat aussi. Merci pour cela et pour tout le reste.

Enfin, merci aux membres du jury pour avoir ajouté l'examen de ma thèse à leur emploi du temps déjà bien chargé.

Bibliography

[1] Henry D.I. Abarbanel and Claude Itzykson. Relativistic eikonal expansion. *Phys.Rev.Lett.*, 23:53, 1969.

[2] R. Amanullah, C. Lidman, D. Rubin, G. Aldering, P. Astier, K. Barbary, M. S. Burns, A. Conley, K. S. Dawson, S. E. Deustua, M. Doi, S. Fabbro, L. Faccioli, H. K. Fakhouri, G. Folatelli, A. S. Fruchter, H. Furusawa, G. Garavini, G. Goldhaber, A. Goobar, D. E. Groom, I. Hook, D. A. Howell, N. Kashikawa, A. G. Kim, R. A. Knop, M. Kowalski, E. Linder, J. Meyers, T. Morokuma, S. Nobili, J. Nordin, P. E. Nugent, L. Östman, R. Pain, N. Panagia, S. Perlmutter, J. Raux, P. Ruiz-Lapuente, A. L. Spadafora, M. Strovink, N. Suzuki, L. Wang, W. M. Wood-Vasey, N. Yasuda, and T. Supernova Cosmology Project. Spectra and Hubble Space Telescope Light Curves of Six Type Ia Supernovae at $0.511 < z < 1.12$ and the Union2 Compilation. *ApJ*, 716:712–738, June 2010.

[3] S. Anselmi, D. López Nacir, and E. Sefusatti. Nonlinear effects of dark energy clustering beyond the acoustic scales. *JCAP*, 7:13, July 2014.

[4] M. Archidiacono, E. Calabrese, and A. Melchiorri. Case for dark radiation. *Phys. Rev. D*, 84(12):123008, December 2011.

[5] É. Aubourg, S. Bailey, J. E. Bautista, F. Beutler, V. Bhardwaj, D. Bizyaev, M. Blanton, M. Blomqvist, A. S. Bolton, J. Bovy, H. Brewington, J. Brinkmann, J. R. Brownstein, A. Burden, N. G. Busca, W. Carithers, C.-H. Chuang, J. Comparat, A. J. Cuesta, K. S. Dawson, T. Delubac, D. J. Eisenstein, A. Font-Ribera, J. Ge, J.-M. Le Goff, S. G. A Gontcho, J. R. Gott, III, J. E. Gunn, H. Guo, J. Guy, J.-C. Hamilton, S. Ho, K. Honscheid, C. Howlett, D. Kirkby, F. S. Kitaura, J.-P. Kneib, K.-G. Lee, D. Long, R. H.

Lupton, M. Vargas Magaña, V. Malanushenko, E. Malanushenko, M. Manera, C. Maraston, D. Margala, C. K. McBride, J. Miralda-Escudé, A. D. Myers, R. C. Nichol, P. Noterdaeme, S. E. Nuza, M. D. Olmstead, D. Oravetz, I. Pâris, N. Padmanabhan, N. Palanque-Delabrouille, K. Pan, M. Pellejero-Ibanez, W. J. Percival, P. Petitjean, M. M. Pieri, F. Prada, B. Reid, N. A. Roe, A. J. Ross, N. P. Ross, G. Rossi, J. A. Rubiño-Martín, A. G. Sánchez, L. Samushia, R. Tanausú Génova Santos, C. G. Scóccola, D. J. Schlegel, D. P. Schneider, H.-J. Seo, E. Sheldon, A. Simmons, R. A. Skibba, A. Slosar, M. A. Strauss, D. Thomas, J. L. Tinker, R. Tojeiro, J. A. Vazquez, M. Viel, D. A. Wake, B. A. Weaver, D. H. Weinberg, W. M. Wood-Vasey, C. Yèche, I. Zehavi, and G.-B. Zhao. Cosmological implications of baryon acoustic oscillation (BAO) measurements. *ArXiv e-prints*, November 2014.

[6] J. M. Bardeen. *Gauge-Invariant Cosmological Perturbations*, page 563. 1988.

[7] J. M. Bardeen, P. J. Steinhardt, and M. S. Turner. Spontaneous creation of almost scale-free density perturbations in an inflationary universe. *Phys. Rev. D*, 28:679–693, August 1983.

[8] V. Barger, D. Marfatia, and K. Whisnant. Progress in the Physics of Massive Neutrinos. *International Journal of Modern Physics E*, 12:569–647, 2003.

[9] S. Bashinsky and U. Seljak. Signatures of relativistic neutrinos in CMB anisotropy and matter clustering. *Phys. Rev. D*, 69(8):083002, April 2004.

[10] C. L. Bennett, D. Larson, J. L. Weiland, N. Jarosik, G. Hinshaw, N. Odegard, K. M. Smith, R. S. Hill, B. Gold, M. Halpern, E. Komatsu, M. R. Nolta, L. Page, D. N. Spergel, E. Wollack, J. Dunkley, A. Kogut, M. Limon, S. S. Meyer, G. S. Tucker, and E. L. Wright. Nine-year Wilkinson Microwave Anisotropy Probe (WMAP) Observations: Final Maps and Results. *ApJS*, 208:20, October 2013.

[11] A. Benoît, P. Ade, A. Amblard, R. Ansari, É. Aubourg, S. Bargot, J. G. Bartlett, J.-P. Bernard, R. S. Bhatia, A. Blanchard, J. J. Bock, A. Boscaleri, F. R. Bouchet, A. Bourrachot, P. Camus, F. Couchot, P. de Bernardis, J. Delabrouille, F.-X. Désert, O. Doré, M. Douspis, L. Dumoulin, X. Dupac, P. Filliatre, P. Fosalba, K. Ganga, F. Gannaway, B. Gautier, M. Giard, Y. Giraud-Héraud, R. Gispert, L. Guglielmi, J.-C. Hamilton, S. Hanany, S. Henrot-

Versillé, J. Kaplan, G. Lagache, J.-M. Lamarre, A. E. Lange, J. F. Macías-Pérez, K. Madet, B. Maffei, C. Magneville, D. P. Marrone, S. Masi, F. Mayet, A. Murphy, F. Naraghi, F. Nati, G. Patanchon, G. Perrin, M. Piat, N. Ponthieu, S. Prunet, J.-L. Puget, C. Renault, C. Rosset, D. Santos, A. Starobinsky, I. Strukov, R. V. Sudiwala, R. Teyssier, M. Tristram, C. Tucker, J.-C. Vanel, D. Vibert, E. Wakui, and D. Yvon. The cosmic microwave background anisotropy power spectrum measured by Archeops. *A&A*, 399:L19–L23, March 2003.

[12] F. Bernardeau. The evolution of the large-scale structure of the universe: beyond the linear regime. *ArXiv e-prints*, November 2013.

[13] F. Bernardeau, S. Colombi, E. Gaztañaga, and R. Scoccimarro. Large-scale structure of the Universe and cosmological perturbation theory. *Phys. Rep.*, 367:1–248, September 2002.

[14] F. Bernardeau, M. Crocce, and R. Scoccimarro. Constructing regularized cosmic propagators. *Phys. Rev. D*, 85(12):123519, June 2012.

[15] F. Bernardeau, A. Taruya, and T. Nishimichi. Cosmic propagators at two-loop order. *Phys. Rev. D*, 89(2):023502, January 2014.

[16] F. Bernardeau, N. van de Rijt, and F. Vernizzi. Resummed propagators in multicomponent cosmic fluids with the eikonal approximation. *Phys. Rev. D*, 85(6):063509, March 2012.

[17] F. Bernardeau, N. Van de Rijt, and F. Vernizzi. Power spectra in the eikonal approximation with adiabatic and nonadiabatic modes. *Phys. Rev. D*, 87(4):043530, February 2013.

[18] J. Bernstein. *Kinetic theory in the expanding universe*. 1988.

[19] B. Bertotti. The Luminosity of Distant Galaxies. *Royal Society of London Proceedings Series A*, 294:195–207, September 1966.

[20] M. Betoule, R. Kessler, J. Guy, J. Mosher, D. Hardin, R. Biswas, P. Astier, P. El-Hage, M. Konig, S. Kuhlmann, J. Marriner, R. Pain, N. Regnault, C. Balland, B. A. Bassett, P. J. Brown, H. Campbell, R. G. Carlberg, F. Cellier-Holzem, D. Cinabro, A. Conley, C. B. D'Andrea, D. L. DePoy,

M. Doi, R. S. Ellis, S. Fabbro, A. V. Filippenko, R. J. Foley, J. A. Frieman, D. Fouchez, L. Galbany, A. Goobar, R. R. Gupta, G. J. Hill, R. Hlozek, C. J. Hogan, I. M. Hook, D. A. Howell, S. W. Jha, L. Le Guillou, G. Leloudas, C. Lidman, J. L. Marshall, A. Möller, A. M. Mourão, J. Neveu, R. Nichol, M. D. Olmstead, N. Palanque-Delabrouille, S. Perlmutter, J. L. Prieto, C. J. Pritchet, M. Richmond, A. G. Riess, V. Ruhlmann-Kleider, M. Sako, K. Schahmaneche, D. P. Schneider, M. Smith, J. Sollerman, M. Sullivan, N. A. Walton, and C. J. Wheeler. Improved cosmological constraints from a joint analysis of the SDSS-II and SNLS supernova samples. *A&A*, 568:A22, August 2014.

[21] S. M. Bilenky, C. Giunti, J. A. Grifols, and E. Massó. Absolute values of neutrino masses: status and prospects. *Phys. Rep.*, 379:69–148, May 2003.

[22] J. Binney and S. Tremaine. *Galactic Dynamics: Second Edition*. Princeton University Press, 2008.

[23] S. Bird, M. Viel, and M. G. Haehnelt. Massive neutrinos and the non-linear matter power spectrum. *MNRAS*, 420:2551–2561, March 2012.

[24] T. Biswas and A. Notari. 'Swiss-cheese' inhomogeneous cosmology and the dark energy problem. *JCAP*, 6:21, June 2008.

[25] D. Blas, M. Garny, and T. Konstandin. On the non-linear scale of cosmological perturbation theory. *JCAP*, 9:24, September 2013.

[26] D. Blas, M. Garny, and T. Konstandin. Cosmological perturbation theory at three-loop order. *JCAP*, 1:10, January 2014.

[27] D. Blas, M. Garny, T. Konstandin, and J. Lesgourgues. Structure formation with massive neutrinos: going beyond linear theory. *ArXiv e-prints*, August 2014.

[28] D. Blas, J. Lesgourgues, and T. Tram. The Cosmic Linear Anisotropy Solving System (CLASS). Part II: Approximation schemes. *JCAP*, 7:34, July 2011.

[29] J. Brandbyge, S. Hannestad, T. Haugbølle, and B. Thomsen. The effect of thermal neutrino motion on the non-linear cosmological matter power spectrum. *JCAP*, 8:20, August 2008.

[30] R. Brandenberger, R. Kahn, and W. H. Press. Cosmological perturbations in the early universe. *Phys. Rev. D*, 28:1809–1821, October 1983.

[31] N. Brouzakis, N. Tetradis, and E. Tzavara. The effect of large scale inhomogeneities on the luminosity distance. *JCAP*, 2:13, February 2007.

[32] N. Brouzakis, N. Tetradis, and E. Tzavara. Light propagation and large-scale inhomogeneities. *JCAP*, 4:8, April 2008.

[33] C. Clarkson, G. F. R. Ellis, A. Faltenbacher, R. Maartens, O. Umeh, and J.-P. Uzan. (Mis)interpreting supernovae observations in a lumpy universe. *MNRAS*, 426:1121–1136, October 2012.

[34] B. T. Cleveland, T. Daily, R. Davis, Jr., J. R. Distel, K. Lande, C. K. Lee, P. S. Wildenhain, and J. Ullman. Measurement of the Solar Electron Neutrino Flux with the Homestake Chlorine Detector. *ApJ*, 496:505–526, March 1998.

[35] T. Clifton and J. Zuntz. Hubble diagram dispersion from large-scale structure. *MNRAS*, 400:2185–2199, December 2009.

[36] A. Coc, J.-P. Uzan, and E. Vangioni. Standard big bang nucleosynthesis and primordial CNO abundances after Planck. *JCAP*, 10:50, October 2014.

[37] S. Colombi. Vlasov-Poisson in 1D for initially cold systems: post-collapse Lagrangian perturbation theory. *MNRAS*, 446:2902–2920, January 2015.

[38] A. Conley, J. Guy, M. Sullivan, N. Regnault, P. Astier, C. Balland, S. Basa, R. G. Carlberg, D. Fouchez, D. Hardin, I. M. Hook, D. A. Howell, R. Pain, N. Palanque-Delabrouille, K. M. Perrett, C. J. Pritchet, J. Rich, V. Ruhlmann-Kleider, D. Balam, S. Baumont, R. S. Ellis, S. Fabbro, H. K. Fakhouri, N. Fourmanoit, S. González-Gaitán, M. L. Graham, M. J. Hudson, E. Hsiao, T. Kronborg, C. Lidman, A. M. Mourao, J. D. Neill, S. Perlmutter, P. Ripoche, N. Suzuki, and E. S. Walker. Supernova Constraints and Systematic Uncertainties from the First Three Years of the Supernova Legacy Survey. *ApJS*, 192:1, January 2011.

[39] A. Cooray, D. E. Holz, and D. Huterer. Cosmology from Supernova Magnification Maps. *ApJL*, 637:L77–L80, February 2006.

[40] L. Cosmai, G. Fanizza, M. Gasperini, and L. Tedesco. Discriminating different models of luminosity-redshift distribution. *Classical and Quantum Gravity*, 30(9):095011, May 2013.

[41] C. L. Cowan, Jr., F. Reines, F. B. Harrison, H. W. Kruse, and A. D. McGuire. Detection of the Free Neutrino: A Confirmation. *Science*, 124:103–104, July 1956.

[42] P. Creminelli, J. Gleyzes, L. Hui, M. Simonović, and F. Vernizzi. Single-field consistency relations of large scale structure part III: test of the equivalence principle. *JCAP*, 6:9, June 2014.

[43] P. Creminelli, J. Gleyzes, M. Simonović, and F. Vernizzi. Single-field consistency relations of large scale structure part II: resummation and redshift space. *JCAP*, 2:51, February 2014.

[44] P. Creminelli, J. Noreña, M. Simonović, and F. Vernizzi. Single-field consistency relations of large scale structure. *JCAP*, 12:25, December 2013.

[45] M. Crocce and R. Scoccimarro. Renormalized cosmological perturbation theory. *Phys. Rev. D*, 73(6):063519, March 2006.

[46] M. Crocce, R. Scoccimarro, and F. Bernardeau. MPTBREEZE: a fast renormalized perturbative scheme. *MNRAS*, 427:2537–2551, December 2012.

[47] R. H. Cyburt, B. D. Fields, and K. A. Olive. Primordial nucleosynthesis with CMB inputs: probing the early universe and light element astrophysics. *Astroparticle Physics*, 17:87–100, April 2002.

[48] N. Dalal, D. E. Holz, X. Chen, and J. A. Frieman. Corrective Lenses for High-Redshift Supernovae. *ApJL*, 585:L11–L14, March 2003.

[49] G. D'Amico and E. Sefusatti. The nonlinear power spectrum in clustering quintessence cosmologies. *JCAP*, 11:13, November 2011.

[50] V. M. Dashevskii and V. I. Slysh. On the Propagation of Light in a Nonhomogeneous Universe. Soviet Astr., 9:671, February 1966.

[51] F. De Bernardis, L. Pagano, P. Serra, A. Melchiorri, and A. Cooray. Anisotropies in the cosmic neutrino background after Wilkinson Microwave Anisotropy Probe five-year data. *JCAP*, 6:13, June 2008.

[52] P. de Bernardis, P. A. R. Ade, J. J. Bock, J. R. Bond, J. Borrill, A. Boscaleri, K. Coble, B. P. Crill, G. De Gasperis, P. C. Farese, P. G. Ferreira, K. Ganga, M. Giacometti, E. Hivon, V. V. Hristov, A. Iacoangeli, A. H. Jaffe, A. E. Lange, L. Martinis, S. Masi, P. V. Mason, P. D. Mauskopf, A. Melchiorri, L. Miglio, T. Montroy, C. B. Netterfield, E. Pascale, F. Piacentini, D. Pogosyan, S. Prunet, S. Rao, G. Romeo, J. E. Ruhl, F. Scaramuzzi, D. Sforna, and N. Vittorio. A flat Universe from high-resolution maps of the cosmic microwave background radiation. *Nature*, 404:955–959, April 2000.

[53] W. de Sitter. Einstein's theory of gravitation and its astronomical consequences. Third paper. *MNRAS*, 78:3–28, November 1917.

[54] S. Dodelson and A. Vallinotto. Learning from the scatter in type Ia supernovae. *Phys. Rev. D*, 74(6):063515, September 2006.

[55] M. Doran. CMBEASY: an object oriented code for the cosmic microwave background. *JCAP*, 10:11, October 2005.

[56] Y. Dubois, C. Pichon, C. Welker, D. Le Borgne, J. Devriendt, C. Laigle, S. Codis, D. Pogosyan, S. Arnouts, K. Benabed, E. Bertin, J. Blaizot, F. Bouchet, J.-F. Cardoso, S. Colombi, V. de Lapparent, V. Desjacques, R. Gavazzi, S. Kassin, T. Kimm, H. McCracken, B. Milliard, S. Peirani, S. Prunet, S. Rouberol, J. Silk, A. Slyz, T. Sousbie, R. Teyssier, L. Tresse, M. Treyer, D. Vibert, and M. Volonteri. Dancing in the dark: galactic properties trace spin swings along the cosmic web. *MNRAS*, 444:1453–1468, October 2014.

[57] H. Dupuy and F. Bernardeau. Describing massive neutrinos in cosmology as a collection of independent flows. *JCAP*, 1:30, January 2014.

[58] H. Dupuy and F. Bernardeau. Cosmological Perturbation Theory for streams of relativistic particles. *JCAP*, 3:30, March 2015.

[59] H. Dupuy and F. Bernardeau. On the importance of nonlinear couplings in large-scale neutrino streams. *ArXiv e-prints*, March 2015.

[60] R. Durrer. *Gauge invariant cosmological perturbation theory. A general study and its application to the texture scenario of structure formation.* 1994.

[61] C. C. Dyer and R. C. Roeder. The Distance-Redshift Relation for Universes with no Intergalactic Medium. *ApJL*, 174:L115, June 1972.

[62] C. C. Dyer and R. C. Roeder. Observations in Locally Inhomogeneous Cosmological Models. *ApJ*, 189:167–176, April 1974.

[63] G. Efstathiou. Cosmological perturbations. In J. A. Peacock, A. F. Heavens, and A. T. Davies, editors, *Physics of the Early Universe*, pages 361–463, 1990.

[64] A. Einstein. Die Grundlage der allgemeinen Relativitätstheorie. *Annalen der Physik*, 354:769–822, 1916.

[65] A. Einstein and E. G. Straus. The Influence of the Expansion of Space on the Gravitation Fields Surrounding the Individual Stars. *Reviews of Modern Physics*, 17:120–124, April 1945.

[66] S. R. Elliott and P. Vogel. Double beta decay. *Annual Review of Nuclear and Particle Science*, 52:115–151, 2002.

[67] G. F. R. Ellis. *Cosmology and Verifiability*, page 113. 1990.

[68] G. F. R. Ellis and T. Buchert. The universe seen at different scales [rapid communication]. *Physics Letters A*, 347:38–46, November 2005.

[69] G. F. R. Ellis and R. Goswami. Variations on Birkhoff's theorem. *General Relativity and Gravitation*, 45:2123–2142, November 2013.

[70] A. Enea Romano. Conditions for low-redshift positive apparent acceleration in smooth inhomogeneous models. *ArXiv e-prints*, June 2012.

[71] AbazajianK. N. *et al.*. Light Sterile Neutrinos: A White Paper. *ArXiv e-prints*, April 2012.

[72] G. Fanizza and F. Nugier. Lensing in the geodesic light-cone coordinates and its (exact) illustration to an off-center observer in Lema#523tre-Tolman-Bondi models. *JCAP*, 2:2, February 2015.

[73] G. Fanizza and L. Tedesco. Inhomogeneous and anisotropic Universe and apparent acceleration. *Phys. Rev. D*, 91(2):023006, January 2015.

[74] É. É. Flanagan, N. Kumar, I. Wasserman, and R. A. Vanderveld. Luminosity distance in "Swiss cheese" cosmology with randomized voids. II. Magnification probability distributions. *Phys. Rev. D*, 85(2):023510, January 2012.

[75] P. Fleury. Swiss-cheese models and the Dyer-Roeder approximation. *JCAP*, 6:54, June 2014.

[76] P. Fleury, H. Dupuy, and J.-P. Uzan. Can All Cosmological Observations Be Accurately Interpreted with a Unique Geometry? *Physical Review Letters*, 111(9):091302, August 2013.

[77] P. Fleury, H. Dupuy, and J.-P. Uzan. Interpretation of the Hubble diagram in a nonhomogeneous universe. *Phys. Rev. D*, 87(12):123526, June 2013.

[78] P. Fleury, C. Pitrou, and J.-P. Uzan. Light propagation in a homogeneous and anisotropic universe. *Phys. Rev. D*, 91(4):043511, February 2015.

[79] A. Friedmann. Über die Krümmung des Raumes. *Zeitschrift fur Physik*, 10:377–386, 1922.

[80] J. A. Frieman. Weak Lensing and the Measurement of q_0; from Type Ia Supernovae. *Comments on Astrophysics*, 18:323, 1996.

[81] F. Führer and Y. Y. Y. Wong. Higher-order massive neutrino perturbations in large-scale structure. *JCAP*, 3:46, March 2015.

[82] M. H. Goroff, B. Grinstein, S.-J. Rey, and M. B. Wise. Coupling of modes of cosmological mass density fluctuations. *ApJ*, 311:6–14, December 1986.

[83] J. E. Gunn. A Fundamental Limitation on the Accuracy of Angular Measurements in Observational Cosmology. *ApJ*, 147:61, January 1967.

[84] A. H. Guth. Inflationary universe: A possible solution to the horizon and flatness problems. *Phys. Rev. D*, 23:347–356, January 1981.

[85] A. H. Guth and S.-Y. Pi. Fluctuations in the new inflationary universe. *Physical Review Letters*, 49:1110–1113, October 1982.

[86] J. Guy, M. Sullivan, A. Conley, N. Regnault, P. Astier, C. Balland, S. Basa, R. G. Carlberg, D. Fouchez, D. Hardin, I. M. Hook, D. A. Howell, R. Pain, N. Palanque-Delabrouille, K. M. Perrett, C. J. Pritchet, J. Rich,

V. Ruhlmann-Kleider, D. Balam, S. Baumont, R. S. Ellis, S. Fabbro, H. K. Fakhouri, N. Fourmanoit, S. González-Gaitán, M. L. Graham, E. Hsiao, T. Kronborg, C. Lidman, A. M. Mourao, S. Perlmutter, P. Ripoche, N. Suzuki, and E. S. Walker. The Supernova Legacy Survey 3-year sample: Type Ia supernovae photometric distances and cosmological constraints. *A&A*, 523:A7, November 2010.

[87] O. Hahn, R. E. Angulo, and T. Abel. The Properties of Cosmic Velocity Fields. *ArXiv e-prints*, April 2014.

[88] S. Hannestad, T. Haugbølle, and C. Schultz. Neutrinos in non-linear structure formation: a simple SPH approach. *JCAP*, 2:45, February 2012.

[89] S. W. Hawking. The development of irregularities in a single bubble inflationary universe. *Physics Letters B*, 115:295–297, September 1982.

[90] G. Hinshaw, D. Larson, E. Komatsu, D. N. Spergel, C. L. Bennett, J. Dunkley, M. R. Nolta, M. Halpern, R. S. Hill, N. Odegard, L. Page, K. M. Smith, J. L. Weiland, B. Gold, N. Jarosik, A. Kogut, M. Limon, S. S. Meyer, G. S. Tucker, E. Wollack, and E. L. Wright. Nine-year Wilkinson Microwave Anisotropy Probe (WMAP) Observations: Cosmological Parameter Results. *ApJS*, 208:19, October 2013.

[91] C. J. Hogan, N. Kaiser, and M. J. Rees. Interpretation of anisotropy in the cosmic background radiation. *Royal Society of London Philosophical Transactions Series A*, 307:97–109, October 1982.

[92] D. E. Holz and E. V. Linder. Safety in Numbers: Gravitational Lensing Degradation of the Luminosity Distance-Redshift Relation. *ApJ*, 631:678–688, October 2005.

[93] W. Hu and N. Sugiyama. Small-Scale Cosmological Perturbations: an Analytic Approach. *ApJ*, 471:542, November 1996.

[94] E. Hubble. A Relation between Distance and Radial Velocity among Extra-Galactic Nebulae. *Proceedings of the National Academy of Science*, 15:168–173, March 1929.

[95] F. Iocco, G. Mangano, G. Miele, O. Pisanti, and P. D. Serpico. Primordial nucleosynthesis: From precision cosmology to fundamental physics. *Phys. Rep.*, 472:1–76, March 2009.

[96] W. Israel. Singular hypersurfaces and thin shells in general relativity. *Nuovo Cim.*, B44S10:1, 1966.

[97] B. Jain and E. Bertschinger. Self-similar Evolution of Gravitational Clustering: Is N = -1 Special? *ApJ*, 456:43, January 1996.

[98] R. Kantowski. Corrections in the Luminosity-Redshift Relations of the Homogeneous Fried-Mann Models. *ApJ*, 155:89, January 1969.

[99] R. Kantowski, T. Vaughan, and D. Branch. The Effects of Inhomogeneities on Evaluating the Deceleration Parameter Q 0. *ApJ*, 447:35, July 1995.

[100] A. Kehagias and A. Riotto. Symmetries and consistency relations in the large scale structure of the universe. *Nuclear Physics B*, 873:514–529, August 2013.

[101] H. Kodama and M. Sasaki. Cosmological Perturbation Theory. *Progress of Theoretical Physics Supplement*, 78:1, 1984.

[102] F. Kottler. *Ann. Phys.* (Berlin), **56**, 401, 1918.

[103] G. Lemaître. Un Univers homogène de masse constante et de rayon croissant rendant compte de la vitesse radiale des nébuleuses extra-galactiques. *Annales de la Société Scientifique de Bruxelles*, 47:49–59, 1927.

[104] J. Lesgourgues, G. Mangano, G. Miele, and S. Pastor. *Neutrino Cosmology.* February 2013.

[105] J. Lesgourgues, S. Matarrese, M. Pietroni, and A. Riotto. Non-linear power spectrum including massive neutrinos: the time-RG flow approach. *JCAP*, 6:17, June 2009.

[106] J. Lesgourgues and T. Tram. The Cosmic Linear Anisotropy Solving System (CLASS) IV: efficient implementation of non-cold relics. *JCAP*, 9:32, September 2011.

[107] A. Lewis, A. Challinor, and A. Lasenby. Efficient Computation of Cosmic Microwave Background Anisotropies in Closed Friedmann-Robertson-Walker Models. *ApJ*, 538:473–476, August 2000.

[108] E. Lifshitz. On the Gravitational stability of the expanding universe. *J.Phys.(USSR)*, 10:116, 1946.

[109] E. M. Lifshitz and I. M. Khalatnikov. Investigations in relativistic cosmology. *Advances in Physics*, 12:185–249, April 1963.

[110] A. D. Linde. New scenario of the inflationary universe: possible solution of the problem of horizon, flatness, inhomogeneity, isotropy and relic monopoles. In M. A. Markov, editor, *Quantum Gravitation. Quantum Theory of Gravitation*, pages 106–112, 1982.

[111] C.-P. Ma and E. Bertschinger. Cosmological Perturbation Theory in the Synchronous and Conformal Newtonian Gauges. *ApJ*, 455:7, December 1995.

[112] N. Makino, M. Sasaki, and Y. Suto. Analytic approach to the perturbative expansion of nonlinear gravitational fluctuations in cosmological density and velocity fields. *Phys. Rev. D*, 46:585–602, July 1992.

[113] K. A. Malik and D. Wands. Cosmological perturbations. *Phys. Rep.*, 475:1–51, May 2009.

[114] G. Mangano, G. Miele, S. Pastor, T. Pinto, O. Pisanti, and P. D. Serpico. Relic neutrino decoupling including flavour oscillations. *Nuclear Physics B*, 729:221–234, November 2005.

[115] A. Mantz, S. W. Allen, and D. Rapetti. The observed growth of massive galaxy clusters - IV. Robust constraints on neutrino properties. *MNRAS*, 406:1805–1814, August 2010.

[116] V. Marra, E. W. Kolb, S. Matarrese, and A. Riotto. Cosmological observables in a Swiss-cheese universe. *Phys. Rev. D*, 76(12):123004, December 2007.

[117] S. Matarrese and M. Pietroni. Resumming cosmic perturbations. *JCAP*, 6:26, June 2007.

[118] R. D. McKeown and P. Vogel. Neutrino masses and oscillations: triumphs and challenges. *Phys. Rep.*, 394:315–356, May 2004.

[119] A. Melchiorri, G. L. Fogli, E. Lisi, A. Marrone, A. Palazzo, P. Serra, and J. Silk. Constraints on the Neutrino Mass from Cosmology and their impact

on world neutrino data. *Nuclear Physics B Proceedings Supplements*, 145:290–294, August 2005.

[120] C. W. Misner, K. S. Thorne, and J. A. Wheeler. *Gravitation*. 1973.

[121] M. P. Mood, J. T. Firouzjaee, and R. Mansouri. Gravitational lensing by a structure in a cosmological background. *Phys. Rev. D*, 88(8):083011, October 2013.

[122] V. F. Mukhanov and G. V. Chibisov. Quantum fluctuations and a nonsingular universe. *Soviet Journal of Experimental and Theoretical Physics Letters*, 33:532, May 1981.

[123] V. F. Mukhanov, H. A. Feldman, and R. H. Brandenberger. Theory of cosmological perturbations. *Phys. Rep.*, 215:203–333, June 1992.

[124] K. A. Olive, G. Steigman, and T. P. Walker. Primordial nucleosynthesis: theory and observations. *Phys. Rep.*, 333:389–407, August 2000.

[125] N. Palanque-Delabrouille, C. Yèche, J. Lesgourgues, G. Rossi, A. Borde, M. Viel, E. Aubourg, D. Kirkby, J.-M. LeGoff, J. Rich, N. Roe, N. P. Ross, D. P. Schneider, and D. Weinberg. Constraint on neutrino masses from SDSS-III/BOSS Lyα forest and other cosmological probes. *ArXiv e-prints*, October 2014.

[126] P. J. E. Peebles. *The large-scale structure of the universe*. 1980.

[127] M. Peloso and M. Pietroni. Galilean invariance and the consistency relation for the nonlinear squeezed bispectrum of large scale structure. *JCAP*, 5:31, May 2013.

[128] A. A. Penzias and R. W. Wilson. A Measurement of Excess Antenna Temperature at 4080 Mc/s. *ApJ*, 142:419–421, July 1965.

[129] S. Perlmutter, G. Aldering, G. Goldhaber, R. A. Knop, P. Nugent, P. G. Castro, S. Deustua, S. Fabbro, A. Goobar, D. E. Groom, I. M. Hook, A. G. Kim, M. Y. Kim, J. C. Lee, N. J. Nunes, R. Pain, C. R. Pennypacker, R. Quimby, C. Lidman, R. S. Ellis, M. Irwin, R. G. McMahon, P. Ruiz-Lapuente, N. Walton, B. Schaefer, B. J. Boyle, A. V. Filippenko, T. Matheson, A. S. Fruchter,

N. Panagia, H. J. M. Newberg, W. J. Couch, and T. S. C. Project. Measurements of Ω and Λ from 42 High-Redshift Supernovae. *ApJ*, 517:565–586, June 1999.

[130] S. T. Petcov. The Nature of Massive Neutrinos. *ArXiv e-prints*, March 2013.

[131] Patrick Peter and Jean-Philippe Uzan. *Primordial cosmology*. Oxford Graduate Texts. Oxford Univ. Press, Oxford, 2009.

[132] C. Pichon and F. Bernardeau. Vorticity generation in large-scale structure caustics. *A&A*, 343:663–681, March 1999.

[133] M. Pietroni. Flowing with time: a new approach to non-linear cosmological perturbations. *JCAP*, 10:36, October 2008.

[134] Planck Collaboration, R. Adam, P. A. R. Ade, N. Aghanim, Y. Akrami, M. I. R. Alves, M. Arnaud, F. Arroja, J. Aumont, C. Baccigalupi, and et al. Planck 2015 results. I. Overview of products and scientific results. *ArXiv e-prints*, February 2015.

[135] Planck Collaboration, P. A. R. Ade, N. Aghanim, C. Armitage-Caplan, M. Arnaud, M. Ashdown, F. Atrio-Barandela, J. Aumont, C. Baccigalupi, A. J. Banday, and et al. Planck 2013 results. XVI. Cosmological parameters. *A&A*, 571:A16, November 2014.

[136] Planck Collaboration, P. A. R. Ade, N. Aghanim, M. Arnaud, F. Arroja, M. Ashdown, J. Aumont, C. Baccigalupi, M. Ballardini, A. J. Banday, and et al. Planck 2015 results. XVII. Constraints on primordial non-Gaussianity. *ArXiv e-prints*, February 2015.

[137] Planck Collaboration, P. A. R. Ade, N. Aghanim, M. Arnaud, M. Ashdown, J. Aumont, C. Baccigalupi, A. J. Banday, R. B. Barreiro, J. G. Bartlett, and et al. Planck 2015 results. XIII. Cosmological parameters. *ArXiv e-prints*, February 2015.

[138] B. Pontecorvo. Inverse beta processes and nonconservation of lepton charge. *Sov.Phys.JETP*, 7:172–173, 1958.

[139] B. Pontecorvo. Neutrino Experiments and the Problem of Conservation of Leptonic Charge. *Sov.Phys.JETP*, 26:984–988, 1968.

[140] M. Pospelov and J. Pradler. Big Bang Nucleosynthesis as a Probe of New Physics. *Annual Review of Nuclear and Particle Science*, 60:539–568, November 2010.

[141] W. H. Press, S. A. Teukolsky, W. T. Vetterling, and B. P. Flannery. *Numerical recipes in FORTRAN. The art of scientific computing.* 1992.

[142] S. Pueblas and R. Scoccimarro. Generation of vorticity and velocity dispersion by orbit crossing. *Phys. Rev. D*, 80(4):043504, August 2009.

[143] M. Redlich, K. Bolejko, S. Meyer, G. F. Lewis, and M. Bartelmann. Probing spatial homogeneity with LTB models: a detailed discussion. *A&A*, 570:A63, October 2014.

[144] S. Refsdal. On the Propagation of Light in Universes with Inhomogeneous Mass Distribution. *ApJ*, 159:357, January 1970.

[145] C. L. Reichardt, L. Shaw, O. Zahn, K. A. Aird, B. A. Benson, L. E. Bleem, J. E. Carlstrom, C. L. Chang, H. M. Cho, T. M. Crawford, A. T. Crites, T. de Haan, M. A. Dobbs, J. Dudley, E. M. George, N. W. Halverson, G. P. Holder, W. L. Holzapfel, S. Hoover, Z. Hou, J. D. Hrubes, M. Joy, R. Keisler, L. Knox, A. T. Lee, E. M. Leitch, M. Lueker, D. Luong-Van, J. J. McMahon, J. Mehl, S. S. Meyer, M. Millea, J. J. Mohr, T. E. Montroy, T. Natoli, S. Padin, T. Plagge, C. Pryke, J. E. Ruhl, K. K. Schaffer, E. Shirokoff, H. G. Spieler, Z. Staniszewski, A. A. Stark, K. Story, A. van Engelen, K. Vanderlinde, J. D. Vieira, and R. Williamson. A Measurement of Secondary Cosmic Microwave Background Anisotropies with Two Years of South Pole Telescope Observations. *ApJ*, 755:70, August 2012.

[146] A. Rest, D. Scolnic, R. J. Foley, M. E. Huber, R. Chornock, G. Narayan, J. L. Tonry, E. Berger, A. M. Soderberg, C. W. Stubbs, A. Riess, R. P. Kirshner, S. J. Smartt, E. Schlafly, S. Rodney, M. T. Botticella, D. Brout, P. Challis, I. Czekala, M. Drout, M. J. Hudson, R. Kotak, C. Leibler, R. Lunnan, G. H. Marion, M. McCrum, D. Milisavljevic, A. Pastorello, N. E. Sanders, K. Smith, E. Stafford, D. Thilker, S. Valenti, W. M. Wood-Vasey, Z. Zheng, W. S. Burgett, K. C. Chambers, L. Denneau, P. W. Draper, H. Flewelling, K. W. Hodapp, N. Kaiser, R.-P. Kudritzki, E. A. Magnier, N. Metcalfe, P. A. Price, W. Sweeney, R. Wainscoat, and C. Waters. Cosmological Constraints from

Measurements of Type Ia Supernovae Discovered during the First 1.5 yr of the Pan-STARRS1 Survey. *ApJ*, 795:44, November 2014.

[147] S. Riemer-Sørensen, D. Parkinson, and T. M. Davis. Combining Planck data with large scale structure information gives a strong neutrino mass constraint. *Phys. Rev. D*, 89(10):103505, May 2014.

[148] A. G. Riess, A. V. Filippenko, P. Challis, A. Clocchiatti, A. Diercks, P. M. Garnavich, R. L. Gilliland, C. J. Hogan, S. Jha, R. P. Kirshner, B. Leibundgut, M. M. Phillips, D. Reiss, B. P. Schmidt, R. A. Schommer, R. C. Smith, J. Spyromilio, C. Stubbs, N. B. Suntzeff, and J. Tonry. Observational Evidence from Supernovae for an Accelerating Universe and a Cosmological Constant. *AJ*, 116:1009–1038, September 1998.

[149] A. E. Romano. Inhomogeneous Cosmological Models and H_0 Observations. *International Journal of Modern Physics D*, 21:50085, December 2012.

[150] A. E. Romano. Can smooth LTB models mimicking the cosmological constant for the luminosity distance also satisfy the age constraint? *General Relativity and Gravitation*, 45:2529–2544, December 2013.

[151] A. E. Romano and P. Chen. Low-redshift formula for the luminosity distance in a LTB model with cosmological constant. *European Physical Journal C*, 74:2780, April 2014.

[152] G. Rossi, N. Palanque-Delabrouille, A. Borde, M. Viel, C. Yèche, J. S. Bolton, J. Rich, and J.-M. Le Goff. Suite of hydrodynamical simulations for the Lyman-α forest with massive neutrinos. *A&A*, 567:A79, July 2014.

[153] S. Saito, M. Takada, and A. Taruya. Impact of Massive Neutrinos on the Nonlinear Matter Power Spectrum. *Physical Review Letters*, 100(19):191301, May 2008.

[154] S. Saito, M. Takada, and A. Taruya. Nonlinear power spectrum in the presence of massive neutrinos: Perturbation theory approach, galaxy bias, and parameter forecasts. *Phys. Rev. D*, 80(8):083528, October 2009.

[155] F. Saracco, M. Pietroni, N. Tetradis, V. Pettorino, and G. Robbers. Nonlinear matter spectra in coupled quintessence. *Phys. Rev. D*, 82(2):023528, July 2010.

[156] S. Sarkar. Big bang nucleosynthesis and physics beyond the standard model. *Reports on Progress in Physics*, 59:1493–1609, December 1996.

[157] R. Scaramella, Y. Mellier, J. Amiaux, C. Burigana, C. S. Carvalho, J. C. Cuillandre, A. da Silva, J. Dinis, A. Derosa, E. Maiorano, P. Franzetti, B. Garilli, M. Maris, M. Meneghetti, I. Tereno, S. Wachter, L. Amendola, M. Cropper, V. Cardone, R. Massey, S. Niemi, H. Hoekstra, T. Kitching, L. Miller, T. Schrabback, E. Semboloni, A. Taylor, M. Viola, T. Maciaszek, A. Ealet, L. Guzzo, K. Jahnke, W. Percival, F. Pasian, M. Sauvage, and the Euclid Collaboration. Euclid space mission: a cosmological challenge for the next 15 years. *ArXiv e-prints*, January 2015.

[158] E. Schucking. The Schwarzschild line element and the expansion of the universe (in german). *Zs. f. Phys.* ***137****, 595*, 1954.

[159] R. Scoccimarro. Transients from initial conditions: a perturbative analysis. *MNRAS*, 299:1097–1118, October 1998.

[160] R. Scoccimarro. A New Angle on Gravitational Clustering. In J. N. Fry, J. R. Buchler, and H. Kandrup, editors, *The Onset of Nonlinearity in Cosmology*, volume 927 of *Annals of the New York Academy of Sciences*, pages 13–23, 2001.

[161] R. Scoccimarro and J. Frieman. Loop Corrections in Nonlinear Cosmological Perturbation Theory. *ApJS*, 105:37, July 1996.

[162] U. Seljak and M. Zaldarriaga. A Line-of-Sight Integration Approach to Cosmic Microwave Background Anisotropies. *ApJ*, 469:437, October 1996.

[163] M. Shoji and E. Komatsu. Third-Order Perturbation Theory with Nonlinear Pressure. *ApJ*, 700:705–719, July 2009.

[164] M. Shoji and E. Komatsu. Erratum: Massive neutrinos in cosmology: Analytic solutions and fluid approximation [Phys. Rev. D 81, 123516 (2010)]. *Phys. Rev. D*, 82(8):089901, October 2010.

[165] J. L. Sievers, R. A. Hlozek, M. R. Nolta, V. Acquaviva, G. E. Addison, P. A. R. Ade, P. Aguirre, M. Amiri, J. W. Appel, L. F. Barrientos, E. S. Battistelli, N. Battaglia, J. R. Bond, B. Brown, B. Burger, E. Calabrese, J. Chervenak,

D. Crichton, S. Das, M. J. Devlin, S. R. Dicker, W. Bertrand Doriese, J. Dunkley, R. Dünner, T. Essinger-Hileman, D. Faber, R. P. Fisher, J. W. Fowler, P. Gallardo, M. S. Gordon, M. B. Gralla, A. Hajian, M. Halpern, M. Hasselfield, C. Hernández-Monteagudo, J. C. Hill, G. C. Hilton, M. Hilton, A. D. Hincks, D. Holtz, K. M. Huffenberger, D. H. Hughes, J. P. Hughes, L. Infante, K. D. Irwin, D. R. Jacobson, B. Johnstone, J. Baptiste Juin, M. Kaul, J. Klein, A. Kosowsky, J. M. Lau, M. Limon, Y.-T. Lin, T. Louis, R. H. Lupton, T. A. Marriage, D. Marsden, K. Martocci, P. Mauskopf, M. McLaren, F. Menanteau, K. Moodley, H. Moseley, C. B. Netterfield, M. D. Niemack, L. A. Page, W. A. Page, L. Parker, B. Partridge, R. Plimpton, H. Quintana, E. D. Reese, B. Reid, F. Rojas, N. Sehgal, B. D. Sherwin, B. L. Schmitt, D. N. Spergel, S. T. Staggs, O. Stryzak, D. S. Swetz, E. R. Switzer, R. Thornton, H. Trac, C. Tucker, M. Uehara, K. Visnjic, R. Warne, G. Wilson, E. Wollack, Y. Zhao, and C. Zunckel. The Atacama Cosmology Telescope: cosmological parameters from three seasons of data. *JCAP*, 10:60, October 2013.

[166] J. Silk. Cosmic Black-Body Radiation and Galaxy Formation. *ApJ*, 151:459, February 1968.

[167] G. F. Smoot, C. L. Bennett, A. Kogut, E. L. Wright, J. Aymon, N. W. Boggess, E. S. Cheng, G. de Amici, S. Gulkis, M. G. Hauser, G. Hinshaw, P. D. Jackson, M. Janssen, E. Kaita, T. Kelsall, P. Keegstra, C. Lineweaver, K. Loewenstein, P. Lubin, J. Mather, S. S. Meyer, S. H. Moseley, T. Murdock, L. Rokke, R. F. Silverberg, L. Tenorio, R. Weiss, and D. T. Wilkinson. Structure in the COBE differential microwave radiometer first-year maps. *ApJL*, 396:L1–L5, September 1992.

[168] G. F. Smoot, M. V. Gorenstein, and R. A. Muller. Detection of anisotropy in the cosmic blackbody radiation. *Physical Review Letters*, 39:898–901, October 1977.

[169] G. Somogyi and R. E. Smith. Cosmological perturbation theory for baryons and dark matter: One-loop corrections in the renormalized perturbation theory framework. *Phys. Rev. D*, 81(2):023524, January 2010.

[170] V. Springel. The cosmological simulation code GADGET-2. *MNRAS*, 364:1105–1134, December 2005.

[171] V. Springel, S. D. M. White, A. Jenkins, C. S. Frenk, N. Yoshida, L. Gao, J. Navarro, R. Thacker, D. Croton, J. Helly, J. A. Peacock, S. Cole, P. Thomas, H. Couchman, A. Evrard, J. Colberg, and F. Pearce. Simulations of the formation, evolution and clustering of galaxies and quasars. *Nature*, 435:629–636, June 2005.

[172] A. A. Starobinsky. A new type of isotropic cosmological models without singularity. *Physics Letters B*, 91:99–102, March 1980.

[173] A. A. Starobinsky. Dynamics of phase transition in the new inflationary universe scenario and generation of perturbations. *Physics Letters B*, 117:175–178, November 1982.

[174] G. Steigman. Primordial Nucleosynthesis in the Precision Cosmology Era. *Annual Review of Nuclear and Particle Science*, 57:463–491, November 2007.

[175] K. T. Story, C. L. Reichardt, Z. Hou, R. Keisler, K. A. Aird, B. A. Benson, L. E. Bleem, J. E. Carlstrom, C. L. Chang, H.-M. Cho, T. M. Crawford, A. T. Crites, T. de Haan, M. A. Dobbs, J. Dudley, B. Follin, E. M. George, N. W. Halverson, G. P. Holder, W. L. Holzapfel, S. Hoover, J. D. Hrubes, M. Joy, L. Knox, A. T. Lee, E. M. Leitch, M. Lueker, D. Luong-Van, J. J. McMahon, J. Mehl, S. S. Meyer, M. Millea, J. J. Mohr, T. E. Montroy, S. Padin, T. Plagge, C. Pryke, J. E. Ruhl, J. T. Sayre, K. K. Schaffer, L. Shaw, E. Shirokoff, H. G. Spieler, Z. Staniszewski, A. A. Stark, A. van Engelen, K. Vanderlinde, J. D. Vieira, R. Williamson, and O. Zahn. A Measurement of the Cosmic Microwave Background Damping Tail from the 2500-Square-Degree SPT-SZ Survey. *ApJ*, 779:86, December 2013.

[176] S. J. Szybka. Light propagation in Swiss-cheese cosmologies. *Phys. Rev. D*, 84(4):044011, August 2011.

[177] A. Taruya, F. Bernardeau, T. Nishimichi, and S. Codis. Direct and fast calculation of regularized cosmological power spectrum at two-loop order. *Phys. Rev. D*, 86(10):103528, November 2012.

[178] I. Tereno, C. Schimd, J.-P. Uzan, M. Kilbinger, F. H. Vincent, and L. Fu. CFHTLS weak-lensing constraints on the neutrino masses. *A&A*, 500:657–665, June 2009.

[179] D. Tseliakhovich and C. Hirata. Relative velocity of dark matter and baryonic fluids and the formation of the first structures. *Phys. Rev. D*, 82(8):083520, October 2010.

[180] C. Uhlemann, M. Kopp, and T. Haugg. Schrödinger method as N-body double and UV completion of dust. *Phys. Rev. D*, 90(2):023517, July 2014.

[181] A. Upadhye, R. Biswas, A. Pope, K. Heitmann, S. Habib, H. Finkel, and N. Frontiere. Large-scale structure formation with massive neutrinos and dynamical dark energy. *Phys. Rev. D*, 89(10):103515, May 2014.

[182] P. Valageas. Using the Zeldovich dynamics to test expansion schemes. *A&A*, 476:31–58, December 2007.

[183] W. Valkenburg. Swiss cheese and a cheesy CMB. *JCAP*, 6:10, June 2009.

[184] N. Van de Rijt. Signatures of the primordial universe in large-scale structure surveys. PhD thesis, École Polytechnique, 2012.

[185] R. A. Vanderveld, É. É. Flanagan, and I. Wasserman. Luminosity distance in "Swiss cheese" cosmology with randomized voids. I. Single void size. *Phys. Rev. D*, 78(8):083511, October 2008.

[186] M. Viel, M. G. Haehnelt, and V. Springel. The effect of neutrinos on the matter distribution as probed by the intergalactic medium. *JCAP*, 6:15, June 2010.

[187] F. Villaescusa-Navarro, J. Miralda-Escudé, C. Peña-Garay, and V. Quilis. Neutrino halos in clusters of galaxies and their weak lensing signature. *JCAP*, 6:27, June 2011.

[188] F. Villaescusa-Navarro, M. Vogelsberger, M. Viel, and A. Loeb. Neutrino signatures on the high-transmission regions of the Lyman α forest. *MNRAS*, 431:3670–3677, June 2013.

[189] C. Wagner, L. Verde, and R. Jimenez. Effects of the Neutrino Mass Splitting on the Nonlinear Matter Power Spectrum. *ApJL*, 752:L31, June 2012.

[190] Y. Wang. Flux-averaging Analysis of Type IA Supernova Data. *ApJ*, 536:531–539, June 2000.

[191] Y. Wang. Supernova Pencil Beam Survey. *ApJ*, 531:676–683, March 2000.

[192] Y. Wang. Observational signatures of the weak lensing magnification of supernovae. *JCAP*, 3:5, March 2005.

[193] S. Weinberg. *Gravitation and Cosmology: Principles and Applications of the General Theory of Relativity*. July 1972.

[194] S. Weinberg. Gravitation and Cosmology: Principles and Applications of the General Theory of Relativity. *American Journal of Physics*, 41:598–599, April 1973.

[195] S. Weinberg. Apparent luminosities in a locally inhomogeneous universe. *ApJL*, 208:L1–L3, August 1976.

[196] S. Weinberg. Adiabatic modes in cosmology. *Phys. Rev. D*, 67(12):123504, June 2003.

[197] H. Weyl. *Phys. Z.,* **20**, 31, 1919.

[198] Y. Y. Y. Wong. Higher order corrections to the large scale matter power spectrum in the presence of massive neutrinos. *JCAP*, 10:35, October 2008.

[199] Y. B. Zel'dovich. Observations in a Universe Homogeneous in the Mean. Soviet Astr., 8:13, August 1964.

[200] Z.-S. Zhang, T.-J. Zhang, H. Wang, and C. Ma. Testing the Copernican principle with the Hubble parameter. *Phys. Rev. D*, 91(6):063506, March 2015.

Résumé de la thèse en français

Cosmologie de précision avec les grandes structures de l'univers

Introduction

Deux thématiques, chacune ancrée dans l'ère de la cosmologie de précision, sont abordées dans cette thèse. Dans un premier temps, c'est le principe cosmologique qui est questionné. Il s'agit de l'hypothèse selon laquelle, à très grande échelle[1] ($\gtrsim$ 100 Mpc), la distribution de matière dans l'univers est homogène et isotrope. En cosmologie moderne, la manière dont on interprète les données observationnelles est grandement influencée par ce principe de base. En collaboration avec Jean-Philippe Uzan et son étudiant Pierre Fleury, nous avons souhaité en savoir plus sur les limites de cette hypothèse. Plus précisément, nous avons testé l'effet induit par la présence de structures dans l'univers en simulant des observations de supernovae dans un univers fictif non homogène. Nous avons en particulier attiré l'attention sur le fait que, dans le contexte de la cosmologie de précision, il pourrait être pertinent d'adapter la modélisation géométrique de l'espace-temps à l'échelle spatiale considérée. En effet, les échelles caractéristiques explorées en cosmologie varient considérablement d'une observable à une autre. Or la géométrie de l'univers réel n'est pas la même à toute échelle.

Le second aspect de la cosmologie de précision traité dans cette thèse est le développement de la théorie des perturbations cosmologiques, notamment via l'exploration des régimes non linéaire et relativiste. Il s'agit de la tâche à laquelle j'ai consacré la grande majorité de mon temps pendant ma thèse. Avec mon directeur de thèse, Francis Bernardeau, j'ai proposé une nouvelle approche analytique visant

[1] pc est le symbole de parsec, qui vérifie 1 pc$\approx 3.1 \times 10^{16}$m.

à décrire efficacement la croissance non linéaire des perturbations dans des fluides où la dispersion en vitesse n'est pas nécessairement négligeable. Cette méthode, basée essentiellement sur une décomposition des fluides en ensembles de flots, est particulièrement adaptée à l'étude du rôle joué par les neutrinos sur la formation des grandes structures de l'univers. La phénoménologie des neutrinos (dans un contexte cosmologique) est donc également un domaine auquel je me suis intéressée pendant ma thèse.

Un exemple illustrant les enjeux de la cosmologie de précision

La cosmologie est une discipline atypique, notamment parce que l'univers est un objet d'étude particulier. Il ne peut être ni étudié de l'extérieur ni comparé à des systèmes similaires. De plus, on l'observe depuis une partie restreinte de celui-ci (la Terre et ses environs) pendant une durée limitée (période durant laquelle des êtres humains sont présents sur Terre). La distance à laquelle on peut observer est en outre finie car il faut du temps à la lumière pour se propager d'un point à un autre et, selon le modèle du Big Bang, l'univers n'a pas toujours existé. On parle d'horizon cosmologique pour définir la frontière de l'univers observable.

En raison de ces spécificités, les modèles cosmologiques contiennent nécessairement des hypothèses invérifiables, dont le principe cosmologique fait partie. En relativité générale, l'application de ce principe se traduit par l'utilisation d'une métrique homogène et isotrope, connue sous le nom de métrique de Friedmann-Lemaître.

L'univers réel n'est bien sûr pas parfaitement homogène. S'il l'était, la croissance des grandes structures par instabilité gravitationnelle n'aurait d'ailleurs pas été possible. L'explication actuellement privilégiée pour décrire l'amorçage de la croissance des structures est en effet la présence de gradients de densité dans l'univers primordial. Plus précisément, selon la théorie de l'inflation, un champ scalaire existait au départ et ses fluctuations quantiques (inévitablement présentes) seraient devenues macroscopiques en raison d'un épisode d'expansion extrêmement rapide (voir [7, 85, 89, 173, 30, 122]). Cela aurait engendré des fluctuations de métrique et donc inévitablement des fluctuations de densité (car en relativité générale la géométrie de l'espace-temps agit sur la matière, et inversement). Le processus d'instabilité gravitationnelle était alors lancé. L'étude de l'évolution de telles perturbations au cours

du temps est généralement réalisée à l'aide de la théorie des perturbations cosmologiques. Dans ce contexte, la métrique de Friedmann-Lemaître est remplacée par une métrique de Friedmann-Lemaître perturbée (c'est à dire une métrique contenant des corrections infinitésimales qui brisent l'homogénéité).

Dans la formulation la plus élémentaire du modèle standard de la cosmologie (en particulier, en l'absence de neutrinos), les caractéristiques de l'univers sont résumées par les valeurs de six paramètres, que l'on appelle paramètres cosmologiques. Ces valeurs ne peuvent être déterminées qu'observationnellement. Plusieurs sources offrent cette possibilité. Parmi elles, les plus largement utilisées sont les supernovae de type Ia (SNIa), les oscillations acoustiques de baryons (BAO) et le fond diffus cosmologique (CMB). Une supernova est un objet astrophysique résultant de l'explosion d'une étoile. Les SNIa, qui sont des supernovae dont le spectre contient du silicium mais pas d'hydrogène, sont utiles notamment pour retracer l'histoire de l'expansion de l'univers. Plus précisément, elles donnent des informations au sujet de l'équation d'état de l'énergie noire (voir [38, 146]). Les BAO sont des oscillations périodiques de la composante baryonique[2] de l'univers. La connaissance de leurs propriétés est également très utile à la cosmologie (voir notamment [5]). Le CMB est un rayonnement émis environ 380 000 ans après le Big Bang, lorsque la température de l'univers est devenue suffisamment basse pour que les photons puissent se propager librement. Les observations du CMB fournissent des estimations extrêmement précises des paramètres cosmologiques, en particulier lorsqu'elles sont combinées à d'autres données astrophysiques ([137]).

La théorie des perturbations cosmologiques appliquée au modèle standard de la cosmologie donne des résultats en très bon accord avec la réalité. Cela est en fait assez surprenant compte tenu de la simplicité du modèle et de la qualité des moyens mis en œuvre pour explorer minutieusement l'univers observable. Par exemple, une telle modélisation présuppose que la matière est distribuée de façon continue, ce qui sous-entend l'existence d'une échelle de lissage, non précisée dans le modèle ([68]). Cela est d'autant plus problématique que certaines observables cosmologiques sont des sources quasi-ponctuelles (d'un point de vue cosmologique), dont les faisceaux très étroits parcourent l'univers en sondant des échelles trop petites pour que le principe cosmologique soit applicable et pour que l'hypothèse de continuité soit valable. En particulier, l'échelle caractéristique associée à la largeur des faisceaux

[2]Baryonique signifie fait de baryons. En particulier la matière standard, faite d'atomes, est baryonique.

de SNIa est de l'ordre de l'unité astronomique[3]. L'utilisation non éclairée du principe cosmologique pourrait donc conduire à des erreurs d'interprétation (voir [33], parmi d'autres références). Ce genre de problématique est caractéristique de l'ère de la cosmologie de précision.

Déjà dans les années soixante, le paradoxe entre la structure réelle de l'univers et sa représentation lisse avait été mis en évidence. Des tentatives d'amélioration de la modélisation avaient alors été proposées ([199, 50, 19, 83, 98, 144]). Plus récemment, l'effet des fluctuations de densité sur les diagrammes de Hubble, qui sont des diagrammes construits principalement à partir de l'observation de SNIa et très utilisés en cosmologie moderne, a été étudié attentivement ([99, 80, 191, 190, 192]). Des approches reposant sur la théorie des perturbations cosmologiques ont également été proposées ([92, 39, 54]), sans toutefois que l'hypothèse de continuité soit remise en question. De tels modèles utilisent des échelles de lissage de l'ordre de la minute d'arc[4] alors que l'on s'attend à ce que l'essentiel de la dispersion induite par les structures dans les diagrammes de Hubble provienne d'échelles inférieures (voir par exemple [48]). De plus, il semble inapproprié de supposer que les fluctuations de densité rencontrées par les faisceaux de SNIa soient représentatives des fluctuations moyennes qui existent dans l'univers puisque, du fait de leur étroitesse, ces faisceaux se propagent beaucoup plus longuement dans des régions sous-denses que dans des régions sur-denses. Lorsqu'il s'agit d'interpréter les diagrammes de Hubble, il serait donc utile de tenir compte d'effets de sélection. Ces difficultés sont discutées de manière approfondie dans [33].

Les simulations numériques sont des alternatives aux modèles analytiques qui permettent de travailler en milieu non homogène. Cependant, leur résolution n'est pas infinie donc, même numériquement, la structure à petite échelle ne peut pas être modélisée avec précision. Dans [33], la limite qui est donnée est de quelques dizaines de kiloparsecs, ce qui est nettement supérieur à la largeur caractéristique d'un faisceau de supernova.

La première étude présentée dans cette thèse est une modélisation analytique de la propagation de la lumière dans un espace-temps de type *Swiss cheese*. Il s'agit d'un espace-temps obtenu en enlevant des sphères de matière à un milieu initialement homogène et isotrope et en remplaçant celles-ci par des masses ponctuelles, identiques aux masses enlevées (voir la figure 2 et les références [65, 158]).

[3] Une unité astronomique vaut environ 1.5×10^{11} m.

[4] La minute d'arc est une unité de mesure angulaire correspondant à un soixantième de degré.

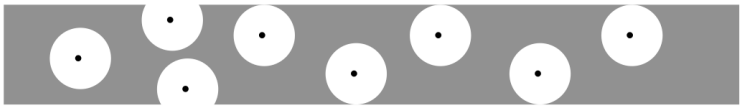

FIGURE 2 – Illustration représentant un espace-temps de type *Swiss cheese*. Le fond est homogène. Chaque sphère est vide sauf en son centre, où une masse ponctuelle est présente. La masse ponctuelle est égale à la densité du fond multipliée par le volume de la zone blanche qui l'entoure.

Notre modèle n'a pas pour vocation d'être réaliste mais de tester l'impact de variations de densité discontinues sur la propagation de la lumière. D'un point de vue théorique, il est autant justifié que la description standard car il s'agit d'une solution exacte de la relativité générale qui a la même dynamique globale que la métrique de Friedmann-Lemaître. Dans un premier temps, nous avons déterminé analytiquement la manière dont la propagation de la lumière est affectée par la traversée d'un trou. Après avoir implémenté le résultat dans un programme Mathematica, nous avons pu facilement prédire l'impact de la traversée d'un plus grand nombre de trous. Il a alors été possible de construire des diagrammes de Hubble théoriques en imaginant des faisceaux de supernovae se propageant dans un tel milieu. Pour y parvenir, nous nous sommes inspirés de données réelles provenant du catalogue SNLS 3 (voir [38]).

Le fait de recourir à des modèles de type *Swiss cheese* pour tester les limites du principe cosmologique n'est pas une idée nouvelle. La particularité de notre approche est qu'il ne s'agit ni d'une solution moderne de type Lemaître-Tolman-Bondi, dans laquelle les masses ponctuelles sont remplacées par des gradients de densité continus (voir [31, 116, 24, 185, 32, 35, 183, 176, 74, 200, 72, 73, 143, 151, 150, 121, 40, 149, 70]), ni d'un retour aux anciens modèles de type *Swiss cheese* ([98] et [62]) car le modèle cosmologique que nous utilisons est totalement ancré dans la cosmologie moderne.

Partant d'un observateur occupant une position quelconque de la partie non vide du *Swiss cheese*, nous avons reconstruit pas à pas les trajectoires suivies par les photons. La première étape consiste en l'identification des coordonnées de l'événement correspondant à la sortie du dernier trou traversé. En pratique, cela revient à résoudre l'équation des géodésiques du genre lumière dans la métrique de Friedmann-Lemaître. À l'intérieur de ce trou, la géométrie n'est pas la même. Elle est décrite par une métrique appelée métrique de Kottler. Nous avons donc ensuite

résolu les équations du mouvement dans la métrique de Kottler, afin d'identifier l'évenement correspondant à l'entrée du dernier trou traversé, puis sommes revenus à la métrique de Friedmann-Lemaître. L'impact de la présence de trous sur l'évolution de la largeur des faisceaux lumineux, et donc sur la luminosité finalement reçue par l'observateur, a quant à lui été étudié en résolvant à chaque étape l'équation de Sachs. Il s'agit d'une information cruciale car c'est cette luminosité qui figure en ordonnée des diagrammes de Hubble. La procédure décrite ci-dessus peut être renouvelée un nombre arbitraire de fois, jusqu'à ce que l'on décide que la source a été atteinte. En abscisse des diagrammes de Hubble, on trouve le décalage vers le rouge cosmologique associé à la source. Il a donc également été nécessaire de décrire l'évolution du nombre d'onde afin de comparer les valeurs à l'émission et à la réception et d'en déduire la valeur du décalage vers le rouge de chaque SNIa.

Dans un premier temps, nous avons traité nos diagrammes comme des données observationnelles standard, c'est à dire que nous avons utilisé le modèle homogène et isotrope pour déterminer (par le test du χ^2) les valeurs des paramètres cosmologiques à utiliser dans les équations pour reproduire au mieux ces données. Utilisant des barres d'erreur réalistes (car semblables à celles du catalogue SNLS 3), nous avons trouvé que l'estimation finale des paramètres cosmologiques peut être très éloignée des valeurs réelles utilisées pour construire notre milieu de propagation. Autrement dit, nous avons illustré la façon dont l'hypothèse d'homogénéité affecte l'interprétation des données. Le fait que l'estimation des paramètres cosmologiques dépende à ce point du modèle n'est pas anodin tant l'idée que l'on se fait de l'univers en cosmologie moderne repose sur cette estimation.

Dans notre étude, nous avons également analysé de vraies observations en supposant que l'univers réel avait une géométrie de type *Swiss cheese*. Nous avons pour cela dû dériver une formule analytique reliant la luminosité des SNIa à leur décalage vers le rouge cosmologique dans des espaces-temps de type *Swiss cheese*. Là encore, pour un même catalogue de données, les résultats obtenus peuvent nettement différer de ce qu'ils sont lorsque l'on suppose que la géométrie de l'univers est bien décrite par la métrique de Friedmann-Lemaître. Ce travail a donné lieu à une publication dans **Physical Review D** en 2013, [77].

L'enjeu est important puisque les résultats parus en 2013 de la mission Planck, [135], avaient révélé un désaccord entre l'estimation des paramètres h et Ω_{m} à l'aide d'observations du CMB et leur estimation à partir d'autres observables (en particulier des SNIa). Dans une deuxième étude publiée dans **Physical Review**

Letter en 2013, [76], nous démontrons que le modèle du *Swiss cheese* permet de rendre compatibles les estimations du paramètre Ω_{m}. Ceci est illustré sur la figure 3. Par ailleurs, les résultats 2015 de la mission Planck, [137], montrent que l'estimation de h par Planck est en fait compatible avec le catalogue récent de SNIa dont il est question dans [20], qui se nomme *Joint Light-curve Analysis*.

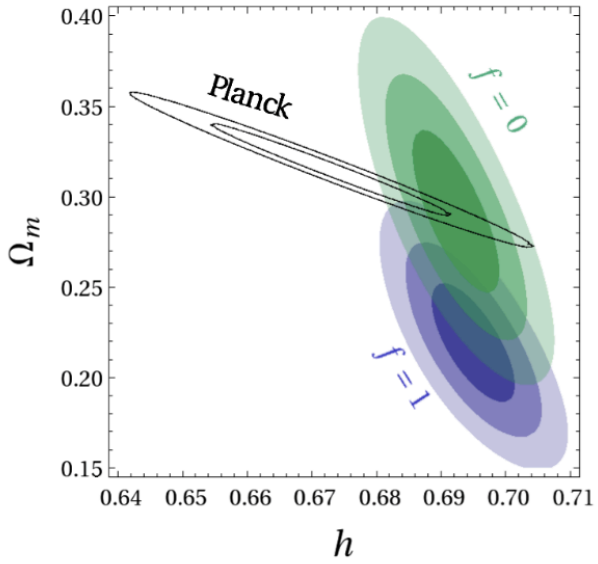

FIGURE 3 – Comparaison des contraintes sur (Ω_{m}, h) obtenues par Planck ([135]) et par le diagramme de Hubble construit à partir du catalogue SNLS 3 ([86]). f est un paramètre indiquant la fraction du volume qui n'est pas sous forme de trous. Par exemple, $f = 1$ correspond à une métrique de Friedmann-Lemaître.

Ces travaux illustrent les enjeux de la cosmologie de précision puisque c'est la structure très fine de l'univers qui est étudiée. Le but n'est pas de proposer de nouveaux modèles mais plutôt d'ajouter un degré de précision aux modèles existants. Dans le cas présent, la nouveauté serait d'adapter la représentation géométrique de l'univers à l'échelle considérée au lieu d'utiliser des modèles homogènes et isotropes, qui ne reflètent que l'univers lissé à grande échelle. On peut également développer la cosmologie de précision en travaillant avec les grandes structures de l'univers. Dans le cadre de la théorie des perturbations cosmologiques, l'effort est actuellement concentré sur le dépassement de la théorie linéaire et sur la prise en compte de constituants de l'univers négligés jusqu'alors dans les modèles. Il s'agit précisément du type d'activité entrepris pendant le reste de ma thèse.

Une nouvelle façon d'étudier les neutrinos en cosmologie

En théorie des perturbations dite standard (voir la revue [13]), on modélise la croissance des structures en décrivant l'effondrement gravitationnel de la matière noire froide, traitée comme un fluide non relativiste sans pression. Dans ce contexte, la physique newtonienne suffit. Un élément-clé de la description est l'hypothèse de flot unique. En effet, l'agitation thermique est minime dans les fluides froids si bien que l'on s'attend à ce que la dispersion en vitesse soit faible tant que les fluctuations de densité n'induisent pas des gradients de vitesse trop importants. C'est seulement à des stades plus avancés que la dispersion en vitesse devient conséquente. En effet, la gravité guide les particules vers les puits de potentiels, et ce quelles que soient leurs vitesses initiales, donc les particules sont amenées à se croiser au bout d'un certain temps. Ce phénomène, appelé croisement de coquilles, est illustré sur la figure 4.

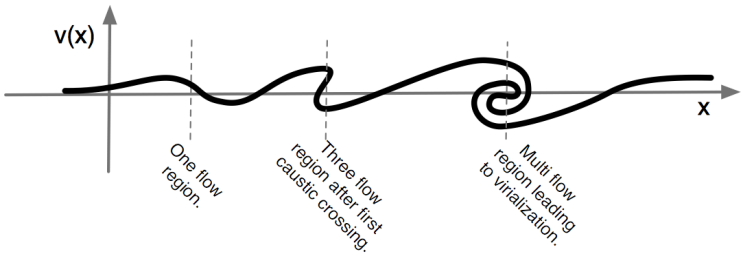

FIGURE 4 – Illustration schématique de l'émergence de régions multi-flots (croisement de coquilles) sous l'effet de la gravité. Les distances et les vitesses sont représentées comme des quantités unidimensionnelles. Auteur : Bernardeau, [12].

C'est durant cette phase tardive de virialisation que les objets astrophysiques tels que les galaxies commencent à se former (voir [22]). Malheureusement, dès lors que le croisement de coquilles est amorcé, l'évolution du système devient très difficile à modéliser analytiquement. Actuellement, les connaissances à ce sujet reposent donc majoritairement sur des simulations numériques à N corps.

Au contraire, avant l'apparition de croisements de coquilles, le fait de négliger la dispersion en vitesse dans les équations du mouvement rend possible de nombreux développements analytiques. On parle d'hypothèse de flot unique. Elle implique qu'à un instant et une position donnés, toutes les particules du fluide possèdent la même vitesse.

En cosmologie de précision, on cherche à décrire la croissance des grandes structures de la manière la plus rigoureuse possible. Afin de pouvoir modéliser analytiquement le rôle joué par des espèces autres que la matière noire froide, nous avons cherché une astuce permettant d'étendre le champ d'application de l'hypothèse de flot unique. L'idée que nous proposons est tout simplement de considérer chaque espèce relativiste non pas comme un fluide à plusieurs flots mais comme un ensemble de fluides à un flot. Plus précisément, à l'instant initial, nous considérons comme un fluide à part entière chaque ensemble de particules dont la vitesse est identique puis nous étudions séparément l'évolution des N flots correspondant aux N vitesses initiales. La discrétisation de l'espace des phases est illustrée sur la figure 5 pour $N = 11$. Les impulsions initiales sont caractérisées non seulement par une norme mais aussi par un sens et, dans les espaces à plusieurs dimensions, par une direction. Dans le cas des neutrinos, une telle décomposition ne pose pas de problème puisque, après leur découplage, les neutrinos n'interagissent plus entre-eux ou avec les autres espèces. Par conséquent, si les conditions initiales sont choisies après le découplage des neutrinos, aucune interaction non gravitationnelle n'a besoin d'être prise en compte. Sur l'image, les variations d'épaisseur des traits représentent des fluctuations de densité.

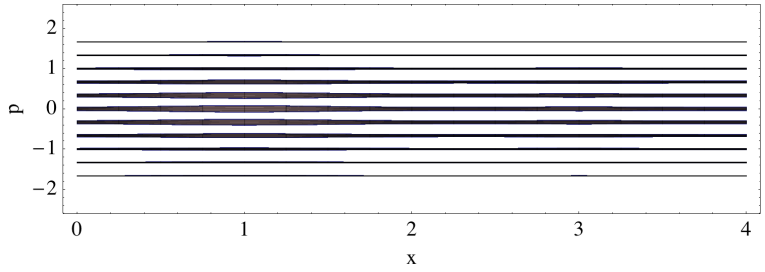

FIGURE 5 – Espace des phases discrétisé à l'instant initial pour un ensemble de onze flots. Dans chaque flot, les impulsions sont initialement homogènes. Les variations d'épaisseur représentent des fluctuations de densité. Par souci de simplicité, les impulsions et les positions ont été représentées comme des quantités unidimensionnelles.

Malgré l'homogénéité des champs de vitesses initiaux, la présence de fluctuations de densité fait apparaître des gradients de vitesse. Pour une masse donnée, les particules sont d'autant plus sensibles à ces fluctuations que la norme de leur vitesse initiale est petite puisque, dans ce cas, elles tombent facilement dans les

puits de potentiel. En particulier, le flot caractérisé par une impulsion initiale nulle se comporte précisément comme le fluide de matière noire froide. Le développement de fluctuations spatiales dans l'espace des impulsions est illustré sur la figure 6. Comme pour la matière noire froide, on s'attend à ce que des régions multi-flots finissent par apparaître. On voit clairement sur la figure 6 que cela se produira beaucoup plus tôt dans les fluides caractérisés par une faible vitesse initiale. Avant ces premiers croisements de coquilles, il est raisonnable de supposer que chaque fluide peut être étudié dans l'hypothèse de flot unique. Remarquons par ailleurs qu'il est probable que ces croisements surviennent uniquement lorsque les neutrinos seront devenus suffisamment lents pour pouvoir être décrits comme des espèces froides.

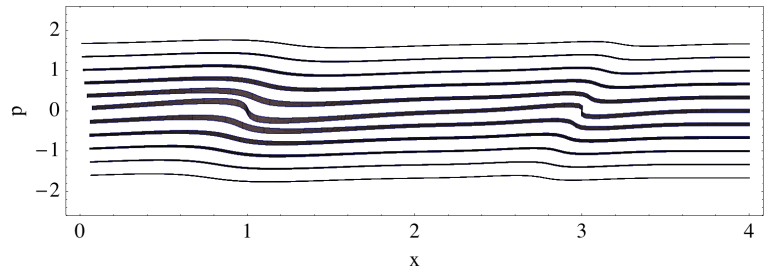

FIGURE 6 – Développement de gradients d'impulsion dans l'espace des phases discrétisé pour un ensemble de onze flots. Ce phénomène est généré par les fluctuations de densité, représentées ici par des variations d'épaisseur des traits.

Dans une telle approche, le comportement global des neutrinos est retrouvé en sommant les contributions des différents flots de la collection, à condition que le nombre de flots soit suffisant pour que l'échantillon soit représentatif. Par exemple, si on caractérise chaque flot par une vitesse initiale appelée $\vec{\tau}$, la fonction de distribution globale de l'espace des phases s'obtiendra de la façon suivante,

$$f^{\mathrm{tot}}(\eta, \mathbf{x}, \mathbf{p}) = \sum_{\vec{\tau}} f_{\vec{\tau}}(\eta, \mathbf{x}, \mathbf{p}), \tag{16}$$

ce qui donne dans la limite continue

$$f^{\mathrm{tot}}(\eta, \mathbf{x}, \mathbf{p}) = \int \mathrm{d}^3\tau f_{\vec{\tau}}(\eta, \mathbf{x}, \mathbf{p}), \tag{17}$$

avec $f_{\vec{\tau}}$ la fonction de distribution du fluide caractérisé par $\vec{\tau}$.

Symboliquement, le fait d'identifier les fluides par leurs vitesses initiales puis

de dériver des équations du mouvement spécifiques à chacun est analogue au choix d'adopter un point de vue lagrangien pour décrire l'évolution d'un fluide. La différence est que, dans la description lagrangienne, c'est la position initiale qui est utilisée comme label. Inversement, la description standard des neutrinos reposant sur l'étude de $f^{\rm tot}(\eta, \mathbf{x}, \mathbf{p})$ se rapproche d'une description eulérienne.

Une fois les flots définis à l'instant initial, le nombre de particules contenues dans chacun d'eux est constant. Mathématiquement, la conservation du nombre de particules se traduit par une équation de continuité. En relativité générale, elle est donnée par la conservation de la quantité J^μ, appelée quadri-courant,

$$J^\mu_{\ ;\mu} = 0. \tag{18}$$

Le quadri-courant est l'analogue quadri-dimensionnel de la densité de courant de la physique classique. Il s'agit donc d'un débit. Par conséquent, il peut s'exprimer en termes d'une densité et d'une vitesse ou d'une impulsion. Les variables que nous avons choisi d'utiliser sont les suivantes :

- la densité numérique comobile $n_c(\eta, \mathbf{x})$, définie comme le nombre de particules par unité de volume comobile d^3x^i,
- le champ d'impulsion comobile $P_i(\eta, \mathbf{x})$.

La densité numérique comobile peut facilement être reliée à la fonction de distribution dans l'espace des phases. En effet, par définition,

$$n_c(\eta, \mathbf{x}) = \int \mathrm{d}^3p_i \ f(\eta, x^i, p_i) \tag{19}$$

et $P_i(\eta, \mathbf{x})$ est tout simplement la valeur moyenne des impulsions comobiles de l'espace des phases,

$$P_i(\eta, \mathbf{x}) = \frac{\int \mathrm{d}^3p_i \ f(\eta, x^i, p_i) p_i}{\int \mathrm{d}^3p_i \ f(\eta, x^i, p_i)}. \tag{20}$$

Par ailleurs, le quadri-courant satisfait la relation (voir par exemple [18])

$$J^\mu(\eta, \mathbf{x}) = -\int \mathrm{d}^3p_i (-g)^{-1/2} \frac{p^\mu}{p^0} f(\eta, x^i, p_i), \tag{21}$$

où g est le déterminant du tenseur métrique.

L'approximation de flot unique est particulièrement utile dans ce contexte. En effet, à un instant η et une position $\mathbf{x}$ donnés, toutes les particules du fluides ont

une impulsion $P_i(\eta, \mathbf{x})$, d'où

$$f(\eta, x^i, p_i) = n_c(\eta, \mathbf{x})\delta_{\rm D}(p_i - P_i(\eta, \mathbf{x})). \tag{22}$$

L'équation de continuité (18) impose alors

$$\partial_\eta n_c + \partial_i \left(\frac{P^i}{P^0} n_c \right) = 0. \tag{23}$$

Dans l'hypothèse du flot unique, le tenseur énergie-impulsion vérifie (voir encore [18])

$$T^{\mu\nu} = -P^\mu J^\nu. \tag{24}$$

En combinant la conservation du quadri-courant à celle du tenseur énergie-impulsion, on trouve finalement

$$P^\mu{}_{;\nu} J^\nu = 0, \tag{25}$$

d'où notre seconde équation du mouvement

$$P^\nu \partial_\nu P_i = \frac{1}{2} P^\sigma P^\nu \partial_i g_{\sigma\nu}. \tag{26}$$

Notre approche permet de suivre individuellement le comportement des différents flots de neutrinos mais, ce qui est intéressant pour la cosmologie, c'est surtout leur comportement global. Nous avons donc exprimé les premiers multipôles de la distribution globale d'énergie en fonction des variables individuelles que nous avions choisies. De manière très générale, ces multipôles sont donnés par (dans l'espace réciproque, voir [111]) :

$$\rho_\nu \equiv -T^0{}_0, \tag{27}$$

$$\left(\bar{\rho}_\nu + \bar{P}_\nu\right) \theta_\nu \equiv \mathrm{i} k^i T^0{}_i, \tag{28}$$

$$\left(\bar{\rho}_\nu + \bar{P}_\nu\right) \sigma_\nu \equiv -\left(\frac{k^i k^j}{k^2} - \frac{1}{3}\delta_{ij} \right) \left(T^i{}_j - \frac{1}{3}\delta^i_j T^k{}_k \right), \tag{29}$$

où $\bar{X}$ désigne la partie homogène de la quantité X et avec ([18])

$$T^{\mu\nu}(\eta, \mathbf{x}) = \int \mathrm{d}^3 p_i (-g)^{-1/2} \frac{p^\mu p^\nu}{p^0} f(\eta, x^i, p_i). \tag{30}$$

Dans notre approche, les intégrales sur les impulsions de l'espace des phases sont à remplacer par des intégrales sur les différents flots, ou de manière équivalente sur les impulsions initiales $\vec{\tau}$. D'après (17) et (22), on a

$$f^{\mathrm{tot}}(\eta, x^i, p_i) = \int \mathrm{d}^3\tau_i \, n_c(\eta, \mathbf{x}; \vec{\tau}) \delta_{\mathrm{D}}(p_i - P_i(\eta, \mathbf{x}; \vec{\tau})), \tag{31}$$

d'où (pour toute fonction $\mathcal{F}$ des impulsions)

$$\int \mathrm{d}^3 p_i \, f^{\mathrm{tot}}(\eta, x^i, p_i) \; \mathcal{F}(p_i) = \int \mathrm{d}^3\tau_i \, n_c(\eta, \mathbf{x}; \vec{\tau}) \; \mathcal{F}(P_i(\eta, \mathbf{x}; \vec{\tau})). \tag{32}$$

Cette formule nous a permis d'exprimer sans difficultés les multipôles en fonction de nos variables. Habituellement, la seule manière de les calculer est d'intégrer la hiérarchie de Boltzmann, obtenue en calculant les moments successifs de l'équation de Boltzmann. En pratique, il est nécessaire de linéariser et de tronquer cette hiérarchie pour qu'elle soit intégrable numériquement. Afin de tester la validité de notre approche, nous avons donc calculé numériquement l'évolution temporelle de nos multipôles dans le régime linéaire et comparé nos résultats aux résultats standard. Ces calculs ont été faits en imposant des conditions initiales adiabatiques, choisies lorsque les neutrinos sont déjà découplés des autres espèces mais encore relativistes. En effet, dans ce contexte, la fonction de distribution initiale des neutrinos est connue et l'hypothèse de flot unique permet d'en déduire les valeurs initiales de nos champs.

Les conclusions que nous avons tirées de ce test numérique sont les suivantes.

- À grande échelle, c'est la discrétisation des normes des impulsions qui est déterminante pour que l'accord entre les deux méthodes soit satisfaisant. En revanche, la discrétisation des directions initiales importe peu. Par exemple, en prenant 12 directions différentes, en tronquant la hiérarchie de Boltzmann à l'ordre 6 et en considérant des neutrinos de masse $m = 0.05$ eV, les erreurs relatives moyennes passent de 10^{-2} à 10^{-4} quand le nombre de normes d'impulsions (dans chaque approche) passe de 16 à 100 lorsque $k = 0.002h/\mathrm{Mpc}$.
- Pour $k \gtrsim 0.01h/\mathrm{Mpc}$, l'intégration numérique est plus ardue car les équations du mouvement des flots de la collection deviennent très différentes les unes des autres (autrement dit, dépendent plus fortement des vitesses initiales). Il faut par exemple utiliser 100 directions différentes pour obtenir une précision de l'ordre du pourcent lorsque $k = 0.1h/\mathrm{Mpc}$.

- En choisissant des masses plus petites, il faut également affiner la discrétisation puisque, dans ce cas, la dépendance des champs de vitesses et de densités vis-à-vis de $\vec{\tau}$ est plus grande.

- Aux temps longs, tous les flots se comportent comme la matière noire froide.

Les tests numériques montrent sans ambiguïté que les deux approches sont compatibles dans le régime linéaire. Par exemple, un accord avec une précision de 10^{-3} (obtenu pour $k = 0.01h/\text{Mpc}$ et $m = 0.3$ eV) est présenté sur la figure 7, qui compare les comportements des premiers multipôles énergétiques. L'inconvénient majeur de notre méthode est que, pour que l'accord soit satisfaisant, le nombre d'équations à résoudre doit généralement être plus important dans notre approche que dans l'approche de Boltzmann. Toutefois, notre modèle analytique est valable au-delà du régime linéaire, ce qui n'est pas le cas de l'approche de Boltzmann. De plus, les grandes similitudes qui existent entre notre étude et celle de la matière noire froide permettent d'espérer d'importants développements basés sur nos équations. Cette étude à été publiée dans **JCAP** en 2014, [57].

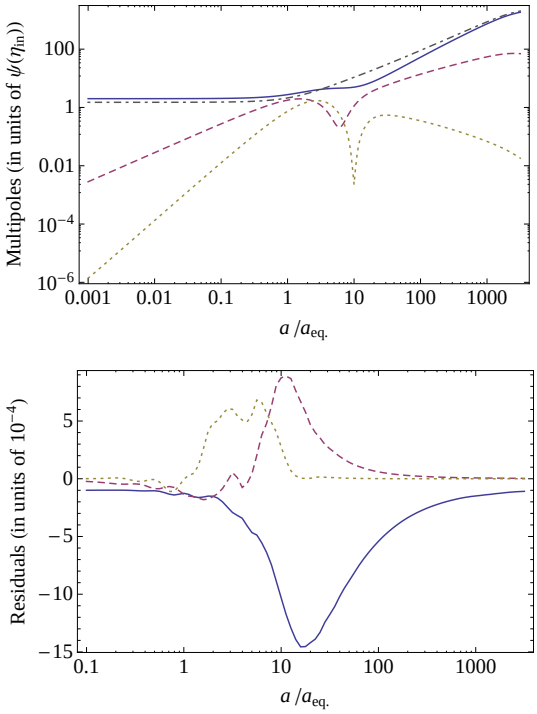

FIGURE 7 – Évolution temporelle du contraste de densité d'énergie (ligne continue), de la divergence des vitesses (tirets) et de la pression anisotrope (points) des neutrinos. Dans la partie haute, les quantités sont calculées à partir de nos équations. La partie basse montre les erreurs relatives entre les deux approches. L'intégration numérique a été réalisée en utilisant 40 normes d'impulsions et 12 directions initiales. k est fixé à $0.01h$/Mpc et m à 0.3 eV.

Vers une extension de la théorie des perturbations cosmologiques au régime relativiste

Par la suite, nous avons utilisé l'approche multi-fluides précédente pour généraliser au cas relativiste certains résultats majeurs de la théorie des perturbations non linéaires. Afin de rendre les équations du mouvement plus faciles à manipuler, nous avons choisi d'éliminer les termes de couplage qui ne sont pas indispensables pour décrire la formation des structures. Plus précisément, nous avons utilisé le rayon de Hubble[5] comme échelle caractéristique et nous nous sommes concentrés sur les échelles subhorizon, c'est à dire les échelles inférieures au rayon de Hubble. En effet,

[5]Le rayon de Hubble donne l'ordre de grandeur du rayon de l'univers observable.

la croissance non linéaire des structures est un processus récent dans l'histoire de l'univers donc les termes qui deviennent petits aux échelles subhorizon ne sont *a priori* pas déterminants dans ce contexte. Le premier résultat que nous avons pu généraliser en travaillant dans la limite subhorizon est le fait que, à tout ordre de la théorie des perturbations, la partie rotationnelle des champs d'impulsions est négligeable. Cela signifie que ces variables sont entièrement caractérisées par leurs divergences. Or cette propriété, également satisfaite par le champ de vitesses du fluide de matière noire froide, est capitale dans la description standard newtonienne (voir [12]). L'intérêt principal de notre approche est l'universalité des équations. En effet, après le découplage, les seuls éléments permettant de distinguer les baryons, la matière noire froide et les neutrinos sont leurs masses et vitesses initiales. En introduisant un $2N$-uplet

$$\Psi_b(\mathbf{k}) = (\delta_{\vec{\tau}_1}(\mathbf{k}), -\theta_{\vec{\tau}_1}(\mathbf{k}), \ldots, \delta_{\vec{\tau}_N}(\mathbf{k}), -\theta_{\vec{\tau}_N}(\mathbf{k}))^T, \tag{33}$$

où chaque δ est un contraste de densité et chaque θ une divergence de vitesse, on peut donc encoder le comportement de tous les fluides cosmiques découplés dans une équation unique (les expressions des matrices ${\Omega_b}^c$ et ${\gamma_b}^{cd}$ sont données dans la thèse) :

$$a(\eta)\partial_a\Psi_b(\mathbf{k},\eta) + {\Omega_b}^c(\mathbf{k},\eta)\Psi_c(\mathbf{k},\eta) = {\gamma_b}^{cd}(\mathbf{k}_1,\mathbf{k}_2,\eta)\Psi_c(\mathbf{k}_1,\eta)\Psi_d(\mathbf{k}_2,\eta). \tag{34}$$

Cette équation est formellement identique à l'équation-clé sur laquelle repose la théorie des perturbations standard dans le régime non linéaire. La différence capitale est que tous les fluides, relativistes ou non, sont ici pris en compte alors que l'équation standard ne modélise que l'évolution de la matière noire froide. Comme expliqué dans la thèse, nous avons également mis en évidence des propriétés d'invariance de manière à généraliser certaines relations de consistance permettant de relier des fonctions de corrélation d'ordre n à des fonctions de corrélation d'ordre $n+1$. Ce travail prépare le terrain pour l'implémentation de techniques de resommation très utiles à la description de la croissance non linéaire des grandes structures de l'univers (voir [45, 117, 133, 46, 177] pour la présentation de telles techniques). Cela a débouché sur une publication dans **JCAP** en 2015, [58].

Une application concrète de la description multi-fluides des neutrinos

En cosmologie, le spectre de puissance de la matière est une quantité cruciale permettant de décrire la distribution statistique de la matière dans l'univers. On le définit comme la fonction de corrélation à deux points des contrastes de densité de matière. La modélisation analytique de l'effet des neutrinos sur ce spectre de puissance dans le régime non linéaire est un travail de longue haleine. Pour atteindre cet objectif, il est utile dans un premier temps d'identifier les échelles auxquelles il sera pertinent de tenir compte des couplages non linéaires dans les équations du mouvement impliquant les neutrinos. Dans ma thèse, j'ai utilisé l'approche multi-fluides décrite ci-dessus dans ce but.

La forme de l'équation (34) permet l'implémentation de l'approximation eikonale, décrite dans [14] et [16] dans le cas non relativiste, qui consiste en la décomposition du membre de droite de (34) en deux domaines appelés *hard domain* et *soft domain* puis en l'élimination du *hard domain*. Le *hard domain* contient les couplages entre modes de longueurs d'onde comparables tandis que le *soft domain* décrit les couplages entre modes de grande et de petite longueurs d'onde. La correction apportée par le *soft domain* par rapport à l'équation linéarisée (c'est à dire l'équation (34) dans laquelle le membre de droite est fixé à zéro) peut être vue comme une perturbation du milieu. Généralement, cette perturbation est décrite par un champ de déplacement, dont l'expression généralisée au régime relativiste est explicitement donnée dans ma thèse. Cela découle directement des propriétés d'invariance que nous avons mises en évidence dans [58]. Comme expliqué dans [179] et [17], lorsque les champs de déplacement ne sont pas les mêmes dans tous les fluides (on parle alors de déplacements non adiabatiques), les perturbations de chacun ne sont plus en phase les unes avec les autres. Cela ralentit la chute des espèces autres que la matière noire froide dans les puits de potentiel, et donc finalement la croissance des structures. Nous avons donc calculé les champs de déplacement relatifs entre matière noire froide et neutrinos et tracé les résultats en fonction de k afin de déterminer les échelles auxquelles l'amortissement du spectre de puissance dû aux couplages entre modes de grande et de petite longueurs d'onde peut être conséquent. L'estimation préliminaire que nous avons trouvée correspond aux échelles dont les nombres d'ondes sont supérieurs (ou de l'ordre de) 0.2 à 0.5 h/Mpc pour des masses de 0.3 eV. Cependant, une étude nettement plus approfondie est nécessaire pour

pouvoir tirer des conclusions solides à ce sujet. Le but de notre travail était plutôt d'attirer l'attention sur la possibilité de généralisation du lien entre approximation eikonale, déplacements relatifs entre fluides cosmiques et amortissement du spectre de la matière dans le régime non linéaire. Les résultats correspondants ont été publiés dans **JCAP** en 2015, [59].

Conclusions et perspectives

Cette thèse fournit des résultats innovants de plusieurs types. Leur point commun est la quête de précision dans la description des phénomènes physiques à l'œuvre dans l'univers.

D'abord, un modèle-jouet simulant la propagation de la lumière dans un espace-temps non homogène est présenté. Dans cette étude, nous avons opté pour la traditionnelle représentation de type *Swiss cheese*. Souvent utilisée dans la littérature, elle permet de travailler avec des solutions exactes de la relativité générale, qui n'altèrent pas la dynamique globale de l'univers tout en le rendant fortement non homogène. Nous avons illustré la façon dont les hypothèses de base, telles que le principe cosmologique, peuvent affecter les conclusions scientifiques, telles que l'estimation des paramètres cosmologiques à partir des diagrammes de Hubble. En général, le biais causé par le fait d'introduire des trous dans un espace homogène et isotrope peut être grand en raison de la grande sensibilité de la luminosité des sources vis-à-vis de la géométrie du milieu traversé. Nous avons montré que ce biais décroît avec la constante cosmologique, ce qui est une chance puisque les observations penchent clairement vers un contenu de l'univers dominé par l'énergie noire (et donc par la constante cosmologique dans le modèle standard). En raison de son extrême simplicité, notre modèle (dont les fluctuations de densité sont exagérément abruptes) surestime probablement le biais. En effet, les grandes structures, le gaz intergalactique, la matière noire, etc. agissent comme des lisseurs dans l'univers réel. Les effets de compensation entre régions de densités inférieure et supérieure à la moyenne sont indéniables. Nous sommes toutefois convaincus que, en cosmologie de précision, cela vaut la peine d'étudier minutieusement ce genre de problématique plutôt que d'accepter qu'il y ait une incohérence entre les échelles auxquelles le principe cosmologique est valide et celles sondées par les SNIa utilisées pour construire les diagrammes de Hubble. N'oublions pas que les paramètres cosmologiques sur lesquels repose la cosmologie moderne dépendent fortement des modèles utilisés

donc le fait de les mesurer avec une très grande précision n'est pas suffisant pour affirmer que leurs valeurs reflètent la réalité.

Cette thèse présente aussi une étude dans laquelle les résultats de la mission Planck d'une part et les observations du catalogue de supernovae SNLS 3 d'autre part sont interprétés en modélisant la géométrie de l'univers par un espace-temps de type *Swiss cheese*. Nous avons montré que l'estimation du paramètre cosmologique Ω_{m} à partir des diagrammes de Hubble peut alors être très différente de ce qu'elle est dans le modèle homogène et isotrope, allant jusqu'à une possible réconciliation avec les résultats de la mission Planck. Évidemment, les espaces-temps de type *Swiss cheese* ne sont pas des représentations réalistes de l'univers. Ils permettent simplement de montrer que l'incompatibilité entre les différentes observables peut venir du fait qu'elles sondent l'univers à des échelles très différentes. Avec l'amélioration de la précision de l'estimation des paramètres cosmologiques, un travail sur la modélisation géométrique de l'espace-temps pourrait être judicieux, voire nécessaire.

Notre approche peut être améliorée de multiples façons. On pourrait notamment introduire des trous de tailles différentes afin d'avoir davantage de libertés concernant la proportion de régions vides. L'étude de données autres que les diagrammes de Hubble, obtenues en remplaçant les photons par d'autres particules, constitue également une piste intéressante. Une modélisation plus réaliste de l'univers, basée sur une étude approfondie de la structure réelle de l'univers, pourrait aussi être bénéfique. Toutefois, pendant ma thèse, je me suis spécialisée dans une autre branche de la cosmologie, à savoir l'étude de la formation des grandes structures de l'univers à l'aide de la théorie des perturbations. Mon collaborateur Pierre Fleury a quant à lui consacré une grande partie de sa thèse (soutenue également cette année) à l'étude de la propagation de la lumière en milieu non homogène et/ou non isotrope (voir notamment [78], [75]).

Le résultat majeur proposé dans cette thèse est une nouvelle façon de décrire les neutrinos en cosmologie. L'idée est de décomposer les neutrinos en plusieurs fluides à un flot de manière à se débarrasser de la dispersion en vitesse dans chacun d'eux. Les équations du mouvement correspondantes, non linéaires, ont été dérivées à partir de lois de conservation dans une métrique de Friedmann-Lemaître perturbée quelconque, tout comme les formules permettant de retrouver les grandeurs physiques globales en sommant sur les différents flots. En utilisant ces formules pour calculer la distribution multipolaire d'énergie, nous avons montré que notre

approche est totalement compatible avec l'intégration de la hiérarchie de Boltzmann dans le régime linéaire. Nous pensons que notre approche fournit une base plus appropriée à l'étude du comportement non linéaire des neutrinos que la hiérarchie de Boltzmann. Elle fournit de plus une information supplémentaire puisque les flots de neutrinos peuvent être examinés individuellement. Cette méthode peut être appliquée aux neutrinos et, plus généralement, à n'importe quelle espèce en chute libre. Dans ce cadre, la matière noire froide apparaît comme un simple fluide de la collection, dont la seule particularité est d'avoir une vitesse initiale nulle. N'importe quelle vitesse (relativiste ou non) et n'importe quelle masse peuvent être gérées par ce formalisme.

Sur cette base, nous avons mené une étude dédiée à l'exploration de la structure de couplage de nos équations restreintes aux échelles subhorizon. L'intérêt de cette hypothèse est de mettre en évidence des propriétés utiles sans éliminer les termes qui sont pertinents pour décrire la croissance non linéaire des structures. Nous avons ainsi pu résumer en une équation les processus en jeu dans l'évolution des perturbations cosmologiques. L'avantage de cette équation est qu'elle est aussi simple que l'équation de la théorie des perturbations standard tout en ayant un champ d'application beaucoup plus large. C'est pourquoi on peut espérer que notre approche constitue un pas de plus vers une généralisation relativiste de la théorie des perturbations non linéaire. Nous avons délibérément travaillé dans une jauge quelconque de manière à faciliter la mise en évidence de propriétés d'invariance, ce qui nous a permis de dériver des relations de consistance et d'étudier les couplages entre modes de grande et de petite longueurs d'onde à l'aide de l'approximation eikonale.

L'un de nos articles a été entièrement dédié à l'implémentation de cette approximation dans nos équations du mouvement. Nous avons ainsi pu monter que, pour des grands nombres d'ondes et des vitesses initiales importantes, les champs caractérisant les neutrinos peuvent être déphasés par rapport à ceux de la matière noire froide pendant une durée importante. Cela ralentit naturellement la croissance des grandes structures de l'univers.

Les perspectives les plus évidentes offertes par ce point de vue multi-flots sont les suivantes. Formellement, les techniques de resommation standard permettant de calculer les corrections non linéaires du spectre de puissance de la matière pourraient être étendues à notre équation globale. Cependant, le formalisme en jeu est très lourd donc le fait de remplacer brutalement les matrices 2×2 par des matrices

$N \times N$, qui possèdent de plus des parties imaginaires dépendantes d'échelle, serait rédhibitoire. La suite exigera donc de trouver des arguments permettant de diminuer la complexité du problème. D'une part, il sera crucial d'identifier les échelles auxquelles à la fois les non-linéarités et les corrections relativistes doivent être prises en compte. La dernière étude présentée dans la thèse est un premier pas en ce sens. En pratique, puisque les non-linéarités se développent tardivement tandis que les plus grandes vitesses correspondent aux époques les plus anciennes, on peut s'attendre à beaucoup de simplifications. D'autre part, la détermination du nombre de flots nécessaire pour que la description soit acceptable (au sens de la cosmologie de précision) sera essentielle. Avec Julien Lesgourgues, j'ai commencé à implémenter les équations du mouvement dans son code `CLASS` ([28]). Les résultats que nous obtiendrons devraient se révéler utiles pour tester efficacement le coût numérique associé et envisager des simplifications bien contrôlées.